The Jovian hectometric radiation

Hans Peter Ladreiter, Hans Peter Ladreiter, Directeurs De, Yolande Leblanc, Helmut Rucker

The Jovian Hectometric Radiation

by Hans Peter Ladreiter

Le rayonnement hectométrique jovien

Directeurs de thèse : Yolande Leblanc et Helmut O. Rucker
Thèse préparée à l'Observatoire de Paris et
à l'Institute of Meteorology and Geophysics, University of Graz (Autriche
Thèse soutenue en 1990

This thesis was performed during the years 1988 - 1990 at the Observatoire de Paris, France, and at the Institute for Meteorology and Geophysics of the University of Graz, Austria.

The Jovian Hectometric Radiation

by Hans Peter Ladreiter

This thesis was performed during the years 1988 - 1990 at the Observatoire de Paris, France, and at the Institute for Meteorology and Geophysics of the University of Graz, Austria.

Acknowledgments

First of all I must express my thanks to my supervisors Dr. Yolande Leblanc (Observatoire de Paris) and UD Dr. Helmut O. Rucker (Space Research Institute of the Austrian Academy of Sciences) for their overall support and for contributing useful ideas during the development of this work. I am also grateful to my colleagues of the "groupe decametrique" at the Observatoire de Paris for their generous hospitality and many discussions on the subject of radio astronomy. In particular, I am grateful to Philippe Zarka, Alain Lecacheux, Sophie Dubus, Jean-Luc Anton, Mohammed Boudjada, and Patrick Galopeau for the kind introduction in the "French way of life".

I continue to be deeply indebted to Professor Siegfried J. Bauer, the head of the Institute for Meteorology and Geophysics at the University of Graz, for the overall support concerning the education when I was a research student. Special thanks to all colleages at the Space Science Institute and at the Institute for Meteorology and Geophysics, especially to Gerald K. F. Rabl, Wolfgang Macher, Wolfgang Voller, Martina Zhang, Gottfried Kirchengast, UD Dr. Reinhart Leitinger, Dr. Erich Putz, and Dr. Valentin Mostetschnig for many helpful discussions on several scientific topics. Additionally, I express my thanks to Wolfgang Voller for his advices to finally obtain an excellent layout of the present work.

But I am indebted most of all to my family, especially my parents and my girl-friend Gertraud for their help and guidance through my life.

Preface

Planetary radio astronomy was "born" since the accidental discovery of the Jovian decametric radio emission in 1955 from ground-based observatories. Since then, there have been many major advances that affect the study of radio wave propagation as well as the possibility of observations via spacecraft missions. The most relevant so far is the recent Voyager mission which has enabled the observation of in situ phenomena in the magnetospheres of the outer planets as well as the observation of low frequency radio emissions emanating from the giant planets Jupiter, Saturn, Uranus, and Neptune. Simultaneously, important advances of the subject "plasma physics" were undertaken which enabled us to easier interpret the Voyager observations.

In the course of the author's activity in the field of planetary radio astronomy, it has been found that no suitable studies exist for investigating the characteristics of the Jovian nonthermal radio emission in the hectometric frequency range. It is a particular aim of the present work to fill this gap.

This study intends to provide a brief survey of physical processes in the Jovian magnetosphere which is relevant in association with the radio emissions. For the hectometric emission component, a detailed analysis is developed to explain the characteristics and phenomena in terms of its source location, beaming properties, and generation mechanism. The work is divided into several chapters which generally discuss the more detailed analyses and elaborations given in the respective appendices. The appendices are of primary interest for readers who aim to obtain a detailed view of the entire work. Each appendix is prefaced by an abstract which contains the most important findings. Appendices A - D were singled out for publication in international journals. At the end of this book there is a list of references both to text books and to published papers. But no attempt has been made to provide a complete list of all important papers since they are far to numerous.

Graz, March 1990 H. P. Ladreiter

Contents

Introduction

The first idea of a magnetic cavity around a planet (the earth) was first postulated by Chapman and Ferraro already in the early thirties. The interest in studies of such a magnetic cavity which is called "magnetosphere" was reinforced since the accidental discovery of the nonthermal Jovian decametric radiation (DAM) by Burke and Franklin (1955). However, it was Shain already in 1950 who first observed a radio emission at 18.3 MHz, but it was not yet attributed to Jupiter. This radiation indicated that Jupiter exhibits an intrinsic magnetic field, whereby the radio emission is caused by electrons spiralling around magnetic field lines in the vicinity of the planet, finding confirmed by the discovery of the Jovian decimetric radiation and the earth's Van Allen belts by the satellites Explorer 1 and 3 in 1958.

Later on (1961), the terrestrial magnetosphere was explored by the satellite Explorer 10 which also determined the boundary of the magnetosphere, the so-called magnetopause. In the solar direction the shape of the magnetopause is approximately a half ellipsoid. The size can be estimated by setting equal the dynamic pressure of the solar wind (supersonic ionized particle stream originating from the upper solar atmosphere) to the magnetic pressure due to the planet's magnetic field. Inside the magnetopause the influence of the planet's magnetic field on the particles gains over the solar wind influence. Thus, physical processes within the magnetosphere are highly controlled by the planetary magnetic field and the rotation of the planet which additionally leads to the generation of electric fields.

Since the Voyager 2 Neptune flyby in August 1989 five well extended planetary magnetospheres are now explored in our solar system: Earth, Jupiter, Saturn, Uranus, and Neptune. All of these magnetospheres have their own characteristics mainly due to different magnetic dipole moments and directions, different planetary spin periods and distances to the sun.

All these magnetized planets emit nonthermal radiation which is either trapped inside the magnetospheric cavity or escaping from the planet into free space. The sources of the trapped radiation with frequencies genearally below 5 kHz are located at the edges of the plasma sheet (current system in the magnetic equatorial plane) and/or the magnetopause boundaries; the radio sources of the escaping radiation are mostly located in the auroral zones where solar wind particles are precipitating into the ionosphere of the planet. In some specific cases, the radiation may also be generated in the magnetic equatorial plane. The various radio sources are characterized by the specific beaming of the generated radiation and the source activity may be affected by solar wind fluctuations. The knowledge of the polarization of the emission is of prime interest for the determination of the radiation mechanism.

Jupiter is the most powerful and complex radio planet. This fact is due to the strength of its magnetic field, to the presence of Van Allen belts, and to the formation of a plasma torus at the orbit of the satellite Io. In the Jovian radio spectrum (Figure 1.3) we can distinguish the decametric and hectometric components which are believed to escape from auroral zones, and the kilometric radiation emitted from sources at the Io plasma torus. The decimetric or synchrotron radiation is originating from the Jovian Van Allen belts.

We have focussed this study on the Jovian hectometric radiation (hereafter HOM) which has been discovered by the Planetary Radio Astronomy experiment aboard the Voyager spacecraft, well before the first encounter in 1979. Except a few studies published after the encounters of Jupiter by Voyager 1 and Voyager 2, many outstanding problems remained unanswered, e.g. is

the HOM just an extension of DAM or is it a distinct component ? Where is the location and what is the extension of the source, and is it a corotating source ? What is the polarization of the emission ? How does the Io plasma torus act on the HOM emission ? What about the generation mechanism of HOM ? In this study we have considered all these questions using V1 and V2 data recorded in 1979, including the V1 and V2 encounters.

In the first chapter we give a description of the Jovian magnetosphere, the interaction with the solar wind, and we discuss the several Jovian radio components. In chapter 2 the characteristics of the hectometric radiation are determined; the effect of latitudinal beaming at 3 frequencies, the local time dependence, the solar wind control on the beaming, and the source extension. In particular we give a hint for the source extension in altitude determined from the low-frequency limit of HOM. We establish that right-hand polarization is associated with sources in the northern hemisphere and left-hand polarization with sources in the southern hemisphere. In chapter 3 we present the ray-tracing concept we have used to determine the source locations of HOM. Additionally we have undertaken a three-dimensional study for modeling HOM observations at the Voyager encounters and shown that the HOM source locations must be in the auroral zones along open field lines connected to the magnetospheric tail and polar cusp. Our results explain in detail the strong latitudinal beaming, the solar wind control, the absence of HOM emission when Voyager 1 was within the Io torus, and the absence of Io-control on the HOM.

Concerning the source geometry and the polarization of the emission our results are in agreement with the radiation mechanism, the so-called "Cyclotron Maser Instability" or CMI as first proposed by Wu and Lee in 1979. In chapter 4 we have developed a treatment of the CMI in a very low density magnetoplasma which represents the conditions as seen at higher altitude auroral zones within the magnetosphere of Jupiter. The results clearly show the limits where some simplifications are justified and where more complicated analyses are required. In the conclusion are summarized the main results which represent the first comprehensive study of the hectometric emission. More extensive observations of HOM will be undertaken with the Ulysses and Galileo missions where radiospectrographs in the hectometric frequency range will be operating. Prospects and predictions concerning the HOM will be outlined.

Chapter 1

The Jovian magnetosphere and radio emissions

1.1 The Jovian magnetosphere

At present time, the best explored magnetospheres are the terrestrial and Jovian magnetospheres. The Jovian magnetosphere, however, is unlike the earth's in its fundamental processes because of the very high magnetic field strength, the rapid planetary spin period (about 10 hours) and, of course, because of the existence of the satellite Io which feeds the Jovian magnetosphere with particles of volcanic origin. The Jovian magnetosphere is powered by slowing down Jupiter's spin, and nearly all of the magnetospheric plasma comes from internal sources (satellite Io, ionosphere and current sheet). Contrary, the magnetosphere of the earth essentially extracts all of its energy and an important fraction of its plasma from the solar wind. The solar wind particles may penetrate into the magnetosphere throughout the auroral zones which have an oval form, encycling the magnetic north and south poles, respectively.

Among the planets in the solar system, Jupiter is unique not only because of its immense size and mass and the variety of phenomena taking place within its environment, but also because of its large magnetic moment. The Jovian magnetosphere usually is described in terms of three principal regions (Figure 1.1).

1.1.1 Outer magnetosphere

In the outer magnetosphere the magnetic field exhibits large temporal and spatial variations in direction as a joint consequence of changes in the solar wind pressure and direction of the interplanetary magnetic field. The outer magnetosphere extends from the magnetopause boundary to approximately 30 - 50 Jovian radii (R_J) (Acuna et al., 1983). On the nightside, the most prominent feature is the magnetic tail extending out to a few Astronomical Units (1 AU $=1.5 \cdot 10^8$ km). The existence of the tail implies that the solar wind must catch the magnetic lines of force at the magnetopause and blow them behind the planet. At increasingly larger radial distances from Jupiter the tail magnetic field tends to lie parallel to the equatorial plane of Jupiter (Rucker et al., 1988). As in the case of the earth, the Jovian magnetotail includes a large scale current sheet

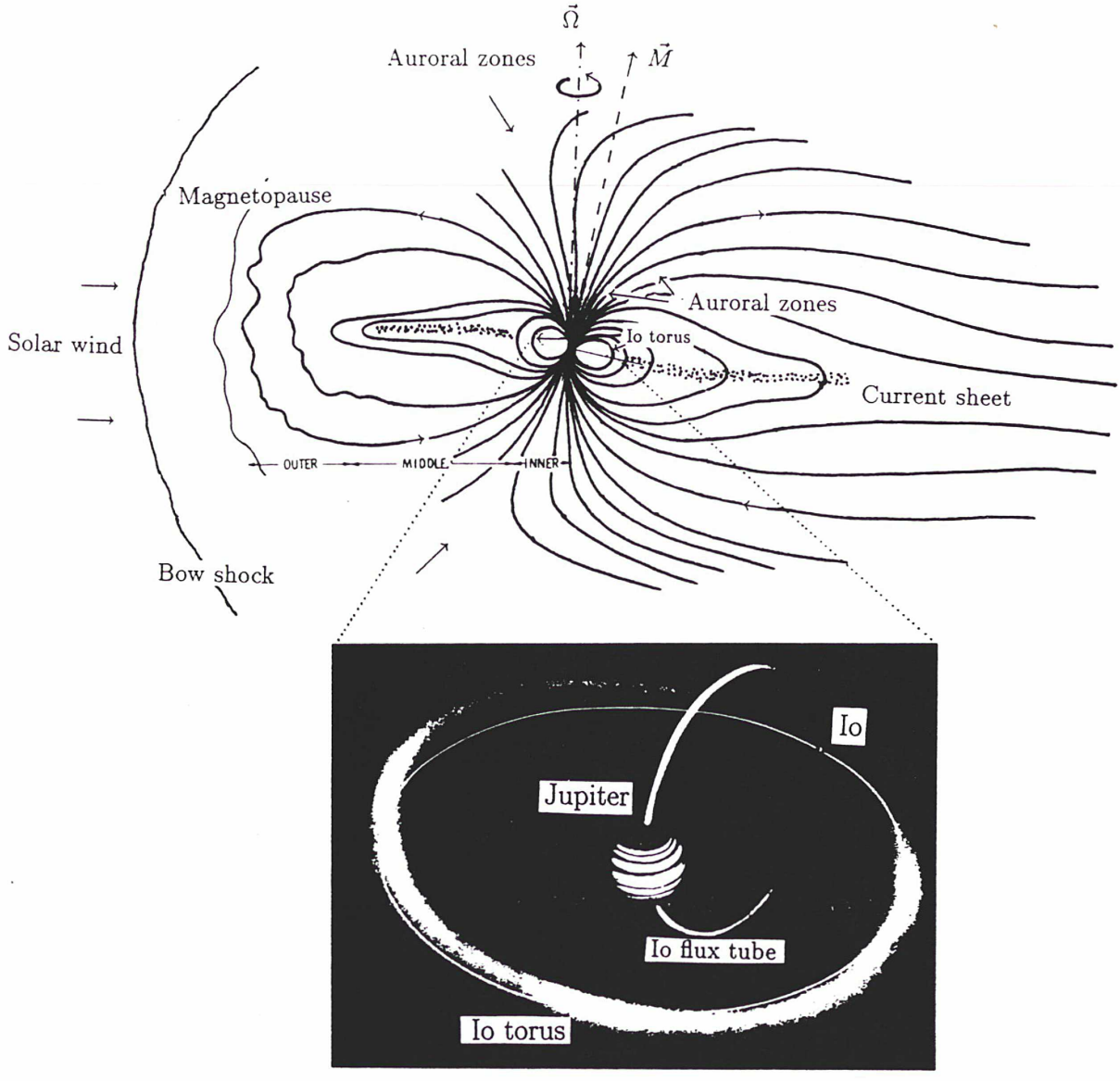

Figure 1.1: Meridional cross section of the Jovian magnetosphere. Three magnetospheric regions can be distinguished: The inner, middle, and outer magnetosphere. For the Jovian radio emissions, the inner magnetosphere including the auroral zones and the Io plasma torus is of primary interest.

separating the northern and southern tail lobes. Crossing the current sheet the field reverses direction. This current sheet which contains an azimuthal current system can be described by a rigid magnetodisc that bends over at distances beyond $r \approx 60 R_J$ (hinge point) to become finally parallel to the planet's equatorial plane. On the dayside, the outer magnetosphere consists of a region which is located just inside the magnetopause. This region is characterized by a southward magnetic component consistent with the orientation of Jupiter's magnetic dipole direction. The extension of the dayside outer magnetosphere is highly dependent on the instantaneous solar

wind pressure which acts on the position of the dayside magnetopause.

1.1.2 Middle magnetosphere

In the middle magnetosphere, which extends from about 6 Jovian radii (R_J) (orbit of Io) to about 30 R_J, the magnetic field morphology is dominated by the field generated by the equatorial azimuthal currents of the current sheet (or plasma sheet). Inside of 6 R_J, the effect of these currents is negligible and the magnetic field can be accurately described by the field which is caused by the current systems in the interior of Jupiter. Beyond approximately 15 R_J, the contribution of the magnetic field due to azimuthal currents exceeds the internal field. The result is a stretching of magnetic field lines in radial direction. This is the reason why beyond 15 - 20 R_J the field lines are open (i.e. only one footpoint at the planet's surface) in contrast to an undisturbed dipole field. Thus, charged particles from the current sheet have access to the planet's auroral zones along open magnetic field lines. Since this scenario takes place at the nightside it is called the tailfield aurora (Connerney et al., 1981).

1.1.3 Inner magnetosphere and Io flux tube

The inner magnetosphere represents the region with a dominating magnetic field which is generated in the interior of Jupiter. For a representation of this internal field, it is convenient to express the flux density $\vec{B}$ as the gradient of a scalar magnetic potential V. By setting the divergence of $\vec{B}$ equal to 0, the resulting Laplace equation $\Delta V = 0$ leads to the expansion of the magnetic field in spherical harmonics. The spherical harmonic coefficients for the Jovian magnetic field are obtained from a least square fit of the measured $\vec{B}$ values along a spacecraft trajectory. Acuna and Ness (1976) used the Pioneer 11 magnetic field measurements to obtain the spherical harmonic coefficients for the magnetic field of Jupiter (O_4 model). The Jovian field can hardly be approximated by a dipole field on Jupiter's surface, since considerable fractions of the quadrupole and octopole terms occur. The magnetic flux density B peaks in the northern hemisphere at 14 Γ [Γ=Gauss] whereas a maximum of only about 10 Γ occurs in the southern hemisphere. The Jovian dipole moment is 4.2 ΓR_J^3 (1 R_J=71400 km) This magnetic field causes adiabatic motion of charged particles. Thereby, the inner satellites of Jupiter (Amalthea, Io) act as particle absorbers when a particle hits the surface of the satellite. At r=1.8 R_J an anticipated ring of particles has been detected by the Pioneer 11 spacecraft (Jovian Van Allen radiation belts).

One of the most prominent features in the Jovian inner magnetosphere is the existence of the Io flux tube. It is the consequence of the interaction between Io and Jupiter as illustrated in Figure 1.2. The corotational electric field which is developed by the relative motion between Io and the magnetic field lines sweeping past the satellite induces a potential difference of approximately 400 kV between the outer and inner faces of the satellite. This potential causes currents to flow from Io toward the Jovian ionosphere, both northward and southward, along the outer portion of the magnetic flux tube linking the satellite with the ionosphere. Return currents flow along the inner portions of the flux tube toward Io. In this model, the circuit is closed by the Jovian ionosphere and the ionosphere of Io. This current system causes the most powerful planetary nonthermal radio emission in our solar system: the Jovian decametric radiation, which was discovered in 1955 by Burke and Franklin. In addition, the inner magnetosphere is fed by

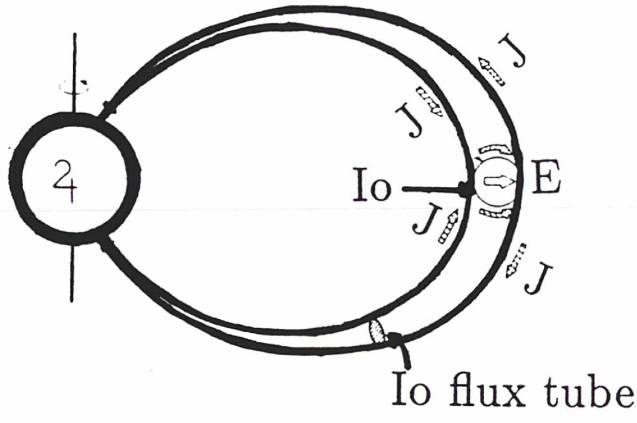

Figure 1.2: Schematic representation of the induced current system flowing approximately parallel to the field lines in the Io flux tube linking Io to the Jovian ionosphere (taken from Acuna et al., 1983).

particles SO, SO_2, O of volcanic origin from the satellite Io. They are ionized immediately after the interaction with the Jovian magnetosphere. The revolution of Io around Jupiter causes a rather uniform distribution of ions and electrons along Io's orbit. The resulting feature is called the Io plasma torus. The peak electron number density of the torus is about 3000/ccm at the orbit of Io and decreases very steeply at the inner side and slowly at the outer side of the plasma torus (Birmingham et al., 1981). Consequently, the Io torus plays a crucial role for the generation as well as propagation of Jovian radio emissions.

1.2 The magnetospheric solar wind interaction: The generation of planetary radio emission

The interaction of the solar wind with a planetary magnetic field is a complicated physical phenomenon. For simplification, it is convenient to define three different steps or effects (Parker, 1969).

1. The first effect of the interaction is the bow shock upstream in the solar wind from the obstacle which is the planetary magnetic field (Figure 1.1). This shock exists because the solar wind bulk speed exceeds both the sound and the Alfven velocity in the solar wind. The solar wind characteristics are modified by the passage through the shock, an increase of the temperature and density and a decrease in speed occur.

2. The second effect is the formation of the magnetopause which represents a dynamic balance between the pressure of the planetary magnetic field and the kinetic and magnetic pressure of the solar wind.

3. The third effect is the stretching out of magnetic field lines of force behind the planet to form an extended magnetotail on the nightside. The space between the last closed field line on the dayside and the first stretched field line on the nightside (Figure 1.1) includes a neutral region where the solar wind plasma easily enters the magnetosphere.

Some of the solar wind particles (mostly protons and electrons) depending on their energy distribution may reach the planet's upper atmosphere. The regions where the solar wind particles can reach the upper atmosphere (thereby producing aurorae borealis in the case of the earth) are called auroral zones. Similar auroral precipitation from the nightside (current sheet) has already been discussed. In general, the footprints of auroral field lines build ovals surrounding the northern and southern magnetic poles. Throughout several physical mechanisms a considerable fraction of the electron energy can be converted into electromagnetic radiation, subsequently producing planetary radio emissions.

1.3 The Jovian escaping radio emission

Among the five known radio planets in our solar system (Earth, Jupiter, Saturn, Uranus, and Neptune) Jupiter is the most extensive concerning the frequency range and complexity, and most powerful concerning the total emitted power. This is demonstrated in Figure 1.3 where the radio emission from the different planets are shown for comparison. To avoid confusion associated with the names of the several radio components, the subsequent abbreviations will be used throughout:

TKR: Terrestrial kilometric radiation

SKR: Saturn kilometric radiation

UKR: Uranus kilometric radiation

NKR: Neptune kilometric radiation

For Jupiter the emission is much more complex and we can distinguish 5 components:

Io DAM: Io-controlled Jovian decametric radiation

non-Io DAM: non Io-controlled Jovian decametric radiation

HOM: Jovian hectometric radiation

bKOM: Jovian broad-bandwidth kilometric radiation

nKOM: Jovian narrow-bandwidth kilometric radiation

The wavelengths of the respective emissions are indicative for the band where the maximum power flux is observed. The average power of these radio components is shown in Figure 1.3 and the dominant role of Jupiter is clearly visible: all emissions except Jupiter's are in the kilometric range[1]; The Jovian spectrum also covers the decametric range which is a consequence of the unique planetary magnetic field strength of Jupiter.

Figure 1.4 shows an example of the wide frequency range of the radio emissions from Jupiter recorded by the Planetary Radio Astronomy (PRA) experiment aboard the Voyager spacecraft.

[1]NKR is not shown in Figure 1.3 but it is expected to be similar to UKR

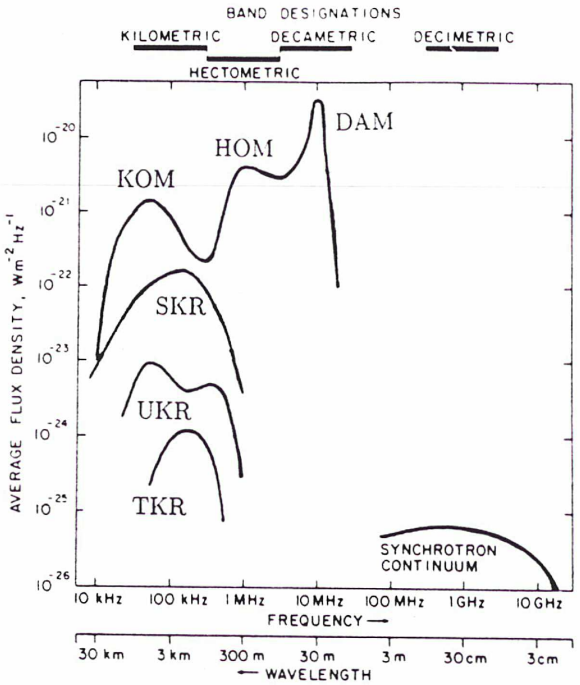

Figure 1.3: Power spectra of the radio planets. Note the dominant role of Jupiter for all frequencies (from Carr et al. 1983).

The radiation extends from 20 kHz to about 40 MHz and is strongly modulated by the Jovian radio spin period lasting exactly 9h 55min 29.7s. The distinct components occur at their characteristic frequency range and are generated at different source regions in the magnetosphere of Jupiter.

1.3.1 Decimetric radiation

The decimetric radiation is a smooth emission which is generated by trapped electrons with high energies in the Jovian radiation belts between 1.6 and 3 R_J (Carr et al., 1983). This synchrotron radiation consists of integral harmonics of $f_c/\sin\alpha$ (f_c being the electron cyclotron frequency and α the electron pitch angle) rather than of f_c (as the lower frequency radio components). The emission covers a frequency range from 80 MHz to 300 GHz with a spectral peak at 800 MHz. A periodic variation in the total flux density is observed as the planet rotates, generally with two maxima and two minima per rotatation. The maxima are detected when the observer is in the magnetic equatorial plane where the polarization is found to be linear. A weakly circular polarized component alternates between right-hand and left-hand polarization as the planet rotates.

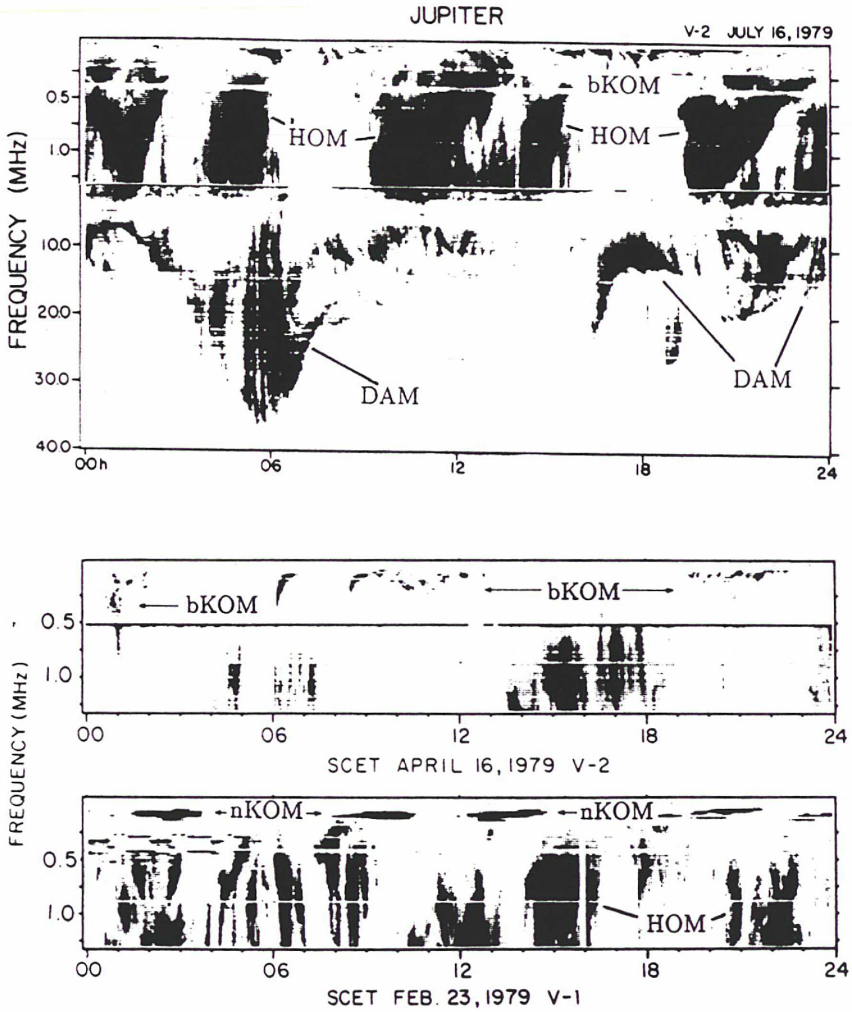

Figure 1.4: Dynamic spectra of the Jovian radio emissions, recorded by the Planetary Radio Astronomy experiment aboard Voyager. Increasing darkness indicates increasing intensity (from Kaiser and Desch, 1984).

1.3.2 Decametric emission

The DAM component which has already been observed from ground based observatories since 35 years is placed within the frequency range of 40 MHz down to approximately 2 MHz with a peak of about 10^{-18}W/m^{2}Hz at 10 MHz. A typical DAM storm is lasting several hours and the emission shows drifting features in a frequency-time spectrogram (Figure 1.4). These features often exhibit an arc like structure (opening or closing parentheses shape) extending over 35 MHz in frequency. Generally, the DAM emission is sensitive to variations in system III longitude (=Central Meridian Longitude CML) and the Jovicentric declination of the observer. The emission tends to be strongest when certain longitudes are facing the observer. In addition, the occurrence and intensity of the Io DAM component is dependent on the orbital phase of Io. Continuous monitoring of DAM by fixed frequency and swept frequency receivers revealed the

characteristic Jovian longitude emission zones known as sources Io-A, Io-B, Io-C, Io-D and their respective dependence on CML and Io-phase (e.g. Carr et al., 1983). Moreover, some of the Io dependent emissions exhibit short-time variations on timescales of milliseconds which are known as S-bursts. In a frequency-time diagram, the S-bursts appear as short-time features which drift toward lower frequencies with time. S-bursts are believed to be generated from distinct electron beams which cause emission of short duration. Other modulations with timescales of seconds are due to interplanetary scintillation effects and are called L-bursts.

In most of the cases (especially above 15 MHz), DAM is right-hand polarized when observed in the northern Jovian hemisphere and left handed when observed from the southern hemisphere. This is consistent with radio waves propagating in the fast extraordinary (R-X) mode. With a few exceptions, almost all of the emissions from the radio planets are generated in the R-X mode, suggesting a common generation mechanism. It is commonly accepted that the Io-dependent emission is emanating from sources located within the Io flux tube at magnetospheric altitudes where the local gyrofrequency is less but nearly equal to the observed wave frequency. The emission is beamed within a hollow cone, the source magnetic field direction being the symmetry axis, with a near perpendicular cone half apical angle. In contrast, the non-Io DAM is generated elsewhere, possibly at higher magnetic latitudes near the tailfield auroral zones or the north and south polar cusps.

1.3.3 Kilometric and hectometric emissions

Contrary to the DAM radiation which is observed from ground based stations, the kilometric and hectometric components were first detected via the PRA-experiment on board the Voyager spacecraft. The kilometric emission lies in the range between 40 kHz and possibly 1 MHz with a spectral peak near 100 kHz. Like the DAM, the KOM is repetitive in terms of the Jovian rotation period.

The broadband kilometric emission (bKOM) recurs favourably when the Jovian northern dipole tip nods toward the observer. The occurrence probability is reduced for higher frequencies. The emission is right-hand polarized when seen in the northern hemisphere and left-hand in the southern hemisphere. The sources of bKOM are located most probably at the edges of the Io plasma torus near the magnetic equatorial plane.

The narrowband kilometric emission (nKOM) is very narrow in bandwidth (20 - 60 kHz) and is a quite smooth emission in contrast to bKOM. The nKOM reoccurrence period is typically 3% - 5% higher compared to the other Jovian emissions. Consequently, it lags the Jovian rotation period. The polarization is contrary to that of bKOM. The nKOM sources are also believed to be near the Io torus but distinct from the bKOM sources.

The HOM component occurs from about 40 kHz (or even below) up to a few MHz (the upper limit is not precisely determined) with a spectral peak at about 1 MHz. From dynamic spectra it cannot unambiguously be seen that the HOM component is distinct from the DAM, but it is certainly distinct from the kilometric components. Very few papers have been devoted to the HOM emission and the authors found some of the beaming characteristics and established a solar wind control. Thereby, increasing solar wind pressure at Jupiter enhances the HOM energy output. In any case, the HOM remains the least investigated radio component without any consensus to date concerning the source location. Furthermore, the polarization behaviour

was not yet understood. It is the main purpose of this work to overcome this lack of investigation in order to explain the characteristics of HOM.

Chapter 2

The Jovian hectometric radiation

2.1 The Voyager mission

One of the greatest advances in the field of radio astronomy was made by the successful Voyager mission which enabled the exploration of the magnetospheres of the outer planets Jupiter, Saturn, Uranus, and Neptune. Since the Neptune flyby of Voyager 2 in August 1989, the Voyager mission became one of the most exciting in the history of space flights. Since 1977, the two Voyagers flew a distance of more than 7 billion km. The trajectories of both Voyagers are shown in Figure 2.1a.

After the launch of both spacecraft in 1977, Jupiter was reached in 1979. Saturn was visited in 1980 by Voyager 1 and 1981 by Voyager 2, which continued its journey to the outer planets and encountered Uranus in 1986 and - very recently - Neptune in 1989. Both Voyagers were favourably designed to receive radio signals from all of the radio planets via the Planetary Radio Astronomy (PRA) experiment (Warwick et al., 1977). The major emphasis of the PRA experiment was to study the freely propagating waves generated in planetary plasmas. In order to observe also the immense frequency range of Jovian emissions, two types of receivers have been implemented on the spacecraft. The high frequency (HF) band receiver consists of 128 channels with a bandwidth of 200 kHz spaced in 307.2 kHz intervals from 1.228 MHz to 40.5504 MHz. The low frequency (LF) band receiver consists of 70 discrete channels with a bandwidth of 1 kHz, equally spaced at 19.2 kHz intervals. The frequency range is from 1.2 kHz up to 1.326 MHz. The basic mode of the instrument is a 6-sec scan from 40.55 MHz to 1.2 kHz during which the receiver dwells at each frequency for a total of 30 msec. The receiver alternates right-hand (RH) and left-hand (LH) polarization measurements at successive frequency dwell points as it steps through the scan range. The detection threshold corresponds to a flux density of $10^{-21}\mathrm{W/m^2Hz}$ in the high frequency range and $2 \cdot 10^{-20}\mathrm{W/m^2Hz}$ in the low frequency range. Two orthogonal antennas (length 10 m) serve to receive the radio signals (Figure 2.1b). For the PRA experiment they are connected as a pair of orthogonal monopoles in order to determine the polarization of the wave. Another experiment, called the Plasma Wave Science (PWS) experiment used the same antenna system to form a balanced electric dipole.

The high band receiver was especially designed for the observation of the Jovian DAM. Simultaneous observations from Voyager 1, Voyager 2, and from the earth allowed stereoscopic

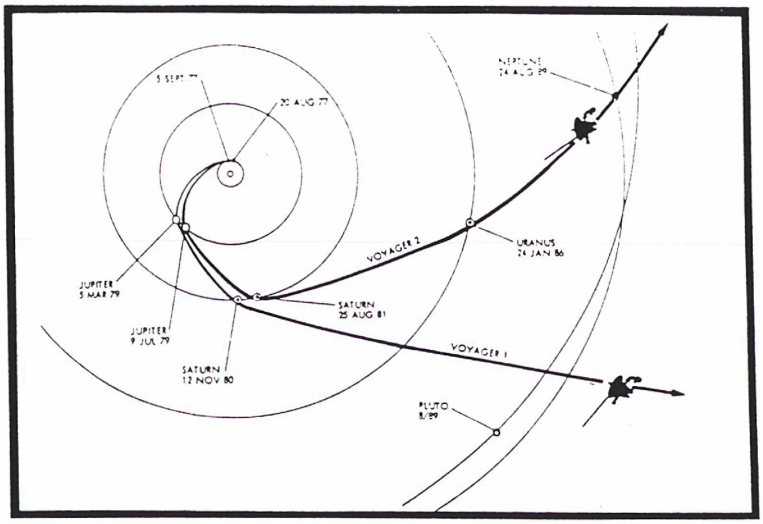

a)

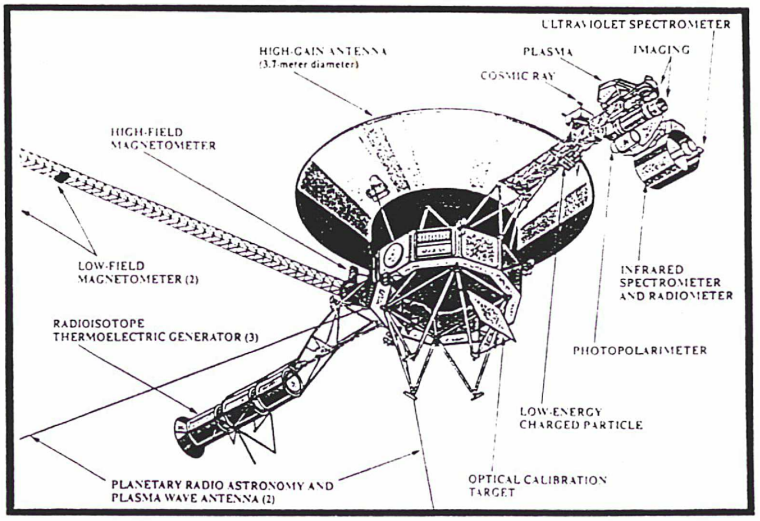

b)

Figure 2.1: (a) Trajectories of the Voyager 1 and Voyager 2 spacecraft. Also shown are the dates of the respective planetary encounters. While Voyager 1 had only a Jupiter and Saturn flyby, Voyager 2 additionally encountered Uranus and Neptune. (b) Overview of some of the experiments aboard Voyager. The antennas of the planetary radio astronomy experiment are erected within a plane perpendicular to the magnetometer boom. The Voyager observations were transmitted to the earth via the high gain antenna.

investigations which helped to determine the DAM beaming characteristics. With the exception of the DAM and the highest frequency part of HOM, no other planetary radio emission was detected in the high band range.

2.2 The hectometric (HOM) observations

It was exclusively the low frequency receiver which measured the kilometric radio emissions from the earth, Jupiter, Saturn, Uranus, and also Neptune. The major part of the Jovian hectometric spectrum, including the spectral peak near 1 MHz, also occurred in the low band. The Jovian hectometric emission was measured simultaneously from Voyager 1 and Voyager 2 in 1979. Moreover, HOM was detectable sometimes in 68 out of the 70 channels (from 39.6 to 1326 kHz) and was the dominant emission above 500 kHz (Figure 1.4a). The HOM is strongly modulated by the Jovian spin period and shows an emission gap around 200° CML. Sometimes, HOM activity was observed down to about 40 kHz especially near the Voyager encounters. The polarization pattern of HOM shows a complicated behaviour, not common with the higher frequency DAM nor with any KOM component (Alexander et al., 1981). These severe constraints on HOM are used to determine the emission characteristics, source locations, and generation processes. None of these properties have been thoroughly investigated before this study. It is the purpose of the present work to enhance the knowledge of planetary radio emissions, especially of the HOM component, whose properties are only poorly known. Any investigation on planetary radio emission also rises our understanding and knowledge of magnetospheric processes and solar wind interactions.

2.3 The phenomenology of the hectometric radiation

2.3.1 Latitudinal beaming and beam width

The Jovian hectometric radiation is the most powerful emission measured by the low frequency band receiver of the Voyager PRA experiment. It has been observed since several years, starting short after the launch of the Voyager spacecraft in 1977 and ending in 1980 just before the Saturn encounters. An extremely high data rate was provided during a period of about 4 months centered on the respective Jupiter encounters of Voyager 1 (March 5, 1979) and Voyager 2 (July 9, 1979). Typical HOM observations recorded at the dayside are shown in Figure 2.2. The emission shows a "gap" near 200° CML. At this longitude, the northern magnetic pole is tilted toward the observer. We notice that the emission gap is wider for V2, which approached Jupiter at higher Jovicentric latitudes. The geometrical explanation of the observed HOM pattern is given in the bottom panel. Assuming that HOM escapes the planet within a quite narrow beam centered near the dipole equatorial plane, the observations are easily accounted for because V2 is out of the beam for a longer period than V1. This essential result of a sharply beamed HOM emission in magnetic latitude was first evidenced by Alexander et al. (1979), studying the cruise phases of V1 and V2 and several earth orbiting satellites.

An important step to characterize the HOM is to determine the average beam width in latitude of the emission. Thereby, the emission activity start and stop times (interpreted as beam crossings) within one Jovian rotation are noted and they can be considered in terms of magnetic latitude taken from the spacecraft trajectory. Thus, the extension of the beam is found in magnetic coordinates. The data are collected over several months centered on the respective encounters. Figure 2.3 presents the average northern beam limit taken from 3 analyzed frequencies, namely f=558 kHz, f=942 kHz, and f=1326 kHz for V1 and V2 observations,

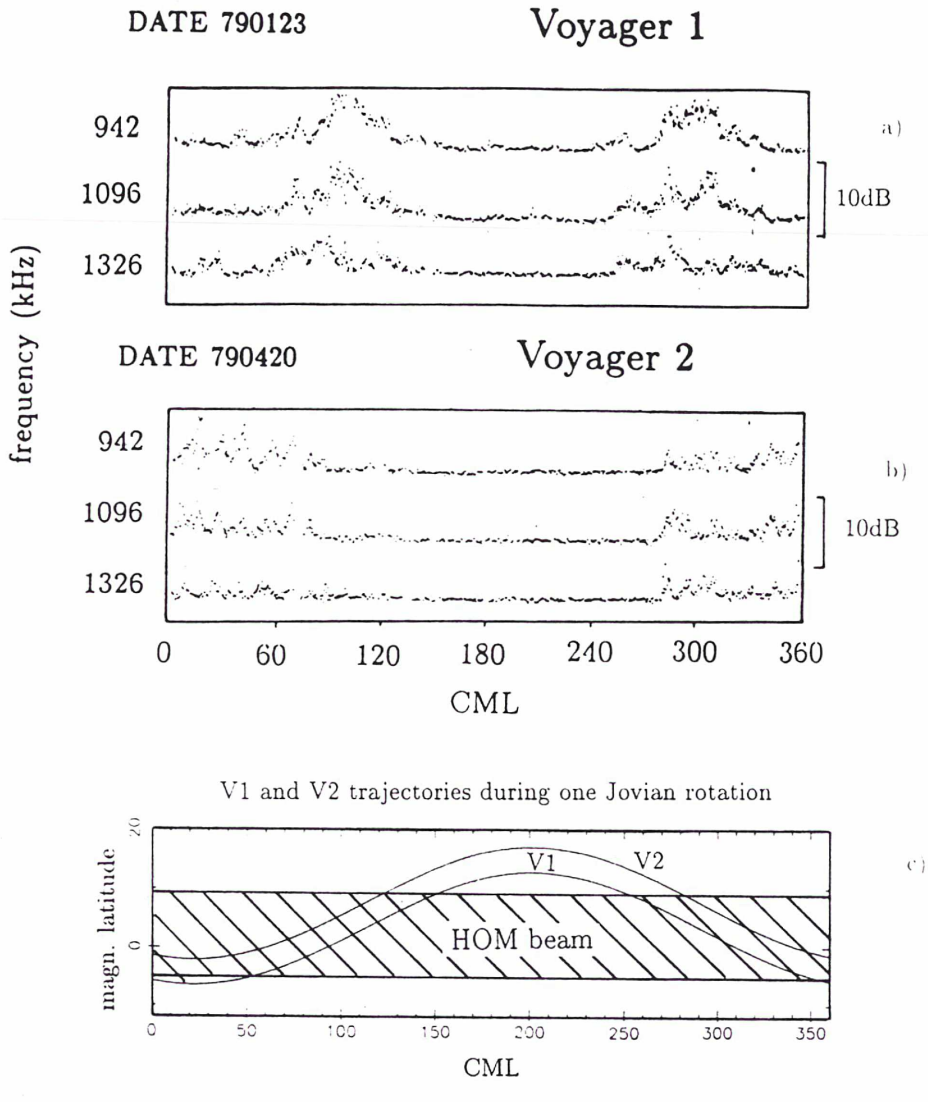

Figure 2.2: Voyager 1 (upper panel) and Voyager 2 (middle panel) observations of the Jovian HOM during one Jovian rotation, respectively. The observed emission pattern can be interpreted in terms of a HOM beaming in magnetic latitude which is sketched in the bottom panel.

respectively. When approaching the planet, the normalized detection threshold (bottom scale) decreases. Consequently, the apparent northern beam limit increases and peaks near the encounter for both spacecraft. Some V1 HOM observations can be used to determine the southern beam extension when leaving the beam at southern magnetic latitudes near 20° CML (Figure 2.2). Assuming that the beam axis (or center) lies exactly between the actual northern and southern beam limits, the average magnetic declination of the beam axis (beam center) was calculated to be +1.6°. Consequently, the whole beam width can be obtained by a mirror image

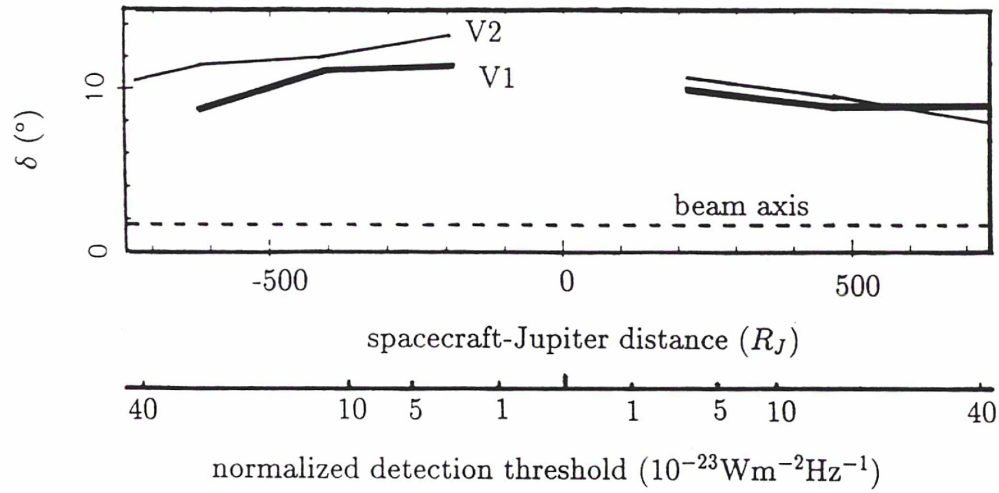

Figure 2.3: Average northern beam extension (average of f=558 kHz, f=942 kHz, and f=1326 kHz) plotted as a function of the normalized (to the earth-Jupiter distance) detection threshold. Thick lines are plotted for V1 and thin lines for V2.

of the V1 and V2 northern beam extensions with respect to the beam axis at 1.6° (dashed line in Figure 2.3). The slight offset of the beam axis from the magnetic equator is most likely due to the asymmetries of the Jovian magnetic field with respect to an idealized dipole field. The apparent total beam width in latitude therefore reaches about 20° near the encounters and 10° farther away from Jupiter, and the beam width is, of course, a function of the normalized detection threshold which decreases when approaching Jupiter. Our results are in agreement with those of Alexander et al. (1979) who obtained a total HOM beam width of 10° at large distances from the planet and the beam axis at 2° - 3° magnetic latitude. We additionally determined the instantaneous beam width from stereoscopic V1 and V2 observations, which also agree with the former results. The detailed work is developed in Ladreiter and Leblanc (1989) (Appendix A) and former results by Alexander et al. (1979) are confirmed.

2.3.2 Local time dependence of the beaming

A further interesting characteristic of the HOM is derived when comparing the occurrence probabilities of dayside and nightside observations. This is visualized in Figure 2.4 where HOM was studied during 40 rotations before and after the respective encounters. Again, we see that the emission gap on the dayside is wider for V2 (notice the higher Jovicentric declination [7°] of the V2 inbound trajectory compared to V1 [3°]). At the nightside the emission gaps exhibit a common behaviour due to similar outbound spacecraft trajectories. The most striking difference between pre- and postencounter observations is the overall change of the shape of the emission gap, being no more symmetrical with respect to 200° - 210° CML at the nightside. Thus, the HOM exhibits a local time effect, the nightside emission pattern being not entirely identical with the dayside pattern. Inspecting Figure 2.3 we also observe that the beam width changes

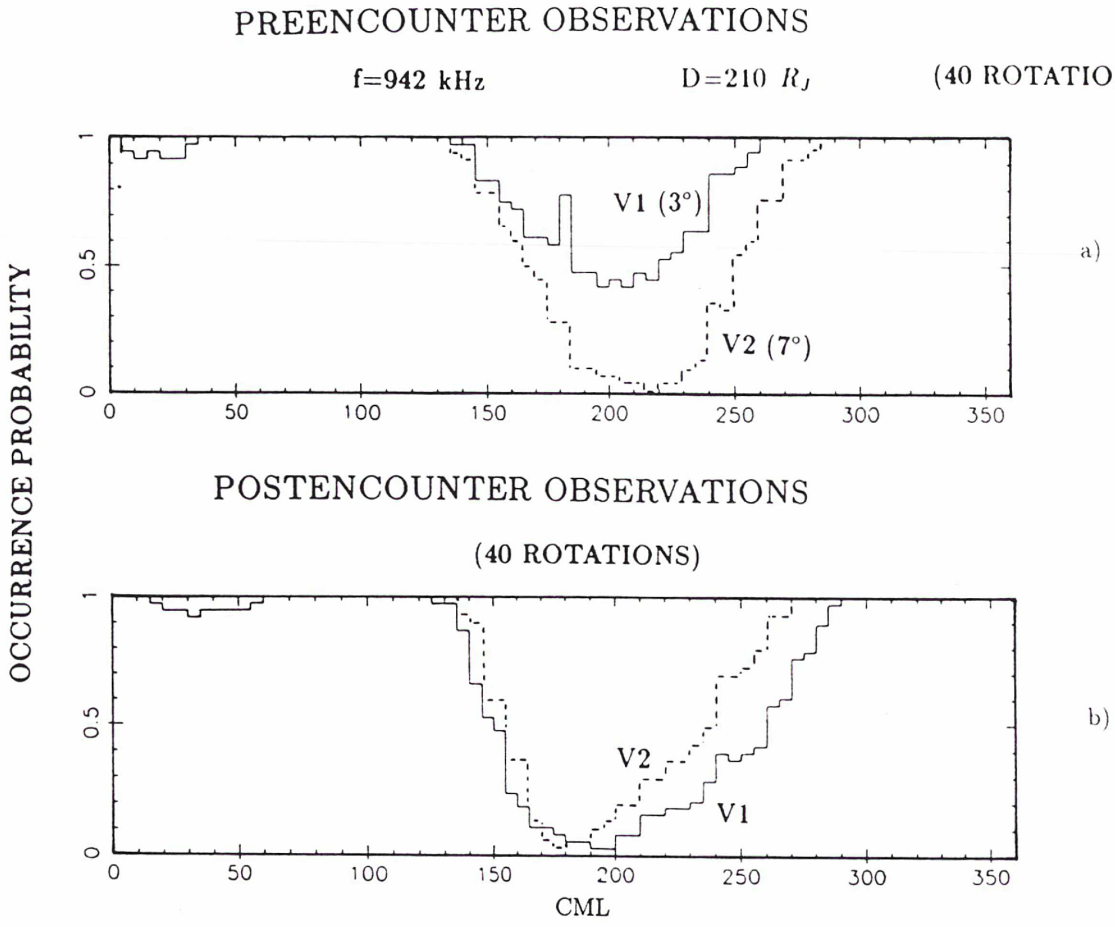

Figure 2.4: Occurrence probabilities of V1 and V2 preencounter (upper panel) and postencounter (lower panel) observations recorded during 40 Jovian rotations, respectively. Notice the high asymmetric shape of the emission gap centered at about 200° CML during nightside observations.

dramatically when the spacecraft switched from the day- to nightside. We are able to state precisely that the beam is a few degrees larger (extending to higher magnetic latitudes) on the dayside than on the nightside.

2.3.3 Polarization

The polarization of HOM shows a puzzling behaviour which is more complex than that of the DAM or KOM emission. In order to investigate the polarization we picked out time periods where the polarization response of the PRA antenna brought out clear results (see Appendix A). A longterm study including 20 Jovian rotations on the nightside has been performed (Voyager 1, f=942 kHz) and the occurrence of right handed (RH) and left handed (LH) polarization is shown in Figure 2.5 (upper panel). By comparing the left-hand (LH) and right-hand (RH) emission, RH emission dominates the northern extension of the beam, whereas the southern beam extension is dominated by left-hand polarization (narrower emission gap near 20° CML). In general the beam contains the two polarizations with a tendency toward RH-polarization at

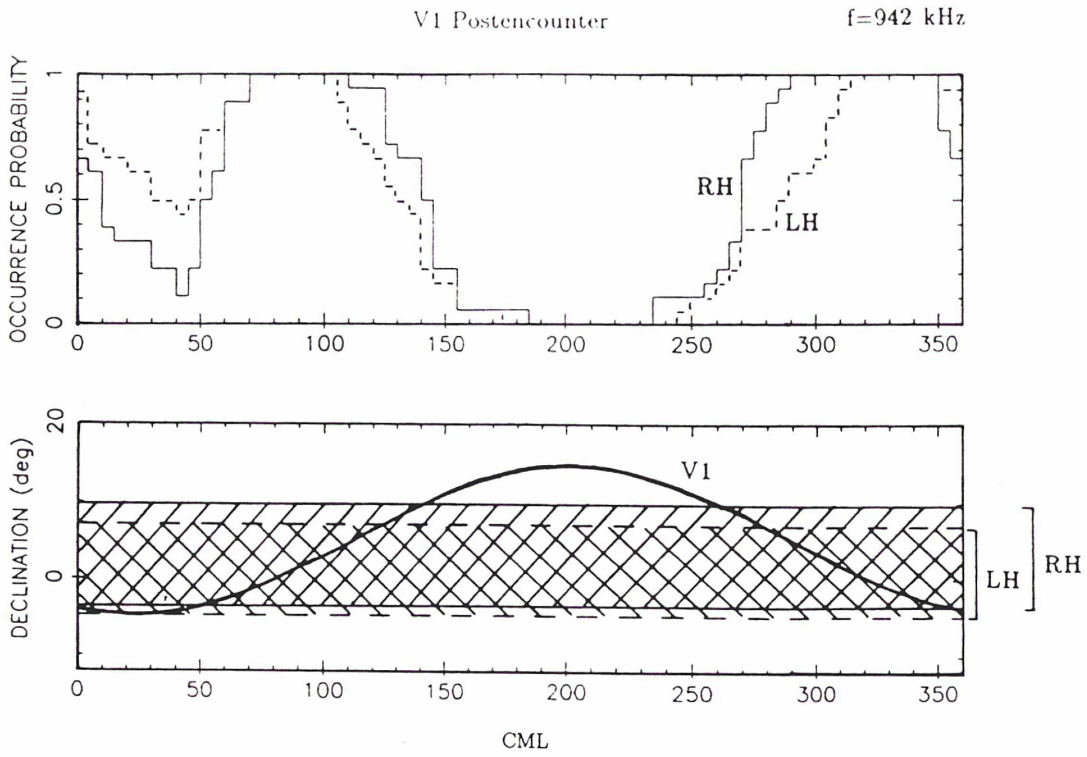

Figure 2.5: Relative occurrence probability of HOM at f=942 kHz for V1 postencounter observations when the two polarizations are treated separately (top panel). A schematic HOM beam which corresponds to the observations is plotted below.

its northern limit and LH-polarization at its southern limit (Figure 2.5, lower panel). Within the mixed polarized HOM beam, northern and southern hemisphere source components compete in intensity and the observer records occasional polarization reversals. The polarization results strongly indicate that the emission is radiated in the fast extraordinary (R-X) propagation mode.

2.3.4 Source extension in altitude

Knowing the propagation mode of HOM, the hectometer source extension in altitude can be derived from the HOM low-frequency limit. The high-frequency limit is not well known but it is generally accepted that it is about 3 MHz and may be as high as 7 MHz. To find the HOM source extension we determined the low-frequency limit of HOM from the PRA data for each Jovian rotation in 1979 for V1 and V2, respectively. The lowest observed HOM frequencies down to 20-40 kHz were observed close to the respective encounters (because of the lowest normalized detection threshold). Since the HOM is propagating in the fast extraordinary (R-X) mode, the source region near the right hand cutoff frequency at 40 kHz extends to altitudes higher than 6 R_J, whereas the sources of the high HOM frequency limit must be located at about 2 R_J from the center of the planet.

2.3.5 Solar wind control

Solar wind influence on planetary radio emissions is well established in the literature in the case of TKR (Gallagher and D'Angelo, 1981) or for SKR (Desch, 1982; Desch and Rucker, 1983) and is now also established for HOM (e.g. Zarka and Genova, 1983; Desch and Barrow, 1984; Rabl et al., 1990). For HOM the solar wind ram pressure and/or density are found to influence the HOM energy output. In this study we have cross-correlated the solar wind parameters density and velocity (10 h averages) with the HOM low-frequency limit and the instantaneous beam width. The solar wind data for V1 were investigated from January 5, 1979 until March 1 and for V2 from January 5 until June 30, which represent the respective preencounter periods in 1979. The solar wind data were ballistically projected from the spacecraft to Jupiter, in a manner described by Desch and Rucker (1983). We have also corrected the artificial data trends due to observations at different spacecraft-Jupiter distances in the HOM parameters as well as in the solar wind data. To see whether the calculated correlation coefficients are statistically significant or not, we used a test based on the Student's distribution (Spiegel, 1976).

According to the results it can now be stated that the arrival of a high density solar wind stream at Jupiter will enhance the HOM energy output, activate low frequency HOM sources located at 6 - 7 R_J and widen the HOM beam to higher magnetic northern latitudes and possibly to higher magnetic southern latitudes.

2.4 Summary of the HOM characteristics

1. The hectometer emission can be described in terms of a narrow, curved sheet at a fixed magnetic latitude (centered at about 2° northward the magnetic dipole equator) into which the emission is beamed to escape Jupiter. The thickness of this sheet is 10°-20° and the emission is local time dependent.

2. The low frequency limit of HOM is found to be about 40 kHz. The high frequency limit is not well-determined but may sometimes reach 3-7 MHz. This results in a source extension from 2 to at least 7 R_J in altitude.

3. The polarization is predominantely right-hand when associated with observations in the northern hemisphere and left-hand in the southern hemisphere; therefore it corresponds to the R-X wave propagation mode.

4. The HOM is strongly correlated with the solar wind. The solar wind density and/or ram pressure enhance the HOM energy, broaden the HOM beam, and activate low-frequency HOM sources at larger distances from the planet.

Chapter 3

Ray-tracing in the Jovian magnetosphere: The hectometric source locations

3.1 The method of ray-tracing

Ray-tracing calculations can help determine or confirm important details about a wave's origin, plasma mode, and polarization. Additionally, ray-tracing can help obtain a better understanding of propagation effects. Information is obtained about source region characteristics such as location and extent. Furthermore, characteristic wave modes and polarization of the wave can be inferred by matching ray-tracing calculations with observations such as the angular extent of an emission. Applied to the magnetosphere of Jupiter, ray-tracing is a useful technique that provides insight into propagation effects caused by the Io plasma torus. This includes refraction and reflection of the hectometric radiation near the torus. The refractory effects create shadow zones for regions where radiation is not allowed, not only because of the characteristics of the generation mechanism, but also because of the intervening plasma between the source region and the spacecraft. Ray-tracing of HOM in the Jovian magnetosphere is therefore a high challenge in the field of radio astronomy. However, results obtained from ray-tracing should be critically tested with respect to the validity of the models used throughout the analysis.

3.2 Ray-tracing concepts

A ray-tracing analysis seems necessary when the characteristic frequencies in the magnetoplasma (e.g. electron plasma frequency f_p, electron cyclotron frequency f_c) are in the same order of magnitude as the frequency of the wave f. Because of the presence of the Io plasma torus, a comprehensive analysis leading to the determination of the HOM source location is not possible without ray-tracing which includes all effects of refraction on a ray in the course of its propagation from the source into free space. The derivation of the mathematical tools required for ray-tracing are given in detail in Appendix E, so only a short version is given here. The ray-tracing computer program is based on the cold plasma formulation of the refractive index (Stix, 1962). A set of

first order differential equations (canonical ray equations), expressed in spherical coordinates, are solved numerically (Appendix E). At a given point in space, the program calculates the refractive index surface for R-X mode waves based on magnetic field and plasma models for the Jovian magnetosphere. Next, the program takes an incremental step perpendicular to the refractive index surface; this denotes the direction of the group velocity and energy flow, and is identical with the ray direction. Then, a new point in space is found and the steps are repeated. The wave normal direction changes according to Snell's law when the wave travels through the magnetoplasma. Generally, the directions of the ray and the wave normal do not differ too much except in regions where the refractive index is considerably less than unity. To perform a ray-tracing study, analytical magnetic field and plasma models must be implemented to describe the plasma in the Jovian magnetosphere.

3.3 Assumptions: Magnetic field and plasma models, and generation mechanism

For the representation of the Jovian magnetic field, we implemented the O_4 model (Acuna and Ness, 1976) providing spherical harmonic coefficients which characterize the dipole, quadrupole, and octopole contributions. The O_4 model has been derived from Pioneer 11 measurements and is supposed to be the best representation of the Jovian magnetic field at present. The electron density model in the Jovian magnetosphere also including the Io plasma torus is provided by Divine and Garrett (1983). Even simplified at best, the Jovian plasma torus acts as a divergent lens for waves in the kilometric and hectometric wavelength range. The Io torus electron number density is displayed in Figure 3.1. The innermost isodensity contour refers to N=3000/ccm and corresponds to a plasma frequency of f_p= 500 kHz. Divine and Garrett give also density and energy models for charged particles of different species in the Io torus and in magnetospheric regions out to 170 R_J.

Since the hectometric emission propagates high above the ionospheric level the use of an ionospheric model is not necessary. It is further assumed that the scale heights of the gradients in the magnetic field and plasma models are small compared to the wavelengths of the HOM range. The electron temperature is believed to be sufficiently small to allow for the cold plasma dispersion relation.

Before performing ray-tracing in a systematic matter one should introduce some constraints due to the generation mechanism of the radiation. The principles of the supposed mechanism are discussed in detail later on, so only general comments are provided here. Most of the radio emissions (and also the HOM) are generated in the extraordinary (R-X) wave mode. The most promising among the generation theories for planetary radio waves is the Cyclotron Maser Instability (CMI) by Wu and Lee (1979). The radiation is generated by the resonance of upgoing loss cone particles with the upper frequency branch of the extraordinary wave mode. For simplified conditions Wu and Lee derived expressions for the wave growth and beaming properties of the emission. It is found that the emission escapes the source in a hollow cone beam, the source field line being the cone axis (Figure 3.2). The sources are located at regions where the wave frequency f is approximately equal to the local electron gyrofrequency f_c. The half cone opening angle θ is nearly perpendicular with respect to the local magnetic field. The mechanism is most efficient if the plasma frequency f_p is considerably less than the gyrofrequency.

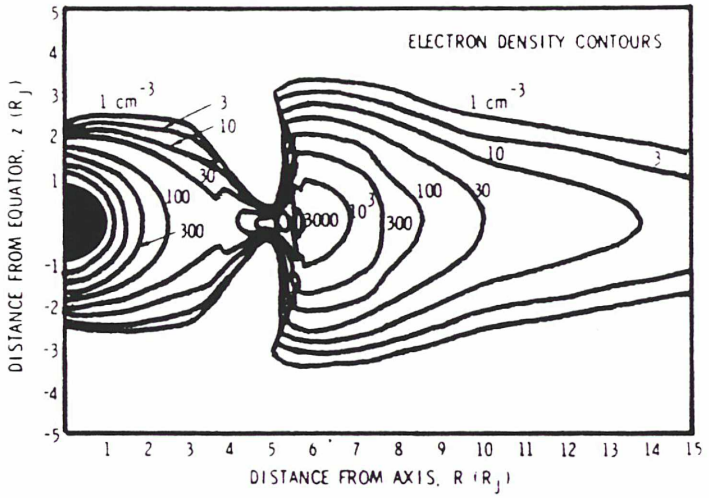

Figure 3.1: Electron density contours for the Jovian plasma density model (from Divine and Garrett, 1983).

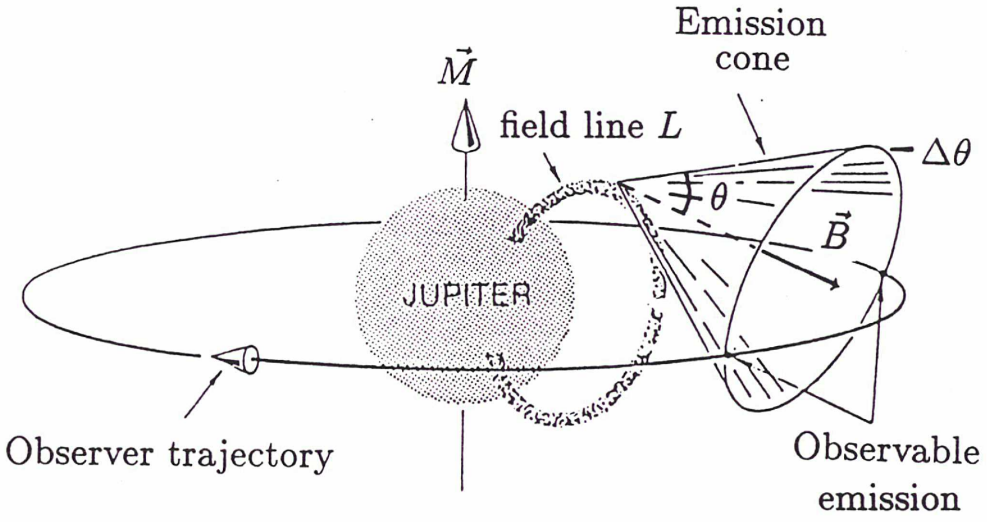

Figure 3.2: Schematic view of a hollow emission cone which is typical for planetary radio emissions. The observer detects activity when crossing the lobes of the cone.

The CMI mechanism is able to explain important details observed so far from planetary radio emissions.

3.4 Ray-tracing calculations

The HOM latitudinal beaming, solar wind control, polarization pattern and local time effect as derived in chapter 1 give severe constraints on the possible source locations together with the use of a generation model which provides some clues about the radiation pattern from the source. A systematic investigation in order to localize the HOM sources is performed via ray-tracing in a meridian plane. Later on, a fully three-dimensional ray-tracing study is performed to establish and confirm the derived HOM sources. We first test several sources (labeled by the dipole shell parameter L) and find the maximum possible wave normal angle θ at which the radiation from these sources can be observed within the HOM beam which occurs in the vicinity of the Jovian magnetic equator. Corresponding to the HOM polarization measurements, only the R-X mode is considered for ray-tracing. According to the CMI, the radio sources are located at magnetospheric heights where the wave frequency is slightly higher than the gyrofrequency. Because of the very low ratio f_p/f_c at a distance of a few Jovian radii where the HOM sources are located, notable wave refraction near the source is not expected.

Figures 3.3 and 3.4 show examples of ray-tracing from several possible source locations (f/f_c=1.05) for varying cone half angles θ and for 2 frequencies, f=300 kHz and f=500 kHz. In all of the plots, the rays associated with the "critical angle θ_{crit}" above which no more emission can be detected by the spacecraft near the magnetic equatorial plane are emphasized by thick lines. Two important facts can be stated by inspection of Figures 3.3 and 3.4. First of all, there exists a focussing of HOM emission parallel to the magnetic equatorial plane when θ is less but close to θ_{crit}. At $\theta = \theta_o$ the rays also point in the required direction but emission consisting of these rays fail to describe the observations near encounter (for a detailed discussion, see Ladreiter and Leblanc, 1990a,b [Appendices B and C]). Secondly, we see a dependence of θ_{crit} as a function of the L parameter of the source: The higher the L value of the assumed source location, the higher the angle θ_{crit} up to which observations are possible.

In Figure 3.5 we have plotted the angle θ_{crit} versus several investigated frequencies. For the development of Figure 3.5, arbitrary source locations in both hemispheres (subscripts N and S) were taken. The dashed lines denote the interpolations for L=10, 15, and 30. Because the Jovian magnetic field can be accurately described by a dipole at larger distances from the planet, we suppose that no important azimuthal asymmetries occur. One important interpretation of Figure 3.5 is that no strong dependence on the initial wave normal angle θ arise for different emission frequencies (for fixed values of L). We further see that emission for nearly perpendicular cone half angles is only possible for sources at high values of L, say L=15-30 (when $\theta_{crit} = 70° - 90°$). For the hectometric component actual cone half angles are not known, but the kilometric radiations from the earth and Saturn, as well as the Jovian decametric radiation are emitted at large wave normal angles (i.e. about $70° - 90°$). Assuming similar values of θ for HOM, the emission source is consequently located at high auroral zones at both hemispheres, probably between L=15 and L=30.

3.5 Location of footpoints of the HOM source field lines

Figure 3.6 shows the footpoints of the derived source locations ($15 < L < 30$) and the tailfield aurorae where particle precipitation is most probable. The footpoints of the HOM sources are

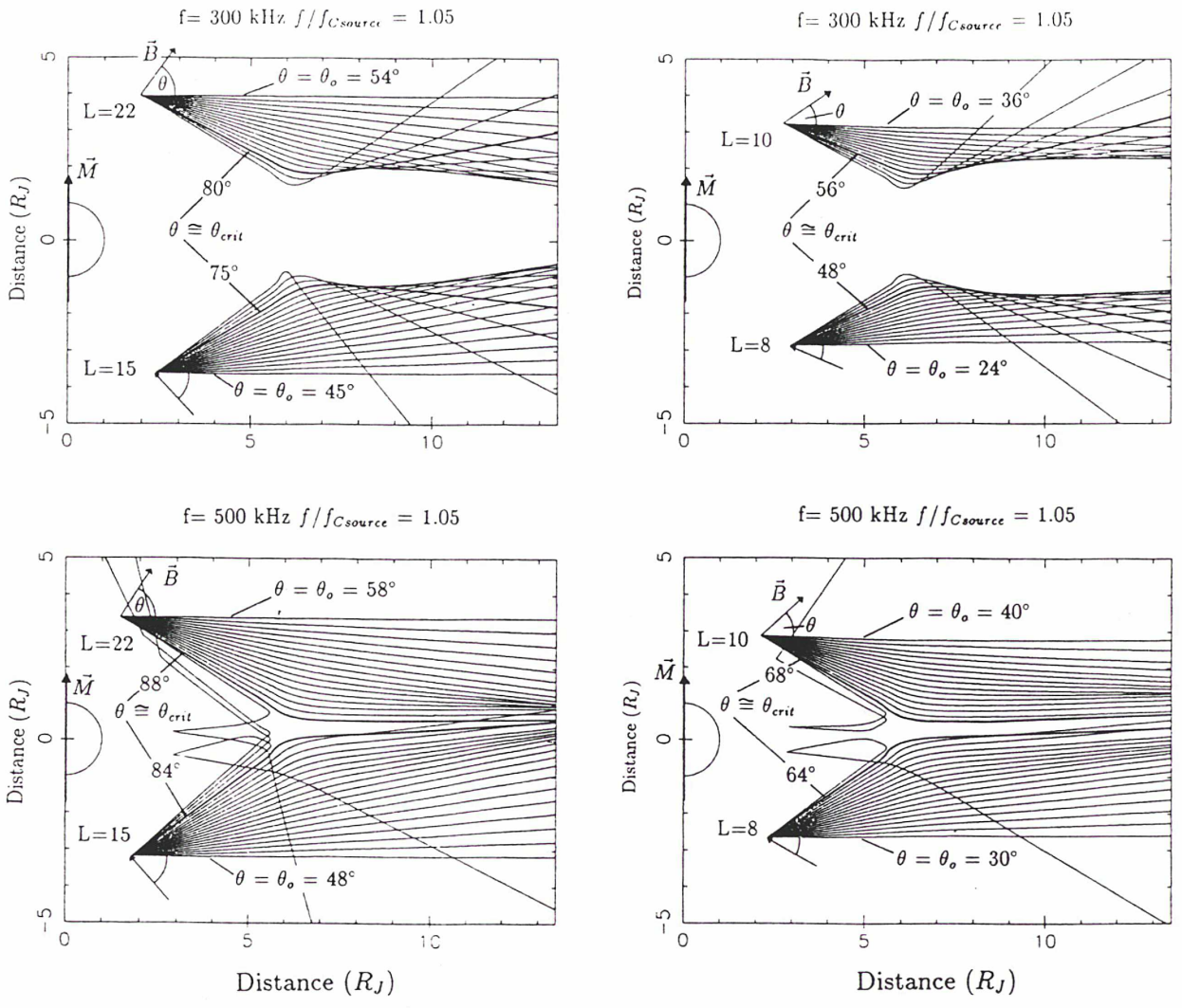

Figure 3.3: (left panels) Ray-tracing of HOM in a meridian plane (CML=200°). The cone half angle θ is varied from θ_o to higher cone half angles including θ_{crit} for sources at L=22 and L=15. The rays with $\theta \approx \theta_{crit}$ (thick lines) reach nearly 90° for L=22. For half cone angles greater than θ_{crit} the final ray direction falls out of the direction of the observed latitudinal beaming. Examples are shown for f=300 kHz (upper panel) and for f=500 kHz (lower panel) in the magnetic frame of reference at CML=200°.

Figure 3.4: (right panels) Same as Figure 3.3 but for sources at field lines L=8 and L=10. Rays originally emitted with θ nearly perpendicular to the local magnetic field are diverted away from the magnetic equator.

overlapping these auroral regions. Thus, the HOM sources have direct access to charged particles from the tail and possibly from the dayside polar cusp. This could easily explain the solar wind control as well as the sharp latitudinal beaming of HOM due to the refraction of rays at the Io torus. The rays become finally directed parallel with respect to the magnetic equatorial plane and could therefore be detected by the Voyager spacecraft (Figures 3.3 and 3.4). HOM source locations at high latitude field lines can therefore account for most of the HOM characteristics.

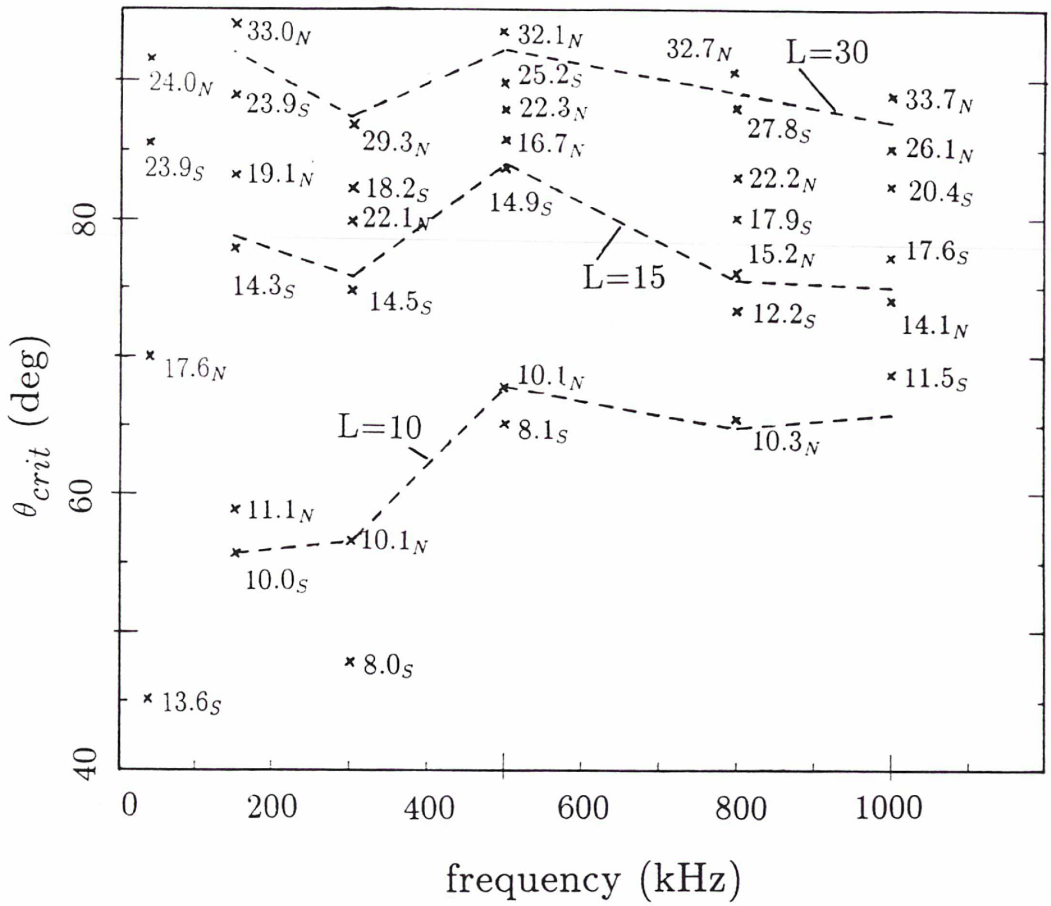

Figure 3.5: The value θ_{crit} as a function of the frequency f and the L parameter of the source field line determined from the ray-tracing calculations at 200° CML. Dashed lines indicate the interpolated θ_{crit} for L=10, 15, and 30 from the given data. N and S refer to sources in the northern and southern hemisphere, respectively.

On the contrary, HOM sources within the Io flux tube can neither explain the observed solar wind control nor the HOM activities down to about 40 kHz. X mode emission at f=40 kHz cannot be generated for r< $7R_J$. For this alone reason, the Io torus can be eliminated as possible source location for HOM.

3.6 Three-dimensional modeling of the HOM

3.6.1 Shadow zone of the emission

The results on the HOM source location were derived from two-dimensional ray-tracing, the ray paths being considered only in a meridian plane. To establish definitely the obtained source locations, we additionally performed a three-dimensional analysis in order to model the hectometric observations from Voyager 1 and Voyager 2. Figure 3.7 displays V1 observations where the emission in the upper panel was observed far from Jupiter (notice scale at the top) whereas

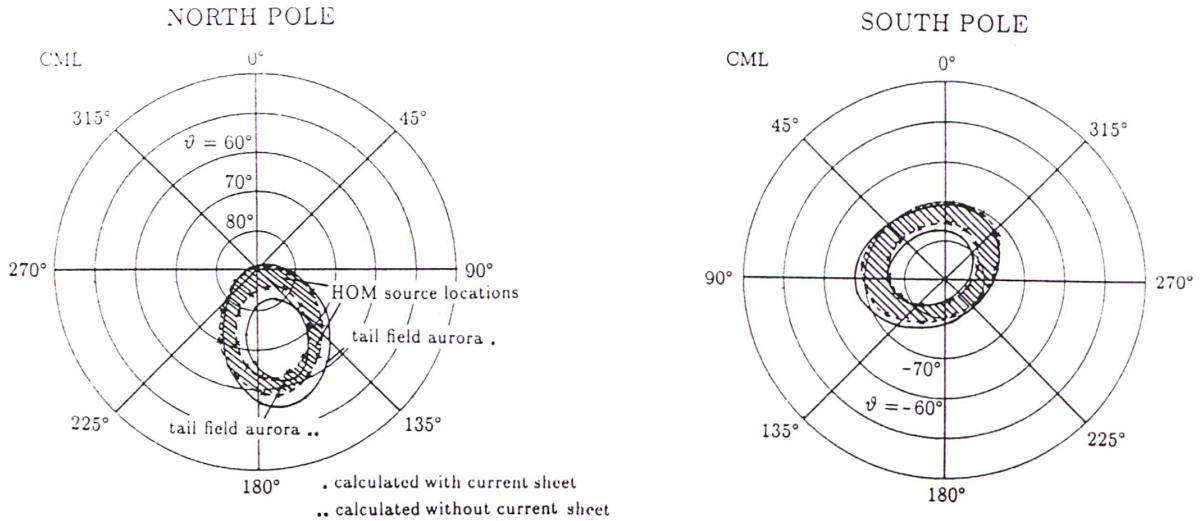

Figure 3.6: Foot points of HOM source field lines ($15 < L < 30$) projected onto the Jovian surface (shaded area) and tail field auroral ovals for the northern and southern hemisphere, respectively. The HOM sources are to a great extent imbedded in the auroral zones.

the lower panel exhibits a recording just before the V1 encounter. The difference concerning the emission patterns between the two panels is striking. The upper panel shows the well known emission gap near 200° CML and emission maxima at system III longitudes where the spacecraft crossed the magnetic equatorial plane (dashed vertical lines). In contrast to this, the lower panel shows no emission during times of magnetic equator crossings. Higher activity zones occur at higher northern and southern magnetic latitudes.

Similar as in Figure 2.2 a straightforward way to interpret these observations is to consider the HOM activity in terms of magnetic latitude. Then, the observations reveal the existence of a "shadow zone" where no emission occurs near the magnetic equatorial plane at short distances from the planet. Farther away, this shadow zone is filled and the emisson is beamed nearly parallel to the magnetic equatorial plane. This trend could already be seen in Figures 3.3 and 3.4: Penetration of rays in the innermost regions of the plasma torus is inhibited because of the enhanced plasma density. Consequently, a shadow zone near the magnetic equator is produced near Jupiter.

We are now interested to study the HOM in the context of a three-dimensional investigation. In order to model the HOM observations, we restrict ourselves to the study of f=500 kHz (typical HOM frequency) and to the source locations already determined in the foregoing sections. To take an intermediate value between L=15 and L=30, we chose L=20 for the further analysis. Figure 3.8 shows the evolution of waves with $\theta = 75°$ from two point sources, one at each hemisphere at L=20. The rays form a shadow zone near the magnetic equator which is consistent with the observations in Figure 3.7b.

We are further interested to study the extension of the shadow zone for the fixed values L=20 and f=500 kHz, but for varying half cone angles θ and Io torus densities which are derived by multiplying the density values of the actual model by Divine and Garrett with a constant factor. The three panels of Figure 3.9 represent the used different density models. We plotted

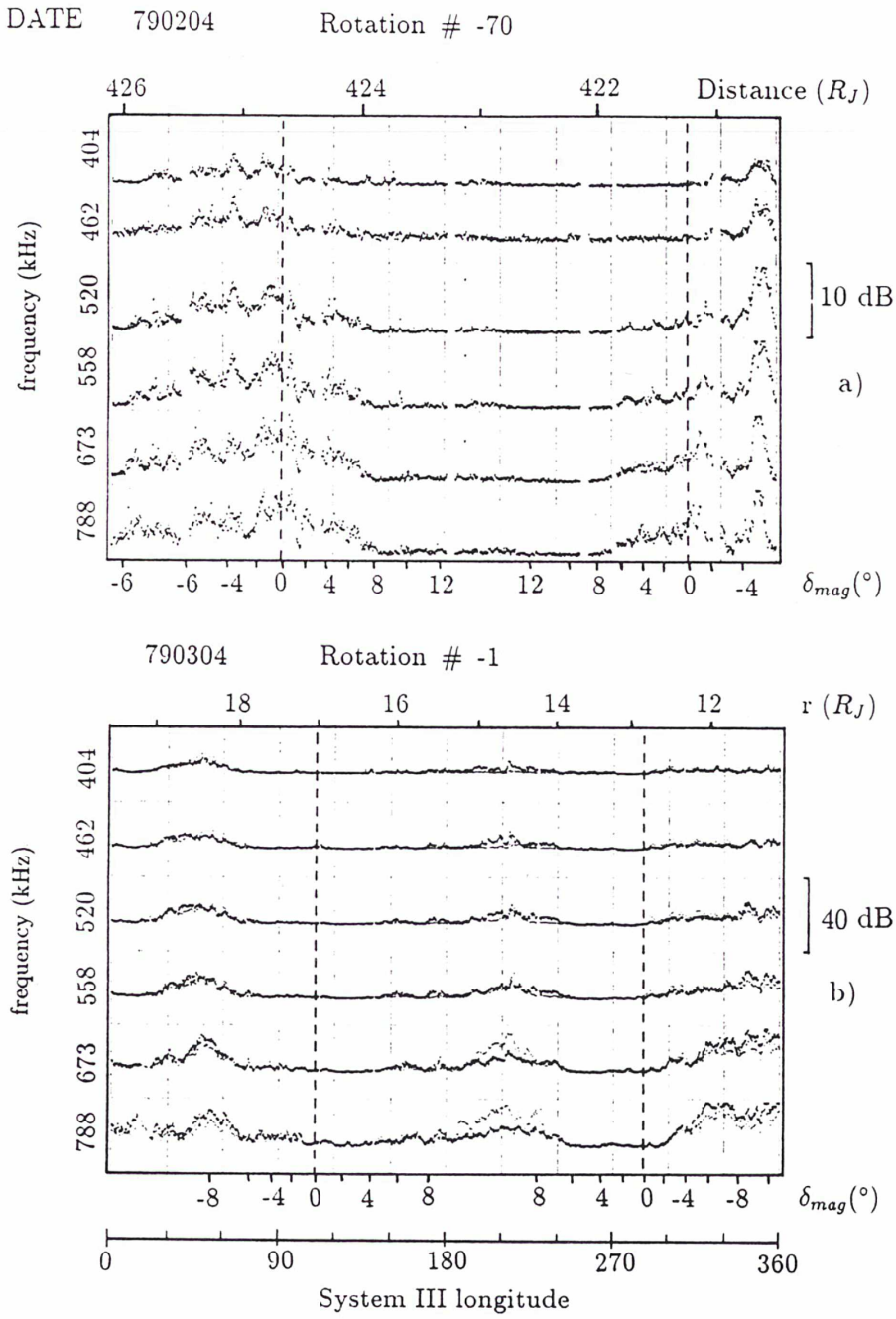

Figure 3.7: PRA observations in the hectometric frequency range as a function of system III longitude, radial distance, and Jovimagnetic declination. We note the absence of emission at high magnetic latitudes for (a),whereas for small distances, the emisson is absent near the magnetic equatorial plane (b).

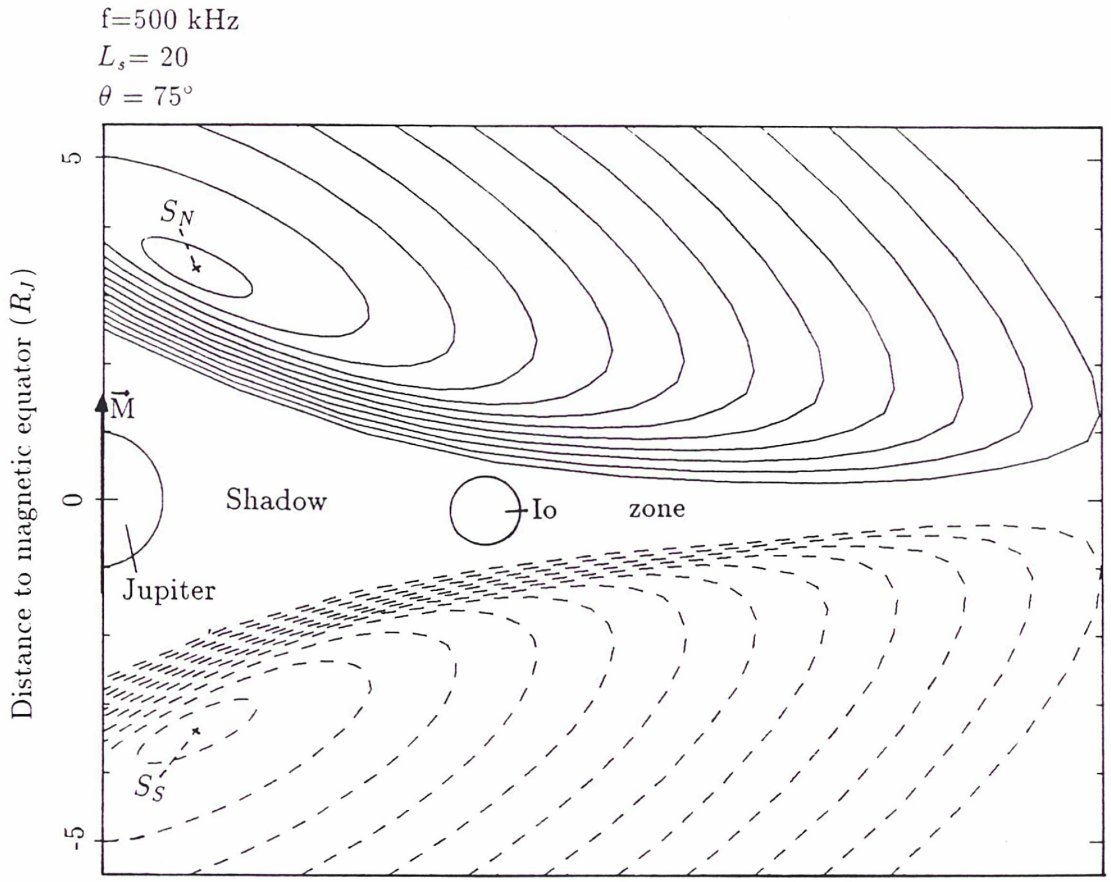

Figure 3.8: Ray-tracing of HOM emission (hollow cones, θ = 75°) emanating from sources located at L=20 in both hemispheres. A shadow zone near the magnetic equatorial plane is produced because of the refraction at the Io torus (size of Io not in scale).

the boundaries of the shadow zone for θ = 70° and θ = 80°. The thick lines on the respective spacecraft trajectories indicate episodes of extremely low emission. Thereby, the shadow zone is present inside about 18 R_J which is approximately predicted in the middle panel (15 % enhanced plasma density) for both half cone angles. Moreover, the middle panel accounts very well for the observations inside of 10 R_J for θ = 80°. However, the recordings around 15 R_J are a somewhat better fit in Figures 3.9a and c, but we consider Figure 3.9b as the best description of the actual situation. The fit is remarkable good when we bear in mind that the formation of the shadow zone is a joint consequence of the beaming properties, source locations, and the refractive properties of the Io torus.

Similar good results for higher frequency HOM components are obtained when the density of the Io torus is enhanced more dramatically. A factor 2-3 for the peak density is sufficient to accurately account also for the HOM emission around 1 MHz. Several authors (e.g. Jones and Leblanc, 1987) suggest in fact a torus peak density that is enhanced by a factor of three with respect to the present one.

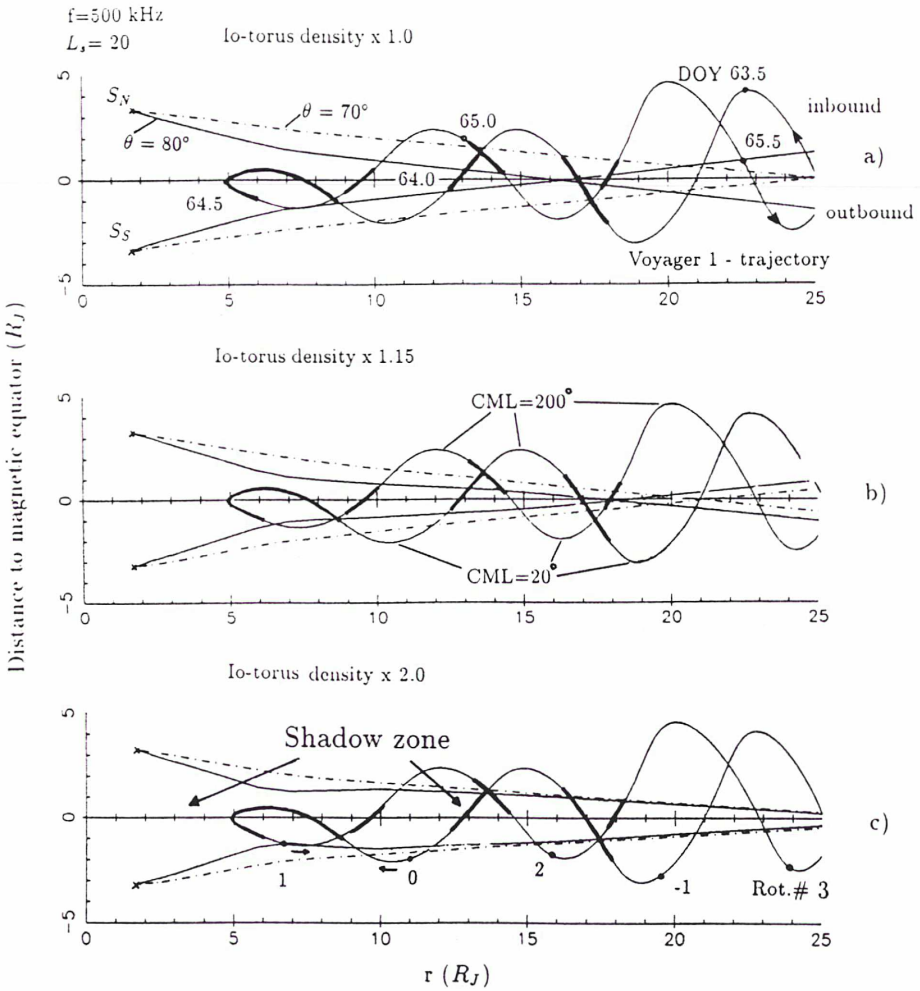

Figure 3.9: HOM shadow zones projected onto a meridian plane for $\theta = 70°$ and $\theta = 80°$. Superimposed is the Voyager 1 trajectory during the encounter period. Significant episodes of lowest or no HOM activity are represented by thick lines on the trajectory. Plots 3.9a,b,c where calculated based on the indicated density models.

3.6.2 Latitudinal beaming and intensity profile

As a last test for the validity of the HOM source locations we perform a simulation of the HOM observations via three-dimensional ray-tracing for given source locations and beaming characteristics. The sources are assumed to be uniformly distributed in longitude along the auroral ovals (L=20) at both hemispheres. The radiation escapes the sources ($f \approx f_c$) within a narrow hollow cone beam within $\theta = 70°$ and $\theta = 80°$ (cone wall half thickness $\Delta\theta = 5°$) and with a maximum intensity at 75°. At the actual point of observation the contributions of all sources are incoherently added including all effects of focussing and diffraction of the waves. To simulate a uniform distribution in longitude, 9 subsources at each hemisphere, equally spaced in longitude, were taken for the calculation. For a detailed discussion of the analysis, the reader

is referred to Appendix C.

We investigated the formation of the HOM latitudinal beaming by plotting the conical emission pattern that Voyager would have observed during two Voyager rotations at different radial distances from the planet. The upper panel of Figure 3.10a shows the situation one Jovian rotation after closest approach (designated as Rotation # 1). The shadow zone is visible at small radial distances and vanishes when the spacecraft is beyond r=16 R_J. The corresponding intensity profile (lower panel) shows emission dropouts when the spacecraft crossed the shadow zone. This situation no longer accounts for observations at large radial distances (Figure 3.10b). The space where the shadow zone occurs in the upper panel of Figure 3.10a is now filled with the narrow HOM emission beam where the intensity is enhanced. Thus, one important result of this investigation is the accurate theoretical modeling of the HOM latitudinal beaming which was first established based on longterm statistical analyses by Alexander et al. (1979). For the sake of illustration, compare Figure 3.10b with Figure 2.2, bottom panel. Furthermore, the calculated HOM profile in the lower panel of Figure 3.10 reveals the well-known HOM emission pattern with the characteristic emission gap near 200° CML.

Figure 3.11 shows a sequence of observations (dashed profiles) during several Jovian rotations. Superimposed the calculated profiles are plotted. Both, the observed and theoretical profiles (calculated for the indicated parameter set) are normalized for each rotation separately. The overall situation which is typical for HOM observations at different distances from the planet is well-fitted and the sudden change in the HOM observations when the spacecraft approached the planet can also be predicted by the model. Although the overall simulation is far from being perfect (we do not expect otherwise, because of the simplifications made in our assumptions) the major structures are explained very well, suggesting that the modulation of HOM can be associated with a source located at high latitude auroral zones.

3.7 Discussion of the results

The results in Figures 3.9, 3.10, and 3.11 were calculated for a set of parameters f/f_c, θ, $\Delta\theta$, the torus density model $\rho(\vec{r})$, and a given L parameter of the source locations (indicated at the top of Figure 3.11). The first three parameters were selected to be in agreement with the cyclotron maser mechanism which is now the most promising theory for the generation of radio emissions. The Io torus density model was determined by in situ observations, but it is an average model, and it suffers (very likely) temporal fluctuations. Therefore, we have verified how that parameter may influence the results. The only free parameter is the L shell of the source field lines. Ladreiter and Leblanc (1990a) have shown, that $15 < L < 30$ accounts for the HOM observations for nearly perpendicular θ. With the use of L=20 (to take an intermediate value) we have shown that the modeled emission is in agreement with the observations for a fully three-dimensional investigation as well. The fact that HOM may be visible at all system III longitudes when the viewing geometry is favourable strongly suggests that HOM is active over a wide range of longitudes. The inferred parameter set may therefore be considered as highly relevant and justified in association with the Jovian hectometric radiation. In addition, the source location of HOM at the auroral zones explains the solar wind control of the HOM since the solar wind particles have direct access to these regions.

The relationship of HOM and DAM is not yet clearly understood at present. Genova et al.

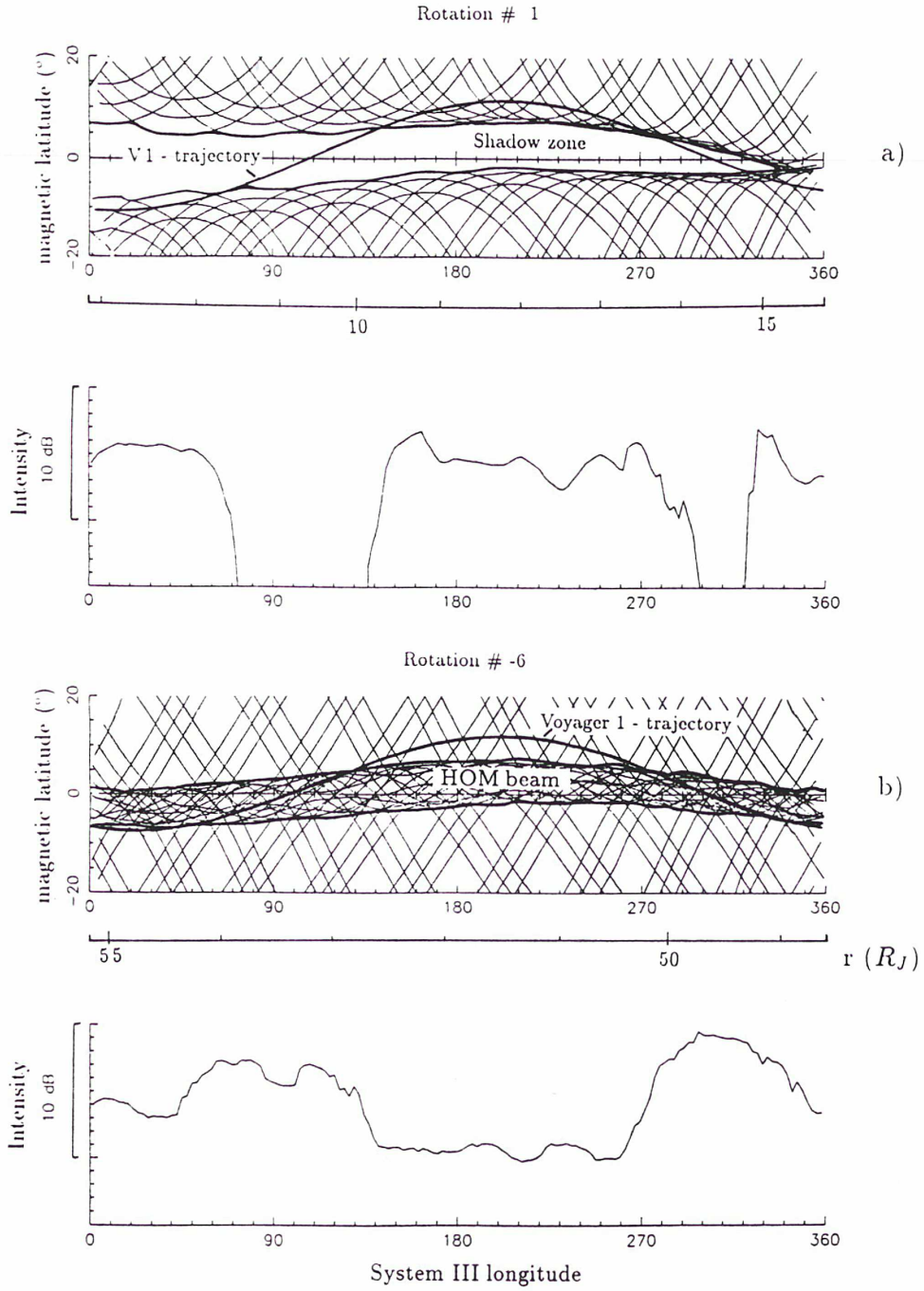

Figure 3.10: Modeled HOM emission cones as if they were seen from Voyager 1 along its trajectory (thick lines) and the corresponding intensity profiles. (a) For short radial distances, a shadow zone for the emission is calculated as observed. (b) For large radial distances, the characteristic HOM beam is formed.

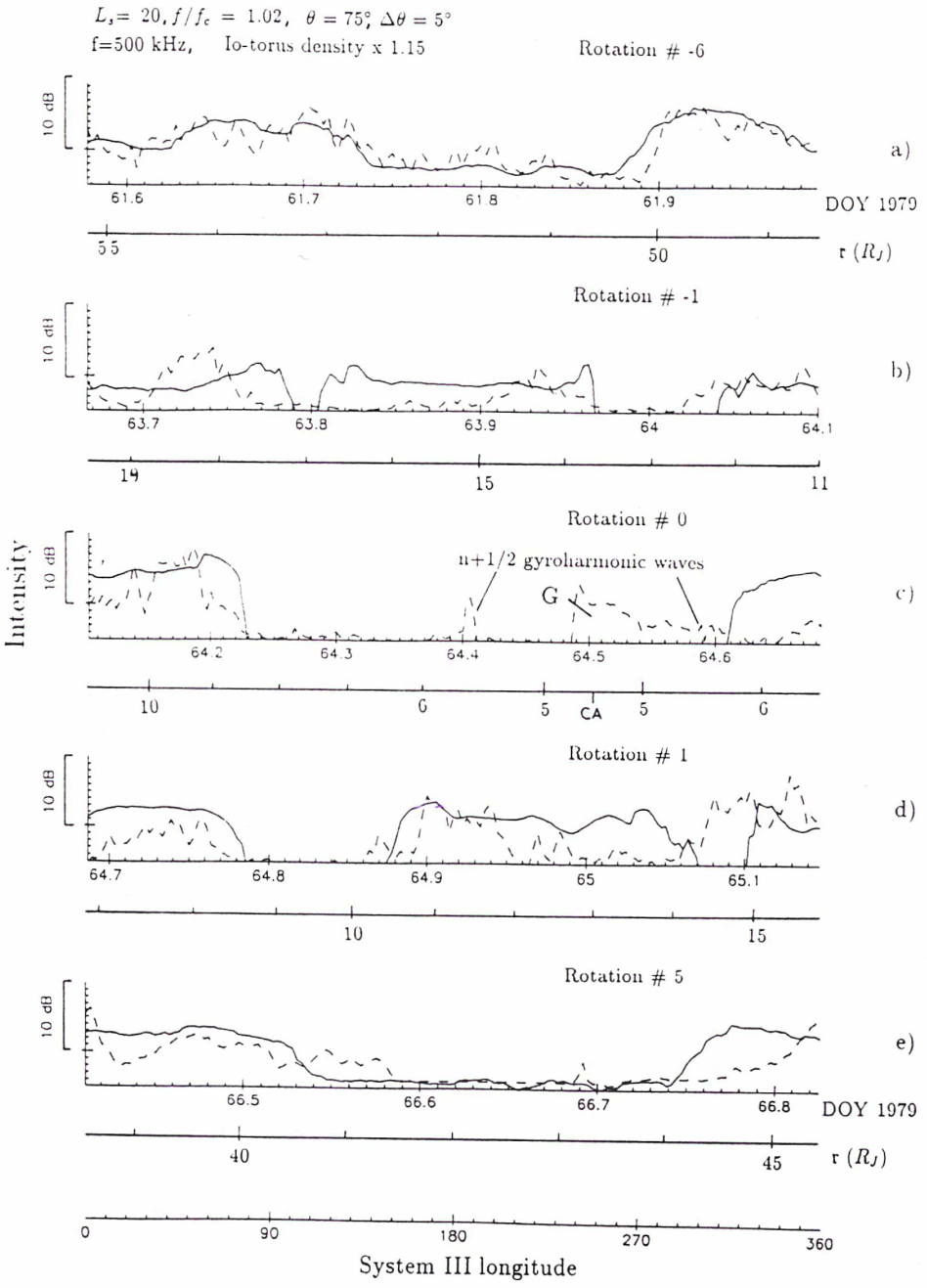

Figure 3.11: Predicted (full line) and observed (dashed line) PRA profiles during some representative Jovian rotations including the V1 closest approach (CA). The calculation was performed for the HOM parameters indicated at the top. The observed change in the HOM observations when the spacecraft approached Jupiter is fairly well predicted which can be seen in the plot sequence (a) - (e). The feature "G" in (c) is not interpreted as HOM.

(1987) reported that the HOM and non-Io DAM should emerge from a common source because of a similar solar wind control of both emissions. However, it has also been suggested in the literature that HOM is a separate component because of its own spectral peak near 1 MHz. As a consequence of our investigation we are now able to state that the HOM spectral peak possibly arises from the focussing of the emission, being caused by the Io plasma torus. Outside the beam, the intensity is considerably weaker, so that the overall flux (over a solid angle of 2π) may be highly overestimated. Consequently, the spectral peak could vanish and the HOM is seen as the low-frequency extension of the non-Io DAM which is also generated at high magnetic latitudes but obviously is less extended in longitude.

Chapter 4

The HOM radiation mechanism

4.1 The Cyclotron Maser Instability

Ten years ago, in 1979, Wu and Lee developed the theory of the cyclotron maser mechanism for the generation of planetary radio emission. This mechanism is commonly accepted to be the relevant theory for auroral radio emissions. Other theories are not discussed here but they are reviewed elsewhere (e.g. Genova, 1987). The Cyclotron Maser Instability (CMI) theory states that radio waves can be generated and amplified by resonance with auroral electrons spiralling around magnetic field lines, having free energy (unstable electrons). The amplification of electromagnetic X-mode waves is generally favoured since the gyration of electrons around magnetic field lines is in the same sense as the E-vector of the fast X-mode.

The purpose of this section is a treatment of the CMI in a very low density magnetoplasma where $f_p/f_c < 0.01$. This represents conditions as found in the higher altitude auroral zones within the magnetospheres of Jupiter (HOM sources) and Saturn (SKR sources). We derive simple expressions relating the normalized (to the light velocity c) parallel bulk velocity $\beta_{\|o}$ of a given electron distribution function to the frequency f of the most amplified wave (in terms of f_c) and to the emergence angle θ when the radio source is situated in a low density magnetoplasma. We first have to study the dispersion relation and the growth rate. This leads to the formulation of the resonance condition which is discussed in detail for $f_p/f_c << 1$.

4.2 Derivation of the relativistic resonance condition

4.2.1 Dispersion relation and growth rate

Under several conditions ($\theta \approx 90°$, n (refractive index) ≈ 1, $f \approx f_c$, $f_p << f_c$, the dispersion relation $\Lambda(w, \vec{k})$ can be significantly simplified (Wu, 1985)

$$\Lambda(w,\vec{k}) = 1 - \frac{c^2k^2}{\omega^2} + \frac{\omega_p^2}{\omega^2}\int d^3v \left(\omega_c \frac{\partial F}{\partial v_\perp} + k_\| v_\perp \frac{\partial F}{\partial v_\|}\right) \frac{v_\perp J_1'^2(k_\perp v_\perp/\omega_c)}{(\omega - \omega_c/\Gamma - k_\| v_\|)} = 0 \qquad (4.1)$$

where $\omega = 2\pi f$, $k_{||}, k_{\perp}$ are the components of the wave vector parallel/perpendicular with respect to the magnetic field $\vec{B}$, F denotes the electron distribution function in the velocity space $(v_{||}, v_{\perp})$, J_1 is the Bessel function, and $\Gamma = 1/\sqrt{1 - v^2/c^2} = 1/\sqrt{1 - \beta^2}$.

It is further assumed that the cold (ionospheric) electrons solely support the wave propagation, whereas the hot precipitating electrons forming the instabilities in the distribution function are only responsible for the amplification of the wave.

The growth rate for the CMI is expressed in terms of the imaginary part ω_i of the angular frequency $\omega = \omega_r + i\omega_i$. An approximate formula for the R-X mode wave is given by Wu (1985):

$$\omega_i = \frac{\pi^2 \omega_p^2}{4\omega} \int_{-\infty}^{+\infty} dv_{||} \int_0^{\infty} dv_{\perp} v_{\perp}^2 \delta[\omega - \omega_c/\Gamma - k_{||} v_{||}] \omega_c \frac{\partial F}{\partial v_{\perp}} \tag{4.2}$$

In Equation (4.2), it is further assumed that $\omega_r >> \omega_i$ $(\rightarrow \omega \approx \omega_r)$, and the argument of the Bessel function J_1' in Equation (4.1) is small leading to $J_1'^2 = 1/4$ and, moreover, the term associated with $\partial F/\partial v_{||}$ can be neglected compared to the term with $\partial F/\partial v_{\perp}$.

Although some of the assumptions made for the derivation of the dispersion relation and the growth rate are very questionable after the recent Viking measurements in the TKR source region (Louarn et al., 1990), they are sufficient for our purpose because the aim of this study is to discuss the resonance condition occurring in the denominator of Equation (4.1) and in the argument of the δ function in Equation (4.2).

4.2.2 Electron distribution function

Before starting to discuss the conditions for wave resonance with energetic particles at the source region, let us study a typical electron distribution function as measured by the S3-3 satellite (Croley et al., 1978). Three unstable features with positive $\partial F(v)/\partial v_{\perp}$ (providing free energy for wave growth) are visible in Figure 4.1. Firstly, the loss cone region associated with the upward side of the distribution function (ascending electrons), secondly, the accelerated downgoing electrons (forming a holelike feature), and thirdly, the trapped electrons near the $v_{\perp}$-axis. The latter are suggested to be trapped throughout a time-varying (or space-varying) parallel electric field (Louarn et al., 1990) between their magnetic mirror point above the ionosphere and a second mirror point due to the parallel electric field along auroral field lines. The corresponding electric potential has been reported to be about 3 kV over a distance of several earth radii (Croley et al., 1978). Although a common conclusion has not been drawn yet, it is generally accepted that TKR is likely to be excited by two instabilities, arising from the loss cone and/or holelike region. These two regions are characterized by a relatively small $\beta_{\perp o}$ which leads to an essential simplification when studying the resonance condition.

4.2.3 Relativistic resonance condition

By inspection of Equation (4.2), we see that a necessary condition for wave growth ($\omega_i > 0$) is the existence of an inversion of population $\partial F/\partial v_{\perp} > 0$ in velocity space along regions where the argument of the δ-function is 0. In other words we have to study the quantity $\partial F/\partial v_{\perp}$ along the resonance contour in velocity space defined by

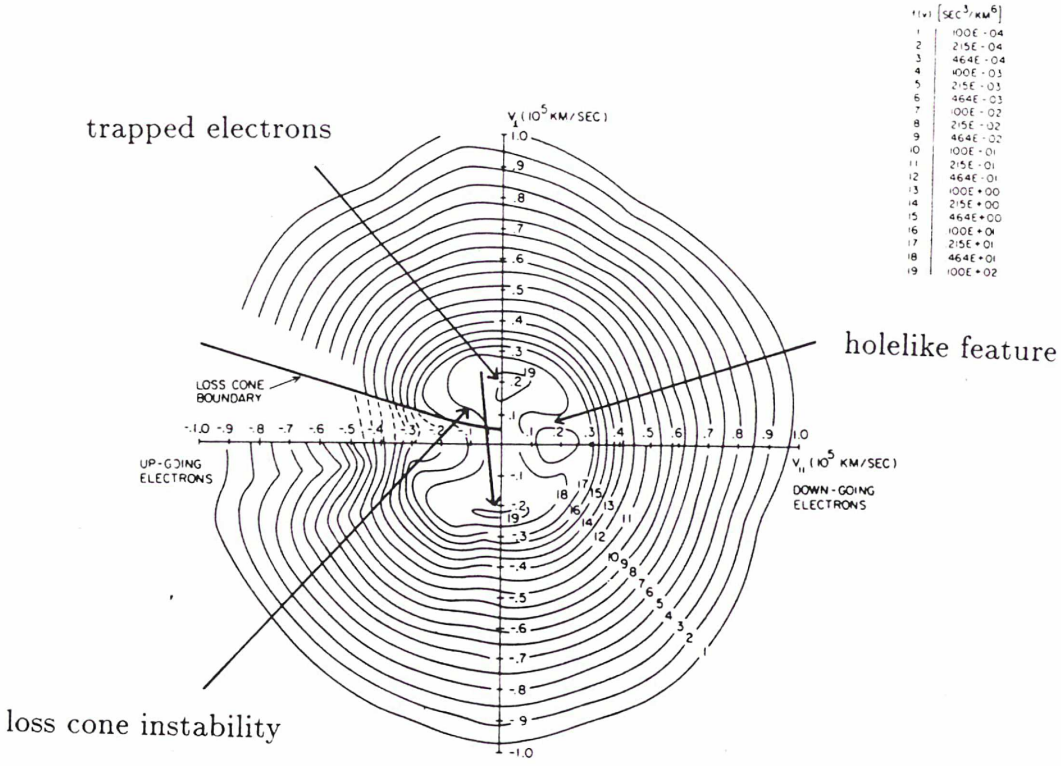

Figure 4.1: Typical electron distribution function taken by the S3-3 satellite in the auroral region of the earth. The three occurring instabilities $\partial F/\partial v_\perp > 0$ are marked by arrows.

$$\omega - \omega_c/\Gamma - k_{||} v_{||} = 0 \tag{4.3}$$

For a given wave $(\vec{k}, f)$ this resonance contour can be found in the velocity space by solving the cold plasma dispersion relation (Budden, 1961; Stix, 1962). For the fast extraordinary (R-X) mode these contours are ellipses entirely placed at either the upward or downward side of the distribution function (Dusenbery and Lyons, 1982). This is visualized in Equation (4.3) where ω must be greater than ω_c/Γ because the R-X cutoff frequency f_{RX} is always higher than f_c. Since the resonance condition must be fulfilled, this can only be achieved when $k_{||} v_{||} > 0$, therefore requesting that $k_{||}$ and $v_{||}$ point in the same direction. Thus, upgoing waves can only be amplified by ascending electrons and downward propagating waves only by descending electrons.

4.2.4 Properties of resonant contours

Regarding the distribution function in Figure 4.1 it is now clear that the resonant ellipses should exhibit small extensions in the $v_\perp$ direction in order to be favourably placed within unstable ($\partial F/\partial v_\perp > 0$) regions. Solving the resonance condition (Equation 4.3) by introducing the dispersion relation $k(\omega) = \omega/c \cdot n(\omega)$ as given by the Appleton-Hartree-formula (Appendix E, Equation E.1), we find the properties of the resonant contours in the normalized (to f_c) $f - f_p$

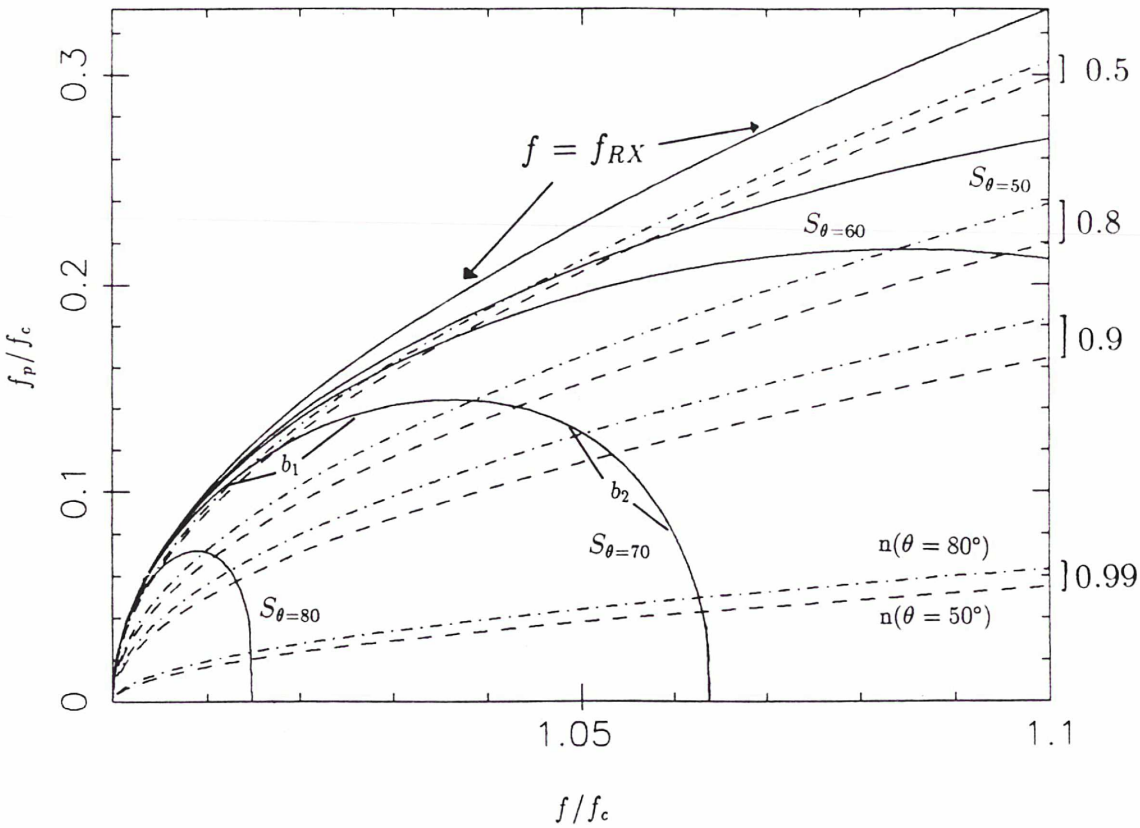

Figure 4.2: Properties of resonant ellipses in the normalized (to f_c) $f - f_p$ space for given wave normal angles θ. The areas where ellipses exist are enclosed by the respective separatrices S_θ on which the ellipses shrink to a point.

space for different wave emergence angles (illustrated in Figure 4.2). For a given θ, we distinguish three areas in the diagram. Firstly, the region above $f = f_{RX}$ (R-X cutoff frequency) where no propagation of R-X mode waves is possible. Secondly, the area outside of the so-called separatrix S_θ and inside $f = f_{RX}$ where no resonant contours exist for the respective θ, and, thirdly, the region inside the separatrix where resonant ellipses do exist. For a given point in the normalized $f - f_p$ space placed exactly on a separatrix, the resonant ellipses shrink to a point. The deeper a point in the normalized $f - f_p$ space is placed inside the separatrix, the larger is the extension of the resonant ellipse.

4.2.5 Adapted resonant contours in the electron distribution function

When considering the loss cone or the hole-like instability providing free energy for the generation of radio emissions, we limit our discussion to ellipses with small extensions in the velocity space. In the normalized $f - f_p$ space, the respective area is located at or slightly inside the regarded separatrix. For points exactly on the separatrix, the formalism greatly simplifies because the ellipse resulting from the relativistic resonance condition (Equation 4.3) shrink to a point and after some algebraic transformations (see Ladreiter, 1990 [Appendix D] for details) one obtains important wave characteristics in terms of the parallel electron bulk velocity $\beta_{\|o}$ of the unstable

region.

$$n \cos\theta = \beta_{\|o} \tag{4.4}$$

$$\frac{f}{f_c} = \frac{1}{\sqrt{1-\beta_{\|o}^2}} \tag{4.5}$$

For the derivation of Equations (4.4) and (4.5) it was also assumed that the distance d of the center of the ellipse from the origin in velocity space is equal to the parallel bulk velocity $\beta_{\|o}$ (see Appendix D, Figure D.2). Equation (4.5) states that in the limit of our assumptions, the ratio f/f_c is only dependent on $\beta_{\|o}$ regardless of the wave normal angle θ. Equation (4.4) requires further analysis to express θ exclusively in terms of $\beta_{\|o}$.

4.3 Amplification of radiation via the cyclotron maser mechanism

4.3.1 The exponential gain factor

Equation (4.2) serves to calculate ω_i for a given electron distribution function (Figure 4.1). However, to see whether or not the initially amplified wave suffers damping along the further ray path, one must calculate the exponential gain factor along the ray path l_1-l_2

$$g = \int_{l1}^{l2} \frac{\omega_i(l)}{v_g(l)} dl \tag{4.6}$$

where v_g denotes the group velocity.

For a net amplification g must be greater than 0. For the terrestrial kilometric radiation, the exponential gain factor was calculated by Omidi and Gurnett (1984) and important results were derived. Because of the lack of measured distribution functions for the auroral regions of Jupiter and Saturn we have to simulate the most important feature - the loss cone - in the electron distribution function. The electrons with very small equatorial pitch angles have their mirror points in the planet's atmosphere and are therefore lost by collisions with atmospheric particles. They consequently produce a lack of ascending electrons for small pitch angles $\partial F/\partial v_\perp > 0$ which leads to the loss cone instability.

We now make important simplifications before calculating g in terms of f_p/f_c and θ. They are listed in the following:

1. The cold plasma determines the wave propagation along the ray path $l_1 - l_2$.
2. Existence of a magnetic dipole field with $\vec{\nabla} B \| \vec{B}$. The direction of $\vec{B}$ is kept constant along the ray path. This is a good approximation near the magnetic polar regions.
3. No refraction of the propagating wave.

4. $f_p/f_c = constant$ along ray path.

5. Instability ($\partial F/\partial v_\perp > 0$) is caused by a loss cone superposed by a parallel electric field.

6. No wave absorption after phase of amplification.

7. ω_i is taken to be constant when the corresponding resonant ellipse is lying within the space of instability.

8. l_1 is the point where the resonant ellipse of the corresponding wave enters the unstable region and l_2 is the point where the semimajor axis b exceeds that region (Appendix D, Figure D.5), ellipses 1 and 2).

9. The loss cone angle α is taken to be 15° but it is not infinitely steep, permitting $\Delta\alpha = 2°$ because the variable interaction altitude of the impacting electrons in the planetary atmospheres produces this scattering in α (Appendix D).

10. Equation (4.2) is solved for a given ratio f_p/f_c (kept constant along the ray path) and generally two solutions are derived near branches b_1 and b_2, respectively.

Since ω_i is constant between l_1 and l_2, Equation (4.6) can be written

$$g = \omega_i \int_{l1}^{l2} \frac{dl}{v_g(l)} = \omega_i T \tag{4.7}$$

where T is the interaction time of the electron - wave resonance.

The exact calculation of T as a function of θ and f_p/f_c is described in Appendix D using the above assumptions. So only the results are presented here in Figure 4.3 for $\theta = 70°$. In the top panel (a) we show the normalized interaction time T against f_p/f_c for the two branches b_1 and b_2 as defined in Figure 4.2. We see that T is generally higher for branch b_1 which corresponds to lower refractive indices n (bottom panel) and consequently to lower group velocities v_g. Moreover, a dramatic increase of T is observed when f_p/f_c is reaching its highest values (≈ 0.14). This can easily be understood in the middle panel (b) which shows the wave-particle interaction length L (between l_1 and l_2). We see a maximum of L reaching $10^{-2} r_o$ when f_p/f_c is near its maximum. Assuming r_o to be about 2 - 3 planetary radii (distance of radio source from the planetary center), we obtain $L \approx 200$ km for the earth and $L \approx 2000$ km for the giant planets Jupiter and Saturn. We note that for branch b_1 when considering low values of f_p/f_c (< 0.01) the interaction length L drops down to lower than $10^{-7} r_o$ which corresponds only to a few meters which might be not realistic. The previous findings can be discussed very critically when considering Figure 4.3c. There we have drawn the refractive indices given at l_1 (full line) and l_2 (dashed line). Especially for b_1, refraction effects arise because of the low refractive index n (Figure 4.3c). It is not possible to calculate these effects since the directions of $\vec{\nabla} n$ are not actually known. However, this is highly relevant for the branch b_1 and is quenching the gain after the phase of amplification.

For a given θ the maximum interaction time T is reached near the vertex of the respective separatrix (hatched areas in Figure D.6 of Appendix D), but also in this region, the increase of the refractive index along the ray path is quite important so that subsequent damping may also overcome the initial gain.

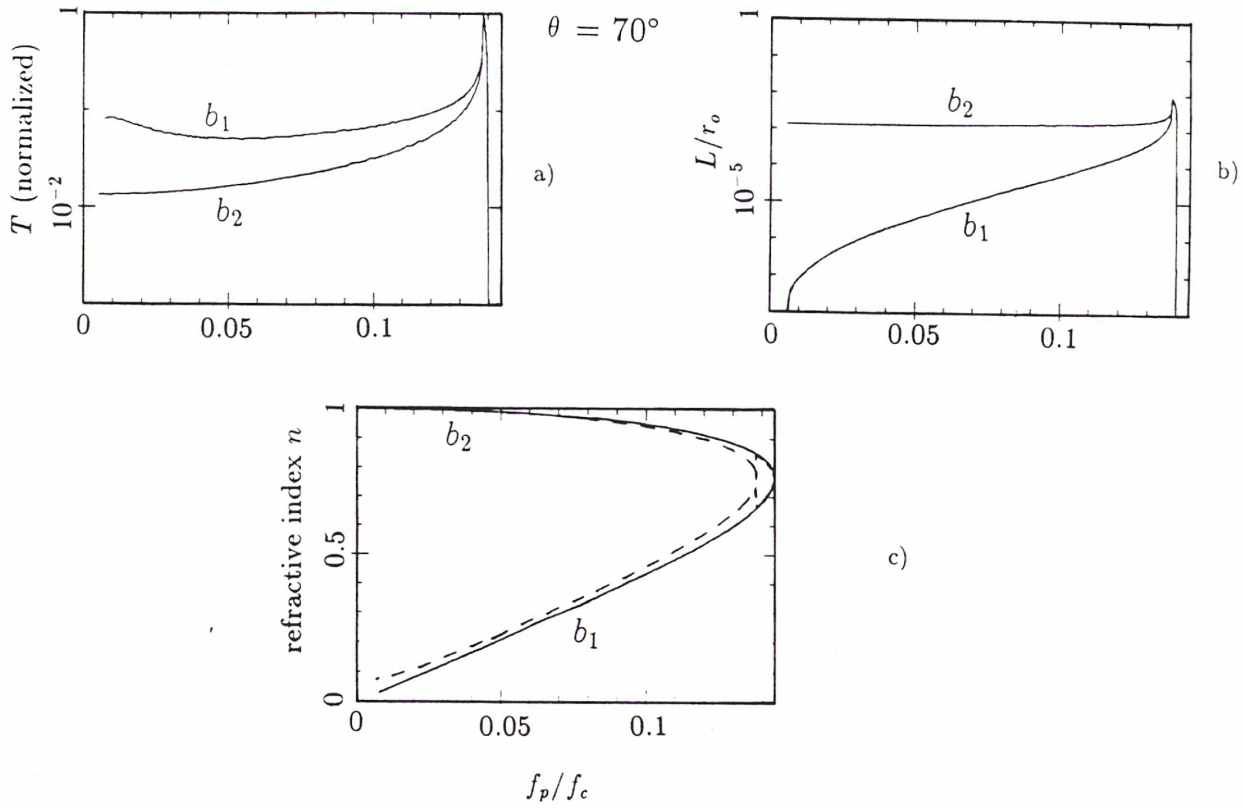

Figure 4.3: (a) Normalized interaction time T, (b) wave-particle interaction length L, and (c) refractive index at l_1 (full line) and l_2 (dashed line) for $\theta = 70°$ as a function of f_p/f_c. For low f_p/f_c, two solutions exist (b_1, b_2).

One solution where we can unambiguously state that damping after the phase of amplification is most unexpected is branch b_2 for lower f_p/f_c. There, the refractive index is near unity and the group velocity nearly the light velocity c which explains the moderate gain. The particle interaction length is $10^{-3}r_o$ (r_o: a few planetary radii) which can be compared to the dimensions of an auroral arc. We are confident that in the limit of our calculations, plasma conditions corresponding to branch b_2 are relevant for the amplification of radio emissions. In contrast, for branch b_1 $n \rightarrow 0$ for $f_p/f_c << 1$ therefore Equation (4.4) cannot be fulfilled for typical values of $\beta_{\|o} \approx 0.1$ and possible amplification is highly questionable.

4.3.2 Results

With the results of the preceding sections (the wave growth as given for branch b_2 [$n \rightarrow 1$] is relevant for the amplification of radio emission), Equation (4.4) can be rewritten in the limit $n \rightarrow 1$ (Figure 4.3c) for branch b_2

$$\cos\theta = \beta_{\|o} \tag{4.8}$$

Thus, we are able to express the wave normal angle θ (Equation 4.8) and the ratio f/f_c at the

source (Equation 4.5) in terms of the parallel bulk velocity $\beta_{\|o}$ when f_p/f_c is very low. The graphs of $\theta(\beta_{\|o})$ and $f/f_c(\beta_{\|o})$ are plotted in Figure 4.4. In addition, we show the scale for the respective electron energies. For energies of 10 keV (which are expected in the Jovian auroral zone) the resulting values for θ and f/f_c are 78° and 1.027, respectively. This, in retrospect, confirms the assumptions for the wave normal angle θ and f/f_c in our three-dimensional ray-tracing study and demonstrates the large degree of consistence when linking the CMI to auroral radio emissions. Further, this investigation agrees with a theoretical study on the Saturnian radio emission (Galopeau et al., 1989). These authors modeled the Saturnian radio spectrum best for a nearly perpendicular θ when $f_p/f_c << 1$.

4.4 Discussion

During the present investigation we analyzed the CMI in plasmas which are largely dominated by the magnetic field ($f_p/f_c < 0.01$). This study is highly important, however, because of the applications to the low-frequency auroral emissions of Jupiter and Saturn. Within the sake of simplifications, we derived the wave emergence angle θ and f/f_c at the source as a function of the parallel bulk velocity $\beta_{\|o}$ provided that the amplification of the wave is due to the loss cone or the holelike instability.

One of our most important findings is that the refractive index at the source is near unity because f/f_c has been shown to be about 1.01 for plausible electron energies (1-10 keV), thus, the source region is sufficiently distinct from the R-X cutoff. The quenching of the interaction time due to the high group velocity v_g in this region is compensated by the long interaction length which is possibly as long as an auroral arc. On the other hand, when $n \rightarrow 0$ in a low density source region, the group velocity is very small which would enhance the gain, but the interaction length is only in the order of meters or even below which is probably not realistic.

Concerning the wave emergent angle θ at the source, which is found to be $\approx 80°$ for electron energies from 1 - 10 keV, the results agree favourably with the study of the theoretical radio spectrum of SKR performed by Galopeau et al. (1989) and are consistent with the large wave normal angles determined in a theoretical study for TKR (Le Queau et al., 1984a,b).

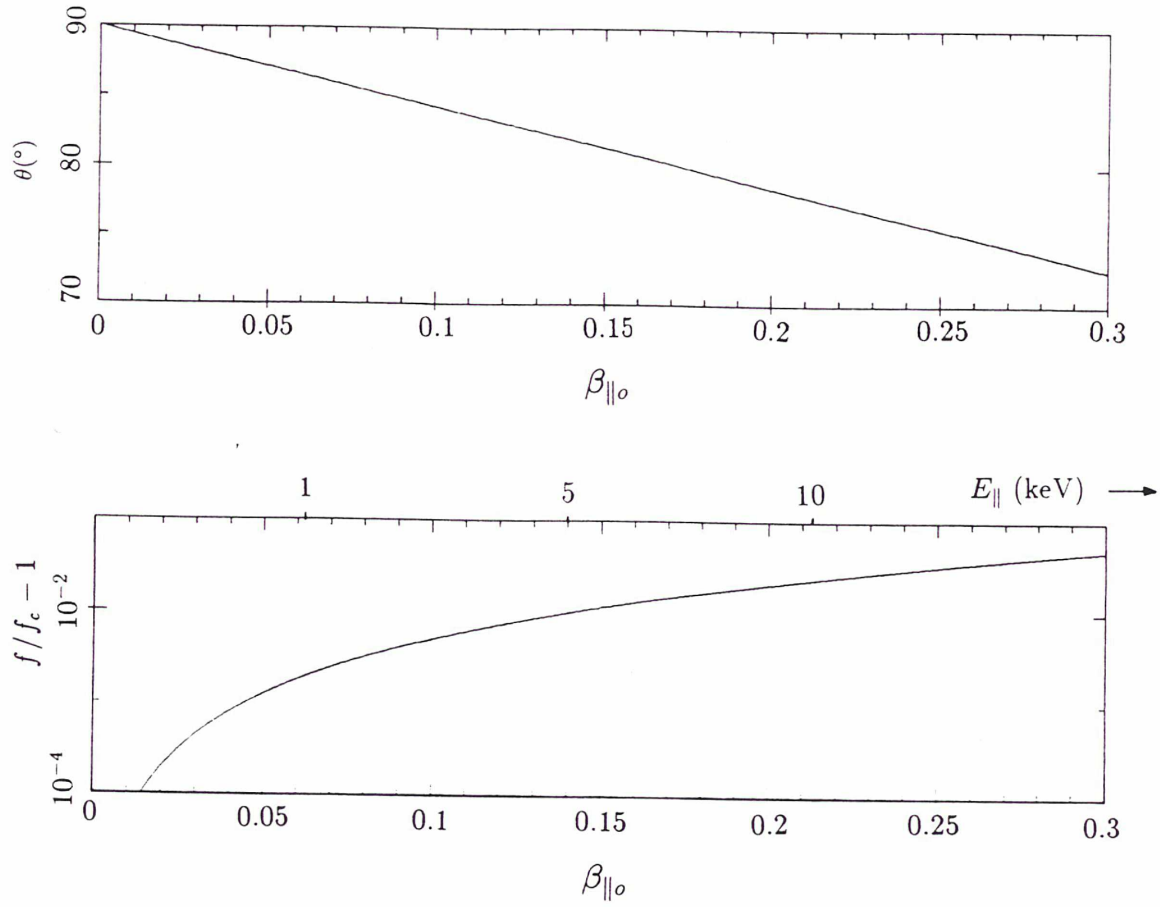

Figure 4.4: Wave emergence angle θ and f/f_c in terms of the parallel bulk velocity $\beta_{\|o}$. The scale for the electron energies E is also given assuming $E_{\|} \approx E$.

Chapter 5

Conclusion and prospects

5.1 HOM characteristics

From observations of the Jovian radio emission at hectometric wavelength (HOM) obtained by Voyager 1 (V1) and Voyager 2 (V2) in 1979, the latitudinal beaming at three selected frequencies f=1326 kHz, 942 kHz, and 558 kHz is determined. We find that the total beam width is between 10° and 20° depending on the normalized (to the earth-Jupiter distance) detection threshold. The beam center of HOM is found to be situated at about +1.6° magnetic (dipole) declination. On the nightside the beam width is a few degrees ($\approx 4°$) narrower compared to the dayside. We establish that right-hand polarization is associated with the northern hemisphere and left-hand polarization with the southern hemisphere which is consistent with wave propagation in the R-X mode. From the analysis of the frequency limits of HOM, we determine a source extension from 2 Jovian radii (R_J) out to about 7 R_J, by assuming an emission close to the R-X cutoff frequency. The beaming results, and the HOM low-frequency limits are compared with the solar wind parameters. We find that increases in the solar wind density and/or pressure are well correlated in time with the lowest frequency limits of HOM and the largest beam widths. A strong correlation is consequently obtained between those two parameters and the HOM energy. This supports the idea that a high density solar wind stream at Jupiter enhances the HOM energy output, extends the source regions to higher altitudes on auroral field lines, and widens the HOM beam to higher magnetic latitudes.

5.2 Ray-tracing and HOM source location

Ray-tracing using realistic magnetic field and plasma models has been performed to locate the Jovian hectometric radiation (HOM) sources. To consider only a few possible source locations, we have assumed that the radiation mechanism is the Cyclotron Maser Instability (CMI), and taken into account the characteristics of the HOM including the results by Ladreiter and Leblanc (1989) (=Appendix A). The emission is assumed to escape from the planet in the extraordinary wave mode within a thin beam of hollow cones whose apexes are distributed uniformly in longitude at the northern and southern hemispheres at altitudes where the gyrofrequency f_c is less but nearly equal to the observed wave frequency. The rays are traced from possible sources

located at f/f_c=1.05 and labeled by the dipole shell parameter L. For each source, we have determined the emergence wave normal angle θ_{crit} above which the rays no longer travel within the HOM emission beam nearby the magnetic equator. We show that the HOM sources cannot be located on field lines within the Io flux tube. However, wave refraction due to the Io torus plays a crucial role for the propagation and beaming of the waves toward the magnetic equator. It is found that HOM sources located at field lines $15 < L < 30$ agree best with the observations when assuming that the cone half angle of emission is about $70° - 90°$ with respect to the local magnetic field. Thus, the source is associated with the tail field aurora where the magnetic field lines connect the polar region to the Jovian magnetic tail and is extended in altitude from 2 to 7 Jovian radii (R_J). Our results explain in detail the radio phenomenology of the hectometric radiation, in particular the strong latitudinal beaming, the solar wind control, the absence of HOM emission when Voyager 1 was within the Io torus, and the absence of Io control on the HOM.

5.3 Three-dimensional modeling of the HOM

To model the Jovian hectometric radiation, we additionally performed three-dimensional ray-tracing at a typical HOM frequency of f=500 kHz. The source locations are assumed to lie along magnetic field lines L=20 as determined by Ladreiter and Leblanc (1990a) (=Appendix B). Furthermore, the sources are distributed uniformly in longitude at magnetospheric heights, where the cyclotron frequency is less but nearly equal to the wave frequency. The emission is beamed at large angles (70°-80°) with respect to the magnetic field and propagates in the extraordinary (R-X) mode. Our study can account for the major characteristics of the HOM radiation as observed by the Planetary Radio Astronomy (PRA) experiment aboard Voyager 1 and Voyager 2 during the encounter period and at large distances from the planet. Thus, geometrical effects are taken into account. The modeled radiation pattern reveals the existence of a shadow zone at the magnetic (dipole) equatorial plane extending to about 20 Jovian radii (R_J), which was actually observed by both Voyagers. The results from our ray-tracing analysis account for the strong latitudinal beaming of the radiation, observed at large radial distances from Jupiter, as well as for the polarization properties. Moreover, the modeled intensity profiles, compared with observations at various distances from Jupiter, show a remarkable agreement. However, a better fit to the observations is obtained when the Io torus electron density (from Divine and Garrett, 1983) is enhanced by 15 %. This study confirms that the HOM sources are located along open magnetic field lines with footprints in the tailfield auroral ovals in both hemispheres. We suggest that HOM is the low-frequency extension of non-Io DAM, since the observed spectral peak of HOM near 1 MHz could be produced by the focussing of the radiation due to refractory effects of the Io torus.

5.4 HOM generation mechanism

Considering the Cyclotron Maser Instability (Wu and Lee, 1979) within low density magnetoplasmas ($f_p/f_c < 0.01$) we derive simple expressions relating the wave emergent angle θ and the ratio f/f_c at the source to the normalized (to c) parallel bulk velocity $\beta_{||o}$ of the instability (characteristic for an electron distribution function) via the equations $\cos(\theta) = \beta_{||o}$ and

$f/f_c = (1 - \beta_{||o}^2)^{-1/2}$. During this investigation we considered the loss cone and holelike instability to be responsible for wave amplification. Both of these regions exhibit a relatively small perpendicular energy. We found that for $\beta_{||o}$ corresponding to 1-10 keV, θ is found to be nearly perpendicular with respect to the magnetic field and θ decreases when $\beta_{||o}$ increases. The wave frequency is slightly above the gyrofrequency, but is substantially distinct from the R-X cutoff; thus, the refractive index is near unity at the radio source. No strong refraction along the ray path is therefore expected for $f_p/f_c << 1$. The results are highly relevant for the lower frequency auroral emissions of Jupiter (low frequency DAM and HOM) and of Saturn (lower frequency SKR) where very low density magnetoplasmas ($f_p/f_c < 0.01$) do in fact exist at the respective source regions. Therefore, these radio components escape from the respective radio sources in form of hollow cone beams with large cone apical angles.

5.5 Summary

Source location: High latitude auroral field lines ($L = 15 - 30$) at heights where $f/f_c \gtrsim 1$. The ratio f_p/f_c is very low ($\approx$ 0.001-0.01).

Source extension: From 2 R_J to 7 R_J along auroral field lines at both hemispheres. The sources are distributed over a wide range of longitudes.

Emission pattern: Hollow cone, half apical angle θ = 70° - 90°, cone wall thickness $\Delta\theta << \theta$

Generation mechanism: Cyclotron Maser Instability (CMI).

Relation to other emissions: Low-frequency extension of non-Io DAM, distinctly different from Io DAM and KOM.

General comments: Occurrence of a shadow zone near the magnetic equatorial plane at distances less than 15-20 R_J. Beyond, the emission is confined within a quite narrow beam (latitudinal extension 10° - 20°) near the magnetic equator. The emission is local time dependent.

5.6 Prospects

The study of the Jovian hectometric radiation enabled us to understand the main characteristics of the radiation such as the properties of HOM as well as the source location in the Jovian magnetosphere. The present analysis also clearly shows a straightforward way how to proceed step by step from the observations of HOM to the emission characteristics, source locations, and finally to a link to the generation mechanism. This finally leads to a comprehensive view of HOM also in the context with other planetary emission components. However, the Voyager spacecraft only explored regions close to the Jovian equatorial plane, so no observations about the HOM activity beamed in high latitudes are available at present. Future spacecraft missions such as Galileo and Ulysses will provide the opportunity to collect further data leading to a deeper study of yet unresolved details concerning the hectometric radiation.

Appendix A

Jovian hectometric radiation - Beaming, polarization, source extension, and solar wind control

Abstract

From observations of the Jovian radio emission at hectometric wavelength (HOM) obtained by Voyager 1 (V1) and Voyager 2 (V2) in 1979, the beaming at three selected frequencies f=1326 kHz, 942 kHz, and 558 kHz is determined. We find that the total beam width is between 10° and 20° depending on the normalized (to earth) detection threshold. The beam center is found to be situated at about +1.6° magnetic (dipole) declination. On the nightside the beam width is a few degrees ($\approx 4°$) narrower compared to the dayside. We further provide evidence that the emission is not uniform in system III longitude (CML). We establish that right-hand polarization is associated with the northern hemisphere and left-hand polarization with the southern hemisphere, without reversal from dayside to nightside observations. From the analysis of the frequency limits of HOM, we determine a source extension from 2 Jovian radii (R_J) out to more than 6 R_J, by assuming an emission close to the R-X cutoff frequency. The beaming results, and the HOM low-frequency limits are compared with the solar wind parameters. We find that increases in the solar wind density and/or pressure are well correlated in time with the lowest frequency limits of HOM and the largest beam widths. A strong correlation is also obtained between those two parameters and the HOM energy. This supports the idea that a high density solar wind stream at Jupiter enhances the HOM energy output, extends the source regions to higher altitudes on auroral field lines, and widens the HOM beam to higher latitudes.

A.1 Introduction

Observations obtained from the Planetary Radio Astronomy (PRA) experiment (Warwick et al., 1977) show that the Jovian radio spectrum consists of 4 distinct components: a decameter wavelength component (DAM), a hectometer wavelength emission (HOM), and two kilometer wavelength components (KOM), namely the broadband (bKOM) and the narrowband (nKOM)

emission. A number of studies have been conducted on the latitudinal beaming of these radio emissions. For the non-Io DAM emission a strong latitudinal beaming has been evidenced from ground - based observations (Gulkis and Carr, 1966; Carr et al., 1970; Carr and Desch, 1976; Barrow, 1981) and more recently from spacecraft and ground-based simultaneous observations (Poquerusse and Lecacheux, 1978; Barrow et al., 1982; Maeda and Carr, 1984, 1988).

The latitudinal beaming of the KOM emission was derived from the occurrence probability in terms of system III (1965) longitude (CML) or of Jovimagnetic latitude of the spacecraft (Kurth et al., 1979; Desch and Kaiser, 1980; Leblanc and Daigne, 1985a,b; Daigne and Leblanc, 1986; Jones and Leblanc, 1987; Leblanc, 1988).

For the HOM component, the latitudinal beaming was first established by Alexander et al. (1979) by comparing RAE 1, IMP 6, Voyager 1 and Voyager 2 observations. These four spacecraft covered Jovigraphic latitudes from -3.2 to 6.5 degrees. Alexander et al. (1979) considered the whole frequency range of emission, namely 0.6 to 1.3 MHz, and the set of simultaneous observations from V1 and V2 obtained in late 1977 and early 1978 when the spacecraft were at a very large distance from Jupiter. They found that the HOM is emitted in a curved thin sheet with an extension of 10° centered on 3° magnetic latitude. This model is in agreement with the degree of correlation between the two spacecraft separated by up to 3° in Jovigraphic latitude. Later on, Alexander et al. (1981) found further a local time dependence of the HOM emission by comparing day and nightside observations. The nightside recordings show an emission gap of HOM intensity at about 60° CML whereas at the dayside there occurred a local maximum of emission at that longitude.

The emission at HOM wavelength has been found to be strongly polarized. Lecacheux et al. (1980) reported that the source of circular polarization of the HOM (left-hand source) is opposite to that of the DAM (right-hand source). On the other hand, Alexander et al. (1981) reported that the fundamental polarization sense of the HOM may have reversed after encounter. This polarization reversal was not understood and attributed to local time variations.

A solar wind control of HOM was demonstrated by Zarka and Genova (1983) and by Desch and Barrow (1984). Further results are given more recently by Barrow and Desch (1989). Zarka and Genova found that the sector structure of the interplanetary magnetic field highly controls the long term intensity fluctuations at hectometer wavelengths. Desch and Barrow (1984) found a significant positive correlation between the solar wind plasma density and the HOM emission output by using a cross correlation analysis. Genova et al. (1987) furthermore showed that the HOM activity is correlated to the non-Io DAM, but not to the Io-DAM, suggesting that the HOM and non-Io DAM are two components of the same radio emission, and implying a $\geq 4R_J$ source extent along high latitude field lines. A recent study of Barrow and Desch (1989) shows that the higher energy HOM is correlated with the solar wind density, pressure, and the interplanetary magnetic field magnitude. They additionally found that the non-Io DAM is also correlated with the solar wind speed which might argue that HOM and non-Io DAM are not emitted from the same source.

The HOM component was not thoroughly investigated, however, and many outstanding problems still remain unanswered; e. g. is the HOM component just an extension of DAM or is it a distinct component ? Where is the location and extension of the source and is it a corotating source ? What is the polarization of HOM after Leblanc and Daigne (1985a) and Lecacheux and Ortega-Molina (1987) have studied the orientation of the electrical plane of the antennas

with respect to the physical plane, at low frequencies ? Does the beaming of the HOM emission also depend on the solar wind ?

In this paper we treat some of these questions using V1 and V2 data from the low-frequency band of the PRA experiment recorded in 1979, including the V1 and V2 encounters. In section A.2, we calculate the angular beam width of the radiation for 3 fixed frequencies from the occurrence of the HOM emission in system III (1965) longitude (CML) and from the spacecraft position. We compare Voyager 1 (V1) and Voyager 2 (V2) results and investigate also the polarization behaviour. Section A.3 deals with the low-frequency limit of HOM and we give a hint for the source extension, assuming that the source is near the cutoff of the fast extraordinary (R-X) mode centered on auroral field lines. In section A.4, we correlate solar wind parameters with the HOM beaming, and with the low-frequency limit of the emission.

A.2 Beaming of the Jovian hectometric radiation

Alexander et al. (1979) derived their emission beam axis by analyzing the emission peaks in the occurrence probability histograms as a function of magnetic latitude rather than a function of CML. The extension of the emission beam was derived somewhat arbitrarily based on the standard deviation in magnetic latitude of the emission peaks.

Our determination of the beam width is made from a different approach and two methods have been used. The first is from analysis of the emission beginning and ending as a function of magnetic latitude, the second is from the occurrence probability, also in terms of magnetic latitude. The results of the beaming will be presented as a function of the spacecraft distance to Jupiter, of the observed HOM frequency, and of local time; also a comparison of the beaming resulting from simultaneous observations will be made. Finally, we investigate the polarization of the emission.

A.2.1 Observations

For our investigation we used V1 and V2 data of the low-frequency band of the PRA experiment recorded in 1979, including the V1 and V2 encounters, respectively. The low-frequency band consists of 70 channels starting from 1.2 to 1326.0 kHz, each of them with a bandwidth of 1 kHz separated by 19.2 kHz. The PRA antenna consists of two crossed monopoles which allow the sense of polarization to be determined. For a detailed description of the PRA experiment, see Warwick et al. (1977).

The occurrence of the HOM emission as a function of system III longitude for a fixed frequency is a quite stable feature for many consecutive rotations for both spacecraft. With a few exceptions near the respective encounters where ghost images occur, the beginning and ending of the emission can be easily detected in a time interval of $\approx$ 4 months centered on the respective encounters. Figure A.1 shows typical HOM emission before encounter during one Jovian rotation for V1 (top panel) and for V2 (center panel). Note that the emission gap centered at about 200° CML is wider for V2 than for V1. Contrary, the V1 data show a little emission gap centered near 20° CML which is not visible in the V2 data. This is due to the higher Jovicentric declination during the inbound trajectory for V2 ($\delta = 7.5°$) compared with V1 ($\delta = 3.2°$). If one assumes

a beamed emission centered near the magnetic equator, V2 exits the beam at its northern side earlier than V1 because of its higher Jovicentric declination. The reentry occurred later for V2 and vice versa for the magnetic southern excursions at about 20° CML. This fact can easily be seen in the bottom panel of Figure A.1 which shows a sketch of the two spacecraft trajectories in a Jovimagnetic coordinate system during one Jovian rotation and an emission beam fixed in magnetic latitude. The recordings at smaller radial distances from Jupiter show narrower emission gaps centered at $\approx 200°$ but still wider for V2 than for V1. In fact, the relative HOM intensity (not normalized to a fixed distance) increased and we detected emission at the edge of the beam near to Jupiter which might not have been detected at larger distances at the same threshold.

A.2.2 Methods of analysis

In the first method, in order to determine the beaming we analyzed at a given time period the emission beginnings and endings in our observations as a function of the (dipole) magnetic latitude. Following this procedure rotation by rotation, we obtain for each rotation one off- and one onset centered around 200° CML which delineate the northern beam limits. Sometimes, also the southern spacecraft beam crossings are visible, in particular during the V1 inbound trajectory (due to the lower Jovicentric declination). If so, the southern limit of the beam is also determined. We named the first beam crossing, occurring after the gap centered at about 200° CML which denotes a beam entry from the magnetic northern side, the EARLY beam northern crossing, while the corresponding southern side exit was named the EARLY beam southern exit. The reentry from the southern side is named the LATE beam southern entry, while the subsequent northern exit is named the LATE northern beam crossing. These beam crossings are indicated in the bottom panel of Figure A.1. Note that the late beam exit occurs in general at the subsequent rotation number but, in order to simplify the situation, the early and late beam data are attributed to that rotation number in which the early beam entry occurs.

The northern and southern beam limits are representing the magnetic dipole latitudes of the respective beam crossings. Performing this calculation during several rotations, we obtain averages and standard deviations for the beam limits. In general the southern beam limit could not be determined with sufficient accuracy because the spacecraft most of the time did not leave the beam at its southern side. For the northern side there are only a few cases where the spacecraft (especially V1 before encounter) observed no beam northern exit during one rotation (no emission gap at 200° CML). If so, we have no exact information about the beam limit in this case. Our calculated average from the northern beam limits for several rotations is therefore less than the true average. By assuming a gaussian distribution of the calculated beam limits from each rotation around the true average, we are able to correct our calculated average to the true one. The same holds for the standard deviation. The determination of the beam limits was performed for three typical hectometer frequencies $f_1 = 1326$ kHz, $f_2 = 942$ kHz, $f_3 = 558$ kHz.

In the second method we determine a system III longitude range which includes a certain probability of emission by regarding a CML diagram of the relative occurrence probability of HOM (Figures A.2a, A.2b). The beam limits are then simply the respective Jovimagnetic declinations of these CML range limits. A similar method was used by Leblanc and Daigne (1985a,b) in order to calculate the beaming of Jovian kilometric radiation. The beam width, defined by a relative occurrence probability higher than 0.5 must correspond approximately to

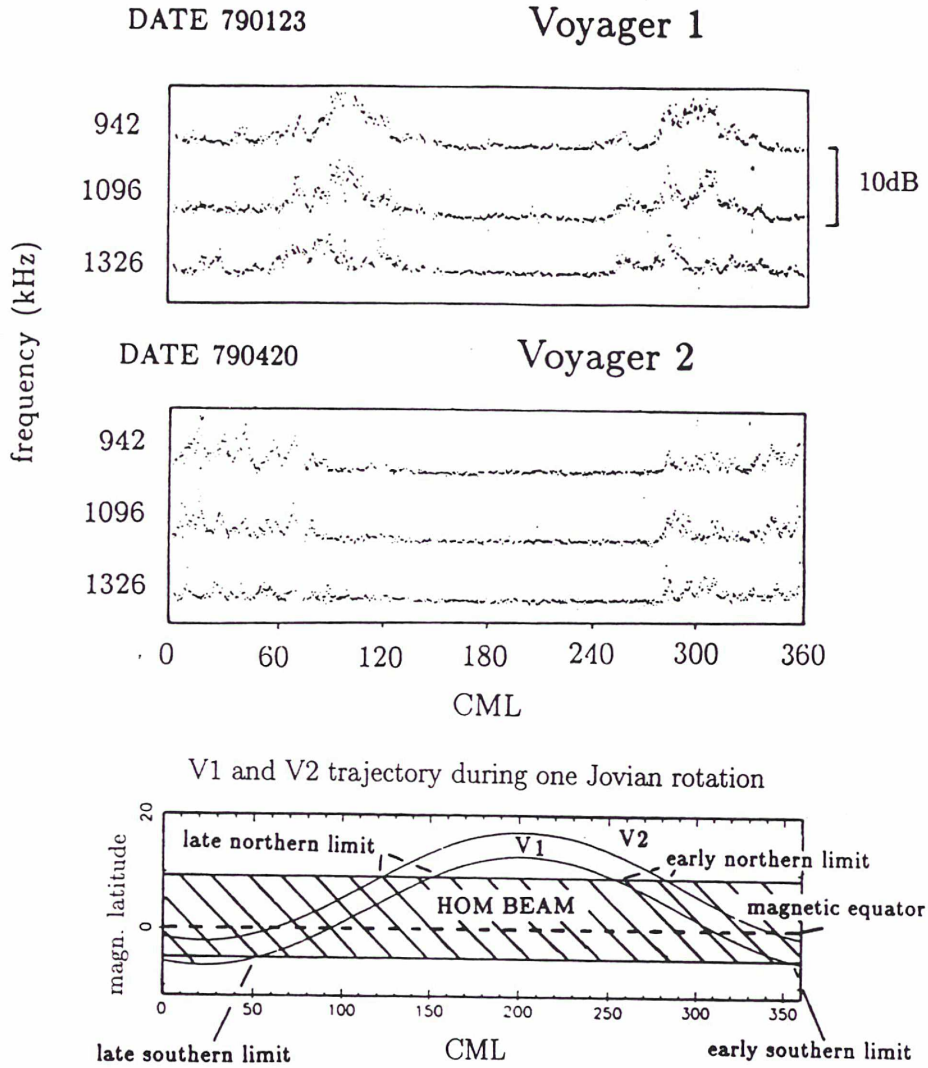

Figure A.1: Recorded HOM emission for V1 (top panel) and V2 (center panel) during one Jovian rotation before the respective encounters for the 3 frequencies indicated. The emission gap near 200° CML is broader for V2 because of the higher Jovicentric declination. Contrary, no emission gap near 20° CML was seen from V2. The bottom panel sketches the V1 and V2 trajectories before the respective encounters separated by a few degrees in Jovicentric latitude. By assuming an HOM emission beam fixed at magnetic latitude, the observations for V1 and V2 are simulated very accurately.

that beam width, calculated by our first method, if the occurrence probability peak reaches 1.

In our beaming calculations, we used V1 data from January 5, 1979 (Rot. number 1777) until May 2 (Rot. number 2061), and V2 data from April 15, 1979 (Rot. number 2020) until August 4 (Rot. number 2286), excluding only a few days centered on the respective encounters to avoid the dramatic change in spacecraft Jovicentric declination. The spacecraft-Jupiter distances are, for V1, 826 R_J before encounter until 798 R_J after encounter. For V2, the corresponding values are 868 R_J before and 238 R_J after encounter. During these time periods, the PRA experiment provided us with a high data rate. When considering the observations, we notice that the

beaming depends on the spacecraft Jupiter distance because of the increasing intensity with respect to a constant threshold. This distance effect was not corrected because the beam width would then be dependent on the choice of the threshold normalized to any assumed distance. Instead, as the intensity is not normalized, the beam width appears to be a function of radial distance due to the variation of the corresponding normalized threshold at 4.04 R_J. Throughout this investigation a detection threshold corresponding to a flux density of $5 \cdot 10^{-20}\mathrm{Wm}^{-2}\mathrm{Hz}^{-1}$ was used for observations at all radial distances. Therefore only results taken from data at the same radial distance can be compared. We divided our basic data set into several "sections" where each section represents a certain radial distance being centered on this section. For V1 the first section is centered at 630 R_J (Rot. number 1812) and the extension of the section is represented by 60 rotations centered on Rot. number 1812. The results obtained from this first section are representative of the beaming at 630 R_J before encounter for V1. Similarly, we defined 8 sections for V1 and 7 for V2. Sections close to the encounters were chosen to be shorter because of the rapid variation of the distance to Jupiter near the encounter. All of the 15 sections are summarized in Table A.1. Sections 8, 9, and 15 represent data recorded at larger distances from Jupiter; they are discussed later on in the text.

Voyager 1/section			1	2	3	4	5	6	7	8
Voyager 2/section	9	10	11	12	13	14				15
Dist. to Jupiter (R_J)	-1120	-756	-630	-420	-210	210	420	630	756	1120
Extension (Jov. rot.)	200	20	60	60	40	40	60	60	20	200

Table A.1: Distance and extension of the 15 investigated sections mentioned in the text.

A.2.3 Results

Hectometer latitudinal beaming

Figure A.3 summarizes the beaming results for all sections defined in Table A.1 by plotting magnetic declination of the HOM northern beam limits (obtained from method a) for f=558 kHz (top panel) and f=1326 kHz (center panel) in terms of radial distance and the corresponding normalized detection threshold. The bottom panel shows the average beam width of HOM (average of the 3 frequencies studied). Linear interpolation has been performed between the obtained results. Full lines denote the early northern beam limit, and dashed lines the late one. The standard deviations are found to be about 2°, somewhat lower for high frequencies and higher for low frequencies.

We can see a trend to higher northern beam limits for both spacecraft when the spacecraft Jupiter distance and therefore also the normalized detection threshold decrease. In general, the early and late northern beam limits show approximately the same values except for the V2 preencounter period at f=1326 kHz. We therefore conclude that the magnetic dipole equator is a good frame of reference for the beaming at hectometer wavelengths. By comparing V1 and V2 results at the same radial distances before encounter, we find that the beam is thicker for V2 than for V1 although we would expect the same beam width at the same distance for both spacecraft. That is obviously not the case and we conclude therefore that the beaming is not stationary in time and we will give a possible explanation in part A.3 by comparing this effect with the solar wind activity.

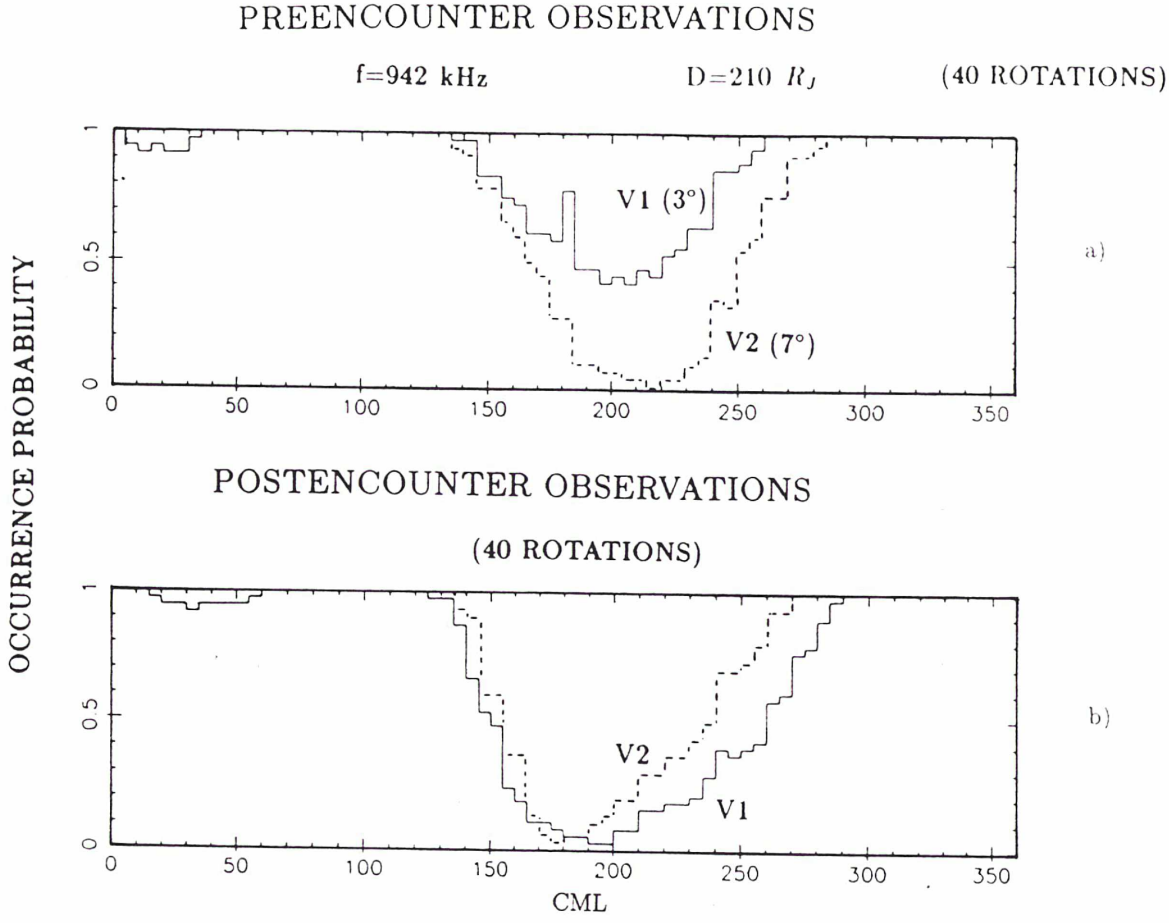

Figure A.2: V1 (full lines) and V2 (dashed lines) emission occurrence as a function of system III longitude observed during 40 Jovian rotations centered at the indicated distance. (a) displays preencounter, and (b) postencounter observations. Notice the high asymmetric shape of the emission gap centered at about 200° CML during nightside observations. The emission gap in (a) is wider for V2 because V2 observed from a higher Jovicentric declination (7°) during the inbound trajectory compared to V1 (3°).

We computed the occurrence probability of the HOM emission during the different periods as defined in sections 1 to 15. Examples are shown in Figures A.2a and A.2b. The magnetic declinations of the respective beam limits are derived in the manner described in method b) and those limits are calculated by assuming the relative emission occurrence probability within the beam to be higher than 0.6. Sections with distances more than 1000 R_J are excluded because of the general decrease of occurrence probability for all system III longitudes farther away from Jupiter. The results are shown in Figure A.4 and confirm all the characteristics of the beaming obtained from the first method. From Figures A.3 and A.4 we conclude also that the beam width is generally the same for the three frequencies studied but, sometimes, the beam width for f=1326 kHz and also f=942 kHz (not plotted, because it is very similar to f=1326 kHz) seems to exceed that for 558 kHz especially for V2 near the encounter on the dayside.

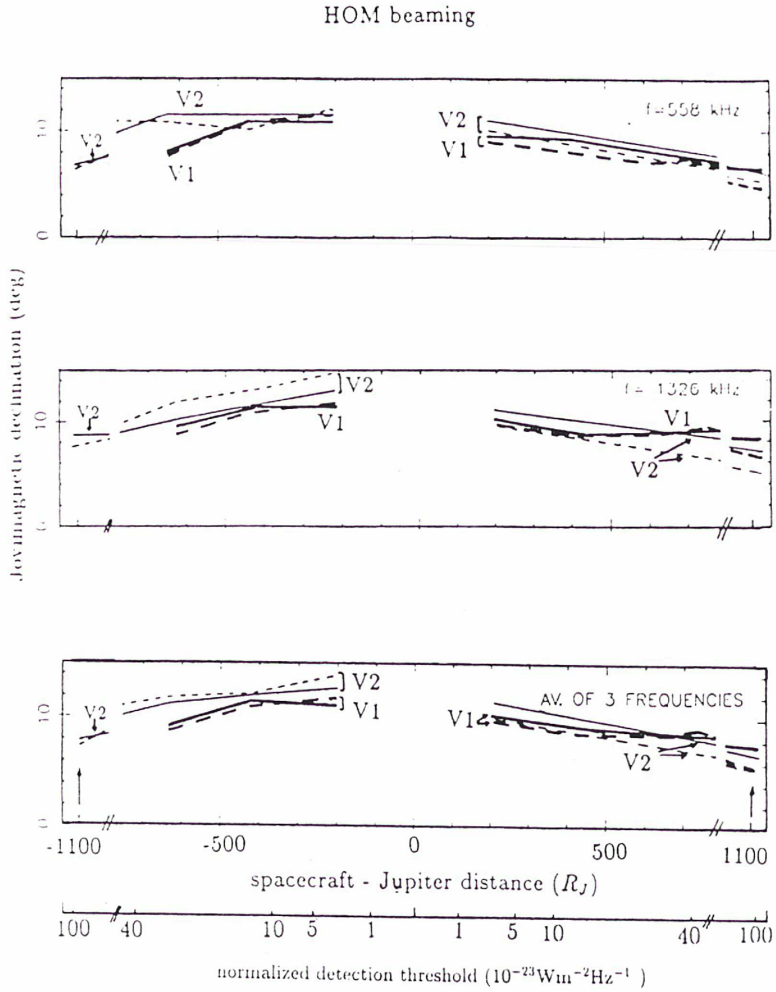

Figure A.3: HOM northern beam extension for f=558 kHz, f=1326 kHz and averaged northern beam limit (average of the 3 frequencies studied) plotted as a function of radial distance and the corresponding normalized (to the earth-Jupiter distance) detection threshold. Full lines denote the early northern beam limit and dashed lines the late one, thick lines are plotted for V1 and thin lines for V2. Negative distances are indicated for preencounter data.

Local time dependence of the beaming

Figure A.2a gives an example of HOM (f=942 kHz) occurrence observed from V1, and from V2, both at $\approx$ 210 R_J at the dayside. We see the larger emission gap for V2 at about 200° CML and no gap at 20°. In Figure A.2b we show nightside observations (also at $\approx$ 210 R_J) and we see a dramatic change of the occurrence probability in system III longitude, especially for V1. This local time dependence even persists when we rule out the change in Jovimagnetic latitude of both spacecraft switching from the day to the nightside because the observations at the nightside show no more the symmetric pattern with respect to the 200° meridian as found for the dayside. Such an effect has already been reported by Alexander et al. (1981) observing the HOM intensity instead of the occurrence probability of the radiation.

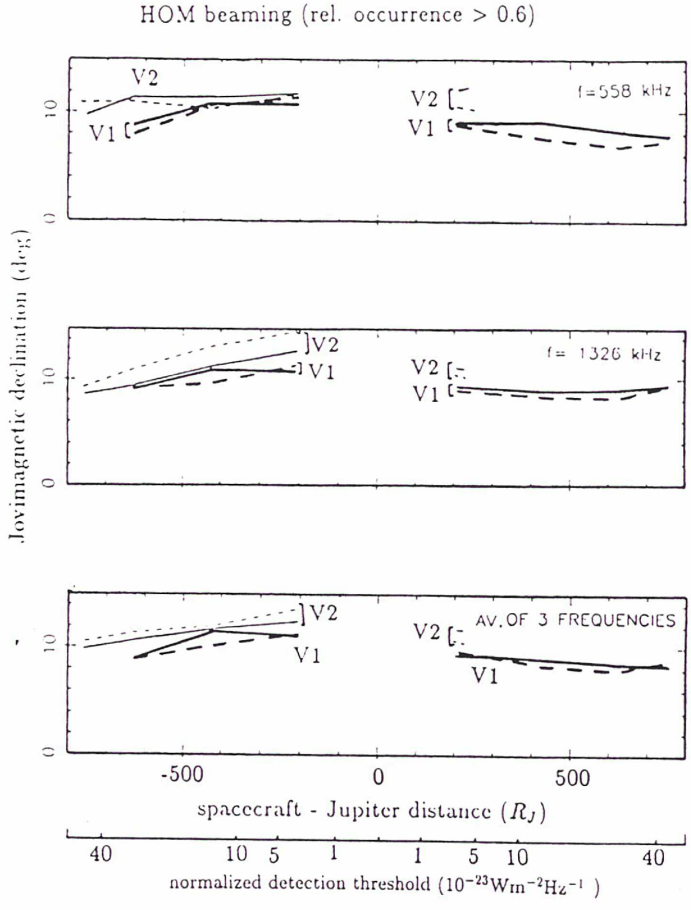

Figure A.4: Same as Figure A.3, but now for beam limits defined by a relative probability of occurrence > 0.6.

This local time effect in the HOM beaming is also shown in Figures A.3 and A.4. We observe that the beam width changes dramatically when the spacecraft switched from the day- to the nightside. We are able to precisely state that the beam is a few degrees larger (extending to higher magnetic declination) on the dayside than on the nightside. A similar effect was found by Leblanc and Daigne (1985a) for the Jovian kilometric radiation.

The local time dependence can also be clearly seen when we compare V1 data after encounter with V2 data before encounter at approximately the same distance (756 R_J), when simultaneous observation was possible (about Rot. number 2050). In this case we took 20 rotations centered on Rot. number 2050 for V1 and V2, respectively. The results are also plotted in Figures A.3 and A.4 (compare distances of about 750 R_J on the day and nightside). The dayside beam calculated from V2 data is significantly larger than that observed by V1 at the nightside.

Further, we investigated low data-rate time periods at larger radial distances from Jupiter. (sections 8, 9, 15 in Table A.1). The corresponding beaming is shown in Figure A.3 (see arrows). Comparing V2 results before encounter with those obtained after encounter, we see the larger beam in the preencounter data as expected. For the V1 data the beam after encounter is also narrower than that for V2 before encounter although the local time dependence is less striking

in this case. In general the average northern beam limit is about 10° magnetic latitude on the dayside and about 8° on the nightside.

General aspects of the HOM beaming and degree of correlation from simultaneous observations by V1 and V2.

Alexander et al. (1979) determined the location of the sheet where the HOM beam is centered and found about 3° northern magnetic latitude based on the B_{min} equator and about 2° when they took the magnetic dipole equator as frame of reference. This sheet which is conical can be visualized as a locus for the instantaneous beam axis when observed over several rotations. We are also able to determine the location of this conical sheet in particular when V1 reached magnetic southern declinations where also the southern beam limits could be seen. Assuming that this sheet is exactly between the northern and southern limits, we took the averages of the beam limits when southern beam information is also present. From these we find that the location of this sheet which denotes the beam center (beam axis) is situated at about 1.6° Jovimagnetic (dipole) latitude. This would be in excellent agreement with the result of Alexander et al. (1979) if they had also assumed the magnetic dipole equator as frame of reference. From our calculations we obtained by assuming that the beam axis is at 1.6° magnetic latitude a total beam width of about 20° when the observations are made close to Jupiter (which corresponds to a very low normalized (to earth, 4.04 AU) threshold of $3.4 \cdot 10^{-23}\mathrm{Wm}^{-2}\mathrm{Hz}^{-1}$ at $\approx 210R_J$) and about 10° farther away (detection threshold of $10^{-21}\mathrm{Wm}^{-2}\mathrm{Hz}^{-1}$ at $\approx 1100R_J$, (Figures A.3 and A.4). The latter result is comparable to the results of Alexander et al. (1979).

We can obtain more information on the beam widths by computing the degree of correlation of simultaneous observations from the two spacecraft. Alexander et al. (1979) have already investigated the correlation of simultaneous observations given by V1 and V2 as a function of the angular separation. They found decreasing correlation when the spacecraft latitude separation increased and, with a least squares fit, they predict 100 % decorrelation for a latitude separation of 4.7°.

We considered the correlation of simultaneous observations of V1 and V2 not only as a function of angular latitude separation δ, but also as a function of the beam half-width β, the angular local time difference θ, and the angular difference α between the Jovicentric latitude of one of the two spacecraft (we took V1 with the lower Jovicentric declination) and the magnetic dipole latitude of the beam axis. In order to understand our analysis better, we have plotted in Figure A.5 the separation from the beam axis (fixed at magnetic declination) of the V1 and V2 spacecraft separated by 5° in Jovigraphic latitude as a function of CML. In the magnetic coordinate system both spacecraft describe a sine function with an amplitude of 9.6° and the highest magnetic latitude at 202° CML. In Figure A.5, $\delta = 5°$, $\beta = 4°$ and $\alpha = \theta = 0°$.

The CML range where V1 or V2 are situated within the beam are marked by brackets (DV1 and DV2, respectively), and the range where the two spacecraft are simultaneously within the beam is denoted as C. Now it is clear that one has to define a degree of correlation for each of the two spacecraft, respectively. The degree of correlation for V1 (hereafter CV1) is defined as the quotient of the CML range where simultaneous observations occur (C) and the total CML range V1 spent in the beam (DV1). The degree of correlation for V2 (CV2) is defined in a similar way. The portions DV1, DV2, CV1, CV2, and C are symmetrically placed around the

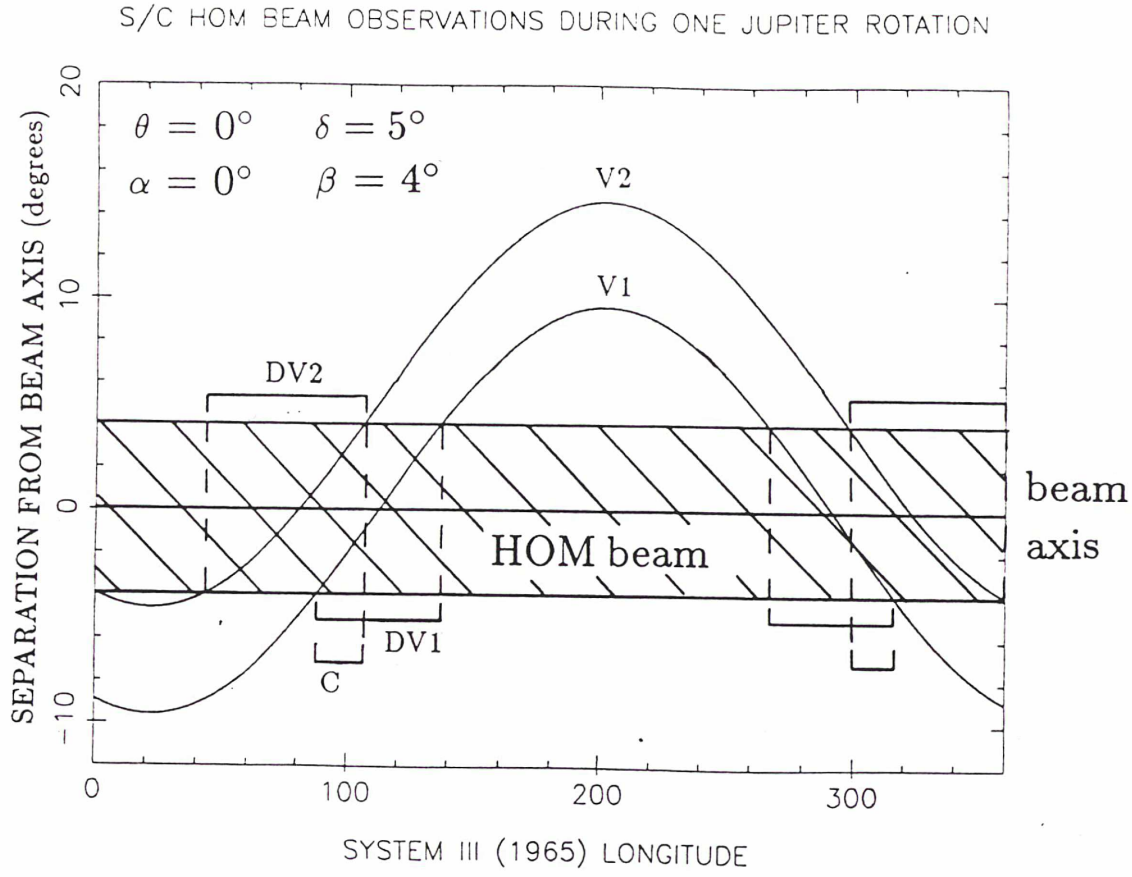

Figure A.5: Schematic plot of the hectometer beam and the two spacecraft trajectories during one Jovian rotation in a Jovimagnetic coordinate system. α denotes the difference between the Jovicentric latitude of V1 and the magnetic declination of the beam axis, θ is the angular local time difference, δ is the spacecraft latitude separation, and β is the beam half-width. In this Figure $\alpha = \theta = 0°$, $\beta = 4°$, and $\delta = 5°$. The CML range during which the beam could be detected by the respective spacecraft is accentuated by brackets. DV1 denotes V1 beam recording, DV2 the V2 beam recording, and during the period C, both spacecraft are within the beam. The degree of correlation seen from the two spacecraft is different (C/DV1 $\neq$ C/DV2).

meridian with 202° system III longitude. From Figure A.5, it is now evident that CV1 and CV2 are functions of δ, β, θ and α.

The results of these considerations are summarized in Figures A.6a-A.6c. They show the quantities CV1 (full line) and CV2 (dashed line) as a function of angular separation δ. The assumed values for the beam half-width β are indicated on each Figure. α is taken to be 2° and the angular local time difference θ is 0°. Note that for the smallest beam width both, CV1 and CV2 are almost linear while for larger beam widths, CV2 in particular is far from linearity. In order to compare observed V1 and V2 correlations (taken from simultaneous observations) with our theoretical correlations, we take the quantities δ and θ from the V1 and V2 trajectories and derive α by assuming the beam axis at a given magnetic latitude. Then the above defined

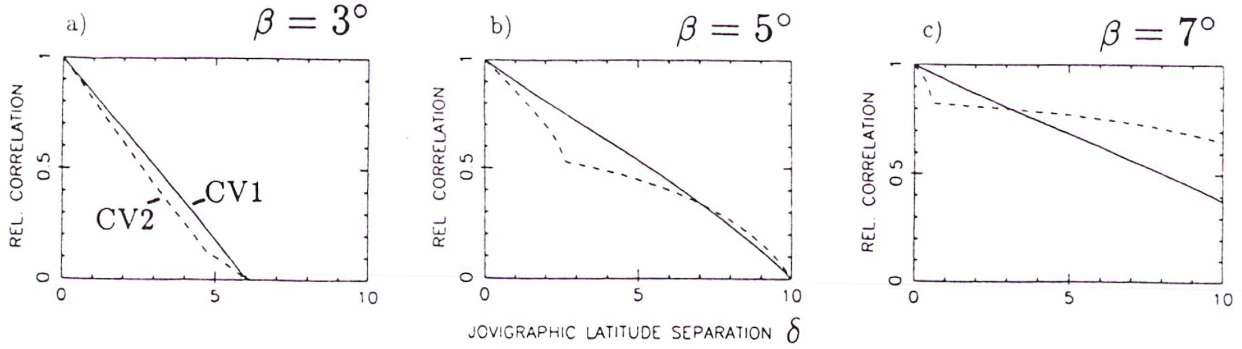

Figure A.6: Calculated correlations of simultaneous HOM observations as a function of $\alpha, \beta, \delta, \theta$. β is varying from 3° (a) to 7° (c). α and θ are taken to be 2° and 0°, respectively. Full lines are displayed for V1 and dashed lines for V2. Note the nonlinearity of CV1 and CV2 at large beam widths β.

correlations CV1 and CV2 are only functions of the beam half-width β and β can be varied to obtain the best fit with the observations.

First of all we try to obtain the beam width for which 100 % decorrelation for a latitude angular separation of 4.7° occurs as found by Alexander et al. (1979).

We take α to be 0°, which means that the magnetic latitude of the beam axis (3°) equals the Jovicentric declination of V1 before encounter ($\approx$ 3°). We further include the small varying local time difference of $\approx$ 2° between V1 and V2 during the respective observations. To fit the observations best (full circles in Figure A.7), we had to introduce a beam half-width $\beta \approx 2.45°$. This beam width is smaller than the estimate of Alexander et al. (1979) ($\beta = 5°$), however.

For comparison with our results, we determined $\alpha = 2°$ (V1 Jovicentric declination before encounter $\approx$ 3.5°, assumed beam axis $\approx$ 1.5°), and $\delta = 4.3°$. Unfortunately, we have only a few observations where we could clearly compare V1 and V2 before encounters, because of an extremely low data rate for V2 during early 1979. A typical case is shown in Figure A.8. V1 data are plotted in the upper panel and V2 data in the lower one. The local time effect has been eliminated by shifting V1 data with respect to the V2 data by the small local time difference. It can be seen that most of the emission is observed by both spacecraft which contradicts Alexander et al. (1979) results. On the other hand, it is shown from our calculated correlations, that only for $\beta > 5°$ both spacecraft observe most of the emission in common when $\delta = 4.3°$ (Figure A.6c).

In the histograms of the relative occurrence probability of emission as a function of CML in Figure 1 of Alexander et al. (1979), we notice that the two emission peaks observed by a single spacecraft do not have the same height, notably for the IMP 6 and RAE 1 satellites. This effect cannot be explained, neither by a latitudinal nor by a direct local time effect. If the HOM emission beam does not depend on system III longitude, one would expect that the observed emission peaks should have the same height in the histograms because the spacecraft crosses the beam twice during one Jovian rotation. In the case of low Jovian magnetic declination of the spacecraft, we expect only one peak which should be centered at 202° CML. The difference of the peak height in the observations could be explained by assuming that the emission is at least weakly enhanced at given system III longitude and is not emitted uniformly. This effect was less clear in the data of the Voyager spacecraft, so this possible anisotropy of the source does not influence our beaming calculations.

To summarize our beaming results, we have verified the strong HOM beaming found by Alexan-

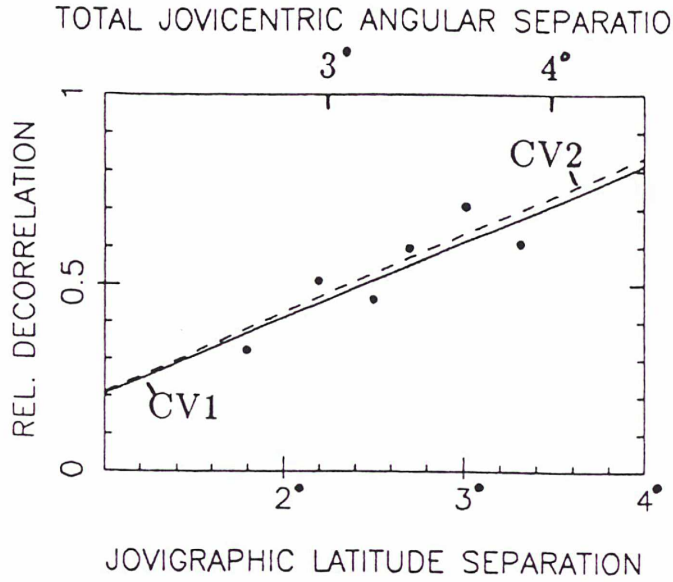

Figure A.7: Comparison of the observed decorrelation of simultaneous HOM observations (V1 and V2) by Alexander et al. (1979) (full circles), and calculated decorrelation. In order to fit their observations best, we had to assume the beam half-width β to be 2.45° ($\alpha = 0°$, $\theta = 2°$). CV1 (full line) denotes V1 correlations and CV2 (dashed line) those for V2. The total angular separation (calculated from $\theta = 2°$) is also indicated at the top.

der et al. (1979). Additionally we give further evidence that the beam width is dependent on the local time of the observer and that the emission may not be uniform in longitude. These findings are supported by the degree of correlation of simultaneous V1 and V2 observations when they were separated by a few degrees in Jovicentric magnetic declination.

A.2.4 Polarization of the hectometric radiation

Contrary to the Jovian emissions at kilometer or decameter wavelengths, the polarization pattern of HOM is complex. In order to investigate the polarization we picked out time periods where the polarization response of the PRA antennas brought out clear results. The polarization response of the PRA antenna system has been investigated by Ortega-Molina and Daigne (1984), who showed that the antenna physical plane of the two crossed equivalent dipoles does not coincide with the antenna electric plane at frequencies below 7 MHz. The orientation of the electric plane was first studied by Leblanc and Daigne (1985a,b) by analyzing the polarization reversals of the Jovian bKOM. The radiation appeared unpolarized when the angle θ between the source direction and the normal to the monopoles was $\theta_c = 70° \pm 3°$, and the azimuth of the source relative to the physical monopoles $\phi_c = 20°$ (see Figure 1 of Leblanc et al., 1987). Only when $\theta < 70°$, was the apparent polarization correct; for $\theta > 70°$ it was opposite to the true polarization. For arbitrary ϕ the antenna electric plane was determined by Lecacheux and Ortega-Molina (1987). In order to determine the true polarization of the incoming waves, we must therefore take into account the variation of the angles θ and ϕ during the V1 and V2 encounters.

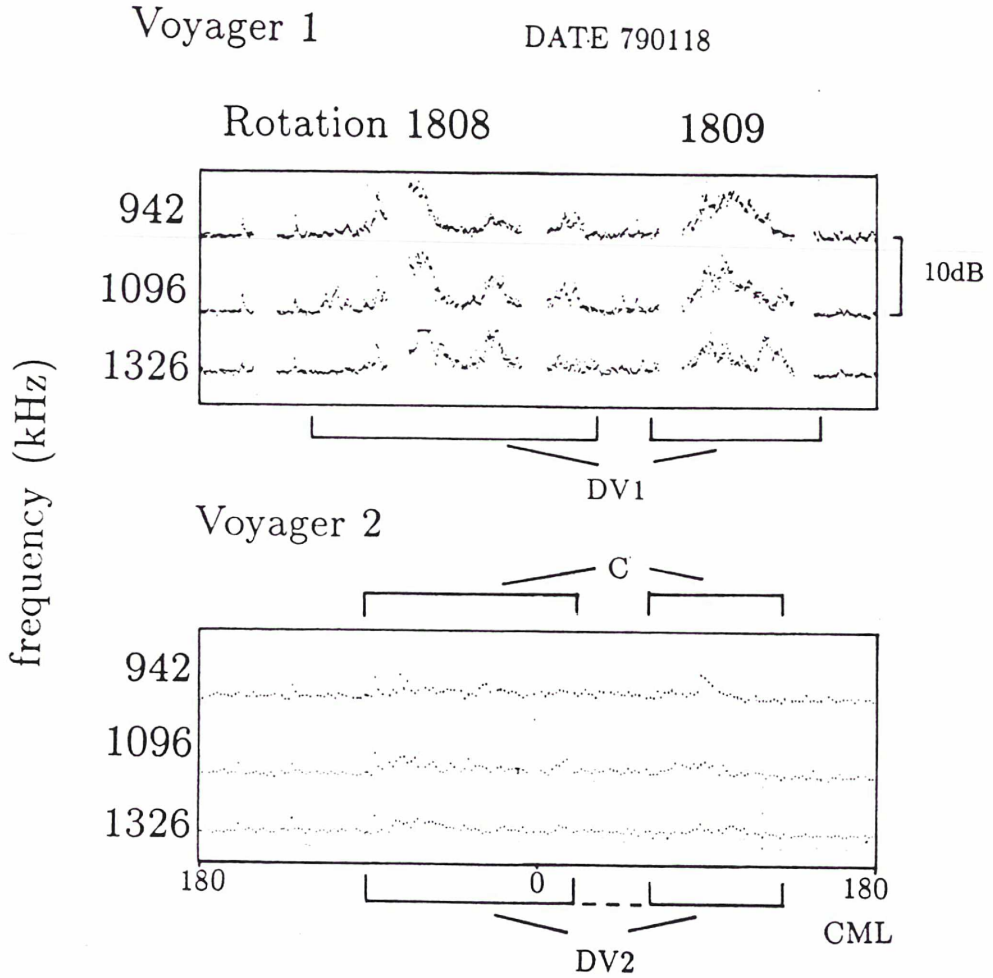

Figure A.8: Typical simultaneous HOM observations of V1 and V2 before the respective encounters. The local time difference is small and eliminated by shifting V1 data with respect to the V2 data. The portions DV1 (for V1), DV2 (for V2) and C (common observations) are graphically pointed out (brackets) and the respective quantities CV1 and CV2 are corresponding to these in Figure A.6c which is calculated for $\beta = 7°$. In this case, we did not consider the weaker emission for V2 near 20° CML (dashed line in the lower panel) as emission gap. The angular latitudinal separation (δ) between the two spacecraft was 4.3°.

Following these considerations, we can only observe clear polarization on the dayside during a few rotations, just before the respective encounters. These observations indicate mostly RH-polarization for the northern hemisphere and LH-polarization for the southern one which gives strong support for an emission in the R-X mode. For the nightside a much longer time interval could be observed with clear polarization responses. For V1 this happened after 790404 (April 4, 1979) and for V2 immediately after the encounter (790709). The top panel of Figure A.9 shows the relative probability of occurrence for the two senses of polarization for V1 observations at f=942 kHz recorded between 790404 and 790413. By comparing the left-hand (LH) and right-hand (RH) emission (corrected following the aforementioned statements), RH emission dominates the northern extension of the beam, whereas the southern beam extension is domi-

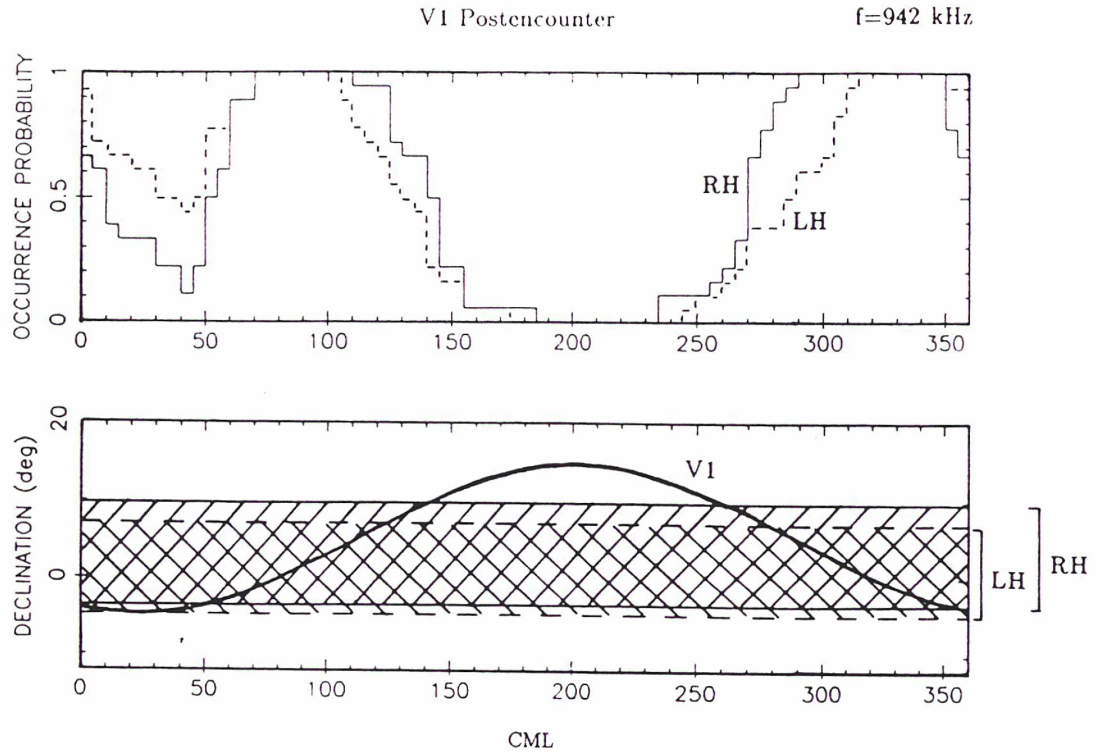

Figure A.9: Relative occurrence probability of HOM at f=942 kHz for V1 postencounter observations when the two polarizations are treated separately (top panel). The full line denotes right-handed (RH) polarization and the dashed line left-handed (LH) polarization. A schematic HOM beam which corresponds to the observations is plotted below.

nated by left-hand polarization (narrower emission gap near 20° CML). This also holds for V2 observations but the effect is less clear. In general the beam contains the two polarizations with a tendency toward RH-polarization at its northern limit and to LH-polarization at its southern limit (see Figure A.9, bottom panel). We further found that the polarization pattern for lower frequencies < 600 kHz becomes different from that at higher frequencies and sometimes even appears to be reversed. A more intensive study on this topic has been made by Ortega-Molina and Lecacheux (1990b).

A.3 HOM source extension in altitude

In this section we will estimate the hectometer source extension in altitude from the HOM low-frequency limit. The high-frequency limit is not well known but it is generally accepted that the HOM high-frequency limit is about 3 MHz and may be as high as 7 MHz (Barrow and Desch, 1989). It has been suggested that the HOM emission is the low-frequency limit of non-Io DAM (Lecacheux et al., 1980; Genova et al., 1987) although there are reasons for treating HOM separately; on one hand, HOM has a distinct spectral peak near 1 MHz (Brown, 1974), and on the other hand the occurrence of the emission as a function of system III longitude differs from that of the non-Io DAM.

To find the HOM source extension we determined the low-frequency limit of HOM from the PRA data for each Jupiter rotation in 1979 for V1 and V2, respectively. In general, the HOM low-frequency limit is within the KOM frequency range, although we did not have any difficulties in distinguishing HOM because bKOM occurs mostly around 200°, and nKOM is a smooth emission (Figure A.10). The HOM low-frequency limit recorded from DOY 5–DOY 180, 1979 is given in Figure A.11 for V1 (upper panel) and for V2 (lower panel). The lowest frequency limits down to 20 - 40 kHz were observed within 200 Jovian rotations of the respective encounters. Here we detected events in the vicinity of Jupiter which might not have been detected farther away because of the natural decrease of intensity (not normalized) with increasing radial distance. On the other hand, on this point, we are in particular interested down to which frequency HOM can be active. In a given time interval, V1 and V2 results do not show the same low-frequency limit but in general the same overall fluctuations.

Assuming that the radiation is emitted in the fast extraordinary (R-X) mode, the source region near the right-hand cutoff frequency at f=40 kHz extends to altitudes higher than 6 R_J (see e.g. a R-X cutoff isocontour plot as given by Green and Gurnett, 1980), whereas the source of the high HOM frequency limit must be situated at about 2 R_J from the center of the planet.

We further investigated the correlation between HOM low-frequency limits simultaneously observed by both spacecraft. Brackets indicate the respective data in Figure A.11. The first pair of brackets delineate a preencounter period for both spacecraft. We found for this first period a higher correlation than for the second period which includes preencounter data for V2 and postencounter data for V1 (second pair of brackets). The data trend due to the aforementioned distance effect was eliminated before correlating the data series. The low-frequency limits measured by V2 on the dayside are therefore not as strongly correlated with the V1 low-frequency limits on the nightside. This supports a local time dependence for the low-frequency limit of hectometric emission, although the effect is not dramatic in this case.

A.4 Solar wind control of the HOM emission

In section A.2 we showed that the beaming is dependent on the observer's distance to Jupiter. We eliminated the dependence on radial distance by comparing results obtained from observations at the same distance and we observed additional fluctuations which cannot be due to a dependence on distance. We will see in this part that these fluctuations are mainly due to solar activity.

As already mentioned, a significant correlation between HOM energy and solar wind parameters, especially the solar wind density, was first etablished by Desch and Barrow, (1984). Barrow and Desch, (1989) additionally found a correlation between HOM energy and both, the solar wind pressure (highly influenced by the density) and the interplanetary magnetic field. They used linear cross correlation and the method of superposed epochs and the results are normalized by expressing the degree of correlation in terms of modified standard error (for the superposed epochs).

In this study we have correlated the solar wind parameters density and velocity (10 hr averages) with the HOM low-frequency limit, and the early and late northern beam limits (Jupiter rotation averages). The two northern beam limits (early and late) were averaged and the obtained beam limit is taken for the analysis. The solar wind data for V1 were investigated from January

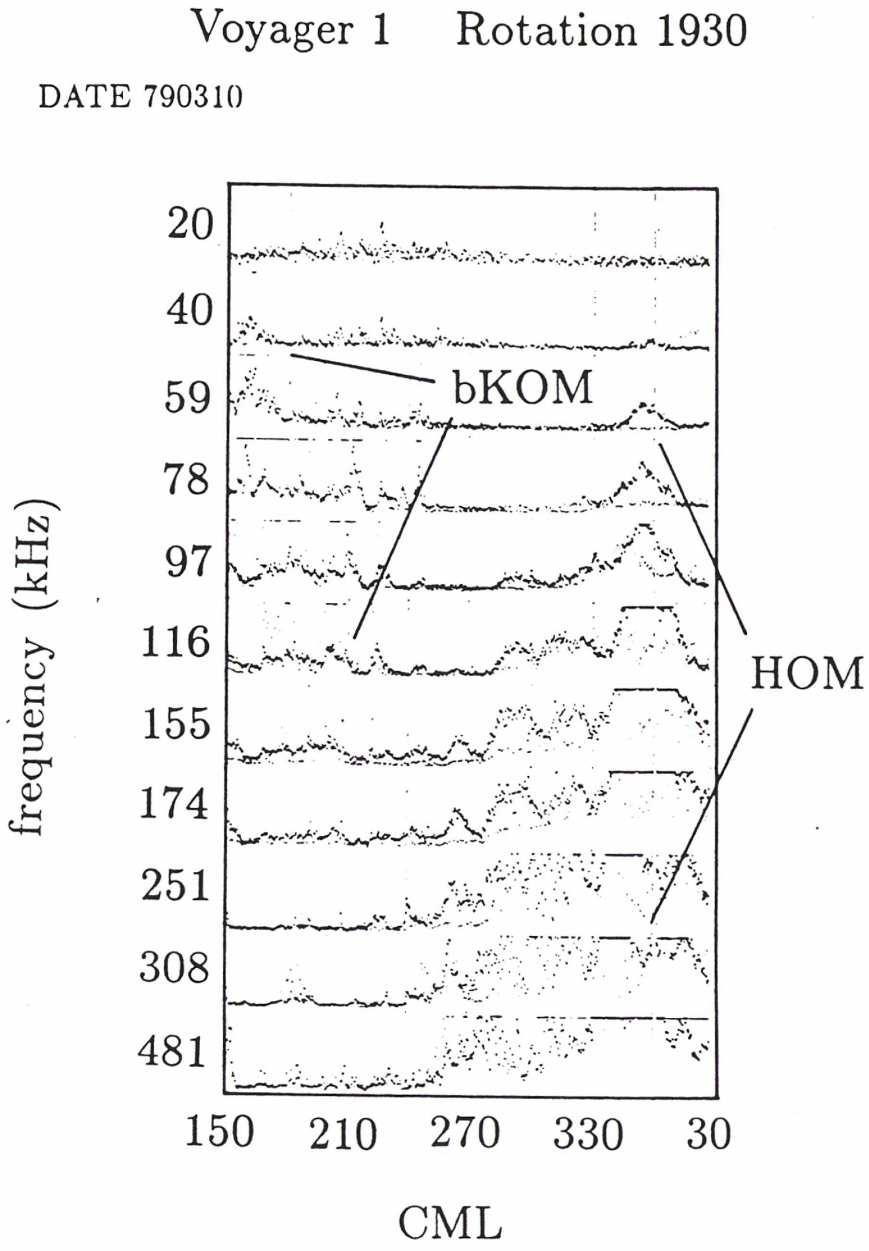

Figure A.10: Example of V1 postencounter data where the HOM emission shows a low-frequency extension down to 40 kHz. The HOM emission can undoubtly be distinguished from bKOM which occurs mostly near 200° CML.

5, 1979 until March 1 and for V2 from January 5 until June 30, which represents the respective preencounter periods in 1979. The solar wind data were ballistically projected from the spacecraft to Jupiter, in the manner described by Desch and Rucker (1983). As the solar wind data are projected from the respective spacecraft to Jupiter, one should expect consistency at the same time at Jupiter. To obtain the highest degree of consistency, we cross-correlated both solar

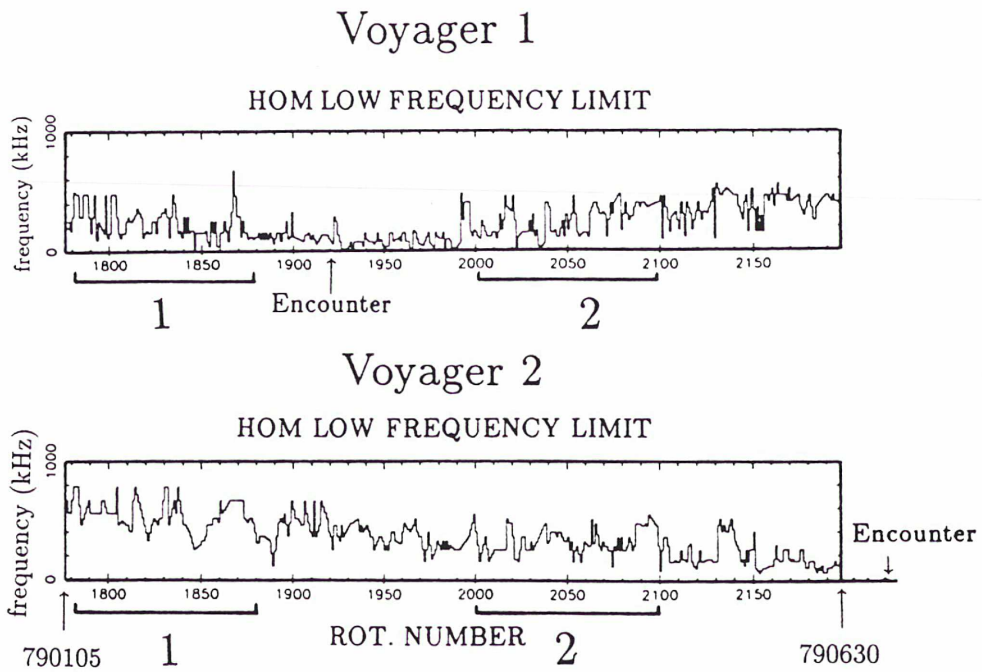

Figure A.11: HOM low-frequency limit for V1 (upper panel) and for V2 (lower panel) during the first 6 months of 1979. A trend to a lower HOM low-frequency limit is visible near the respective encounters, due to the enhanced relative emission intensity. The first pair of brackets (at the left side of the plots) delineate dayside periods for both spacecraft for which correlation was performed. The second pair denotes the time periods where simultaneous observations from the dayside (V2) and the nightside (V1) at the same radial distance were possible.

wind data series and shifted one with respect to the other, if necessary. We have also corrected the artificial data trends due to the observations at different spacecraft-Jupiter distances in the HOM output parameters (low-frequency limit and northern beam limit).

Concerning the statistical significance of the correlations we used a different method for the determination as done by Desch and Barrow (1984). Our method, which is described by Spiegel (1976), represents a test for the significance of the correlation coefficient based on the Student's t-distribution. This distribution replaces the gaussian distribution if the number of data points ν of the correlated time series is not infinite. If $\nu > 30$, the difference between the two distributions is quite small, however. The correlation is significant, when the following equation is true for a given correlation coefficient r:

$$\frac{|r| \cdot \sqrt{\nu - 2}}{\sqrt{1 - r^2}} > t \qquad \text{(A.1)}$$

The quantity t is given in tables (see e.g. Spiegel, 1976). For high ν the 95 % confidence level of significance is reached when Equation (A.1) is true for t=1.65, and the 99 % confidence level for t=2.33.

This test is valid for significance for only one correlation coefficient between two time series with lag time 0. We are therefore forced to modify the test somewhat to obtain the significance level for a few correlation coefficients centered at lag time 0. Since Desch and Barrow (1984) found that the HOM emission output does not lag very much the solar wind input, whenever, we only accept in our analysis correlation coefficients of lag times from -2 to +3 data points (= Jovian rotations). This leads to 6 correlation coefficients $r(-2), \cdots, r(3)$, and the highest (in case of positive correlation), or the lowest one (in case of negative correlation) is taken for the test (Equation A.1). The negative lag times which denote acausality (because in this cases the HOM output is seen earlier than the solar wind input) is included because of the uncertainty of solar wind propagation from the spacecraft to Jupiter. Because of the use of 6 coefficients we have to modify the quantity t to 2.33 for the 95 % confidence level and to 2.93 for the 99 % confidence level.

To test our method, we have correlated solar wind density (hereafter SWD) and HOM energy for V1 and V2 observations and we confirm significant correlation for V2 observations (higher than the 99 % confidence level, hereafter denoted as C_{99}) as already reported by Barrow and Desch (1989). For V1 the correlation is not as strong but higher than the 95 % confidence level (C_{95}).

The solar wind density, the HOM energy, and the HOM low-frequency limit are given for V1 in Figure A.12, and for V2 in Figure A.13. Linear interpolated data replace original data gaps in all of the quantities. The HOM intensity is obtained by integrating the intensity values over the HOM frequency range.

A.4.1 Results

Table A.2 summarizes all correlations performed for V1 and V2 data and their degree of significance. The correlation between the solar wind density increases and the HOM low-frequency limit (LFL) is shown to be only poor (hereafter denoted as C_{poor}) for V1 data, whereas for V2 the correlation reaches C_{99}.

The solar wind density correlates well with the northern beam limit (for V1: C_{99}, for V2: C_{95}). Care is needed correctly to interpret these results especially for V1 because as in this case many points ($\approx$ 30%) were interpolated in the original data. This may artificially produce higher correlation. For V2 this problem does not occur because of the sufficiently high Jovicentric declination of the spacecraft (see also section A.2).

The strong correlation between the solar wind density and HOM emission led us to correlate also the HOM energy with the other HOM parameters and we found that some correlations become even stronger. In detail, we found that the HOM energy is correlated extremely well ($>> C_{99}$) with the HOM low-frequency limit for the two spacecraft. This means that the frequency range increases when the intensity increases. Also significant correlation was found for the beam limit for V2, but only poor correlation for V1. For the calculations of V2 data we did not include all data from January 5 - June 30 because many interpolated values ($\approx$ 50%) occur at the first 4 months for the beam limit. Therefore only data from April 28 to June 30 were considered in the analysis. As already mentioned the V2 data are more reliable than V1 concerning the beam limit data.

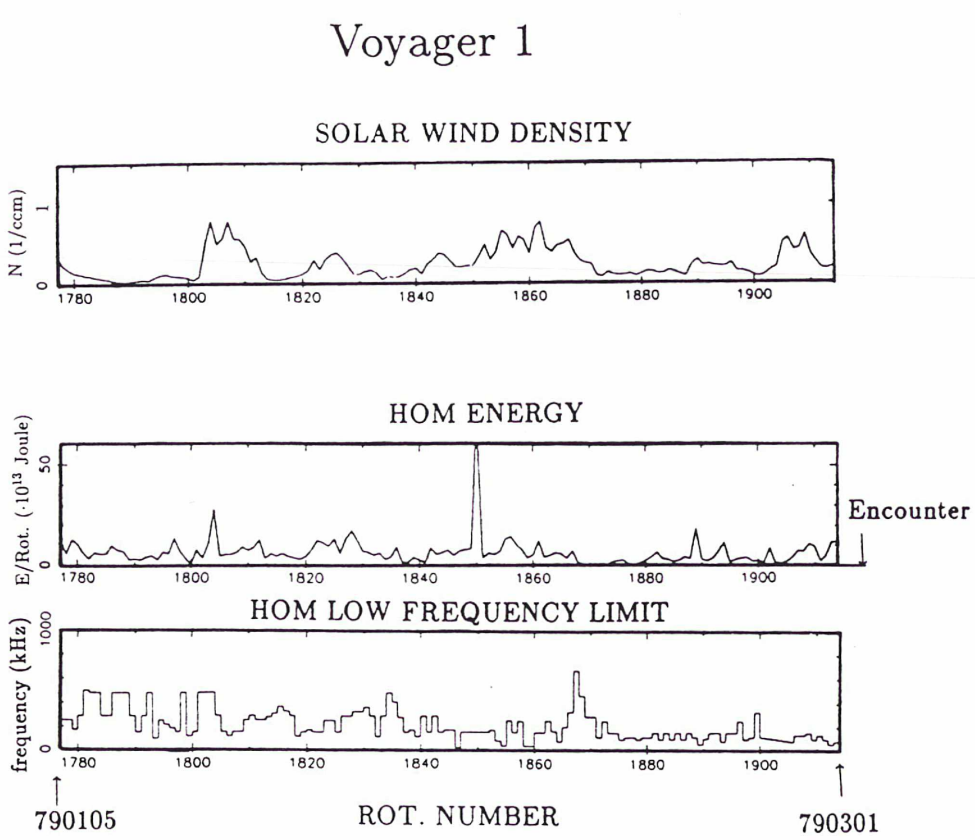

Figure A.12: V1 solar wind density, HOM low-frequency limit, and HOM energy for the V1 preencounter portion of 1979.

At last no apparent correlation is seen between the solar wind speed and any of the HOM emission parameters. Concerning the HOM energy, this was also concluded by Desch and Barrow (1984).

The main conclusion of our analysis is that the solar wind density does not only influence the HOM energy, but also the HOM low-frequency limit and at least partially the hectometer beaming. The solar wind pressure gives similar results due to the proportionally higher fluctuations of the density compared to the velocity. We also demonstrated that the HOM energy influences even stronger the HOM emission geometry, in particular the HOM low-frequency limit but, this is no causal relationship since it is in fact the solar wind which influences the HOM energy and the other HOM parameters.

correlated parameters	V1	lag (Jov. rot.)	V2	lag (Jov. rot.)
SWD - HOM energy	C_{95}	-1	$>> C_{99}$	-1
SWD - HOM-LFL	C_{poor}	-	C_{99}	-1
SWD - HOM beam	C_{99}	-1	C_{95}	0
HOM energy - HOM-LFL	$>> C_{99}$	-1	$>> C_{99}$	0
HOM energy - HOM beam	C_{poor}	-	C_{99}	0

Table A.2: Summary of correlations between the solar wind and HOM emission. Note that the V1 beam limit data are less reliable than that for V2 and therefore artificial high correlations might be produced.

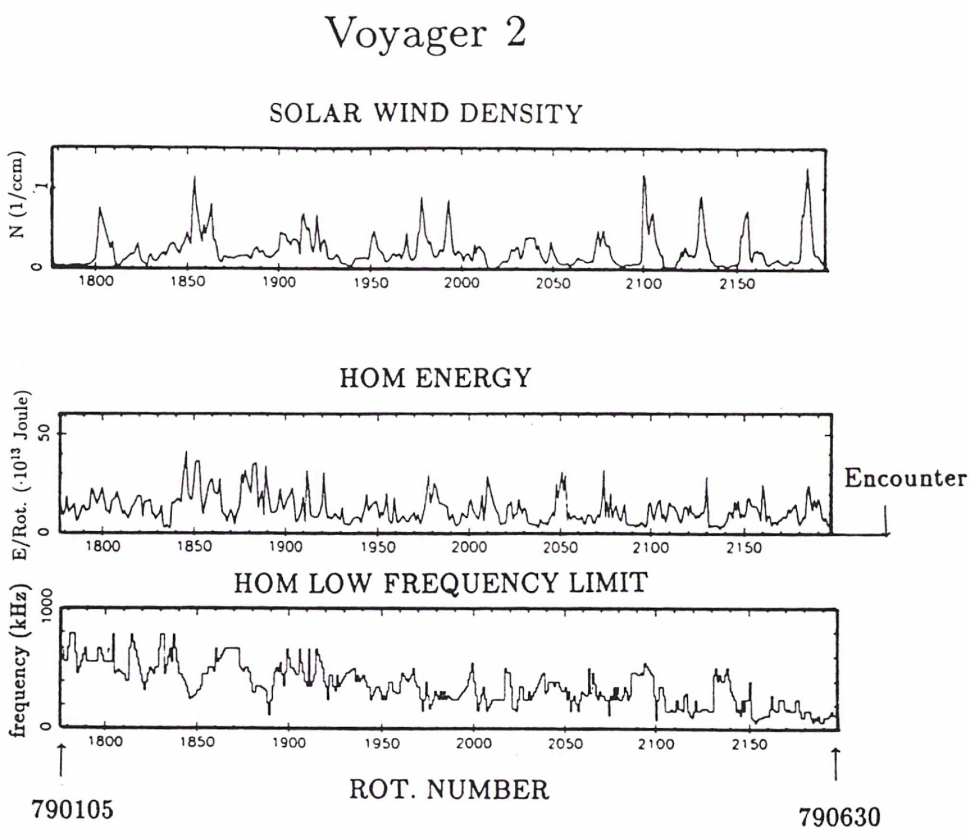

Figure A.13: Same as Figure A.12 but for V2 data in the preencounter period.

We have seen that the solar wind density and in particular the HOM energy influence the other HOM parameters. Therefore we reanalyzed the hectometer beaming for the respective spacecraft by comparing them with solar wind activity during the observations. In general we found there a higher HOM beam width for V2 compared to V1 (see Figures A.3 and A.4) for dayside observations. The difference between the V1 and V2 beam northern excursions was especially striking (about 2°) at distances of 630 R_J and 210 R_J. Figure A.14 compares V1 and V2 solar wind density and HOM energy measured at about 210 R_J on the dayside. We note the higher solar wind density and the higher HOM energy for V2 observations. Similar results were found for observations at distances of 630 R_J on the dayside where also a thicker beam was seen from V2. No apparent difference in the solar wind density could be seen at 420R_J, however, where we observed approximately the same beam width for the two spacecraft (Figures A.3 and A.4).

A.5 Conclusion

In this paper we present further support for strong HOM beaming with the beam axis situated to the north of the magnetic dipole equator (1.6°). On the dayside the emission beam width was found to be about $10° - 20°$ for the normalized detection thresholds 10^{-21}Wm^{-2}Hz^{-1} - $3.4 \cdot 10^{-23}$ Wm^{-2}Hz^{-1}, respectively. On the nightside the beam was found to be narrower (by about 4°

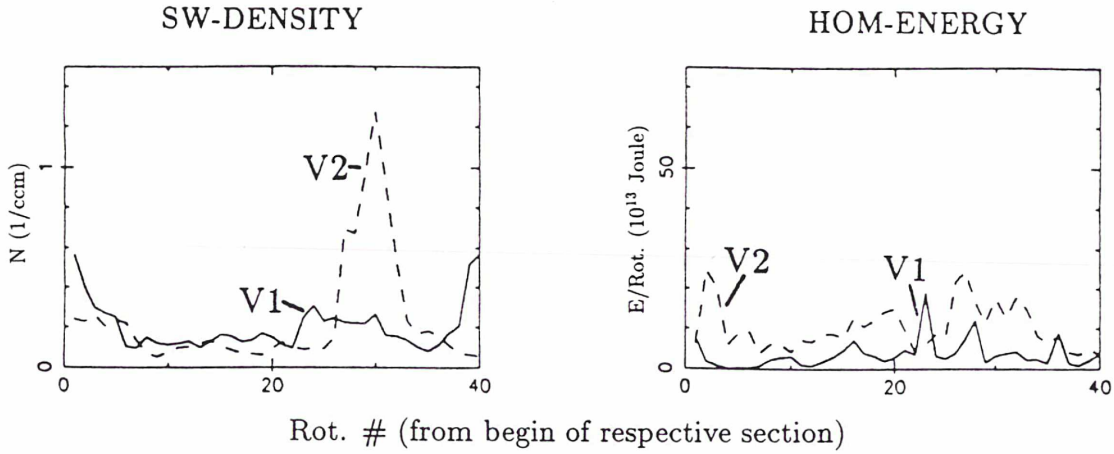

Figure A.14: V1 and V2 solar wind density (left panel) and HOM energy (right panel) measured on dayside at about 210 R_J during 60 Jovian rotations (sections 3 and 13, respectively). Full lines denote V1 and dashed lines V2 data. Higher solar wind densities and HOM energies are generally seen from V2. The respective beam widths are displayed in Figures A.3 and A.44 and higher values are given there for V2.

compared to the dayside). We further calculated the theoretical correlation of simultaneous observations of the V1 and V2 spacecraft and found agreement with the observations. This result is compatible with the beam half-width of 5° and beam axis of 3° magnetic northern latitude found by Alexander et al. (1979). For DAM emission, Warwick (1963) derived from ground based observations an emission beam half angle of 9°, whereas Poquerusse and Lecacheux (1978) concluded from combined spacecraft and ground based observations a beaming of the Io controlled DAM of less than 9°. As found by Leblanc and Daigne (1985a,b), bKOM is emitted above 11° northern and southern magnetic latitude, thicker on the dayside and thinner on the nightside.

We analyzed PRA data at three frequencies and mostly found the maximum beam width between 942 kHz and 1326 kHz which is fully compatible with the results of Brown (1974), who found the spectral peak of hectometric emission at about 1 MHz.

The polarization measurements of the HOM data indicate that right-hand polarization is associated with the northern hemisphere and left-hand polarization with the southern one, without reversal from dayside to nightside observations.

Analyzing the HOM low-frequency limit in the PRA data, we see that HOM is sometimes emitted at frequencies as low as 40 kHz. The observations are strongly influenced by the increase of relative intensity when the spacecraft-Jupiter distance decreases. Nevertheless, a hectometer source extension from about 2 to 6 or 7 R_J is deduced with the assumption that the emission is emitted in the R-X mode near the R-X cutoff frequency. The strong influence of HOM by the solar wind and the location of the low-frequency sources farther away than 6 R_J from the planet give strong evidence that the sources of hectometric emission are located along auroral field lines on each hemisphere as already suggested by Genova et al. (1987).

The relationship between solar wind activity and HOM emission intensity was first derived by Zarka and Genova (1983), Desch and Barrow (1984), and by Barrow and Desch (1989). In both

of the more recent studies, correlation was found between the solar wind parameters such as density and/or pressure and the HOM intensity. We extended these calculations for the other HOM parameters such as the HOM low-frequency limit and the beaming. The solar wind density and/or pressure also influences the HOM low-frequency limit and the HOM beaming. The solar wind speed does not influence any HOM parameter.

The HOM energy correlates even more strongly with the HOM low-frequency limit and the beaming than does the solar wind. Interpretating these results, we conclude that the solar wind density and/or pressure exerts an influence not only on the HOM intensity but also on the HOM source extension and beaming. The arrival of a high density solar wind stream at Jupiter will therefore enhance the HOM energy output, activate low-frequency HOM sources located at 6-7 R_J on auroral field lines, and widen the HOM beam to higher magnetic northern latitudes and possibly to higher magnetic southern latitudes.

A number of results on the phenomenology of the HOM emission have been given in this paper and theoretical considerations concerning the exact source location should assume a source which emits radiation according to these characteristics. Ray-tracing calculations are under way in order to clearify this topic.

Appendix B

Source location of the Jovian hectometric radiation via ray-tracing technique

Abstract

Ray-tracing using realistic magnetic field and plasma models has been performed to locate the Jovian hectometric radiation (HOM) sources. To consider only a few possible source locations, we have assumed that the radiation mechanism is the Cyclotron Maser Instability (CMI), and taken into account the characteristics of the HOM including the recent results by Ladreiter and Leblanc (1989) (hereafter Paper 1). The emission is assumed to escape from the planet in the extraordinary wave mode within a thin beam of hollow cones whose apexes are distributed uniformly in longitude at the northern and southern hemispheres at altitudes where the gyrofrequency f_c is less but nearly equal to the observed wave frequency. The rays are traced from possible sources located at f/f_c=1.05 and labeled by the dipole shell parameter L. For each source, we have determined the emergence wave normal angle θ_{crit} above which the rays no longer travel within the HOM emission beam nearby the magnetic equator (Paper 1). We show that the HOM sources cannot be located on field lines within the Io flux tube. However, wave refraction due to the Io torus plays a crucial role for the propagation and beaming of the waves toward the magnetic equator. It is found that HOM sources located at field lines $15 < L < 30$ agree best with the observations when assuming that the cone half angle of emission is about $70° - 90°$ with respect to the local magnetic field. Thus, the source is associated with the tail field aurora where the magnetic field lines connect the polar region to the Jovian magnetic tail and is extended in altitude from 2 to 7 Jovian radii (R_J). Our results explain in detail the radio phenomenology of the hectometric radiation, in particular the strong latitudinal beaming, the lowest observed frequencies ($\approx$ 40 kHz), the solar wind control, the absence of HOM emission when Voyager 1 was within the Io torus, and the absence of Io control on the HOM. The results are discussed in the context of the other Jovian radio sources, namely the sources of the non-Io decametric (DAM) and kilometric (KOM) emissions.

B.1 Introduction

The radio spectrum of Jupiter which is known as the most powerful emitter in our solar system consists of four distinct components: the decametric components (Io DAM and non-Io DAM); the kilometric emission (KOM) which contains a broadband (bKOM) and a narrowband (nKOM) component; and an emission at hectometric wavelengths, the so-called Jovian hectometric radiation (HOM). Since the accidental discovery of DAM by Burke and Franklin (1955) from ground-based observations, the DAM component has been investigated for more than three decades. The kilometric and hectometric components were discovered later on by the Voyager 1 and 2 spacecraft which both encountered Jupiter in 1979. This paper focuses exclusively on the HOM component. Most of the studies of HOM concern the phenomenology and the beaming of the emission, and its dependence on solar wind. Alexander et al. (1979) found that HOM is strongly beamed in a curved thin sheet centered somewhat north at the magnetic dipole equator with a beam width of about 10°. During their investigation they show that HOM is well organized when it is considered as a function of the magnetic declination of the observer. The periodic variations of HOM in terms of central meridian longitude (CML) are due to the varying Jovicentric declination of the spacecraft within one Jovian rotation. Alexander et al. (1981) confirmed the HOM beaming model and found additionally a local time dependence of the radiation. Furthermore, they investigated the spectral properties of the HOM and DAM emissions and found a slight change in the occurrence probability of the radiation when switching from the HOM to the DAM frequencies. Lecacheux et al. (1980) also investigated HOM data and found spectral characteristics which could not be explained by the variation of the Jovicentric declination of the observer.

A solar wind control of HOM was established by Zarka and Genova (1983) and Desch and Barrow (1984). Further results were more recently given by Barrow and Desch (1989). Zarka and Genova (1983) found that the sector structure of the interplanetary magnetic field highly controls the long-term intensity fluctuations at hectometer wavelengths. Desch and Barrow (1984) derived a significant positive correlation between the solar wind plasma density and the HOM emission output by using a cross-correlation analysis. Genova et al. (1987) furthermore showed that the HOM activity is correlated to the non-Io DAM activity, but not to the Io DAM, suggesting that the HOM and non-Io DAM are two components of the same radio emission. The study of Barrow and Desch (1989) exhibits that the higher energy HOM is in correlation with the solar wind density, pressure, and the interplanetary magnetic field magnitude.

In a recent study, Ladreiter and Leblanc (1989) (hereafter Paper 1) reexamined the latitudinal beaming of HOM by using pre- and postencounter data of Voyager 1 (V1) and Voyager 2 (V2) in 1979. In general, the results of Alexander et al. (1979) were confirmed,but the beam width was found to be larger ($10° - 20°$) depending upon the detection threshold. In addition, a source extension in altitude from 2 to about 7 Jovian radii (R_J) from the center of Jupiter was derived based on a HOM low-frequency limit approximately equal to 40 kHz. It was also found that the solar wind ram pressure and the HOM energy correlate with the HOM beam width and the low-frequency extension of the emission. The correlation works in such a way that an enhanced solar wind ram pressure increases the HOM energy, widens the HOM beam, and activates lower frequency HOM sources farther away from the planet.

As far as the polarization of the emission is concerned, Kaiser et al. (1979) reported that the source of circular polarization of the HOM (left-hand source) is opposite to that of the

DAM (right-hand source). On the other hand, Alexander et al. (1981) reported that the fundamental polarization sense of the HOM may have been reversed after the encounter. This polarization reversal was not understood and was attributed to local time variations. It has now been established, in Paper 1 and by Ortega-Molina and Lecacheux (1990b) that right-hand (RH) polarization is associated with the northern hemisphere and left-hand polarization (LH) with the southern one. These results are consistent with an emission excited in the right-hand extraordinary (R-X) mode from both hemispheres. The observed polarization reversal from dayside to nightside is due to the change of the antenna geometry with respect to the spacecraft trajectory and the position of the radio sources.

Lecacheux (1981) has investigated the location of radio sources at 300 kHz using a ray-tracing technique. The obtained source locations for both the ordinary and the extraordinary mode are situated in the southern hemisphere at the Jovimagnetic cartesian coordinates $X = 5.0 - 5.2\ R_J$ and $Y \approx -2.2\ R_J$. However, it is difficult to find a physical generation mechanism which is able to emit radiation from that specific point. Moreover, no distinct source location has been given for $f \neq 300$ kHz. In the absence of a definitive source location for the hectometric radiation, further work has to be done to find its radio-emitting regions, and this paper can be considered as a first step in this respect.

The ray-tracing technique is a powerful tool to locate the radio sources, but it is important to point out that there exists no unique solution for the source regions. Therefore, it is necessary to introduce a distinct generation mechanism at the source and to take into account the characteristics of the emission.

Most of the ray-tracing work has been done for the earth and the Jovian magnetosphere in order to find the sources of terrestrial kilometric radiation (TKR) and of the Jovian radio emissions. For the earth, the first ray-tracing of TKR was done by Jones and Grard (1976) using the assumption that TKR propagates in the ordinary (L-O) wave mode. The ray-tracing study performed by Green et al. (1977), results in an R-X emission mode for TKR. We notice that at that time, no direct satellite measurements were available. Now it is established by spacecraft measurements that the auroral radio emissions from the planets earth, Jupiter, Saturn, and Uranus are generated in the extraordinary (R-X) mode. Hashimoto (1984) presented the first three-dimensional ray-tracing based on the Cyclotron Maser Instability theory (CMI) (Wu and Lee, 1979) which is the relevant generation mechanism for the auroral radio emissions. Hashimoto (1984) traced L-O and R-X waves with initial wave normal angles from 60° to 90° with respect to the magnetic field vector. He pointed out that it is the combination of L-O and R-X mode waves that describe the observations of the angular extent and the predominance of the R-X mode of TKR.

For the Jovian decametric radiation, the first three-dimensional ray-tracing was done by Hashimoto and Goldstein (1983). Their calculations closely match the observations of DAM activity, and they confirm that the decametric radiation sources may well be described by hollow emission cones. A very comprehensive study on the Jovian decametric arcs was performed by Menietti et al. (1984). They ray traced DAM emission and varied the propagation angle at the source until the observations were fitted. They concluded that the initial wave normal angle is a function of the emission frequency (also suggested by Goldstein and Thieman, 1981) and found this angle to be $\approx 80°$ at 10 MHz (the vertex frequency of the arc). This angle decreases to $\approx 70°$ at the high (30 MHz) and low-frequency (2 MHz) extensions of an arc. Electron ener-

gies in the order of 10 keV are required to match the proposed wave normal angles. Electrons with energies of that order of magnitude are assumed to precipitate in the Jovian auroral region according to a study of Horanyi et al. (1988).

For the Jovian kilometric radiation, ray-tracing was performed by Green and Gurnett (1980) by assuming that KOM is radiated in the L-O mode from Io torus field lines near the planet. They were able to predict an observed shadow zone where no emission can be detected because of the Io plasma torus. Since Leblanc and Daigne (1985a,b) reanalyzed the polarization measurements and established that the correct sense of polarization of KOM is right-handed, the results of Green and Gurnett (1980) have to be reinterpreted. Alternative studies by Jones (1980, 1981, 1986) and Leblanc and Daigne (1985a,b) locate the sources of the Jovian kilometric radiation at the Io torus by suggesting a Z to O mode conversion mechanism. In that approach, the beaming is the result of the radiation mechanism itself.

The purpose of this paper is to determine the source location of the HOM by using a ray-tracing technique. To consider only a few possible source locations, we have assumed that the generation mechanism is the CMI, and have introduced the characteristics of the emission. These characteristics are summarized in section B.2. We have also considered the observations during the Voyager 1 (V1) closest approach which are relevant to our study. In section B.3 we have developed a simple geometrical model and assumed that an emission of hollow cones should fulfill the observation of a beamed emission. It will be demonstrated that magnetic field lines linked to the Io torus can be eliminated as possible sources for HOM. In section B.4 we introduce our ray-tracing calculations, the rays being traced from the point of observation back to their sources near Jupiter. We will show that the Io torus plays a crucial role for the propagation and refraction of waves at hectometric wavelengths. This leads finally to the determination of the HOM radio-emitting regions. The results are discussed in the context of the other Jovian radio components, in particular the non-Io DAM and KOM (section B.5).

B.2 Observations

Shortly after the discovery of the low-frequency spectrum of Jovian radio emission by the Planetary Radio Astronomy (PRA) experiment aboard Voyager 1 and 2, the HOM emission was thoroughly explored for the first time. The PRA experiment (Warwick et al., 1977) consists of a radio receiver that steps in frequency from 1.2 kHz up to 40 MHz and an orthogonal pair of crossed monopoles which allow the sense of polarization to be determined. The instrument is operative in two distinct frequency bands; the low-frequency band contains 70 channels separated by 19.2 kHz with a bandwidth of 1 kHz, respectively, from 1.2 to 1326 kHz. The most striking feature in the low-frequency band is the appearance of the HOM and KOM emissions. The high-frequency band extends from 1.2 to 40 MHz where HOM may be observed at the lowest frequencies, and DAM from about 5 to 40 MHz. DAM mostly occurs in the form of nested families of arcs on a frequency-time diagram whereas HOM generally does not exhibit an arclike structure. However, some drifting features in the HOM frequency range have been interpreted as the lower legs of arcs that have their vertices in the DAM range (Boischot et al., 1981). Carr et al. (1983) pointed out that DAM emission is sometimes entering frequencies below 2 MHz. Then, the HOM high-frequency limit can no longer be distinguished from the DAM. The purpose of this study is actually to know if HOM is related to DAM, and the knowledge of HOM location

is a first step in this respect. In our investigation we are concerned with frequencies below 1 MHz where the major part of HOM is observed. The results of several studies concerning the HOM are already mentioned in the introduction and can be summarized as follows:

1. The hectometer emission can be described in terms of a narrow, curved sheet at a fixed magnetic latitude (centered at about 2° northward the magnetic dipole equator) into which the emission is beamed to escape Jupiter. The thickness of this sheet is reported to be about 10°, but may reach over 20° because of a higher detection sensitivity near the encounter. Moreover, the emission depends on local time. The fact that HOM is strongly beamed in latitude plays a key role in our further analysis to search for HOM source locations.

2. The low-frequency limit of HOM is found to be of the order of 40 kHz. No exact determination about the high-frequency limit of HOM has been reported so far, but it is generally accepted that this limit is about 3 MHz and may sometimes reach 7 MHz. Following a R-X cutoff contour plot (see e.g. Green and Gurnett, 1980), it was concluded in Paper 1 that the HOM source extension in altitude is from 2 to about 7 R_J (from Jupiter's center) when considering the high- and low-frequency limits of HOM.

3. The polarization pattern of HOM is more complex than that of the DAM or KOM. Nevertheless it is now established that the polarization is predominantly right-handed when associated with observations in the northern hemisphere and therefore it corresponds to the R-X wave propagation mode.

4. The HOM is strongly correlated with the solar wind. The solar wind density and/or ram pressure influence the HOM energy, and the sector structure of the interplanetary magnetic field triggers this correlation. The density and/or ram pressure also influence the HOM beaming and the low-frequency limit. Enhanced solar wind activity produces a higher HOM energy output, broadens the HOM beam, and activates low-frequency HOM sources at large distances from the planet. It has been generally found that the solar wind speed does not influence any HOM output parameter.

5. The occurrences of the hectometer and the kilometer emissions are different when ordered in terms of system III (1965) longitude (CML). Although the frequency range of the two emissions may sometimes be overlapped at low HOM frequencies ($f \leq 400$ kHz), the broadband kilometric radiation (bKOM) occurs around 200° CML, whereas HOM is situated around 0° CML. This is explained by a different latitudinal beaming of the bKOM compared to HOM (for the latitudinal beaming of bKOM, see Leblanc and Daigne, 1985a).

6. When comparing the hectometer emission with the higher frequency non-Io DAM, no striking change is visible to distinguish one from the other. The occurrence in terms of CML of the radiation changes slightly when switching from the non-Io DAM to the HOM frequencies (see Alexander et al., 1981, Figure 6). On the other hand the occurrence of the HOM at the lowest frequencies generally exhibits a smaller extension in system III longitude than at the higher frequencies (see Paper 1, Figure 10).

7. No Io control of the HOM has been observed so far.

8. By the inspection of Voyager 1 observations at Jupiter's closest approach (CA), we notice an absence of HOM (Figure B.1), although the spacecraft was near the magnetic equatorial plane. A strong HOM emission would be expected there, however, because of the latitudinal beaming of HOM (Alexander et al., 1979; Paper 1). Instead, a bursty emission is observed which has been interpreted as upper hybrid resonance noise (Warwick et al., 1979) and n + 1/2 gyroharmonic waves (Birmingham et al., 1981). This absence of HOM can not only be due to wave refraction through the Io torus since the high-frequency part of the HOM is affected, too. The HOM emission pattern near the closest approach is therefore assumed to be a consequence of a specific source location.

All these characteristics must be taken into account for the determination of the source location. It is the purpose of the subsequent sections to eliminate step by step locations which cannot apply for those requirements.

B.3 HOM source location: A geometrical approach

In this section we present a geometrical approach to have a first indication about the HOM source locations. All effects of ray refraction are neglected which correspond to a complete absence of the Io plasma torus. Furthermore, the wave refraction at the source which is thought to be small (Hashimoto and Goldstein, 1983) is also neglected.

Let us assume that the radiation escapes from the planet in the form of thin hollow cones distributed at all longitudes in the northern and southern hemispheres. The sources are thought to be the apexes of these cones located in altitudes where the wave frequency is somewhat higher but nearly equal to the local gyrofrequency. In a first attempt, we will search for field lines labeled with the dipole shell parameter L on which the sources may be located to produce radiation along the magnetic equatorial plane. Thus, we will analyze the emission cone half angle θ_o as a joint function of the L parameter of the source field line and the wave frequency f (which is taken to equal the gyrofrequency f_c) in the Jovian dipole field. The angle between the direction of the wave normal (parallel to the magnetic equatorial plane) and the direction of the magnetic field vector at the source (Figure B.2) is defined to be θ_o (later on, the cone half angle will be generally labeled as θ). Only sources on field lines which exhibit a sufficiently high cone half angle θ_o for all frequencies can be considered as possible source locations. On the other hand, HOM was detected within a sheet with a thickness of about 20° centered 2° degrees northward of the magnetic equatorial plane (Alexander et al., 1979; Paper 1). This implies that the radiation is propagating in a small range of directions nearly parallel to the magnetic equatorial plane. As we will show in this section, only emission cones which have one edge directed nearly parallel to the magnetic equatoral plane in the magnetic meridian plane provide an emission maximum there as required for the HOM beaming model.

For a given wave frequency f (which is assumed to be equal to the local gyrofrequency f_c) corresponding to a given altitude on a field line labeled L, the initial wave propagation angle θ_o is a function of the shell parameter L and the frequency f when we introduce a dipole field model. In a dipole field the cone half angle θ_o between the local magnetic field vector and horizontal direction (parallel to the magnetic equatorial plane) is only a function of the polar angle ϑ

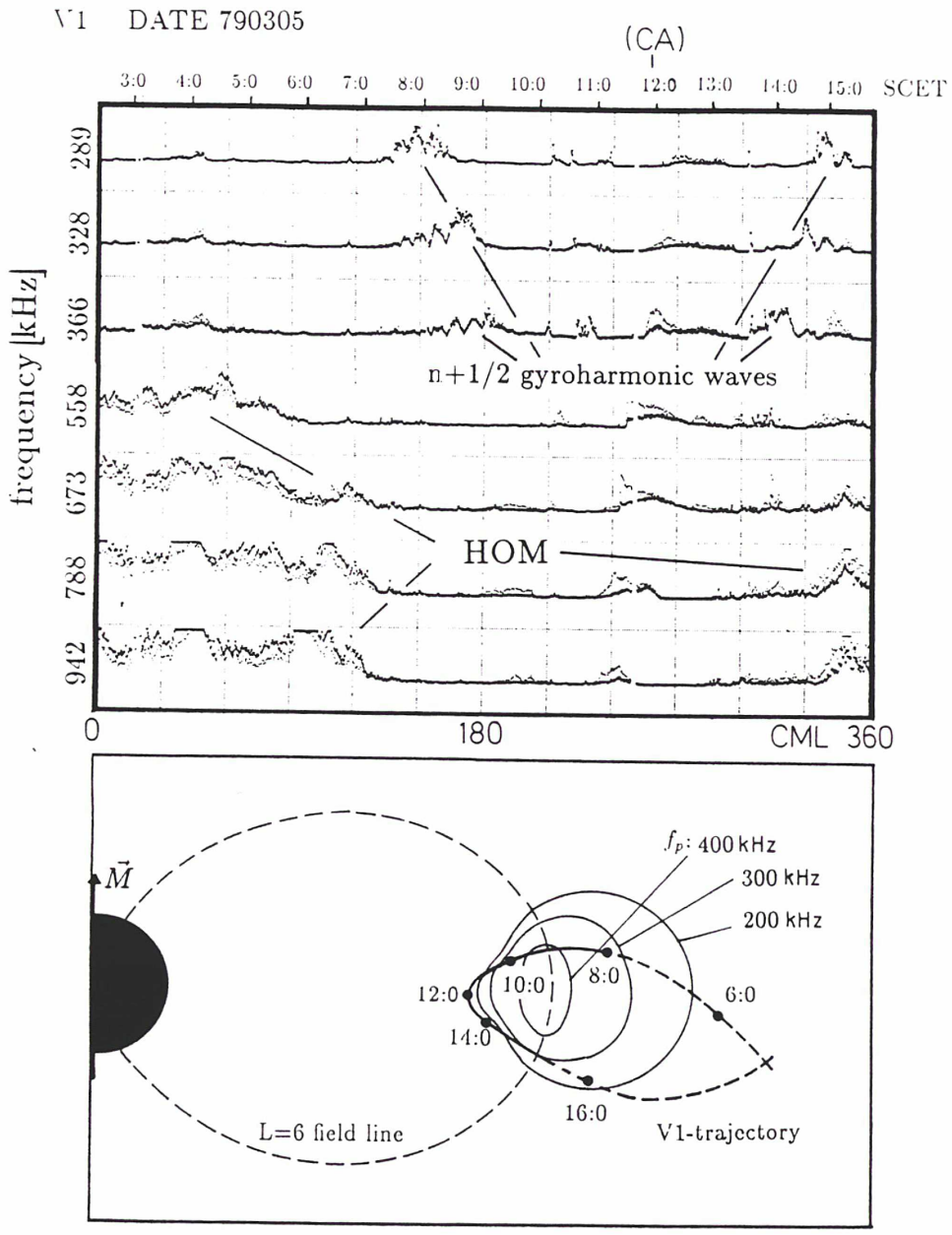

Figure B.1: PRA observations during the Voyager 1 closest approach and (bottom) sketched plot of the spacecraft trajectory (from Lecacheux, 1981). HOM emission was not observed along the part of the V1 trajectory near closest approach (full thick line). The feature occurring near 1100-1200 spacercraft event time (SCET) at higher frequencies and drifting in time to lower frequencies has been interpreted as upper hybrid noise and n+1/2 gyroharmonic waves. The magnetic latitude of V1 is near 0° which usually favours strong HOM activity.

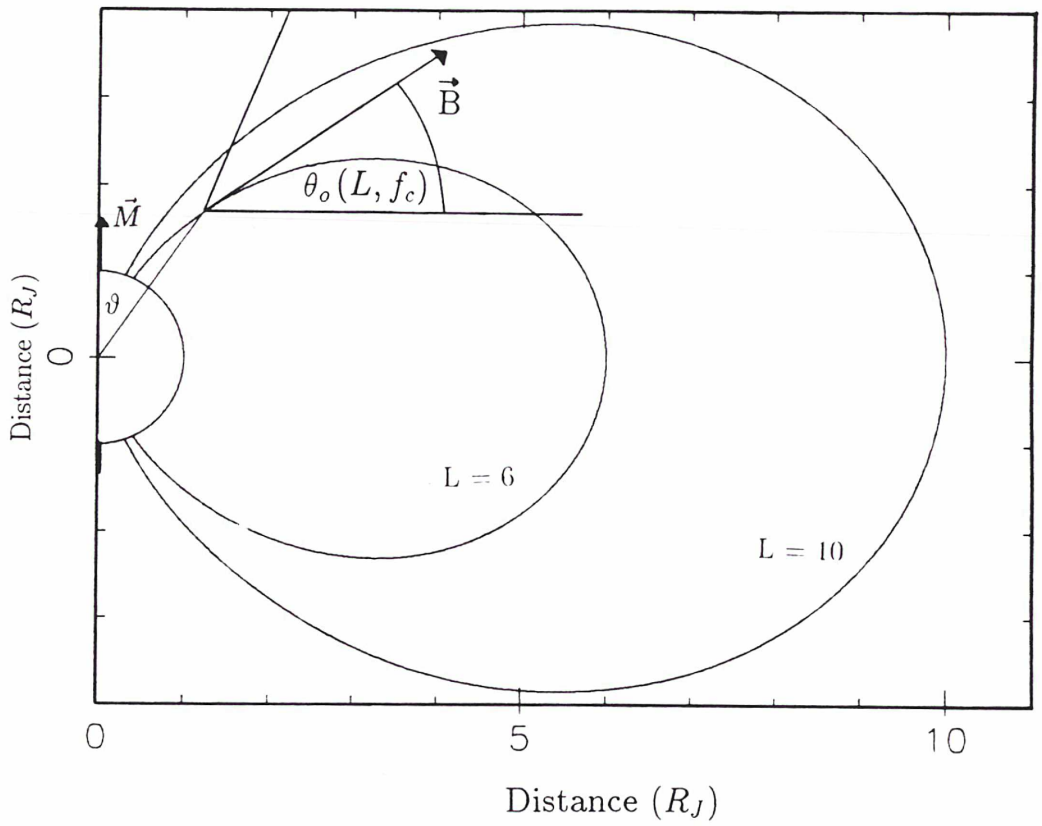

Figure B.2: Intersection through the magnetic meridian plane of a dipole field where the edges of an emission cone appear as straight lines symmetrically placed with respect to the local magnetic field direction which denotes the cone axis. The cone half angle θ_o can be expressed as a function of the shell parameter L and the gyrofrequency f_c which is assumed to be equal to the wave's frequency f.

$$\tan\theta_o = \frac{2 - 3\sin^2\vartheta}{3\sin\vartheta\cos\vartheta} \tag{B.1}$$

the gyrofrequency can be expressed as follows

$$f_c = \frac{eB}{2\pi m} \tag{B.2}$$

with e equal to the unit charge and m equal to the electron mass. Finally, the expression for B in a dipole field is

$$B = \frac{M_J}{L^3\sin^6\vartheta}\sqrt{1 + 3\cos^2\vartheta} \tag{B.3}$$

where M_J is the Jovian dipole moment, equal to $4.28\Gamma R_J^3$ (Γ represents Gauss).

B can be calculated from Equation (B.2) for a given f_c. Then, ϑ can be determined numerically for a given L by inversion of Equation (B.3). Finally we end up with θ_o via Equation (B.1), and thus θ_o is derived as a function of f_c=f for a given shell parameter L.

Figure B.3 shows the cone half angle θ_o as a function of f and L. Several field lines with L between 6 and 60 are displayed for frequencies between 40 and 1000 kHz. The shell parameters L appear as parameter lines in the f-θ_o plot. For L=6 which denotes a field line in the Io plasma torus, θ_o is less than 30° at f=1000 kHz and is approximately equal to 0° at f=300 kHz. This is inconsistent with the large cone half angles required by the CMI mechanism when the ratio f_p/f_c is very small, which is the case in the Jovian magnetosphere at distances larger than 3 R_J (except near the Io torus). We therefore conclude that a hectometer source in the Io plasma torus is not compatible with an emission in hollow cone beams. Furthermore, the torus field lines cannot provide source regions with cyclotron frequencies down to 40 kHz. Since $f_c < f_{RX}$, this holds also for the R-X cutoff frequency f_{RX}. Instead, magnetic field lines with a high shell parameter (L > 20) appear to be favoured candidates in the hollow cone emission model. First, these field lines exhibit larger cone half angles θ_o, about 50°-70° from 400 to 1000 kHz. Second, for f > 400 kHz, θ_o is only a small varying function of f for field lines with high-L parameters. Third, waves with frequencies as low as 40 kHz may be excited on these field lines. One important result of this preliminary approach is that field lines L < 10 must be excluded as the sources of HOM if we take into account the lowest frequencies (40 kHz) reached by HOM. This is shown in Figure B.3 where θ_o becomes $\approx$ 0° for f=40 kHz and L=10. For the lowest HOM frequencies ($f \leq$ 400 kHz), θ_o reaches very low values even for field lines with higher L. Therefore we conclude that the refractive effects near the Io torus cannot be neglected for the lower HOM frequencies.

B.3.1 Simulation of the HOM latitudinal beaming

We suppose that the intensity of the radiation is distributed uniformly along the sheet of the hollow cones but is distributed as an error function with a characteristic half-width a perpendicular to this sheet. This sheet half-width a of the emission cone was derived to be very small (< 1°) (Le Queau, 1988). Let us consider all of the emission cones distributed uniformly on each hemisphere. Then we can simplify the situation by considering projections onto a celestial sphere surrounding Jupiter. A given event is represented by a point on this sphere at the corresponding magnetic declination and system III (CML) longitude. Since in our model the hollow emission cones are distributed along all longitudes at both hemispheres, the azimuthal dependence vanishes, and we can express the emission intensity produced by all of these hollow cones as a symmetric function of magnetic latitude δ. For a given frequency, this intensity function will further depend on the L parameter of the magnetic field line on which the source is assumed, on the cone half angle θ and also on the characteristic cone half- width a.

Figure B.4 gives an example of the emission intensity, which is incoherently calculated, versus magnetic latitude δ for sources on field lines L= 40, 20, 6, and for the parameters a = 1°, f_c = f=1000 kHz, and the cone half angle θ = 60°. For this set of parameters, only field lines with L=20 would provide an intensity maximum near the magnetic equator. From Figure B.3 we can see that for L=20 and f=1000 kHz, θ_o is about 60°; thus one edge of the emission cone is directed parallel to the magnetic equatorial plane in the magnetic meridian and produces an intensity maximum there. The second edge produces a local maximum at δ = 60° (Figure B.4). On the other hand, field lines with L=6 produce the highest intensity maximum near $\delta \approx$ 35° which is in disagreement with the observations. Again, we see that the Io torus cannot be the source of HOM emission hollow cones in this simplified model. From Figure B.3 we see that θ_o is

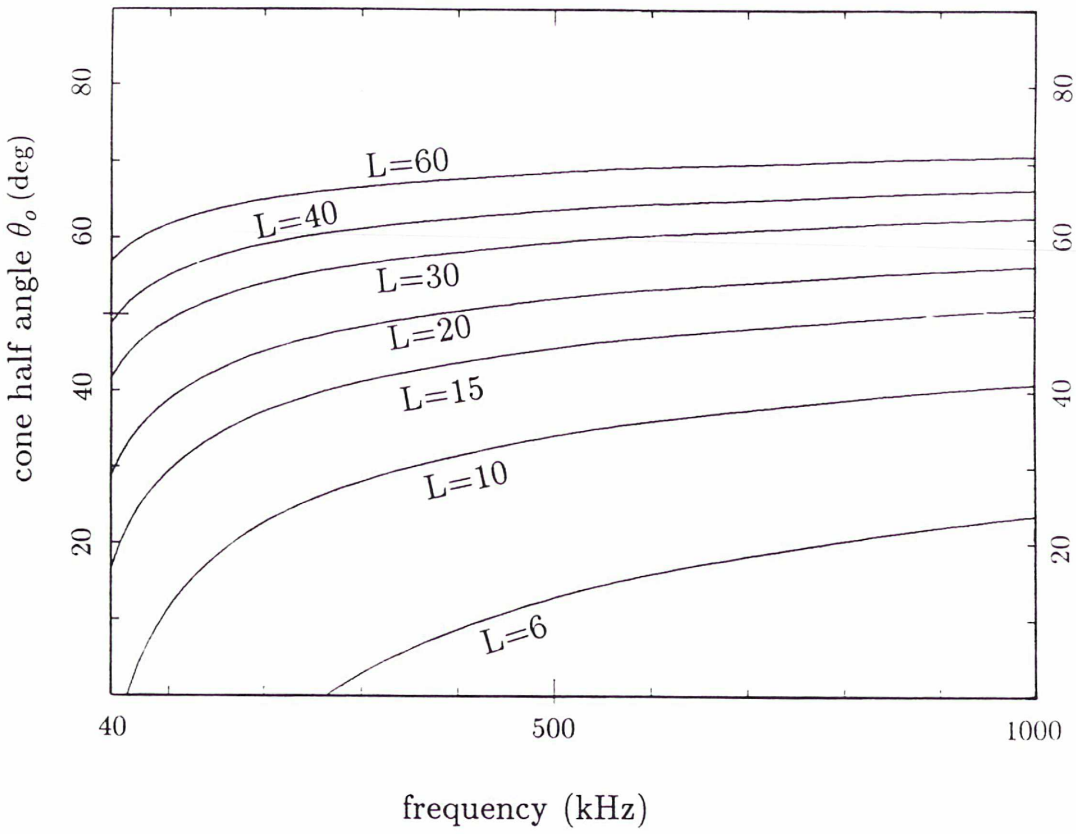

Figure B.3: Cone half angle θ_o as a function of the wave frequency f (assumed to be equal to the gyrofrequency f_c) and the shell parameter L (appearing as parameter line) for the Jovian dipole field. Sources at field lines $L < 10$ have a very small cone half angle θ_o which even approaches 0° for the lowest HOM frequencies (40 kHz).

only a small varying function of f for high L parameters when excluding the lowest frequencies. Therefore a variation of the value f in Figure B.4 would not dramatically change the topology except for the lowest frequencies ($f \leq 400$ kHz). Furthermore, when varying the sheet half thickness a, the intensity peaks are nearly unchanged in magnetic declination δ. At last, when changing θ to higher values, field lines with higher L will successively fulfill the requirements (intensity peak near $\delta = 0°$). We have further demonstrated that the intensity maxima of the radiation in terms of magnetic declination coincide with the directions of the wings of the emission cones in the meridian plane which contains the radio source. Therefore the subsequent ray-tracing will consider only rays in the meridian plane. We notice that the shapes of the three curves corresponding to the respective emission cones are different because a uniform intensity distribution along the emission cones does not translate into a uniform distribution in terms of magnetic latitude.

B.3.2 Discussion of results

Although we started with oversimplified assumptions (no wave refraction along its propagation, no refraction at the source), we can eliminate the field lines with $L < 10$ as possible source

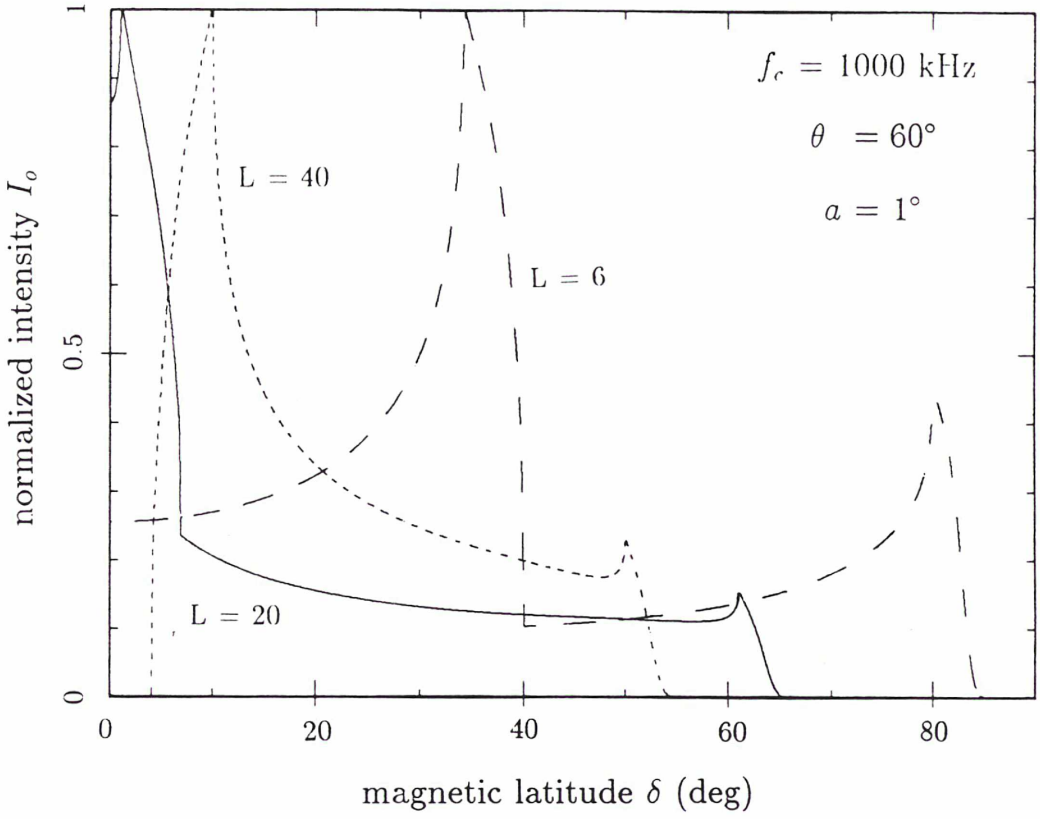

Figure B.4: Calculated normalized emission intensity versus magnetic latitude δ for sources on field lines with L =40, 20, and 6. The emission hollow cones are assumed to be distributed uniformly in longitude on both hemispheres at altitudes where $f_c = f$=1000 kHz (calculated from the Jovian dipole). For one set of conditions (characteristic half-width of the emission cone $a = 1°$, $f_c = f$=1000 kHz, and $\theta = 60°$), a source at field lines with L=20 exhibits an intensity peak near the magnetic equator.

locations for HOM when hollow cone emission is assumed. In this model, the sources are restricted to field lines in high magnetic latitude in the polar region. On the contrary, we see that the exclusion of all refractory effects does not lead to satisfying results concerning an exact source location, and problems arise concerning the low cone half angle θ for the lowest HOM frequencies. We therefore expect that the Io plasma torus highly influences the HOM emission, in particular in the lower frequencies. To confirm our findings and to locate the sources properly, a ray-tracing study including all effects of refraction is required. This is performed in the subsequent section.

B.4 Ray-tracing of Jovian hectometric radiation

B.4.1 Concept of ray-tracing

In the previous section, we had an indication of the hectometer source field lines from a first approach. To find the location of these sources more accurately, we performed a ray-tracing

study including all effects of refraction which a ray suffers during its propagation from the source into free space. The computer program is based on the Stix (1962) cold plasma formulation of the refraction index. The Haselgrove (1955) first-order differential equations (canonical ray equations, see Budden, 1961) are solved numerically. At a given point in space, the program calculates a refraction index surface for R-X mode waves based on a B-field model and a realistic plasma model. Next, the program takes an incremental step perpendicular to the surface of refraction index; this denotes the direction of the group velocity and energy flow, and is identical to the ray direction. Then, a new point in space is found where the refraction index surface can be calculated and the steps are repeated. The wave normal direction changes according to Snell's law when the wave travels through the magnetoplasma. The directions of the ray (energy flow) and of the wave normal (perpendicular to planes of constant phase) are very similar when the refractive index n does not differ very much from unity, but a substantial difference occurs when n approaches 0 (at the R-X cutoff frequency).

B.4.2 Magnetic field and plasma models

The computed ray paths in the program are dependent on the involved magnetic field and plasma models. For the description of the Jovian magnetic field, we have taken the O-4 model (Acuna and Ness, 1976) which provides spherical harmonic coefficients which correspond to the dipole, quadrupole and octopole terms. The influence of the Jovian current sheet on the magnetic field, described by Connerney et al. (1981), is also included, but the effect on waves at hectometric wavelengths remains, although it is very small. A realistic plasma model given in analytical expressions is taken from Divine and Garrett (1983). In their analysis they give density and energy models not only for charged particles in the Io torus, but also for the remaining magnetospheric regions up to 170 R_J. As we ray trace radiation at hectometric wavelengths we do not need to include an ionospheric model and the oblateness of Jupiter as was done by Hashimoto and Goldstein (1983). It is further assumed that the density and magnetic field gradients are small compared to the wavelength, so that no partial reflection occurs. Moreover, the electron temperature is assumed to be sufficiently low to allow for the cold plasma dispersion relation.

B.4.3 Generation mechanism of the radiation

Before starting our ray-tracing calculations, one must introduce some restrictions for the wave propagation at its source due to a distinct generation mechanism. We have considered the Cyclotron Maser Instability (CMI) by Wu and Lee (1979). This theory is able to explain in detail most of the properties of auroral radio emissions from the earth (AKR), Jupiter (DAM), Saturn (SKR), and also possibly from Uranus (UKR). Wu and Lee (1979) assumed that AKR is generated by the resonance of upgoing loss cone particles with the upper frequency branch of the extraordinary (R-X) mode. For simplified conditions, they were able to derive an expression for the growth rates of R-X and also L-O waves and found that R-X waves are favoured over L-O waves. Moreover, the theory predicts an initial wave normal angle θ with respect to the magnetic field which is primarily dependent upon the distribution of suprathermal electrons precipitating in the auroral zones. This angle θ is roughly perpendicular as confirmed by in situ measurements in the earth's magnetosphere. Since the pioneer work by Wu and Lee, many

studies have been published on this topic (e.g. Dusenbery and Lions, 1982; Le Queau et al., 1984a,b; Omidi and Gurnett, 1984; Omidi et al., 1984; Wu, 1985; Zarka et al., 1986).

Including assumptions about the generation mechanism, the input required for our ray-tracing calculation may be summarized as follows. The rays are traced from possible sources (labeled by the dipole shell parameter L) located at $f/f_c = 1.05$. For each source the propagation angle θ with respect to the magnetic field is varied and we determine the wave emergence angle above which the rays no longer travel within the HOM emission beam. According to the predictions of the CMI and the polarization measurements of HOM, only the R-X mode is considered for ray-tracing. From this analysis, we expect to derive the parameter L on which the HOM sources are located as a function of the cone half angle θ.

As already stated, we take f/f_c=1.05 to be valid at the sources in our analysis. However, we varied this value in order to see how low the ratio f/f_c can go without the rays suffering important refraction during the propagation in the vicinity of the source. We found that for f/f_c below 1.01-1.02, refractory effects near the source arise for rays with the largest emergence angles ($\approx 90°$). We can therefore extend the validity of our ray-tracing results which will be derived in the subsequent sections to ratios $f/f_c > 1.01$. Below this value, the ray paths near the source strongly depend on f/f_c which is not accurately known.

B.4.4 Ray-tracing computation

The HOM spectrum is largely extended in its frequency range, and therefore we made calculations for the specific frequencies f = 40, 150, 300, 500, 800, and 1000 kHz. An example is shown in Figure B.5 where we have traced rays at f=150 kHz, which is near the lower end of the HOM frequency range. All rays are released at CML=200° where the magnetic dipole meridian plane coincides with the Jovigraphic meridian plane. Generally, the ray paths divert a little in the azimuthal direction, but in this study we have only considered projections onto a meridian plane. Rays off the meridian plane are not taken into account but a three-dimensional treatment of the HOM emission cones is in progress. For each source, the wave normal angle is chosen such that the wave is finally traveling parallel to the magnetic equatorial plane. This direction approximately coincides with the direction of center of the HOM emission beam at 2° magnetic latitude. Each source is located at the apex of the corresponding emission cone. The cones exhibit different initial wave normal angles θ depending predominantly on the L value of the specific source field line. The shell parameter L is calculated from the centered dipole which is tilted by 9.6° with respect to the rotation axis. The magnetic north pole intersects the Jovian surface at CML $\approx$ 200° (northern hemisphere). Since the hectometer sources with f < 1000 kHz lie farther away than 3 R_J from the planet, the parameter L derived from the dipole represents the real magnetic configuration with sufficient accuracy. Some examples for sources with arbitrary L are plotted in Figure B.5. We additionally show the second wing of the emission cone which is symmetrically placed to the first wing with respect to the magnetic field in the magnetic meridian plane. Sources which lie closer to the magnetic equator (low L) are linked to cones with a smaller angle θ (in order to emit radiation which becomes finally parallel to the magnetic equatorial plane) than the sources situated at higher altitude field lines.

We recall that θ_o is one possible value of the cone half angle to allow one edge of the emission cone to be directed parallel to the magnetic equatoral plane. θ_o has already been determined as

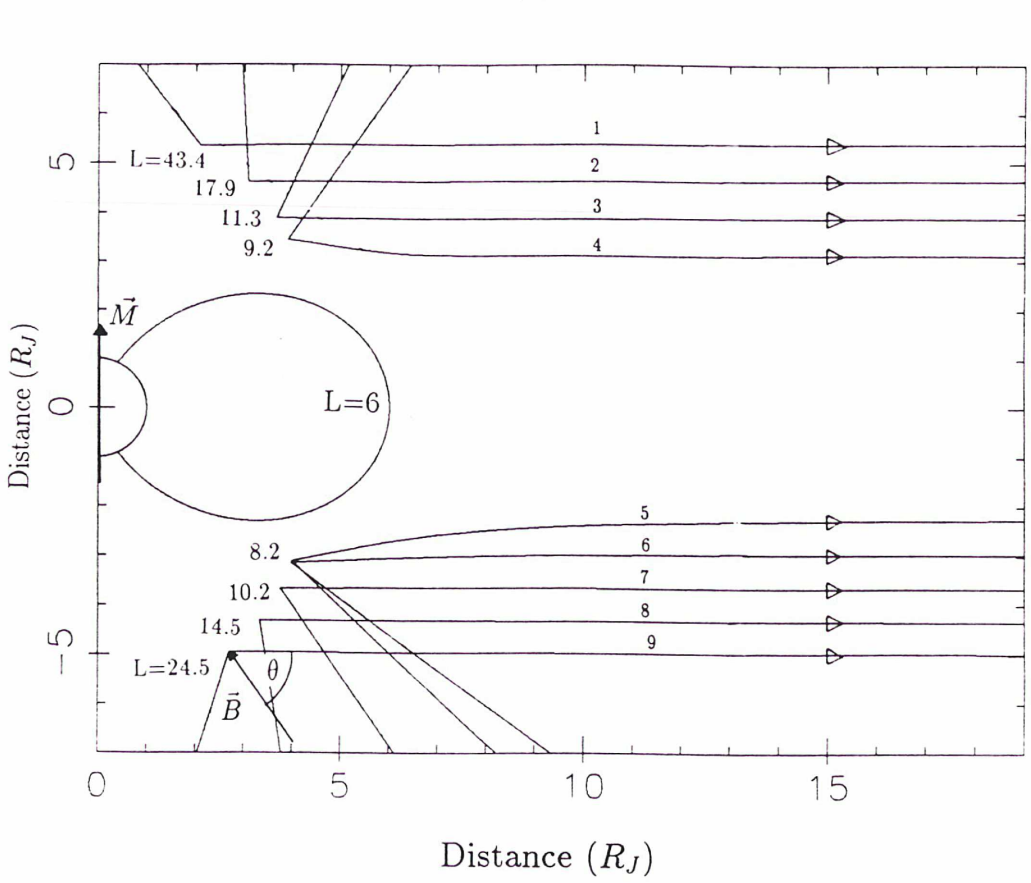

Figure B.5: Ray-tracing (f=150 kHz) for sources located at f/f_c=1.05 in the northern and southern hemispheres, and labeled by the shell parameter L. The wave normal angle at each source is chosen such that the wave finally propagates parallel to the magnetic equatorial plane. The second wing of the emission cone not directed toward the magnetic equatorial plane is also shown. Although rays 5 and 6 start with different wave normal angles θ from the same source (L=8.2), they finally reach the same outward direction because ray 5 is highly refracted by the Io torus.

a function of the parameter L and the frequency f in section B.3 for the Jovian dipole field. In general, waves starting from the source with a cone half angle $\theta > \theta_o$ may also be finally directed nearly parallel to the magnetic equatorial plane because of the refraction near the high density Io plasma torus (see ray 5 in Figure B.5). Let us determine now the maximum value θ which will be denoted as θ_{crit}, above which the final ray direction falls out of the observed beaming near the magnetic equator. Observations near the encounter show that HOM may be visible up to magnetic northern latitudes of 10° – 15° and possibly also at the same magnetic southern latitudes. Thus the ray is considered to fall out of the HOM beam when its final direction deviates more than ±15° from the magnetic equator.

Figure B.6 exhibits our findings for f=300 kHz (top panel) and f=500 kHz (bottom panel) for two specific source locations, respectively, in Jovimagnetic coordinates. The ray paths are projected onto the CML=200° meridian plane. For both frequencies the Io torus significantly

refracts the rays toward the direction of the magnetic equator, and it can be clearly seen that the critical angle θ_{crit} up to which the torus focuses the rays in that direction is predominantly a function of the L parameter of the regarded source field line. The sources on field lines L=22 in the northern hemisphere and L=15 in the southern hemisphere are displayed for the two frequencies. The cone half angle θ is increased from θ_o as defined in Figure B.3 by steps of 2° including the critical angle θ_{crit} which is deduced by allowing the rays to have a final direction deviating by only ±15° from the magnetic equatorial plane. When f=300 kHz, we derive for θ_{crit} the values 75° (L=15) and 80° (L=22), and for f=500 kHz, the values 84° (L=15) and 88° (L=22). We conclude that the relation $\theta_{crit}(L)$ is not a dramatically varying function of the frequency. Moreover, the Io torus highly influences the angle θ_{crit}, and an absence of the torus would decrease θ_{crit} down to about 60° for f=300 kHz when L=15. Therefore we emphasize that the presence of Io plasma torus plays a crucial role for emission at hectometric wavelengths in the way that the emission is beamed in the direction of the magnetic equator. This happens predominantly for large θ when we consider sources on field lines with high L. However, for source locations at field lines near the Io plasma torus, this is not the case (Figure B.7).

Figure B.7 shows the same situation as Figure B.6 but now for field lines L=10 and L=8 for f=300 and 500 kHz, respectively. At sufficiently high wave normal angles θ, the torus diffracts the waves away from the magnetic equator, so that the critical angle θ_{crit} becomes very low. The required HOM beaming can only be obtained if we assume low cone half angles θ of the order of 50° – 60°. As will be discussed later, this requires unplausible high electron energies to generate waves with such low cone half angles when f_p/f_c at the source is very low.

Regarding Figures B.6 and B.7, the Io torus produces a shadow zone near the magnetic equator at small radial distances; therefore HOM should be visible only above and below the magnetic equator but not in the proximity of $\delta = 0°$. In fact, V1 PRA observations on March 4, 1979 (rotation 1918), near the V1 encounter ($r \approx 15\ R_J$) exhibit HOM emission centered at CML=200° where the magnetic latitude of the spacecraft is highest within one Jovian rotation. At 110° CML which corresponds to $\delta = 0°$, no HOM emission at lower frequencies has been detected. To give more detail on this important point, investigations including in particular PRA data near the Voyager encounters are in progress.

Regarding the polarization, a mixture of right-hand polarization (rays from the northern hemisphere) and left-hand polarization (from the southern hemisphere) is expected at distances beyond the shadow zones in Figure B.6 near the magnetic equatorial plane. That is exactly what is observed for HOM in Paper 1 (Figure 9) although a higher frequency HOM component (942 kHz) was studied there.

As was done similarly in Figures B.6 and B.7, we investigated source locations for the hectometric frequencies f =40, 150, 300, 500, 800, and 1000 kHz and searched for the critical angle θ_{crit} as a function of the L parameter of the source field line for each frequency. The results are displayed in a frequency-θ_{crit} diagram as shown in Figure B.8. The L parameters of the source field lines are plotted corresponding to the calculated θ_{crit} dependent on the frequency of the emission. The index N refers to sources in the northern hemisphere and S to sources in the southern one. We see that θ_{crit} is a small varying function of the shell parameter L for $L \geq 15$. For $L < 15$, θ_{crit} decreases substantially with L. Moreover, for a given L, θ_{crit} is somewhat higher for sources in the southern hemisphere (except for f=40 kHz which is discussed below). This is explained by the fact that the Io torus does not lie exactly in the dipole equatorial plane. The deviation

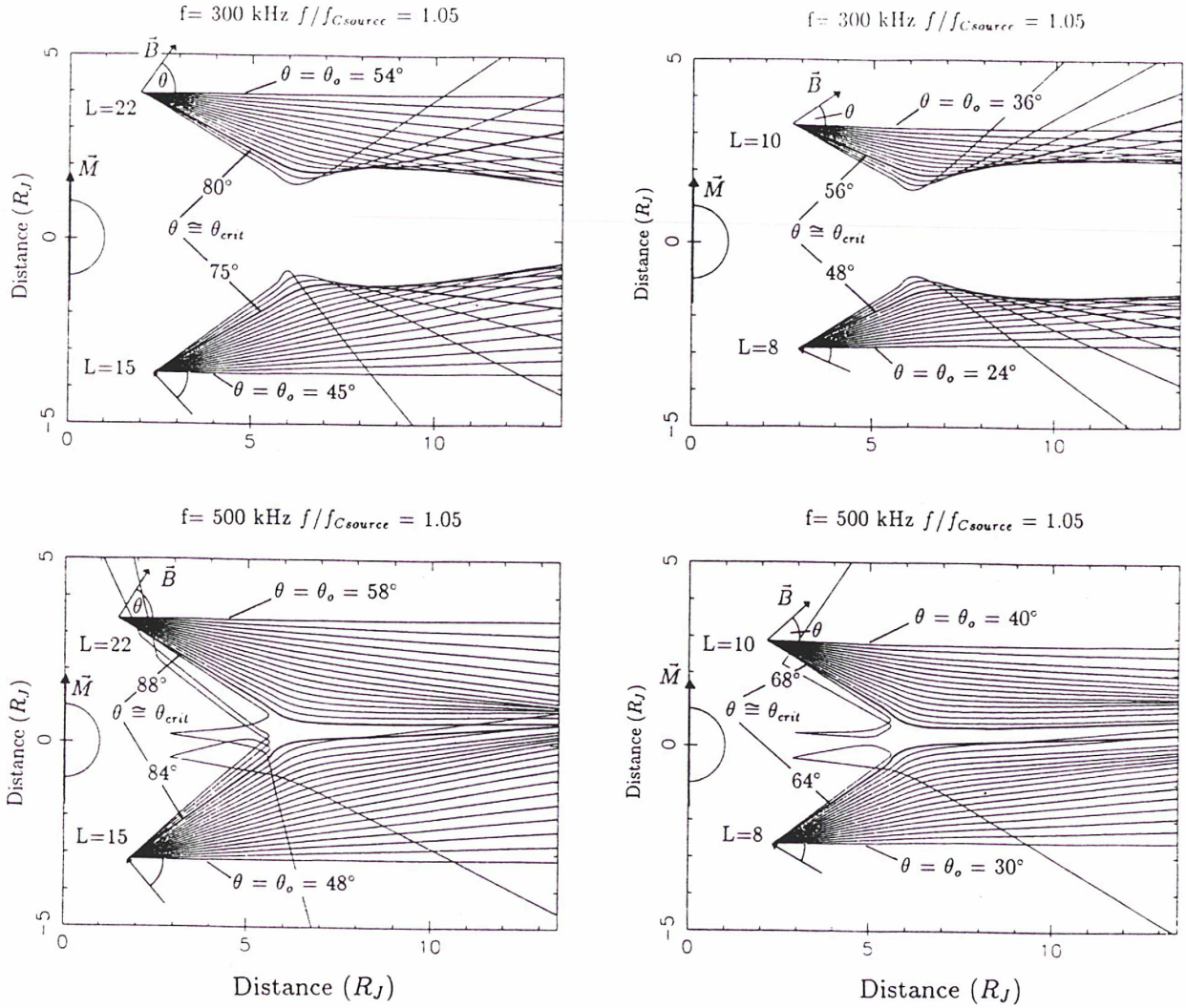

Figure B.6: (left panels) Variation of the cone half angle θ from θ_o to higher cone half angles including θ_{crit} for sources at L=22 and L=15. The rays for which $\theta \approx \theta_{crit}$ are accentuated and reach nearly 90° for L=22. For cone half angles greater than θ_{crit}, the final ray direction falls out of the direction of the observed beaming near the magnetic equator. Examples are shown for (top) f=300 kHz and (bottom) f=500 kHz in the magnetic frame of reference at CML=200°.

Figure B.7: (right panels) Same as Figure B.6 but for sources at field lines L=8 and L=10. Rays originally emitted with a θ nearly perpendicular to the local magnetic field are diverted away from the magnetic equator.

is most important for CML=20° and CML=200°. To point this effect out clearly we took CML=200° for the construction of Figure B.8. For other CMLs the hemispherical asymmetry is more moderate. The dashed lines in Figure B.8 denote θ_{crit} as a function of the frequency for L=10, L=15 and L=30. The lines are derived by linear interpolation (or extrapolation) from the given data in Figure B.8. Sources on L=15 to L=30 roughly account for θ_{crit} being situated between 70° and 90°. We did not interpolate data obtained from f=40 kHz because of the high

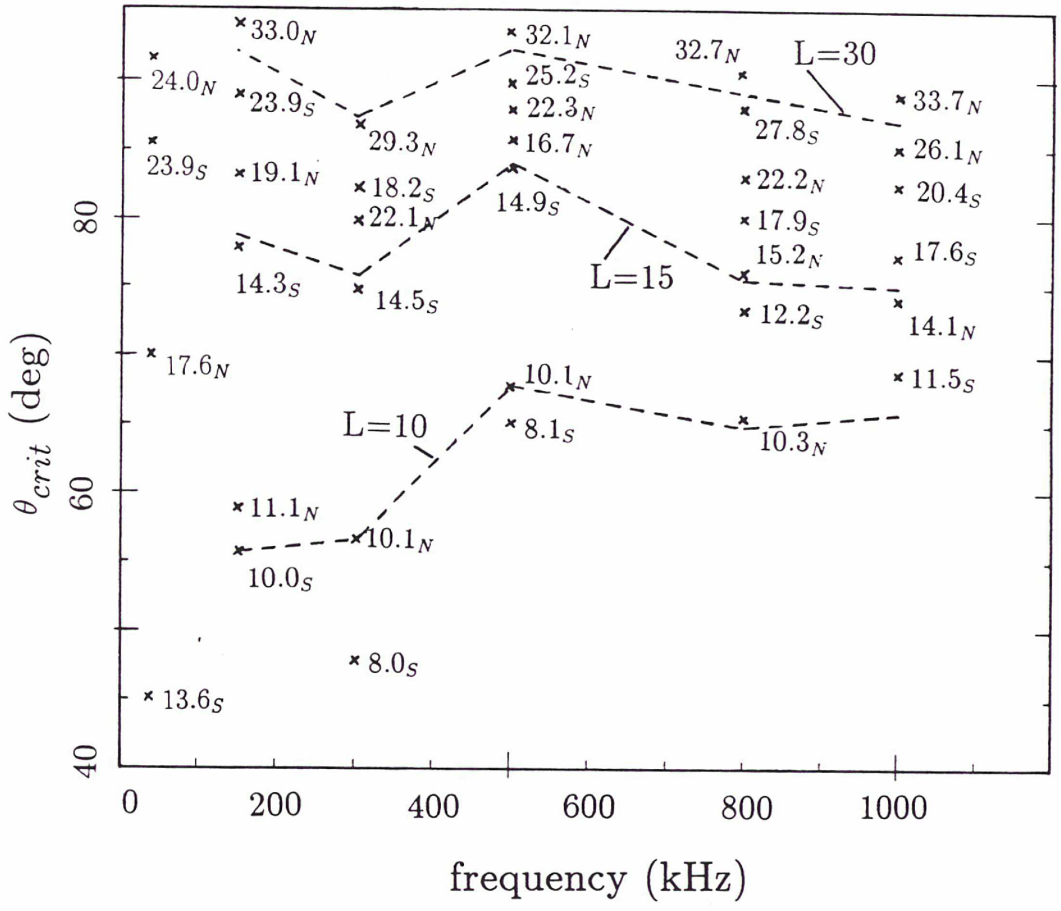

Figure B.8: θ_{crit} as a function of the emission frequency f and the L parameter of the source field line determined from the ray-tracing calculations for 200° CML. Dashed lines indicate the interpolated θ_{crit} L=10, L=15, and L=30 from the given data. N and S refer to the northern and southern hemispheres, respectively.

hemispherical asymmetry.

At f=40 kHz, the lowest observed frequency, the ray- tracing results show that θ_{crit} is no longer a monotonic function of the shell parameter L: the radiation is beamed parallel to the magnetic equatorial plane for $L > 20$ and $\theta_{crit} \leq 90°$ but only for a rather limited range of θ. For $L < 20$, all the rays propagate in the same direction for a large range of θ and this direction is sometimes distinct from the HOM beaming. Contrary to the higher HOM frequencies, the substantial asymmetry between both hemispheres is preliminary due to plasma sheet currents which influence the magnetic field strength and consequently also the ray paths.

We have demonstrated that a final ray direction parallel to the magnetic equatorial plane can be achieved for both $\theta \approx \theta_o$ and $\theta \lesssim \theta_{crit}$ which we have determined by ray-tracing in Figures B.6 and B.7. A priori we cannot decide which of the two possibilities accounts for the real situation, but when considering the observations, we can draw conclusions which may favour $\theta \lesssim \theta_{crit}$ over $\theta \approx \theta_o$. If θ were θ_o for all HOM frequencies, the Io torus would have no influence on the emission, and θ would be very low at the lowest frequencies. This problem was already encountered in section

B.3. In contrast, assuming that $\theta \lesssim \theta_{crit}$, we do not need to introduce a substantial decrease of θ when f decreases to the lowest hectometric frequencies (Figure B.8). For $\theta \lesssim \theta_{crit}$ the rays are not initially parallel to the magnetic equatorial plane. It is the passage near the Io torus that refracts the rays in the required direction and produces the sharp latitudinal beaming for HOM.

Moreover, the assumption $\theta \lesssim \theta_{crit}$ is strongly supported by the fact that HOM was detected near the torus when the Voyager 1 – Jupiter distance was larger than 6–7 R_J. This is also shown in Figures B.6 and B.7, which can both account approximately for the HOM observations in Figure B.1 assuming $\theta \lesssim \theta_{crit}$. In contrast, an emission with $\theta = \theta_o$ for which the waves are not influenced by the torus could not be observed by V1 within a large period near the closest approach.

During our ray-tracing analysis, we could see that for $f \approx 600 - 700$ kHz, the waves are not entirely refracted parallel to the magnetic equatorial plane for $\theta \lesssim \theta_{crit}$. This is caused by the fact that in the Io torus model, the peak density is not higher than a corresponding plasma frequency of ≈ 600 kHz. However, it has also been reported that V1 probably did not pass through the region of peak density, and that V2 did encounter higher densities outside the torus than did V1; it is not inconceivable that the plasma frequencies in the torus could exceed 1 MHz (cf. Jones, 1981). This is further supported by the fact that bKOM (which is probably generated at the torus) is sometimes active up to 1 MHz. If this is the case, HOM frequencies of the order of 1 MHz are also highly refracted when traveling in the proximity of the torus.

We were able to verify that the results obtained for θ_o in Figure B.3 are similar to the respective ray-tracing results for θ_o (including all effects of refraction) when the rays initially travel in directions parallel to the magnetic equatorial plane for the following reasons: (1) The dipole term accurately represents the magnetic field at the distances considered. (2) Rays with an initial direction in the magnetic equatorial plane are not visibly influenced by refraction effects of the Io torus. (3) The refraction at the source is negligible because the ratio f_p/f_c is very low ($< 10^{-2}$). (4) The assumption f/f_c=1.05 for ray-tracing in contrast to f/f_c=1.0 in Figure B.3 is not critical to the value θ_o. The similarity can be seen by a comparison of θ_o in Figures B.6 and B.7 to the respective values in Figure B.3.

Our source location for a given HOM frequency on a distinct field line labeled L is now only dependent on the cone half angle θ. When assuming a distinct θ, the shell parameter L for which θ_{crit} is greater but nearly equal to θ can be derived from Figure B.8. The cone half angle θ therefore plays a key role in determining the source location. It depends predominantly on the energy of the suprathermal electrons which are responsible for the generation of the auroral radio emissions and on the ratio f_p/f_c at the source. Staelin (1981) reported that electrons with a longitudinal (with respect to the magnetic field) velocity $v_{||}$ of 0.1 c (c = speed of light) and a total velocity v of 0.25 c ($\approx$ 15 keV) may provide an emission cone half angle of $\theta = 71°$. He estimated $v_{||}$ from the drift of a series of Jovian millisecond S-bursts downward in frequency. More recently, Horanyi et al. (1988) pointed out that energetic electrons with energies in excess of 10 keV precipitate into the upper atmosphere of Jupiter to explain the observed Lyman band emissions. These energies would also provide cone half angles somewhere between 70° and 80°.

In order to model Jovian decametric radiation arcs, Menietti et al. (1984) found that hollow emission cones are able to describe the specific arc pattern provided that the cone half angle θ is varied with frequency. They found θ to be $\approx 80°$ for the arc vertex frequency which is situated at about 10 MHz, and θ decreases down to about 70° at the high-frequency ($\approx$ 30 MHz) and at the low-frequency ($\approx$ 2 MHz) extension of an arc. They further showed that θ

is only a mild function of the assumed ratio f/f_c at the source which varied from 1.02 to 1.2 in their investigation. A cone half angle of $\theta = 79°$ has already been suggested by Dulk (1967) to account for the Io related components of DAM. With his emission cone model, he could account in a rough way for the active Io phase regions (Io-A and Io-B source). Goldstein and Goertz (1983) reported that DAM emission can be explained in terms of a thin conical sheet with an opening angle of $70° - 90°$. More recently, Bagenal and Leblanc (1988) investigated the Io DAM source geometry and found an opening angle of $\approx 70 - 72°$ to account for Io-A and Io-B observations. It is noteworthy that similar cone half angles are suggested for the auroral kilometric radiation (AKR) by Le Queau et al. (1985). In their theoretical studies, the authors accounted for θ to be of the order of $70° - 80°$ for AKR. For Jovian HOM, the ratio f_p/f_c is very small at the source regions which supports the assumption of a large (nearly perpendicular) cone half angle (e.g. Wong et al., 1982).

It is, however, difficult to extrapolate these results to the HOM sources at a distance of several Jovian radii from the planet, but in the absence of direct measurements, we will consider similar cone half angles as already established for Jovian DAM and AKR in order to avoid the assumption of unplausible high electron energies in the case of a small θ. Thus for our further investigation, we will consider $\theta > 70°$ in the absence of lower cone half angles for other radio components.

B.4.5 Determination of HOM sources

As previously stated, the ray-tracing calculations were performed for CML=200°, although the PRA observations at HOM frequencies usually exhibit an emission gap near that longitude. It was derived by Alexander et al. (1979) and in Paper 1 that this gap is exclusively a consequence of the strong latitudinal beaming of HOM near the magnetic equator. On the other hand, it is not necessary to trace rays for all system III longitudes for the following reason: for the distances where the hectometric radiation sources are located, the Jovian magnetic field exhibits a strong dipole character, and therefore no substantial azimuthal dependence in a Jovimagnetic coordinate system. We verified this by tracing a few rays as we did for the construction of Figure B.8 but from different system III longitudes. We noticed that the calculated angles θ_{crit} as a function of L for a given HOM frequency deviate at maximum only by $3° - 4°$ from the values of θ_{crit} reported in Figure B.8. This is the consequence of the strong magnetic field asymmetry on Jupiter's surface which is weakened at larger distances from the planet. The Io torus is nearly symmetric with respect to the magnetic dipole equator, and therefore there exists only a small refraction effect dependent on the azimuth. Consequently, we extend the validity of Figure B.8 out to all system III longitudes without a significant error.

For our purpose, we have estimated the probable cone half angle θ as between 70° and 90° (based on the information given for other auroral radio emissions). Regarding Figure B.8, the field line L=15 is roughly associated with $\theta_{crit} \geq 70°$ and L=30 with $\theta_{crit} \geq 90°$. Thus, in so far as θ is not better determined, we suggest that HOM sources are located at field lines having a shell parameter somewhere between L=15 and L=30. The HOM sources are consequently determined to be distinct from Io torus field lines and are therefore not linked to Io dependent DAM sources via magnetic field lines. From Figure B.8 we see that there is no dramatic dependence of the initial wave normal angle θ on the emission frequency for the derived source locations. Consequently, along a given field line, the cone half angle does not change very much from the

highest to the lowest hectometric frequencies. If L of the source field lines were about 8−10, then the cone half angle would be a strong function of frequency and would decrease substantially for the lowest HOM frequencies.

B.4.6 Location of the footpoints of HOM source field lines

After the determination of the possible L parameters for the HOM source field lines, we projected the footpoints of these field lines onto the Jovian surface. We performed this for the field lines L=15 and L=30, and we expect the HOM sources on field lines with their footpoints lying between the L=15 and the L=30 ovals on the surface depending on the exact value of the cone half angle θ. Since the Jovian field is not an exact dipole, points with the same L parameters (derived from the dipole) calculated at different altitudes (as done for the several frequencies in Figure B.8) generally do not lie on the same line of force. In any case, the deviation is not substantial, so we assume that points with the same L values are situated approximately on the same line of force. The use of the centered dipole approximation is justified by noting that at distances of the Jovian HOM sources (farther than 3 R_J), the dipole is largely dominating Jupiter's magnetic field structure. Moreover, the calculation is most simplified when considering the L shell parameter instead of the invariant latitude calculated from the O_4 model. For L=15 and L=30 we identified the foot points on the Jovian surface starting from 3 R_J ($f_c \approx$ 1000 kHz). The result is shown in Figure B.9 for the north and south polar regions, respectively. The dashed lines indicate the projection of the field lines L=15 and L=30 onto the surface. The hatched area indicates the location of foot points linked with possible HOM source field lines with L parameters between 15 and 30. The solid line gives the tail field auroral oval for each hemisphere. They are calculated by Connerney et al. (1981), the outer oval with inclusion of the current sheet and the inner one without it. The tail field auroral zone can be visualized as the boundary of field lines connecting to the magnetic tail from polar regions. We notice that our determined HOM sources lie within these calculated tail field auroral zones which have direct access to particles precipitating from the tail. We consider this source location to be most compatible with both the observations and the generation mechanism. Since HOM exhibits a local time effect, not all of the field lines along the auroral ovals shown in Figure B.9 may be active at the same time. We will discuss the consequence of the obtained HOM source locations and applications to the phenomenology of the emission in the context of the other Jovian radiation sources.

B.5 Discussion

We derived the HOM source locations by performing a ray-tracing study and considering the emission characteristics in detail. The obtained source location depends on the validity that HOM can be represented in an emission of hollow cones distributed in longitude at the northern and southern hemispheres. Furthermore, we assumed that the radiation is generated slightly above the local gyrofrequency in the extraordinary wave mode. Our ray-tracing investigation based on the observations of HOM strongly indicates that the HOM sources lie within the tail field aurora whose field lines connect the polar regions to the Jovian magnetic tail, at distances from 2 to 7 R_J from Jupiter's center. The exact source location in magnetic latitude is related

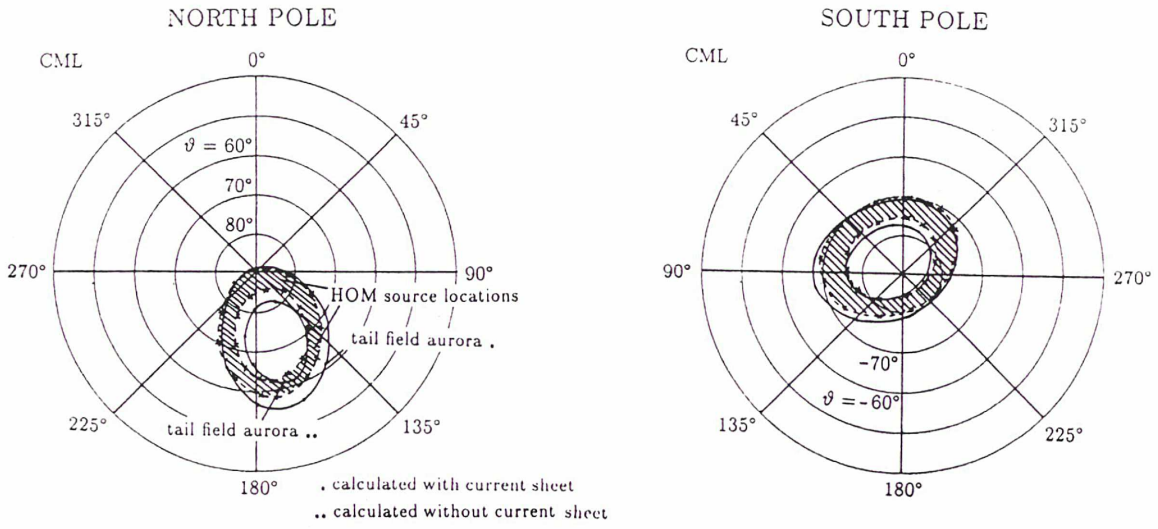

Figure B.9: Foot points of HOM source field lines projected onto the Jovian surface (hatched area) and tail field auroral ovals (taken from Connerney et al., 1981) for the northern and southern hemisphere, respectively. The outer auroral oval was calculated with the inclusion of the Jovian current sheet and the inner one without it. The HOM sources are located remarkably well within the space between these ovals.

to the assumed cone half angle θ. However, an HOM source at the tail field auroral region accounts for a large variety of the phenomenology observed so far. (1) The strong latitudinal beaming of the emission is caused by the wave refraction at the Io plasma torus. In addition, to account properly for observations at $f \geq 1$ MHz, a peak electron density corresponding to a plasma frequency of 1 MHz is required in the torus. (2) The extension of the HOM down to 40 kHz is accounted for with an initial wave normal angle somewhat lower than that for the higher HOM frequencies, but still $\theta > 70°$. In contrast, sources at (and near) Io torus field lines could not provide emission at frequencies as low as 40 kHz. (3) The location of the radio source in the tail field aurora may convincingly explain the solar wind control observed for the HOM emission. High energetic particles originating from the solar wind precipitate into the auroral zone and therefore directly influence the conditions of generation. (4) The absence of HOM emission for distances less than $\approx 6\ R_J$ is due to both the location of the sources at high altitude polar regions and the refraction of the radiation at the edges of the plasma torus. (5) The emission is not influenced by Io as would be expected for a source in the tail field auroral zone.

The location of the other Jovian radio sources has already been treated by a large number of researchers, and it is well established that the Io DAM sources lie along field lines connecting the Io torus. Our findings argue therefore for distinct Io DAM and HOM sources which were also derived by Genova et al. (1987) from a different line of reasoning. Concerning the non-Io DAM a definitive conclusion is less easy to draw. As the refractory effects of the Io torus gradually die away for frequencies higher than $\approx 2 - 3$ MHz (Lecacheux, 1981), one cannot claim that HOM and non-Io DAM are distinct sources when considering solely the slight change in the occurrence probability of both emissions. Moreover, Genova et al. (1987) suggest that the HOM and the non-Io DAM emanate from the same source situated at high altitude field lines. A recent study,

performed by Maeda and Carr (1988), deals with the radiation sources of non-Io DAM. In their unique analysis, they determined the location of the source field line by investigating non-Io DAM storms viewed from the earth, Voyager 1, and Voyager 2, each at different zenographic latitudes and longitudes. Figure B.10 shows the foot points on the Jovian surface of possible source locations of non-Io DAM in terms of the cone half angle θ. The foot points at the start and end of a non-Io storm are shown by the open and solid circles labeled with the same letter. The UV aurora, Io flux tube, and tail field aurora are displayed with thick solid, thick dashed, and thin dashed lines, respectively. Figure B.10a exhibits the source region when $\theta = 45°$; Figure B.10b when $\theta = 55°$; and for Figure B.10c a variable cone half angle of $39° - 58°$ determined in their analysis is used. The authors suggest the source region to be situated at field lines connecting the UV auroral zone which is distinct from the tail field aurora except for a short interval in system III longitude centered at $\approx 140°$ CML. Despite the fact that it is difficult to provide electron energies sufficiently high to account for cone half angles of about 45° when f_p/f_c at the source is very low, it is interesting to note that the authors derive the source to be at the tail field aurora when they take θ to be 55°. From our results we therefore cannot exclude the possibility that HOM is the low-frequency extension of non-Io DAM as suggested by Genova et al. (1987). However, HOM shows a spectral emission peak near 1 MHz (Brown, 1974), a fact that should also be kept in mind to make the link between non-Io DAM and HOM.

A further interesting question concerns a possible link between broadband kilometric radiation (bKOM) and HOM. From our investigations, we are able to state that bKOM cannot be the low-frequency extension of HOM, since bKOM occurs statistically in the CML range of $170° - 300°$ and HOM in the remaining CML range. Moreover bKOM activity tends to cover a larger CML interval at the lower frequencies, in contrast to the HOM observations. Therefore bKOM sources at the Io torus as suggested by Jones (1981, 1986) and Jones and Leblanc (1987) are favoured over an auroral source region.

Finally, one should compare the Jovian hectometric emission with the other planetary auroral emissions. In a way similar to HOM, a solar wind control was established for the Saturnian kilometric radiation (SKR) (Desch, 1982; Desch and Rucker, 1983) and for the terrestrial kilometric radiation (Gallagher and D'Angelo, 1981); moreover, for both Saturn and the earth, the solar wind influence is stronger than for the Jovian HOM. Furthermore, all of these planetary emission components exhibit a local time dependence.

The exact source locations of SKR are well established (Kaiser et al., 1980, 1981; Kaiser and Desch, 1982; Lecacheux and Genova, 1983) to be situated at magnetic field lines connected with the UV aurorae (Sandel et al., 1982) and polar cusp (Behannon et al., 1981); thus the solar wind has direct access to the radio source. For the earth, it is also well-known that the source is located in the auroral zones (Gurnett, 1974; Gurnett and Green, 1978). The source locations of HOM in the Jovian tail field auroral regions complete the analogy to TKR and SKR. Like these emissions, HOM sources are active along a large range of altitudes on auroral field lines, are controlled by the solar wind which has direct access to the radio sources and are local time dependent. But HOM covers a somewhat higher frequency range because of the stronger magnetic field of Jupiter.

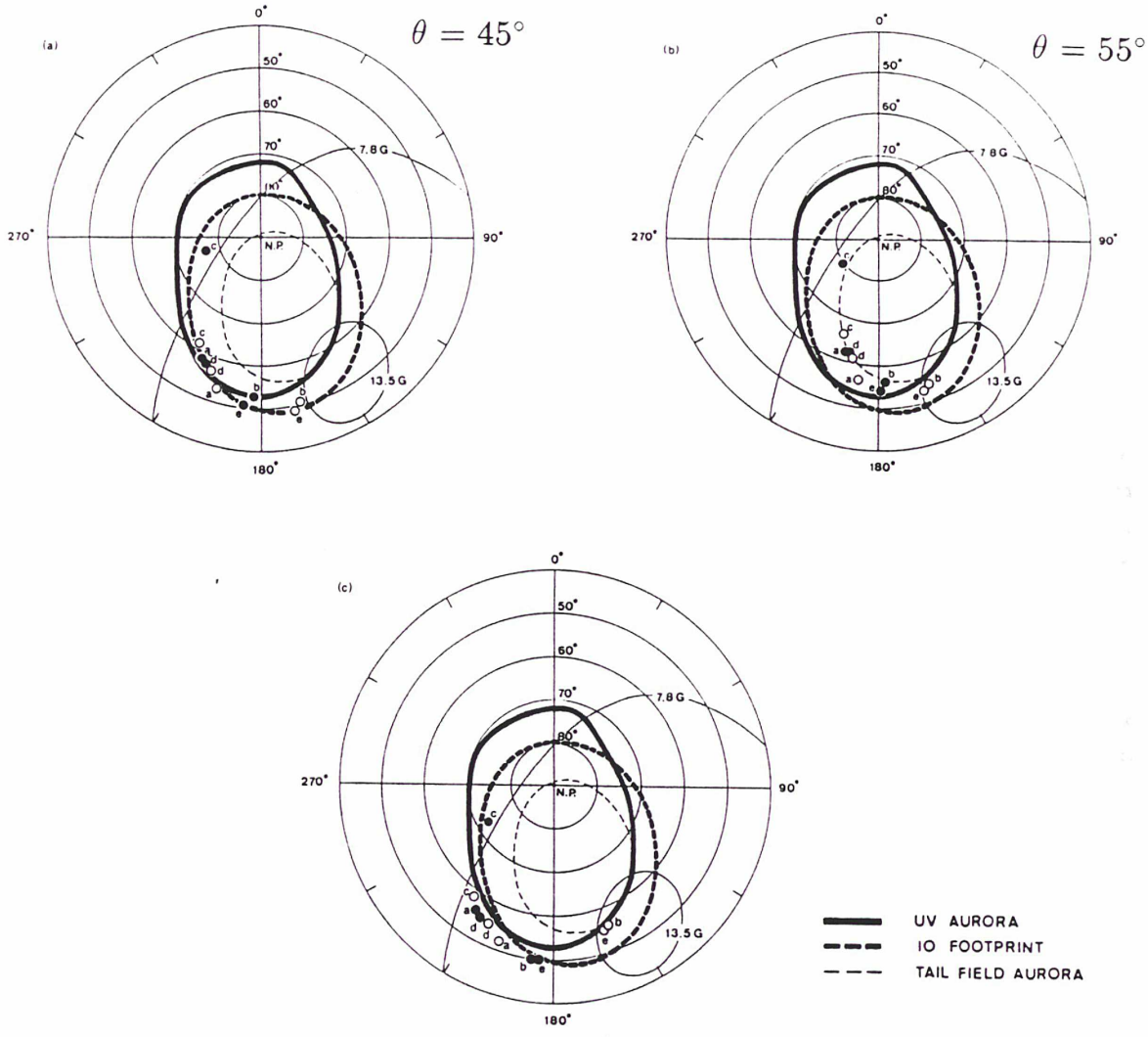

Figure B.10: Foot point locations which link the non-Io DAM (21.86 MHz) sources to the Jovian ionosphere in the northern hemisphere (from Maeda and Carr, 1988). The foot points at the start and end of a non-Io DAM storm are shown by the open and solid circles labeled with the same letter, respectively. The results are displayed for three cases: (*a*) θ (cone half angle)=45°, (*b*) $\theta = 55°$, and (*c*) varying cone half angle derived from the observations. In the case of $\theta = 55°$ HOM could be interpreted to be the low-frequency extension of the non-Io DAM.

Appendix C

Modeling of the Jovian hectometric radiation: A three-dimensional study

Abstract

To model the Jovian hectometric radiation (HOM), we performed three-dimensional ray-tracing at a frequency of f=500 kHz. The source locations are assumed to lie along magnetic field lines L=20 as determined by Ladreiter and Leblanc (1990a). Furthermore, they are distributed uniformly in longitude at magnetospheric heights, where the cyclotron frequency is less but nearly equal to the wave frequency. The emission is beamed at large angles (70°-80°) with respect to the magnetic field and propagates in the extraordinary (R-X) mode. Our study can account for the major characteristics of the HOM radiation as observed by the Planetary Radio Astronomy (PRA) experiment aboard Voyager 1 and Voyager 2 during the encounter period and at large distances from the planet. Thus, geometrical effects are taken into account. The modeled radiation pattern reveals the existence of a shadow zone at the magnetic (dipole) equatorial plane extending to about 20 Jovian radii (R_J), which was actually observed by both Voyagers. The results from our ray-tracing analysis account for the strong latitudinal beaming of the radiation, observed at large radial distances from Jupiter, as well as for the polarization properties. Moreover, the modeled intensity profiles, compared with observations in the vicinity and far from Jupiter, show a remarkable agreement. However, a better fit to the observations is obtained when the Io torus electron density (from Divine and Garrett, 1983) is enhanced by 15 %. This study confirms that the HOM source locations are located along open magnetic field lines with footprints in the tailfield auroral ovals in both hemispheres. We suggest that HOM is the low-frequency extension of non-Io DAM, since the observed spectral peak of HOM near 1 MHz could be produced by the focussing of the radiation due to refractory effects of the Io torus.

C.1 Introduction

Since the Voyager 1 spacecraft approached Jupiter as near as 4.9 Jovian radii (R_J), the Planetary Radio Astronomy (PRA) receiver (Warwick et al., 1977) was able to collect a rich variety of radiation phenomena, which had never before been seen. This data set provides the first opportunity to observe the Jovian radiation from inside the Io plasma torus. Besides the well known decametric radiation which has been observed from ground based stations for more than three decades now, the Voyager spacecraft discovered emission below 1 MHz, the Jovian kilometric radiation (KOM) and the higher frequency hectometric radiation (HOM). The hectometric component covers a large frequency range and may sometimes be active down to 40 kHz (Boischot, 1988; Ladreiter and Leblanc, 1989). The high-frequency limit is not well-determined but certainly reaches up to 3 MHz (see e.g. Carr et al., 1983), and it is suggested to be as high as 7 MHz (Barrow and Desch, 1989). Most of the studies of hectometric radiation are concentrated on the observations in the low band of the PRA receiver which scans 70 channels from 1326 kHz down to 1.2 kHz in steps of 19.2 kHz.

The latitudinal beaming of HOM was first established by Alexander et al. (1979). They emphasized that HOM is strongly dependent on the magnetic latitude of the spacecraft and that the radiation is sharply beamed within a thin sheet (thickness of 10°) near, but centered somewhat north (about 2°) the magnetic dipole equatorial plane. The periodic variations of HOM in terms of system III longitude are consequently due to the varying Jovimagnetic declination of the observer within one Jovian rotation. Statistical observations (Alexander et al., 1981) confirmed this latitudinal beaming of HOM and additionally provided evidence for a local time dependence of the emission. Ladreiter and Leblanc (1989, hereafter Paper 1) re-examined the latitudinal beaming of HOM and found that the total beam width is between 10° and 20°, depending on the normalized detection threshold. Additionally, we showed that the HOM beam width is 4° narrower on the nightside than on the dayside.

The solar wind control of HOM was investigated by several authors (Zarka and Genova, 1983; Desch and Barrow, 1984; Genova et al., 1987; Barrow and Desch, 1989). It has been shown that the HOM energy output depends on the solar wind density, pressure, and the sector structure of the interplanetary magnetic field (IMF). However, Rabl et al. (1990) demonstrate that the IMF sector transitions are not responsible for stimulating the HOM energy output. In Paper 1, we additionally found the low-frequency extension and the HOM beam width to be influenced by the solar wind. The solar wind control on HOM argues for sources located on open magnetospheric field lines rather than on closed ones.

The HOM component often exhibits a mixed, and sometimes time-varying polarization pattern. Previous studies (Kaiser et al. 1979, Alexander et al., 1981; Boischot et al., 1981) could not convincingly explain the rather complicated polarization behaviour of HOM. After the determination of the electric antenna plane of the PRA experiment by Leblanc and Daigne (1985a) and the determination of the polarization response of the antennas (Lecacheux and Ortega-Molina, 1987; Ortega-Molina and Lecacheux, 1990a), it has now been established that right-hand polarization (RH) is mainly associated with the northern hemisphere, and left-hand (LH) polarization with the southern hemisphere. Thus the polarization of HOM is consistent with emission in the extraordinary (R-X) mode (Paper 1, Ortega-Molina and Lecacheux, 1990b).

A first step in finding the HOM radio emitting regions in the Jovian magnetosphere was made

by Lecacheux (1981). He performed a ray-tracing study in a meridian plane taking into account PRA-observations within the Io plasma torus. For f=300 kHz, he found a source in the southern hemisphere located at $L = 6 - 7\ R_J$. The fact that this source is not located in a region where the wave frequency is clearly related to the plasma frequency or gyrofrequency makes the results not entirely convincing.

Very recently, Ladreiter and Leblanc (1990a, hereafter Paper 2) determined the source locations of the hectometric radiation via ray-tracing analysis (also in a magnetic meridian plane). In that work, they introduced the characteristics of the HOM as found by Alexander et al. (1979) and Paper 1. To put further constraints on the source locations, we considered the Cyclotron Maser Instability (CMI) (Wu and Lee, 1979) as the relevant generation mechanism based on the HOM polarization measurements. The results strongly suggest the tail field auroral zones to be favoured candidates for the sources of HOM. The sources cover a wide range in longitude in both hemispheres which is consistent with the beaming of HOM in magnetic latitude. The obtained HOM sources, which are confined between L=15 and L=30 at radial distances where the wave frequency is slightly higher than the local gyrofrequency, also convincingly explain the solar wind control of HOM since the solar wind particles have direct access to the radio sources through the magnetic tail or the polar cusp.

The purpose of this study is to account for the HOM observations by assuming the source locations and emission characteristics as determined in Paper 2. In particular, we have taken advantage of the fact that Voyager 1 passed very close to the planet, and we noticed that during the period of its closest approach, HOM was not observed near the magnetic equatorial plane. In turn, when the spacecraft was at larger distances ($> 20R_J$) from the planet, the emission occurred favourably at low magnetic latitudes. A fully three-dimensional investigation has been performed in order to model the HOM observations and to make detailed comparisons with the observed pattern.

Our analysis is similar to that already performed by Gulkis and Carr (1987) in the case of Uranus. These authors also modeled Uranian PRA observations also by inferring initial source parameters. In the case of Jupiter, the procedure is more difficult because the excursions of the Voyager spacecraft in magnetic latitude are very limited, and because of the existence of the Io torus which alters the ray paths considerably. Thus, a three-dimensional ray-tracing study for the hectometric frequency range is necessary.

In section C.2, we present typical HOM observations and discuss the change in the HOM emission pattern on a fixed frequency plot when Voyager 1 was approaching Jupiter. In section C.3, the ray-tracing procedure is briefly presented, and we introduce the HOM source locations and emission characteristics from Paper 2. In section C.4, we show that a shadow zone near the magnetic equator is produced for distances less than about $20R_J$. This shadow zone is due to the presence of the Io torus which behaves like a divergent lens for frequencies in the hectometric range. In turn, it focusses the radiation near the magnetic equatorial plane farther away from Jupiter. In section C.5, the modeled intensity curves, which are obtained from a detailed investigation for f=500 kHz, are compared with the observed pattern. We simulate the overall features when the spacecraft was near the planet and account for the strong HOM latitudinal beaming which is observed at large distances. The implications of these results are discussed in the conclusion (section C.6).

C.2 Observations

Figure C.1 displays PRA observations for the indicated frequencies as seen by Voyager 1. Figure C.1a was recorded during one Jovian rotation approximately 1 month (70 Jovian rotations) before the V1 encounter (therefore labeled Rotation # -70) and represents a typical HOM profile as measured far from the planet (The spacecraft-Jupiter distance is indicated at the top). The emission peaks twice within one Jovian rotation at System III longitudes (or CML) $\approx 60° - 110°$ and CML $\approx 300° - 350°$. The peaks are quite symmetrically placed with respect to CML $\approx 202°$, where the northern magnetic pole is tilted toward the spacecraft by 9.6° with respect to the rotation axis. At that longitude, a wide emission gap occurred where no significant HOM activity arised. The lower panel (Figure C.1b) was recorded 1 Jovian rotation before the encounter, and the emission topology has completely changed. First of all, the emission gap seen in Figure C.1a is mostly filled by strong activity around CML= 200°, which is flanked by low activity zones centered on CML $\approx 120°$ and CML $\approx 270°$, respectively. Finally, a range of activity also occurred around CML $\approx 45°$ and CML $\approx 330°$.

A straightforward way to understand these features is to consider the HOM as a function of magnetic (dipole) latitude δ_{mag} (indicated at the bottom of each panel) rather than a function of CML, as was successfully done by Alexander et al. (1979) and in Paper 1. Thereby, the most significant changes are easily seen. In the upper panel (Figure C.1a), when the spacecraft was far from the planet, the emission is commonly restricted to magnetic latitudes in the vicinity of the magnetic equator which is indicated by the vertical dashed lines. The emission gap is associated with the highest magnetic latitudes reached by the spacecraft within a Jovian rotation. In Figure C.1b (near V1's closest approach), this scenario is no longer accounted for: at the times of spacecraft magnetic equator crossings, the radiation is absent and restricted only to magnetic latitudes well above or below the magnetic equator i.e. the contrary of which was observed at large distances from Jupiter. In Figure C.1, preencounter observations are selected out for our study but postencounter observations show the same characteristics.

The emission characteristics in Figure C.1b lend support to the hypothesis that the radiation is unable to penetrate regions corresponding to low magnetic latitudes near Jupiter. This builds a region of no illumination near the Jovimagnetic equatorial plane which will be called the shadow zone. This shadow zone is expected to be the consequence of specific emission properties at the source (i.e. source location and beaming pattern) and of the presence of the Io plasma torus located at about 6 R_J from the planet. The occultation zone due to the emission properties at the radio sources depends on the choice of the source locations and the propagation angles. The extension of the shadow zone is further strongly influenced by the Io torus which becomes opaque especially for the lower frequency range of HOM. Substantial refraction, however, may occur up to frequencies of a few MHz (Lecacheux, 1981), depending on the torus peak electron density.

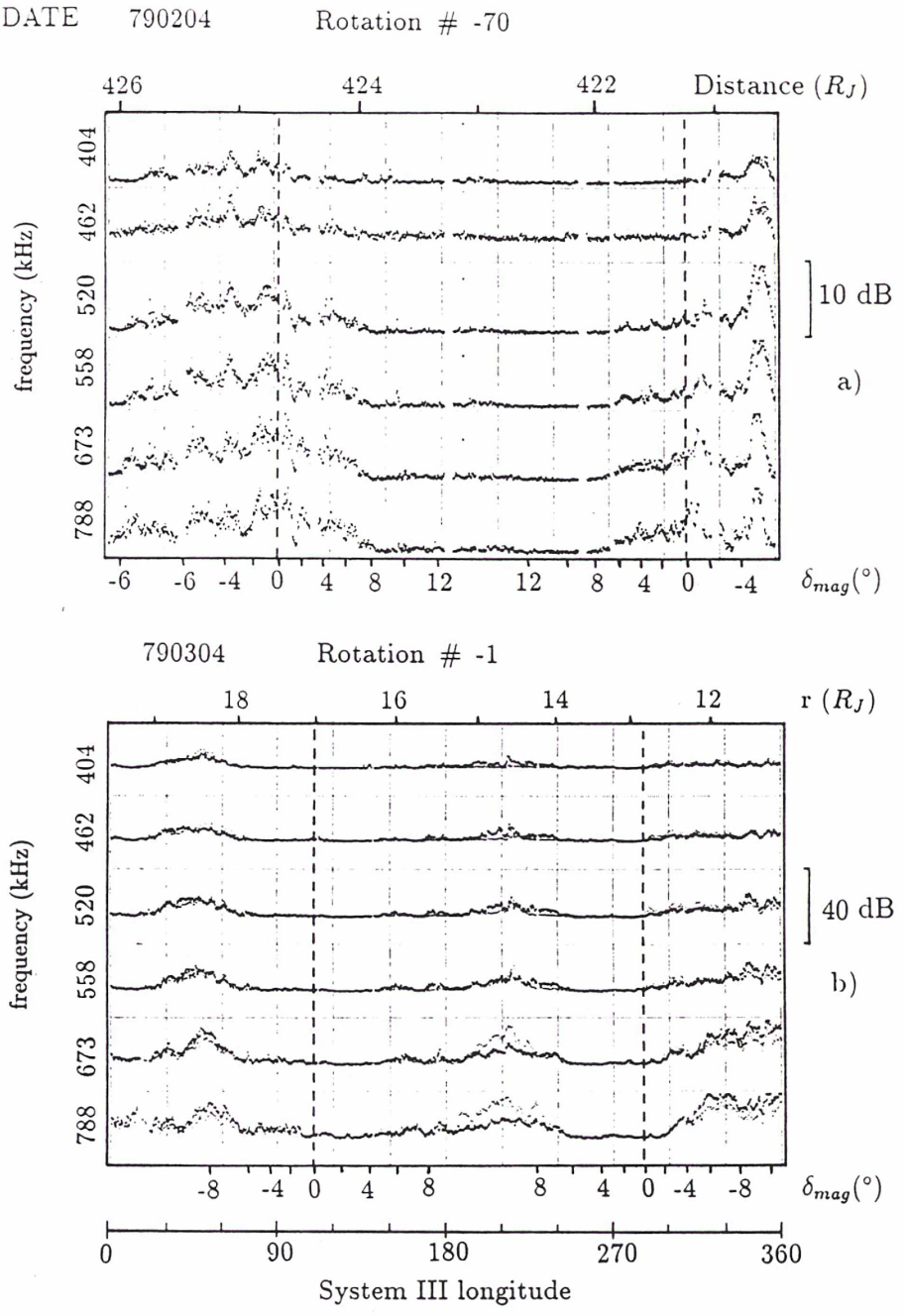

Figure C.1: Voyager 1 PRA observations in the hectometric frequency range as a function of system III longitude, radial distance, and Jovimagnetic declination. The rotation numbers are counted with respect to the encounter. The vertical dashed lines indicate magnetic equator crossings of the spacecraft. RH-polarization is indicated by dotted lines and LH-polarization by full lines. (a) Observations at large distances from Jupiter. Note the absence of emission at higher magnetic latitudes. (b) Observations just before the V1 encounter. Note the absence of radiation near the magnetic equator.

C.3 Development of the model

C.3.1 Ray-tracing

Before examining the shadow zone of HOM and the modeled intensity profile, one should mention a few words about the ray-tracing procedure used throughout this paper. The procedure of ray-tracing was described in detail in Paper 2, so only a short review is given here. The program is based on the numerical integration of Haselgrove's first order differential equations (Haselgrove, 1955; Budden, 1961) in order to determine, step by step, the final ray path from the radio source throughout the Jovian magnetosphere. The ray equations require analytical magnetic field and plasma models which are provided by Acuna and Ness (1976) (O_4 model), Connerney et al. (1981) (distortion of magnetic field by plasma sheet currents), and Divine and Garrett (1983) (plasma model, including Io torus).

C.3.2 HOM source location and emission mechanism

The HOM sources and propagation properties used in our presentation were determined in Paper 2. Thus, we assume that the sources are located on L=20 (to take an intermediate value between L=15 and L=30) and are distributed uniformly in longitude at both hemispheres. For L=15 (L=30) somewhat smaller (larger) wave normal angles would be required than for L=20 in order to successfully simulate the HOM latitudinal beaming (Paper 2, Figure 8). For the sake of simplification, we have restricted ourselves to the detailed investigation of radiation at f=500 kHz, but the trends for other frequencies will also be shortly discussed. For L=20 and f=500 kHz, the critical emergence angle above which the HOM observations are no longer accounted for, is about 86° (see Paper 2, section 4.4 and Figure 8). Our selected value for θ should therefore be less than 86°. We have used an emergence angle $\theta = 75°$, and a cone half-width $\Delta\theta = 5°$. The two values are justified if we consider the cyclotron maser mechanism which predicts nearly perpendicular emergence angles (Wong et al., 1982), and a small cone half-width (Le Queau, 1988) when the source is at a level where f_p/f_c is very small, which is the case for HOM ($f_p/f_c <$ 0.01, see Paper 2). Finally one has to introduce the ratio f/f_c at the radio source (f_c being the electron gyrofrequency). We select $f/f_c = 1.02$ in accordance with the CMI which predicts ratios f/f_c nearly equal but slightly greater than 1. The refraction of rays near the source depends on the assumed ratio f/f_c and cone half angle θ. In our case, refraction of the rays at the source does not occur down to $f/f_c \approx 1.01$ for an R-X mode wave; therefore the results are not crucial to variations of f/f_c provided that $f/f_c > 1.01$. This can also be seen in Paper 2 were we used f/f_c=1.05. However, the actual value for HOM is not known and may be anywhere between f/f_c=1.01 and f/f_c=1.05. In addition, the major features of the results are found to be not considerably affected by the specific choice of $\Delta\theta$ if $1° < \Delta\theta < 10°$.

On this point, we should emphasize that we do not perform a parameter study by varying source parameters in order to fit the observations. Instead, we selected a set of parameters from Paper 2 to confirm and extend the relevance of the source locations and emission characteristics in the frame of a three-dimensional treatment.

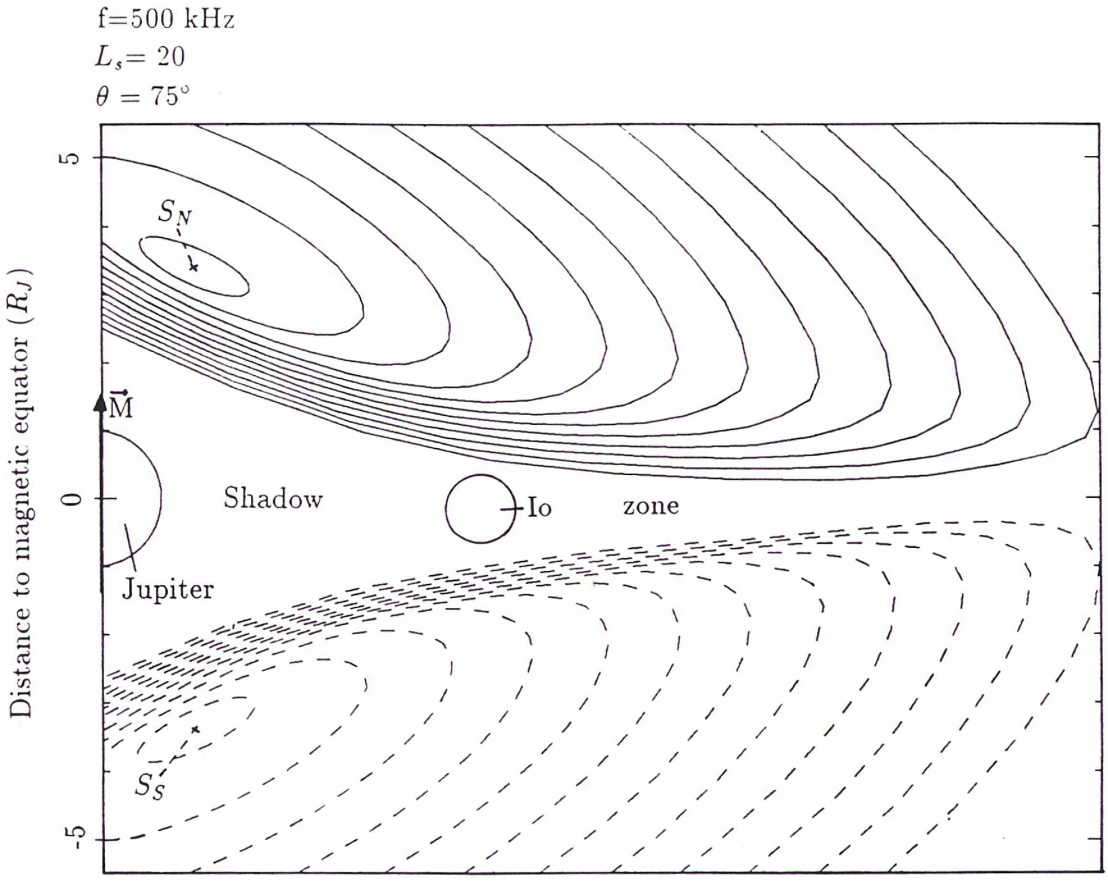

Figure C.2: Ray-tracing of HOM hollow emission cones (θ = 75°) emanating from sources located at L=20 in both hemispheres. A shadow zone near the magnetic equatorial plane due to refractory effects of the Io torus is produced.

C.4 Results on the HOM shadow zone

We have performed ray-tracing calculations by using source parameters as described in section C.3. The hollow cone sources are located at L=20 in both hemispheres. Since the Io torus does not lie exactly within the magnetic equatorial plane, the extension of the shadow zone is a slight function of the magnetic longitude (or system III longitude) of the observer. Here, we have used an intermediate value obtained from sources at a magnetic longitude l_{mag} = 90° where the Io torus crosses the magnetic equatorial plane. A comprehensive view of the situation is given in Figure C.2 where we display the evolution of the HOM hollow cones calculated by ray-tracing. For HOM, the Io torus behaves like a divergent lens which prevents the rays from entering low magnetic latitude regions near the planet but, in turn, focusses the radiation near the magnetic equatorial plane farther away from Jupiter.

We analysed this phenomenon in more detail by plotting the extension of the shadow zone (as determined in Figure C.2) projected onto a meridian plane in Figure C.3. Two different wave normal angles are considered, namely θ = 80° (full line) and θ = 70° (dashed dotted line).

Superimposed is displayed the Voyager 1 trajectory for a few rotations around the encounter which took place on March 5, 1200 (DOY 64.5). We selected three different Io torus density models by simple multiplication of the model given by Divine and Garrett (1983) with a constant factor. Figure C.3 enables us to derive the following conclusions. First, the extension of the shadow zone in radial distance is a strong function of the density model because of the small angle of intersection of the shadow boundaries near the magnetic equator, but the dependence on the wave normal angle θ is much smaller, in particular for Figures C.3b and C.3c. Second, the final direction of the rays which form up the shadow zone (nearly identical with the direction of the shadow zone boundaries) is nearly unchanged far from the planet for all density models. Thus, temporal changes in the torus density (or density gradients) should have no dramatic consequence on the emission pattern as observed far from the planet. This, in turn, represents a way to account for the quite stable and repetitive HOM characteristics. Third, the modeled shadow zone can be directly compared with the observations, and we see that the main features of HOM are qualitatively well reproduced in particular the emission dropouts (marked by thick lines) which were observed at distances less than about $20R_J$. Figures C.3a and C.3b best fit the observations with a shadow zone extending to a distance somewhat less than 20 R_J. In addition, Figure C.3b accurately fits the observation inside of 10 R_J for large wave normal angles (θ = 80°) whereas Figure C.3c accounts best for the observations near 15 R_J but completely fails to predict the radial extension of the shadow zone. Therefore, we feel that a somewhat enhanced (by 15 %) torus model as assumed in Figure C.3b represents the overall situation best. This is remarkably good if we know that the modeling of the shadow zone is a joint consequence of the beaming properties, the source locations and the refractive effects of the Io torus.

It is noteworthy that these conclusions can be extended to the higher frequency HOM component. Several tests (not shown) for higher frequencies yield similar results, but the torus density had to be enhanced more substantially. To match the observations at f=1000 kHz, the actual Io torus density model (Divine and Garrett, 1983) must be multiplied by a factor of 2-3. In fact, it suffices to enhance the density only in the inner region of the torus, since the higher frequencies are able to enter deeper in the Io torus. Furthermore, the shadow zone is found to be narrower for the higher frequency range of HOM which also agrees with the observations.

Since Voyager 2 encountered higher densities outside the Io torus than did Voyager 1 (Jones and Leblanc, 1989), the plasma model by Divine and Garrett (obtained from V1 observations) may represent a low limit of the actual torus density. This is further supported by the fact that the broadband kilometric radiation (bKOM) which is most probably produced at the Io torus may by active up to 1 MHz at times (Jones, 1981, 1986; Jones and Leblanc, 1987) suggesting a torus peak density that is enhanced by a factor of three to the present one.

We selected V1 data for a detailed analysis because it approached Jupiter much closer than did V2. However, also the V2 observations (especially on the dayside) also reveal the existence of a shadow zone as found for V1. For f=500 kHz, the shadow zone for V2 extends at least to $20R_J$ in the magnetic equatorial plane, but we are not able to state unambiguously that the shadow zone for V2 is larger than that for V1.

In our analysis, we introduced the torus density model by Divine and Garrett (1983) who used assumptions about the ion temperatures reported by Bagenal and Sullivan (1981). These ion temperatures were revised later on by Bagenal et al. (1985) because of an error made in the earlier analysis. Consequently, the Divine and Garrett model should also be revised. However, by

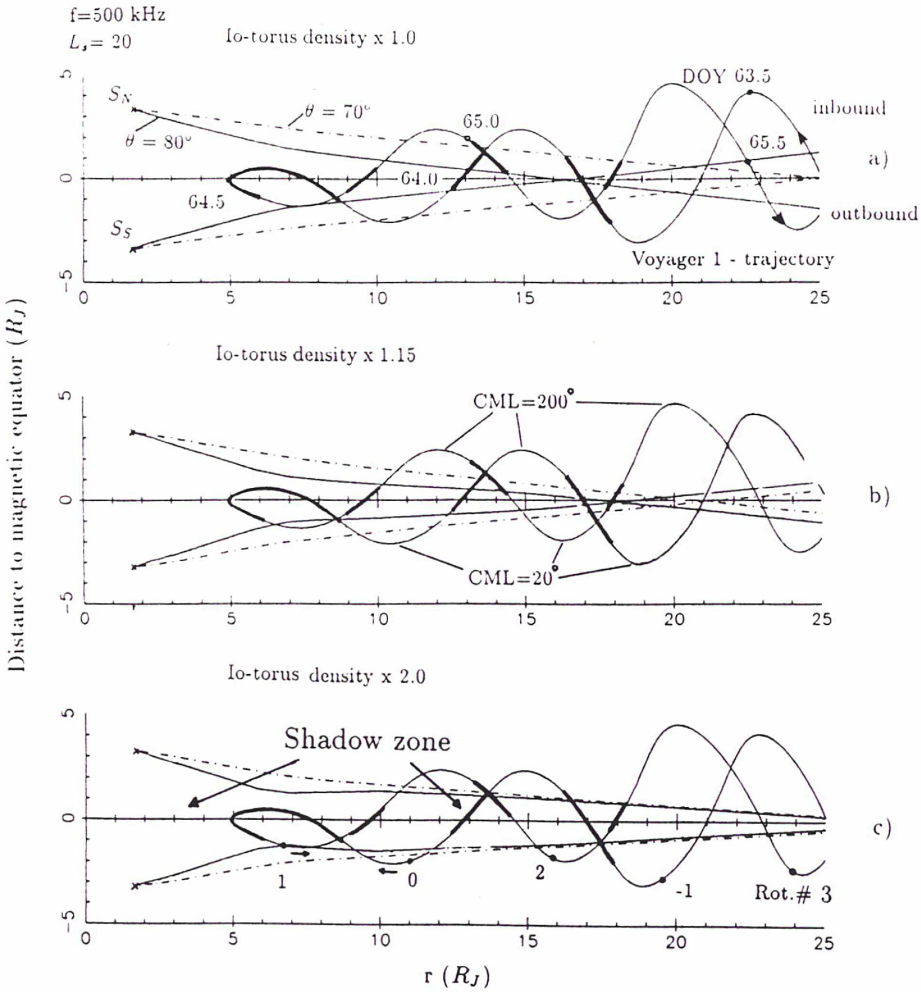

Figure C.3: HOM shadow zones projected onto a meridian plane for $\theta = 70°$ and $\theta = 80°$. Superimposed is the Voyager 1 trajectory during the encounter period. Significant episodes of lowest or no HOM activity are represented by thick lines on the trajectory. (a) Calculation made with the Io torus density model of Divine and Garrett (1983). (b) The same model multiplied by 1.15. (c) The same model multiplied by 2. The numbers indicated on the Voyager trajectory refer to rotation numbers with respect to the encounter.

inspecting the torus electron number densities shown in Figure 11 of Divine and Garrett (1983), we can unambiguously state that it corresponds much closer to the revised density model by Bagenal et al. (1985) (their Figure 1) than to the old model (Figure 12 of Bagenal and Sullivan, 1981). The Divine and Garrett model is therefore the best analytical model available at present time. However, a new Io torus model is in progress (Bagenal, private communication) which is possibly somewhat larger in vertical extension. This new model may therefore improve our fit without assuming a somewhat enhanced torus density.

C.5 Modeling of the HOM-profile

C.5.1 Description of analysis

We now intend to simulate the emission intensity pattern as would have been observed by Voyager 1 when the selected emission characteristics and source locations are entirely accounted for. To simplify the calculation in our model, the originally continuously (in magnetic longitude) distributed sources are replaced by 9 equally spaced subsources in each hemisphere, respectively. These subsources behave identically, having the same power and, of course, the same emission lobes. Each subsource is located on a magnetospheric height where f/f_c=1.02 (f=500 kHz) and consists of an emission cone with an opening angle $\theta = 75°$ and cone half-width $\Delta\theta = 5°$. The conical radiation pattern of a subsource is simulated by initializing the azimuthal angle in steps of 9° around the magnetic field line which defines the cone axis. This procedure is perfomed for $\theta = 70°$, 75°, and 80° in order to determine the outer limits of the emission lobes as well. Thus, 120 rays were launched per subsource. The normalized subsource beam profile is specified by the following function (taken from Gulkis and Carr, 1987, Equation 2 and Figure 5)

$$f(\theta) = \frac{1}{2}(1 + \cos[36 \cdot (\theta - 75)]) \tag{C.1}$$

$$f(\theta) = 0 \qquad [\theta > 80°], [\theta < 70°]$$

adapted for our purpose. $f(\theta)$ is the relative power per unit solid angle radiated in any direction making an angle θ with respect to the positive direction of $\vec{B}$ in the northern hemisphere or to the negative direction of $\vec{B}$ in the southern hemisphere. $f(\theta)$ becomes zero when $36 \cdot (\theta - 75)$ is not in the range [-180., 180.] i.e. for all θ less than 70° and greater than 80° and has a maximum for $\theta = 75°$. The three-dimensional subsource beam pattern is found by rotation of $f(\theta)$ around the source magnetic field line.

Contrary to the study of Gulkis and Carr who elaborated a straight line propagation from the radio source to the spacecraft, we performed a ray-tracing study since the ray paths are considerably altered when passing in the vicinity of the Io-torus. For one given subsource, we traced 120 rays, 40 for each of the three cone half opening angles ($\theta = 70°$, 75°, 80°). For a given θ, the whole emission cone generally appears as a distorted trace when projected onto a sphere surrounding Jupiter at a given distance of observation. If the point of observation lies within the trace calculated for $\theta = 75°$ and one of those calculated for $\theta = 70°$ or $\theta = 80°$, the actual cone half angle of the ray which intersects the point of observation is determined by linear interpolation from the angles θ of the corresponding traces. The interpolated θ is then used for the calculation of $f(\theta)$ via Equation (C.1). If the observer is located outside the region defined by the three traces on the sphere, Equation (C.1) becomes zero. Since the subsources are supposed to radiate independently, the calculated intensity profile for a given point in space consists of the algebraic sum of the contributions of the subsources, corrections being made for the varying spacecraft-subsource distance. For the intensity calculation, we took 9 equally spaced subsources in longitude (40 degrees separation !) at each hemisphere instead of a continuous distribution. To overcome the error which arises from this assumption we calculated the average intensity along 40 degrees in magnetic longitude centered around the

actual point of observation. Furthermore, all effects of focussing and diffraction of radiation are included throughout the determination of the final intensity profile. The assumption of equal activity along the entire radio ring in the auroral zones does not require detailed knowledge concerning the question of whether the sources rotate with the planet or are fixed in local time. In fact, both of these characteristics may account for HOM, but only the local time effect has been thouroughly studied at the present time (Alexander et al., 1981; Paper 1).

C.5.2 Application to the observed latitudinal beaming

To check the validity of our inferred HOM sources and emission parameters, we have modeled the HOM latitudinal beaming, and compared it with the observations of Alexander et al., 1979; and Paper 1. The modeled conical emission pattern that Voyager would have observed during its trip through the Jovian magnetosphere is shown in Figure C.4 for two representative rotations. In the upper panels of Figures C.4a and C.4b are displayed the traces of the HOM emission cones on a sphere surrounding Jupiter at the actual Voyager 1 distance. The Voyager trajectory occurs as a sinusoidal curve when plotted against magnetic latitude. The plot sequence for Rotation # +1 shows the shadow zone which causes the emission gaps when Voyager 1 was very close to the planet. The calculated intensity profile is plotted below and will be compared with the observations in the next section.

Figure C.4b exhibits the situation for Rotation # -6 which is representative for observations far from the planet. The area where the shadow zone is apparent during Rotation # +1 is replaced by a sharply beamed, strong emission in the vicinity of the magnetic equator arising from the superposition of many emission cones. The variation of the beam with respect to the magnetic dipole equator is predominantly due to the slight offset of the Io torus with respect to the magnetic equatorial plane. The close correspondence of our modeled results to those obtained by earlier statistical studies can be demonstrated by comparison of Figure C.4b with Figure 1 (occurrence probability vs. CML for V1 observations) and Figure 6 (sketched plot of HOM beam) of Alexander et al. (1979) and also with Figure 1 of Paper 1. Thus, our model unambiguously accounts for the beaming at hectometer wavelengths.

Assuming that the rays emanating from the northern hemisphere exhibit RH-polarization and those from the southern hemisphere LH-polarization, the HOM beam should show a rather complicated and puzzling polarization behaviour, which is exactly what was observed (see e.g. Alexander et al., 1981). When considering the observations near the encounter (Figure C.1b), RH-polarization is associated with positive magnetic latitudes and LH-polarization with negative magnetic latitudes, and this is predicted as shown in Figure C.4a. However, we note that a polarization reversal often occurred at low frequencies (Figure C.1b). This polarization reversal has not yet been understood.

C.5.3 Comparison with intensity profiles

In Figure C.5 we compare the modeled HOM profile (full line), which is calculated for the parameter set indicated at the top, with the observations displayed in 4 min running averages of total intensity (dashed line). Five representative rotations are displayed, nearly symmetrically placed with respect to the Voyager 1 encounter. In Figures C.5a and C.5e, Rotation # -6

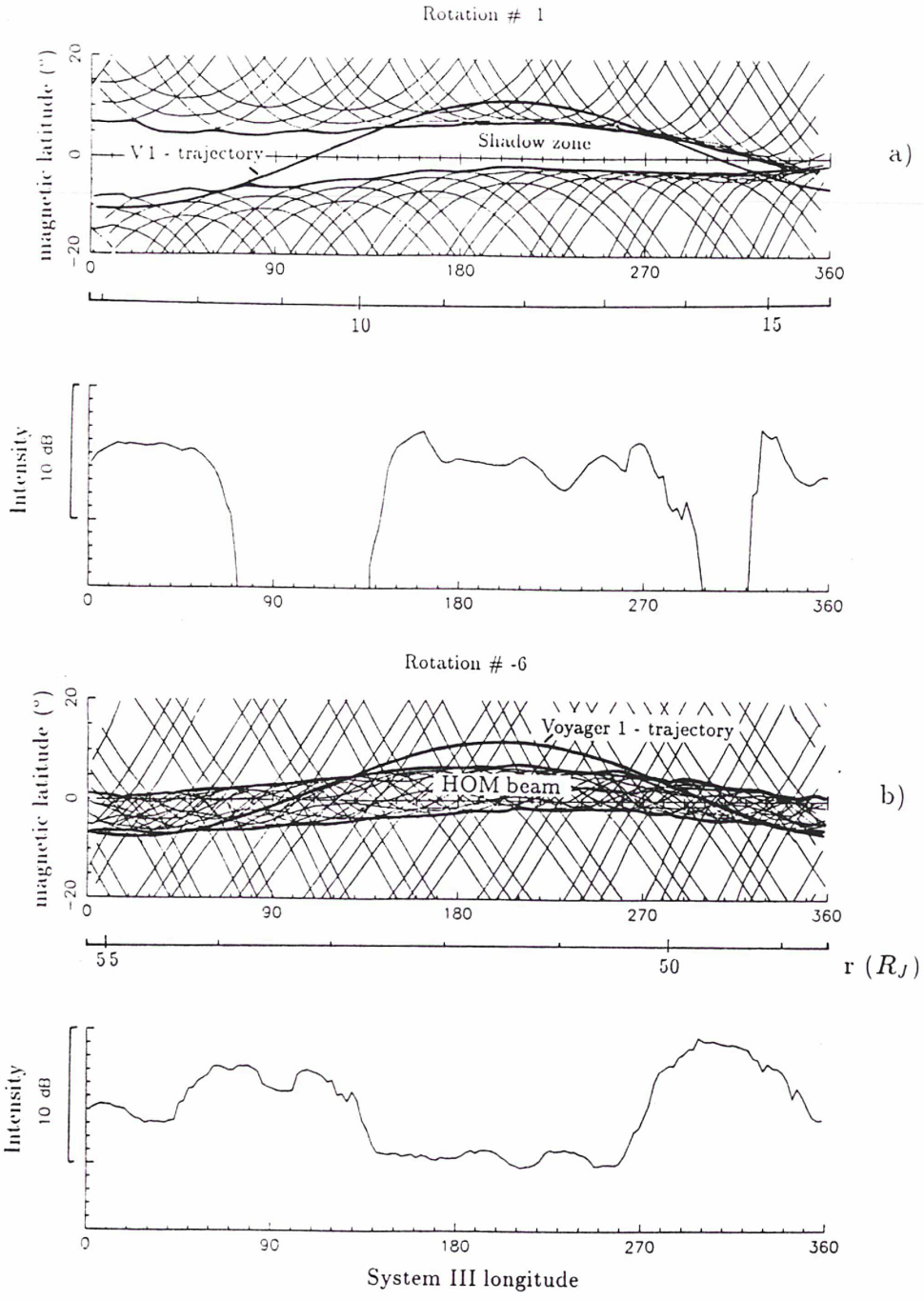

Figure C.4: Modeled HOM emission cones as if they were seen from Voyager 1 along its trajectory (thick lines) and the corresponding intensity profiles. (a) Situation close to Jupiter. The radiation is inhibited to enter low magnetic latitudes because of the Io torus. The shadow zone becomes smaller when the spacecraft-Jupiter distance increases. (b) Situation far from Jupiter. The HOM is now sharply beamed and is confined mainly to low magnetic latitudes.

and Rotation # +5 exhibit similar intensity profiles, which are representative for observations far from Jupiter. The predicted profiles fit the data extremely well by also exhibiting a large emission gap near CML=200°. When the spacecraft came closer to Jupiter, the measured PRA profile changed dramatically (Figure C.5b) and so did the modeled one. The major features are predicted; only the shadow zone around DOY 63.8 is wider than predicted. The observed emission during the encounter rotation (Figure C.5c) is fitted very well by the modeled curve although the predicted emission intensity at the end of the rotation is stronger than the observed one. Notice that the major predicted emission offset (near DOY 64.2) occurs at the correct time. At the closest approach (labeled CA) n+1/2 gyroharmonic waves and upper hybrid resonance emission occurred, associated with Voyager's traversal of the Io torus (Birmingham et al.,1981). The "ghost" feature (labeled G in Figure C.5c) at DOY 64.5 is not interpreted as HOM. Shortly after CA (Figure C.5d), the first observed lack of emission (around DOY 64.8) is accurately predicted. The other lack of emission near DOY 65 occurred about 90 minutes before the modeled one. We notice the symmetric behaviour of the radiation pattern with respect to the encounter by comparing Rotations # -1 and # +1. Because of the high temporal variability of HOM mainly due to external control, the profiles are normalized for each rotation separately. This is justified by the fact that our model can, of course, only simulate stationary emission. Although the overall simulation is far from being perfect (we do not expect otherwise, because of the simplifications made in our assumptions) the major structures are explained very well, suggesting that the modulation of HOM can be associated with a source located at high latitude auroral zones.

The results in Figures C.3, C.4 and C.5 were calculated for a set of parameters f/f_c, θ, $\Delta\theta$, the torus density model $\rho(\vec{r})$, and the value L of the source locations. The first three parameters were selected to be in agreement with the cyclotron maser mechanism which is now the most promising theory for radio emission. The Io torus density model was determined by in situ observations, but it is an average model, and it suffers (very likely) temporal fluctuations. Therefore, we have verified how that parameter may influence the results. The only free parameter is the L shell of the source field lines. In Paper 2 we have shown, that $15 < L < 30$ accounts for the observations for nearly perpendicular θ. On the contrary, as found in Paper 2, for sources at lower magnetic latitudes (e.g. L=10) the observations could no more be fitted for nearly perpendicular θ. Thus, when maintaining large wave normal angles (consistent with the CMI) the accurate fits in Figures C.4 and C.5 would vanish. Here we have used L=20 and shown that the modeled emission is in agreement with the observations for a fully three-dimensional investigation as well. The fact that HOM may be visible at all system III longitudes when the viewing geometry is favourable strongly suggests that HOM is active over a wide range of longitudes. The inferred parameter set may therefore be considered as highly relevant in association with the Jovian hectometric radiation.

C.6 Summary and Conclusion

We have performed a fully three-dimensional ray-tracing study to model the Jovian hectometric radiation. The source locations are assumed to lie along magnetic field lines with L=20 as determined by Ladreiter and Leblanc (1990a). We have demonstrated that cyclotron resonant X-mode sources distributed in a large range of longitudes in both Jovian hemispheres

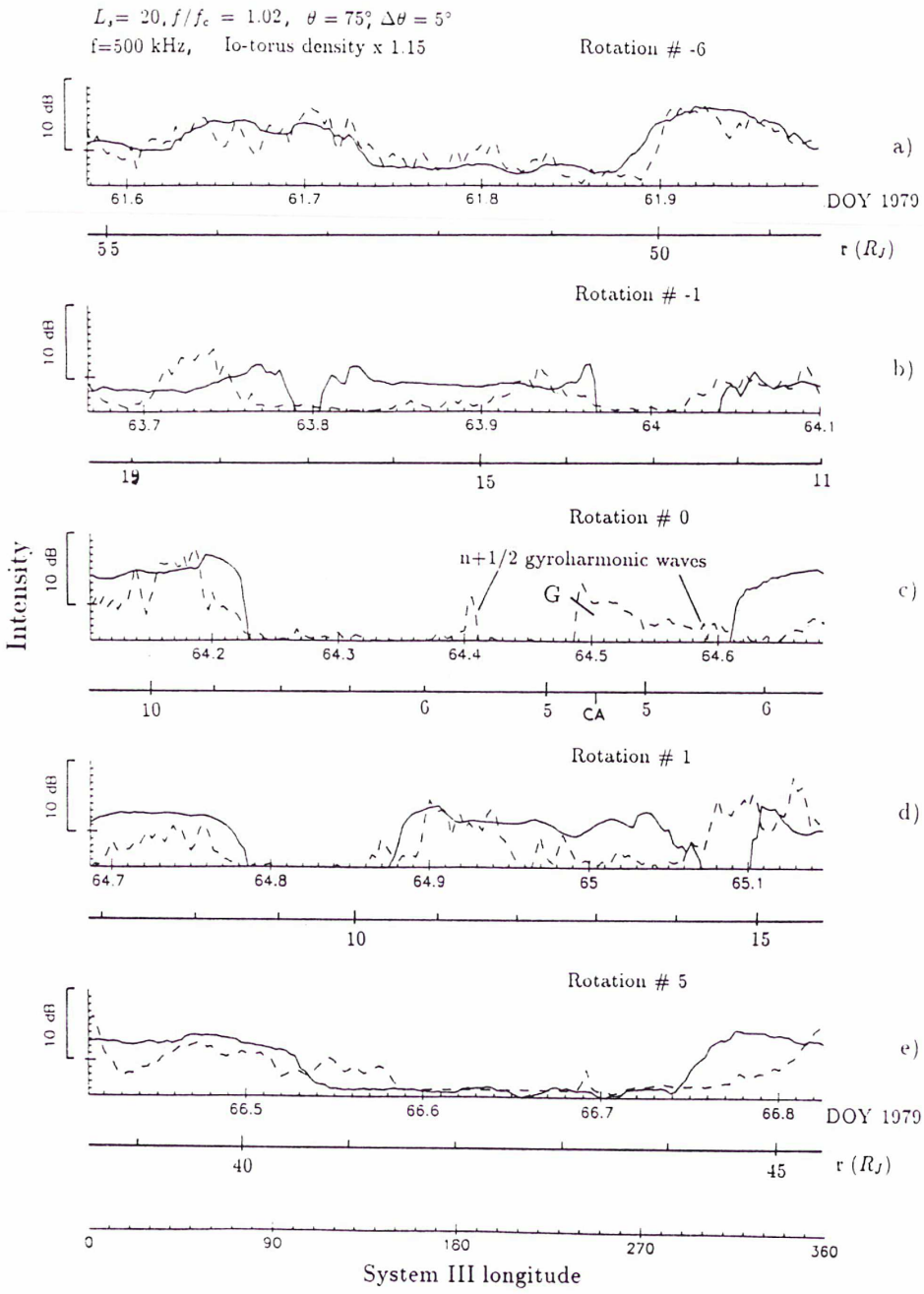

Figure C.5: Predicted (full line) and observed (dashed line) PRA profiles during some representative Jovian rotations including the V1 closest approach (CA). The total intensity has been smoothed by 4 min running averages. Negative rotation numbers refer to preencounter periods. For each rotation, the intensities are normalized separately. The selected parameter set is indicated at the top. (a) and (e): Rotations #-6 and #+5 represent observations as typically seen at large distances from Jupiter. Note the emission gap centered about CML=200°. (b) and (d): Rotations #-1 and #+1 display observations in the vicinity of the planet. Note the HOM activity around CML=200°. (c): Rotation # 0 (encounter); the "ghost" feature (labeled G) is not interpreted as HOM.

can account for the major characteristics of the HOM radiation. In particular, our modeling reveals the existence of a shadow zone at the magnetic equatorial plane extending to about 20 R_J which was actually observed by V1 and V2. We have been able to simulate the strong HOM latitudinal beaming which was observed at large radial distances from the planet as well as the complex polarization within the HOM beam arising from the mixing of the contributions from both hemispheres. For hectometric wavelengths, the Io torus behaves like a divergent lens which prevents the rays from penetrating into low magnetic regimes near the planet but, in turn, focusses the radiation near the magnetic equatorial plane far from Jupiter. Additionally, the comparison between the predicted and observed intensity profiles exhibits a remarkable agreement when bearing in mind that the calculated curves depend on the source locations, emission characteristics, and the Io torus density model. However, to better fit the HOM observations, a somewhat enhanced density model is needed, in agreement with Jones (1981) who modeled the Jovian kilometric radiation.

The ray-tracing calculations were thoroughly performed for f=500 kHz. However, we also tested the situation for higher frequency HOM. It is found that the shadow zone narrows for the higher frequency components and that an increase of the Io torus peak density by a factor of 2-3 is required to fully account for f=1000 kHz also. We have considered in detail V1 observations because it approached Jupiter much closer than did V2. However, we verified that our modeled HOM pattern is also in agreement with V2 observations. In this study we have taken into account radial and longitudinal effects of the HOM observations. The effects when varying the HOM source locations in magnetic latitude have already been discussed in Paper 2.

To consider only the cruise portion of one single spacecraft is not sufficient for the derivation of significant results. The quite stable and repetitive pattern of HOM, well defined in system III longitude when observed at large distances from Jupiter might lead to the assumption of a source confined to a small range of longitudes (Ortega-Molina and Lecacheux, 1990b) which, in turn, hardly accounts for the phenomena observed near closest approach nor for the HOM beaming.

The main result of this study is that the HOM source locations are along open magnetic field lines with foot prints at the auroral ovals, confined within a wide range of longitudes and located in both hemispheres. In this context, the solar wind control on HOM can be simply understood.

During the modeling of the HOM emission pattern, we pointed out that the sharp HOM beaming is the consequence of the focussing of the radiation near the magnetic equatorial plane due to the refractory effects of the Io torus. However, without this focussing, the HOM intensity as seen by the spacecraft would have been lower than actually observed. Since this focussing effect is supposed to be strong for emission in the HOM frequency range, the spectral peak of HOM might be produced artifically. This, in turn, implies that HOM is most probably the low-frequency extension of the non-Io DAM as already suggested by Genova et al. (1987), but HOM is possibly active in a wider range of longitudes. Future spacecraft missions such as Galileo and Ulysses will provide the opportunity to collect further data leading to a deeper study of yet unresolved details concerning the hectometric radiation.

Appendix D

The Cyclotron Maser Instability - Application to low density magnetoplasmas

Abstract

Considering the Cyclotron Maser Instability (Wu and Lee, 1979) within low density magnetoplasmas ($f_p/f_c < 0.01$) we derive simple expressions relating the wave emergent angle θ and the ratio f/f_c at the source to the normalized (to c) parallel bulk velocity $\beta_{||o}$ of the instability (characteristic for an electron distribution function) via the equations $\cos(\theta) = \beta_{||o}$ and $f/f_c = (1 - \beta_{||o}^2)^{-1/2}$. During this investigation we considered the loss cone and holelike instability to be responsible for amplification. Both of these regions exhibit a relatively small perpendicular energy. We found that for $\beta_{||o}$ corresponding to 1-10 keV, θ is found to be nearly perpendicular with respect to the magnetic field and is decreasing when $\beta_{||o}$ increases. The wave frequency is slightly above the gyrofrequency, but is substantially away from the R-X cutoff; thus, the refractive index is near unity at the radio source. No strong refraction along the ray path is therefore expected for $f_p/f_c << 1$. The results are highly relevant for the lower frequency auroral emissions of Jupiter (low frequency DAM and HOM) and of Saturn (lower frequency SKR) where very low density magnetoplasmas ($f_p/f_c < 0.01$) do in fact exist at the respective source regions.

D.1 Introduction

Among the theories proposed to explain the generation mechanism of the auroral kilometric radiation (AKR) and its analogies at Jupiter (DAM, HOM) and at Saturn (SKR), the Cyclotron Maser Instability (CMI) (Wu and Lee, 1979) agrees best with wave and particle observations in the source region of AKR. Since this pioneer work, many investigators picked up this topic and performed improvements on this theory. Shortly speaking, the CMI theory demonstrates that weakly relativistic electrons which are precipitating along auroral field lines are able to amplify in particular electromagnetic R-X mode waves near the R-X cutoff frequency via the

cyclotron maser mechanism. Wu and Lee (1979) derived the growth rate of the wave in terms of the imaginary part of the angular frequency ω_i of the wave. They assume that the background electrons of ionospheric origin (relatively cold electrons) are responsible for the propagation of the wave, and that the unstable energetic electrons, which are anticipated to form a loss cone feature in the distribution function, are responsible solely for the amplification. During this investigation, they additionally found that R-X waves are favoured over L-O waves. Later on, Wong et al. (1982) and Wu et al. (1982) solved the dispersion relation with the inclusion of the effects of the hot electrons. They pointed out that the angular dependence with respect to the magnetic field of the most amplified wave is a strong function of the ratio f_p/f_c (denoting the electron plasma and cyclotron frequency, respectively) and of the ratio n_e/n_b, n_e being the density of the energetic electrons and n_b that of the background (cold) electrons. One of their main conclusions was that, if the source of AKR shows a density cavity for cold electrons which is confirmed by recent satellite measurements (Louarn et al., 1990) due to a strong parallel electric field, the possibility of amplification is restricted to waves lying in a relatively small range of θ near $\pi/2$ provided that f_p/f_c is low (in the order of 0.005). Moreover, the R-X cutoff frequency is then situated slightly below the electron gyrofrequency which is in strong contrast to the cold plasma dispersion relation. Dusenbery and Lyons (1982) studied the relativistic resonance condition and found that the interaction length between the amplified waves and the resonant particles is very small and they provided evidence that also the "hole" region which represents an instability excited by downgoing electrons may give rise for amplification of initially downward propagating waves. This fact was approved by Le Queau et al. (1984a,b) who performed a fully analytical treatment of the CMI. They concluded that initial upward propagating waves (destabilized by the loss cone feature) would be heavily damped when penetrating through regions of decreasing magnetic field magnitude. Contrary, initially downgoing waves could be amplified nearly until they are reflected as a consequence of the increasing magnetic field to finally travel upwards and escape into free space.

In recent years, researchers started to treat the CMI in an inhomogenious medium. Omidi and Gurnett (1984) performed ray-tracing in a medium with varying magnetic field magnitude. They concluded that the electron distribution function as measured by the S3-3 satellite is not able to produce AKR in the requested intensity. By steepening the slopes of the loss cone instability region in the distribution function they could easily compose the observed wave amplitudes. This work is very comprehensive since it shows that initially high amplification may be quenched or even compensated by heavy damping that the waves suffer throughout the further propagation in free space. During their investigation they showed evidence that it is the loss cone feature which is most likely the unstable region in the electron distribution, but did not refuse the possibility of amplification of downgoing waves by the holelike feature. Le Queau et al. (1985) developed an analytical inhomogeneous treatment of the CMI and obtained expressions for the wave emergence angle θ as a function of $\epsilon = (f_p/f_c)^2$ and gave a maximum value ϵ_c above which no amplification is possible. A similar inhomogeneous treatment of the CMI lead Zarka et al. (1986) to derive the spectrum of terrestrial kilometric radiation and Galopeau et al. (1989) that of the Saturnian kilometric radiation.

Strangeway (1985) and Pritchett and Strangeway (1985) thoroughly studied the effect of hot electrons on the dispersion relation and discovered significant changes compared to the cold plasma theory. Similar to Wong et al. (1982), Pritchett and Strangeway (1985) acquired the highest net gain for waves with nearly perpendicular emergence angle θ at the source in case

of AKR. They treated the CMI only as a local phenomenon so it cannot be decided from their investigations, whether or not the amplified wave suffers damping when traveling away from the source.

Although a large amount of publications on the CMI theory has been performed, a comprehensive study is required to link the solutions of the whole dispersion relation to an inhomogeneous treatment of the theory. A major step in this regard was done by Pritchett and Winglee (1989) who performed two dimensional particle simulation in an auroral arc and determined the overall growth via three dimensional ray-tracing. They obtained the observed wave amplitudes within a distance of wave particle interaction in the order of the dimensions of an auroral arc.

Furthermore, no general consensus has been reached about the unstable feature in the electron distribution function which is most likely responsible for the generation of planetary radio emissions. Recently, Louarn et al. (1990) put evidence that also the region of "trapped electrons" (appearing at the $v_\perp$-axis) in the distribution function may provide free energy for the amplification of waves, thus enhances the number of unstable regions (loss cone, holelike region, trapped electrons) which compete for providing the largest amount of free energy.

This paper does not aim to settle the controversy of the preferred instability region. Instead the purpose is a treatment of the CMI in a very low density magnetoplasma where $f_p/f_c < 0.01$. Most of the papers dealing with the CMI so far considered $f_p/f_c \geq 0.01$ to be applicable to the terrestrial auroral radio emissions. Our study concerns the sources of the lower frequency radio emissions from Jupiter (DAM low frequencies, HOM) and Saturn (SKR lower frequencies) which are supposed to be located in regions where $f_p/f_c < 0.01$. We derive simple expressions relating the normalized (to the light velocity c) parallel bulk velocity $\beta_{\|o}$ of a given electron distribution function to the frequency f of the most amplified wave (in terms of f_c) and to the emergence angle θ when the radio source is located in a low density magnetoplasma. To achieve this, we first recall a typical electron distribution function to see the characteristics of the regions of free energy which are necessary for wave amplification (section D.2). We discuss the relativistic resonance condition to derive the waves $(\vec{k}, f)$ for which the resonant contours are largely embodied in an assumed loss cone instability for a given f_c and f_p. Similar studies were presented by Dusenbery and Lyons (1982) and applied to the conditions in the earth's aurora. We shall see that for a given θ there are several possiblities for amplification depending upon the values f_p and f_c in the source region. Further, it will be demonstrated, that an homogeneous treatment leads to strong overestimations of the growth (section D.3). Nevertheless for a plasma with $f_p/f_c < 0.01$ we derive a very simple criterion which leads to an expression of the quantities θ and f/f_c at the source in terms of the parallel bulk velocity $\beta_{\|o}$. We discuss our results within the context of the findings already established for the Jovian and Saturnian radio emissions (section D.4).

D.2 Derivation of the relativistic resonance condition

D.2.1 Properties of the electron distribution function

Before starting to discuss the conditions for wave resonance with energetic particles at the source region, let us study a typical electron distribution function $F(v)$ as measured by the S3-3 satellite (Croley et al., 1978). Three unstable features with positive $\partial F(v)/\partial v_\perp$ are visible

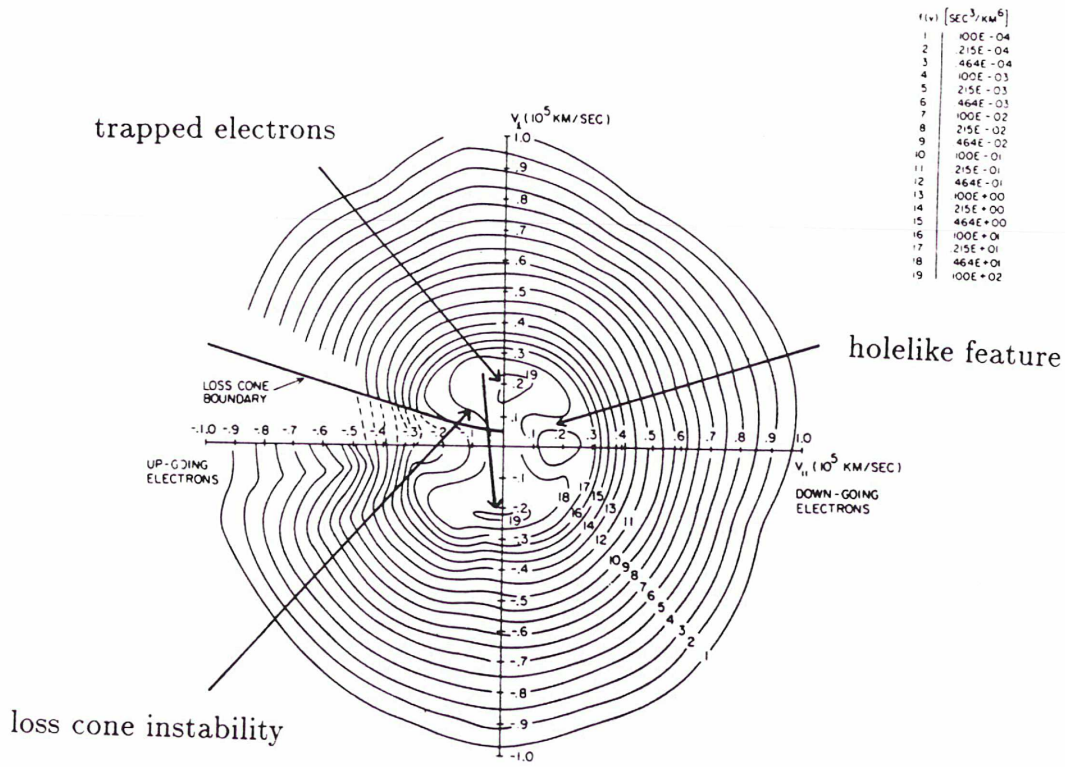

Figure D.1: Typical electron distribution function taken by the S3-3 satellite in the auroral region of the earth. Three types of instabilities are present in the distribution specified by arrows: 1) loss cone region (upward side), 2) holelike feature (downward side), 3) trapped electrons (near $v_\perp$-axis).

in Figure D.1; Firstly, the loss cone region associated with the upward side of the distribution function (ascending electrons), secondly, the accelerated downgoing electrons (forming a holelike feature), and thirdly, the trapped electrons near the $v_\perp$-axis. The latter are suggested to be trapped throughout a time-varying (or space-varying) parallel electric field (Louarn et al., 1990) between their magnetic mirror point above the ionosphere and a second mirror point due to the parallel electric field along auroral field lines. The corresponding electric potential has been reported to be about 3 kV over a distance of several earth radii (Croley et al., 1978). Although a common conclusion has not yet been drawn, it is generally accepted that AKR is likely to be excited by the two former instabilities, the loss cone and/or holelike region. These two regions are characterized by a relatively small $\beta_{\perp o}$ which leads to some simplification when studying the resonance condition.

D.2.2 Dispersion relation and growth rate

Under several conditions ($\theta \approx 90°$, n (refractive index) ≈ 1, $f \approx f_c$, $f_p << f_c$, the dispersion relation $\Lambda(w, \vec{k})$ can be significantly simplified (Wu and Lee, 1985)

$$\Lambda(w,\vec{k}) = 1 - \frac{c^2k^2}{\omega^2} + \frac{\omega_p^2}{\omega^2}\int d^3v \left(\omega_c\frac{\partial F}{\partial v_\perp} + k_{||}v_\perp\frac{\partial F}{\partial v_{||}}\right)\frac{v_\perp J_1'^2(k_\perp v_\perp/\omega_c)}{(\omega - \omega_c/\Gamma - k_{||}v_{||})} = 0 \qquad \text{(D.1)}$$

where $\omega = 2\pi f$, $k_{||}, k_\perp$ are the components of the wave vector parallel/perpendicular with respect to the magnetic field $\vec{B}$, F denotes the electron distribution function in the velocity space $(v_{||}, v_\perp)$, J_1 is the Bessel function, and $\Gamma = 1/\sqrt{1 - v^2/c^2} = 1/\sqrt{1-\beta^2}$.

It is further assumed that the cold (ionospheric) electrons support solely the wave propagation, whereas the hot precipitating electrons forming the instabilities in the distribution function are only responsible for the amplification of the wave.

The growth rate for the CMI is expressed in terms of the imaginary part ω_i of the angular frequency $\omega = \omega_r + i\omega_i$. An approximate formula for the R-X mode wave is given by Wu (1985):

$$\omega_i = \frac{\pi^2\omega_p^2}{4\omega}\int_{-\infty}^{+\infty} dv_{||}\int_0^\infty dv_\perp v_\perp^2\,\delta[\omega - \omega_c/\Gamma - k_{||}v_{||}]\omega_c\frac{\partial F}{\partial v_\perp} \qquad \text{(D.2)}$$

By deriving Equation (D.2), it is further assumed that $\omega \approx \omega_r$, and the argument of the Bessel function J_1' in Equation (D.1) is small leading to $J_1'^2 = 1/4$ and, moreover, the term associated with $\partial F/\partial v_{||}$ can be neglected compared with the term $\partial F/\partial v_\perp$ because of

$$k_{||}v_\perp\frac{\partial F}{\partial v_{||}} << \omega_c\frac{\partial F}{\partial v_\perp} \qquad \text{(D.3)}$$

when $n \approx 1$ and $\partial F/\partial v_{||} \approx \partial F/\partial v_\perp$

Although some of the assumptions made for the derivation of the dispersion relation and the growth rate are very questionable after the recent Viking measurements in the AKR source region (Louarn et al., 1990), it is sufficient for our purpose because our aim in particular is the discussion of the resonance condition occurring in the denominator of Equation (D.1) and as argument of the δ function in Equation (D.2). More accurate formulae for Equations (D.1) and D.2, in particular the introduction of the hot electrons for the wave's propagation are given by Wong et al. (1982).

D.2.3 Resonance condition

By inspection of Equation (D.2), we see that a necessary condition for wave growth ($\omega_i > 0$) is the existence of an inversion of population $\partial F/\partial v_\perp > 0$ in velocity space along regions where the argument of the δ-function is 0. In other words we have to study the quantity $\partial F/\partial v_\perp$ along the resonance contour in velocity space defined by

$$\omega - \omega_c/\Gamma - k_{||}v_{||} = 0 \qquad \text{(D.4)}$$

For a given wave $(\vec{k}, f)$ this resonance contour can be found in the velocity space by solving the cold plasma dispersion relation (Budden, 1961; Stix, 1962). For the fast extraordinary (R-X) mode these contours are ellipses entirely placed at either the upward or downward side of the

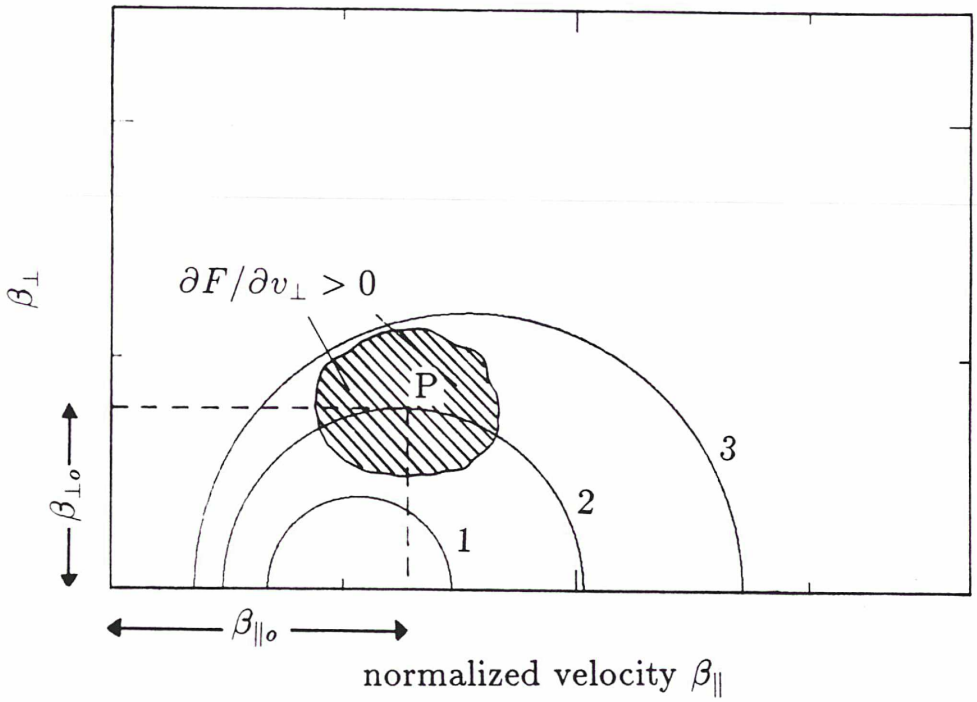

Figure D.2: Extension of an instability ($\partial F/\partial v_\perp > 0$, dashed area) in the velocity space. Ellipses 1 and 3 are not intersecting this unstable region along their curves, which leads to damping of the corresponding waves. Ellipse 2 encounters also the unstable area, and the corresponding wave may be amplified; the net gain depends on the balance of growth and damping along the ellipse (Equation D.2). Note that the growth can be optimized when d (Equation D.6) equals $\beta_{\|o}$ (Le Queau et al., 1985). P denotes the point where $\partial F/\partial v_\perp = max$, with the coordinates $\beta_{\|o}$, $\beta_{\perp o}$.

distribution function (Dusenbery and Lyons, 1982). This is visualized in Equation (D.4) where ω must be greater than ω_c/Γ because the R-X cutoff frequency f_{RX} is always higher than f_c. This can only be achieved when $k_\| v_\| > 0$, therefore it is requested that $k_\|$ and $v_\|$ point in the same direction. Upgoing waves can therefore only be amplified by ascending electrons and downward propagating waves only by descending electrons.

A qualitative estimation of the growth can be acquired by studying the location of the resonant ellipse for a given wave $(\vec{k}, f)$ with respect to the instabilities in the distribution function. An example is sketched in Figure D.2 (adapted from Le Queau et al., 1985). The hatched region denotes $\partial F/\partial v_\perp > 0$. The innermost and outermost ellipses are not crossing this unstable area and the corresponding waves therefore do not give rise for amplification. The ellipse in the middle is largely embodied in the unstable region and may lead to amplification. The net gain depends on the balance of growth and damping when integrating along the resonant contour (Equation D.2). The growth is optimized when the distance d of the ellipse from the origin of the velocity space equals $\beta_{\|o}$ (Le Queau et al., 1985).

D.2.4 Resonant ellipses in velocity space

Using the resonance condition (Equation D.4) and the cold plasma dispersion relation $\Lambda_c(\omega, \vec{k})$ (e.g. Budden, 1961) the coordinates of the center d, the semimajor axis b, and semiminor axis a of the ellipse can be calculated for a given θ and for plasma parameters f_p/f_c, f/f_c (Dusenbery and Lyons, 1982).

$$\frac{(\beta_{||} - d)^2}{a^2} + \frac{\beta_\perp}{b^2} = 1 \tag{D.5}$$

$$d = \frac{h_{||} f/f_c}{1 + h_{||}^2} \tag{D.6}$$

$$a = \frac{1 + h_{||}^2 - f^2/f_c^2}{(1 + h_{||}^2)^2} \tag{D.7}$$

$$b = a(1 + h_{||}^2) \tag{D.8}$$

where $h_{||} = k_{||}c/\omega_c$, $k_{||} = k_{||}(f_p/f_c, f/f_c, \theta)$ via $\Lambda_c(\omega, \vec{k})$,

$\beta_{||}$, $\beta_\perp$, a, b, d in units of the velocity of light c.

From Equations (D.7) and (D.8) it can easily be seen that the ellipses are elongated in the $\beta_\perp$-direction ($b > a$). For θ nearly perpendicular ($h_{||} << 1$) the ellipses are well approximated by circles $a \approx b$.

Now let us systematically study the resonant contours for any arbitrary wave $(\vec{k}, f)$ in a given plasma (f_p, f_c) to see which waves are adapted for growth in a given instability (characterized by $\beta_{||o}, \beta_{\perp o}$). The findings can be visualized in a f/f_c-f_p/f_c diagram (Figure D.3). For a given θ, we can distinguish three areas in the diagram; first the region above the curve $f = f_{RX}$ where no propagation is possible ($f < f_{RX}$), second, the region outside the curve labeled S_θ and within the curve $f = f_{RX}$ where no resonant ellipses can be found for the respective value of θ. The third region lies within the S_θ-contour. In this space which we call the resonant space, resonant ellipses exist and it depends on the electron distribution function, whether they encounter a space with $\partial F/\partial v_\perp > 0$ or not. The curve S_θ encircling the resonance space represents the so-called separatrix (Le Queau et al., 1985) where the resonant ellipses shrink to a point. The index θ denotes that its position in Figure D.3 is only a function of θ.

To thoroughly study the properties of the resonant ellipses we have plotted in Figure D.4 the quantities d and b (a is not shown because very similar to b) against f/f_c and f_p/f_c for $\theta = 70°$ and 80°, respectively. Despite the different scaling, no obvious difference is visible concerning the shapes in Figure D.4 when comparing $\theta = 70°$ and $\theta = 80°$. We clearly see the separatrices $S_{\theta=70}$ and $S_{\theta=80}$ (Figures D.4a, D.4b) where b, a are 0. They correspond of course to the respective separatrices in Figure D.3. We note that b expands very dramatically when studying points slightly inside the separatrix. This means that ellipses with small radii are restricted to regions very close to the separatrix except for $\theta \leq 90°$ which exhibits small ellipses anywhere in the resonant region (not shown). The larger the value $\beta_{\perp o}$ in the distribution function, the farther

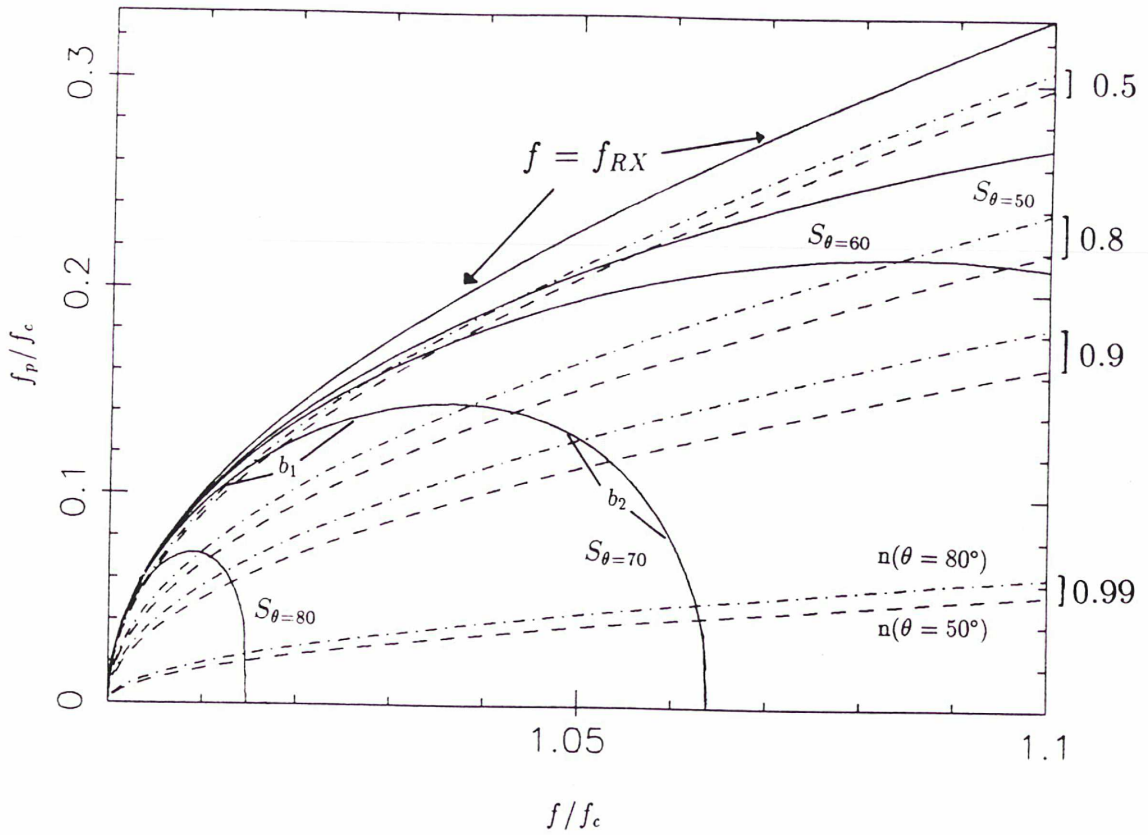

Figure D.3: Resonant ellipses in the f/f_c - f_p/f_c space for given wave normal angles θ. The areas where ellipses exist are enclosed by the respective separatrices S_θ on which the ellipses shrink to a point. Additionally shown are refractive index isocontours for $\theta = 50°$ and $80°$, respectively.

away from the separatrix we find conditions for which the resonant contours lie favourably within the space of instability. In general, a large $\beta_{\perp o}$ is needed to have conditions located considerably away from the separatrix. If therefore $\beta_{\perp o}$ is not too large, the location of the separatrix S_θ itself is a good approximation for plasma parameters f_p, f_c, f/f_c to be adapted for amplification of waves with emergence angle θ. Assuming a ratio f_p/f_c for a given θ there exist in general two small ranges of values f/f_c situated slightly inside the separatrix for which small resonant ellipses are possible. We will come back again to this fact later on.

Concerning the distance d (Figures D.4c, D.4d) this value is almost constant for the upper limit of f/f_c within the separatrix and very sharply tends to 0 when approaching $f/f_c \to 0$ near the separatrix. There, d is furthermore a strong function of f_p/f_c.

D.2.5 Adaption of resonant contours to the electron distribution function

Studying the particle distribution function measured by the S3-3 satellite we could see that resonant contours with a rather small extension are required to be largely embodied either in the loss cone or in the holelike instability. By inspection of Figure D.4 it was derived that such contours are associated with f_p/f_c, f/f_c lying closely to, but inside the separatrix for a given θ.

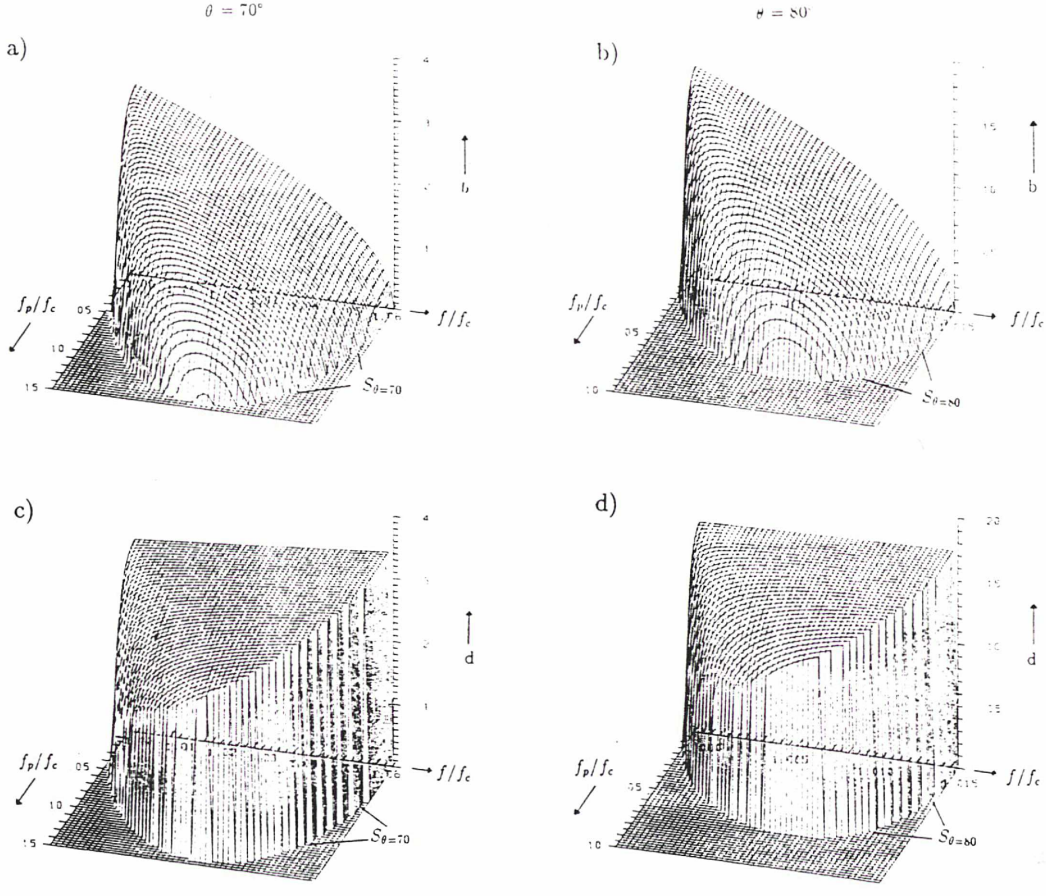

Figure D.4: Semimajor axis b and d (distance of the center of the ellipse from origin in velocity space) for values f/f_c and f_p/f_c inside the separatrix. Note the change in scaling for $\theta = 80°$.

In the limit, when setting $a, b = 0$, we obtain from Equation (D.7).

$h_{||}^2 = (f/f_c)^2 - 1$

using $h_{||} = k_{||}c/\omega_c = n_{||}\omega/\omega_c = n\cos\theta \cdot f/f_c$

$$n\cos\theta = \frac{\sqrt{f^2/f_c^2 - 1}}{f/f_c}$$

replacing $h_{||}^2$ by $(f/f_c)^2 - 1$ in Equation (D.6)

$$d = \frac{\sqrt{f^2/f_c^2 - 1}}{f/f_c} \tag{D.9}$$

which finally leads to

$$n\cos\theta = d = \beta_{||o} \tag{D.10}$$

$d = \beta_{\|o}$ was derived by Le Queau et al. (1985) in order to optimize the growth (see Figure D.2). In fact, the largest part of the resonant ellipse intersects the unstable region provided that d (distance of the center of the ellipse to the origin in the velocity space) and the parallel bulk velocity of the instability are equal.

Using $d = \beta_{\|o}$ one obtains by inversion of Equation (D.9)

$$f/f_c = \frac{1}{\sqrt{1 - \beta_{\|o}^2}} \tag{D.11}$$

Provided that $\beta_{\perp o}$ is small, Equation (D.11) relates $\beta_{\|o}$ to f/f_c, so that the Doppler shifted frequency of the amplified wave is a function of the parallel energy of the unstable electrons. Further, the product of the refractive index and the cosine of the wave normal angle is equal to the parallel bulk velocity (Equation D.10). Thus, the angle θ cannot yet be determined from $\beta_{\|o}$. To solve this problem, we will perform an investigation in section D.3 in order to determine for which n the largest growth is expected, when keeping θ constant.

To give a short review of the findings in this section, we analyzed the resonant ellipses for waves $(\vec{k}, f)$ in a plasma with given f_p, f_c. It is found that for a given θ, the possibility of existence of resonant contours is restricted to a region enclosed by S_θ. When θ decreases, the corresponding S_θ expands to higher values of f/f_p and f_c/f_p. Out of S_θ there exist either no electrons which can resonate with the wave or wave propagation is inhibited because $f < f_{RX}$.

For plasma parameters lying within the separatrix S_θ, we have studied the properties of the resonant contours for varying f_p/f_c and f/f_c. The result is that ellipses with small extensions which are required for waves to be possibly amplified via the loss cone or the holelike feature, are produced for plasma conditions which are confined along the separatrix S_θ and slightly inside of it. Allowing for these conditions, Equations (D.10) and (D.11) could be determined. Equation (D.11) already relates $\beta_{\|o}$ to f/f_c and is independent from f_p/f_c, n and θ. Equation (D.10) requires further analysis to derive θ soley from $\beta_{\|o}$ which is the purpose of the next section.

D.3 Amplification of the radiation

D.3.1 The exponential gain factor

In section D.2 we used an approximate expression for the growth ω_i (Equation D.2). Omidi and Gurnett (1984) demonstrated that it is not sufficient to calculate the growth only at the source region because subsequent damping along the further ray path may occur and quench or even overcome the initial growth. To see whether or not there remains a net gain, one must calculate the exponential gain factor g (Omidi and Gurnett, 1984)

$$g = \int_{l1}^{l2} \frac{\omega_i(l)}{v_g(l)} dl \tag{D.12}$$

where v_g denotes the group velocity.

To obtain a large net gain it is not only necessary to have a positive value of ω_i along the ray path dl, but also to have small group velocities to maintain the amplification process for a

longer time. A detailed calculation of the gain factor within the measured S3-3 satellite electron distribution has already been performed by Omidi and Gurnett (1984).

In this paper we will focus our attention on the calculation of Equation (D.12) in an idealized distribution function which exhibits a loss cone instability. We intend to calculate the expected growth for waves with a constant θ for all possible values f_p/f_c inside S_θ. From this analysis we expect to derive the value of n for which a wave with given θ is most probably amplified.

When the used distribution function is not precisely specified, there is no way to calculate ω_i via Equation (D.2). Therefore several constraints have to be made to calculate g via Equation (D.12). They are listed in the following and should kept in mind to avoid misinterpretations when evaluating the degree of validity of the obtained results.

1. The cold plasma governs the wave propagation along the ray path $l_1 - l_2$
2. Existence of a magnetic dipole field with $\vec{\nabla}B \| \vec{B}$. The direction of $\vec{B}$ is kept constant along ray path. This is a good approximation near the magnetic polar regions.
3. No refraction of the propagating wave
4. $f_p/f_c = constant$ along ray path near the source
5. The instability ($\partial F/\partial v_\perp > 0$) is caused by a loss cone superposed by a parallel electric field
6. No wave absorption after phase of amplification
7. ω_i is taken to be constant when the corresponding resonant ellipse is lying within the space of instability
8. l_1 is the point where the resonant ellipse of the corresponding wave enters the unstable region and l_2 is the point where the semimajor axis b exceeds that region (Figure D.5, ellipses 1 and 2).

D.3.2 The loss cone instability

Before calculating Equation (D.12) it is necessary to specify the loss cone feature in the modeled distribution function. Persson (1966) showed that in the presence of a parallel electric field, the loss cone boundary is given by the hyperbola

$$v_\parallel^2 - \left(\frac{B_m}{B} - 1\right) v_\perp^2 + \frac{2e}{m}(V_m - V) = 0 \tag{D.13}$$

B_m and B are the magnetic flux densities at the mirror point and at the observation point, V_m and V are the magnetic potentials at the mirror point and at the point of observation, m denotes the electron mass and e the unit charge. An absence of the electric potential reduces Equation (D.13) to

$$\frac{v_\parallel^2}{v_\perp^2} = \frac{1}{\tan^2 \alpha} = \frac{B_m}{B} - 1 \tag{D.14}$$

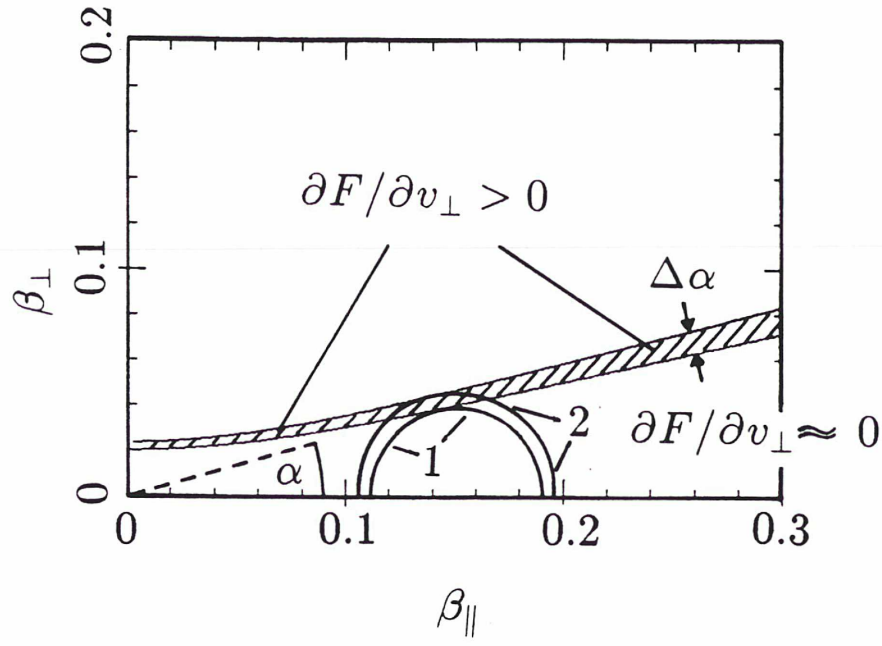

Figure D.5: Loss cone instability used throughout our analysis. The loss cone angle α is typical for a source located between 2 and 3 planetary radii. Positive growth is assumed for waves whose resonant ellipses have access to the unstable region. The two ellipses mark entrance (1) and leave (2) from the instability (corresponding to Y_1 and Y_2 in Figure D.6). For ΔV (potential difference between the radio source and the ionosphere), 2 kV is assumed corresponding to best fits of the S3-3 measurements (Croley et al., 1978). Notice that the ellipses between 1 and 2 are mainly embodied in regions $\partial F/\partial v_\perp < 0$. Close below the loss cone instability, $\partial F/\partial v_\perp \approx 0$, thus considerable quenching of the gain is not expected.

where α is the loss cone angle.

If all electrons were lost below a given mirror point B_m, the slopes of the loss cone boundaries would be infinitely steep, thus leading locally to $\partial F/\partial v_\perp \to \infty$. A more realistic view is that the mirror point in the ionosphere (where the electrons are lost) is statistically varying for each electron within the electron mean free path. Therefore the electron distribution in the loss cone does not drop down abruptly, but within an angle $\Delta\alpha$ reported to be in the order of $0.5 - 2°$ (Omidi and Gurnett, 1984). Consequently, a loss cone angle ($\alpha \approx 15°$) calculated for a distribution function at 2-3 planetary radii (Equation D.14) will be used together with $\Delta\alpha = 2°$ (Figure D.5) to determine the gain factor g. Auroral radio sources like at the earth (AKR), Jupiter (low frequency DAM, high frequency HOM), and Saturn (SKR) are typically found at 2-3 planetary radii. Within this approximation, we do not limit our loss cone instability around a given value $\beta_{\parallel o}$. Instead, it is assumed that the unstable region covers a large range of $\beta_\parallel$. The more realistic restriction to $\beta_{\parallel o}$ will be performed later.

Since ω_i is constant in our approximation between l_1 and l_2 Equation (D.12) may be written

$$g = \omega_i \int_{l1}^{l2} \frac{dl}{v_g(l)} = \omega_i T \tag{D.15}$$

where T is the interaction time of electron - wave resonance.

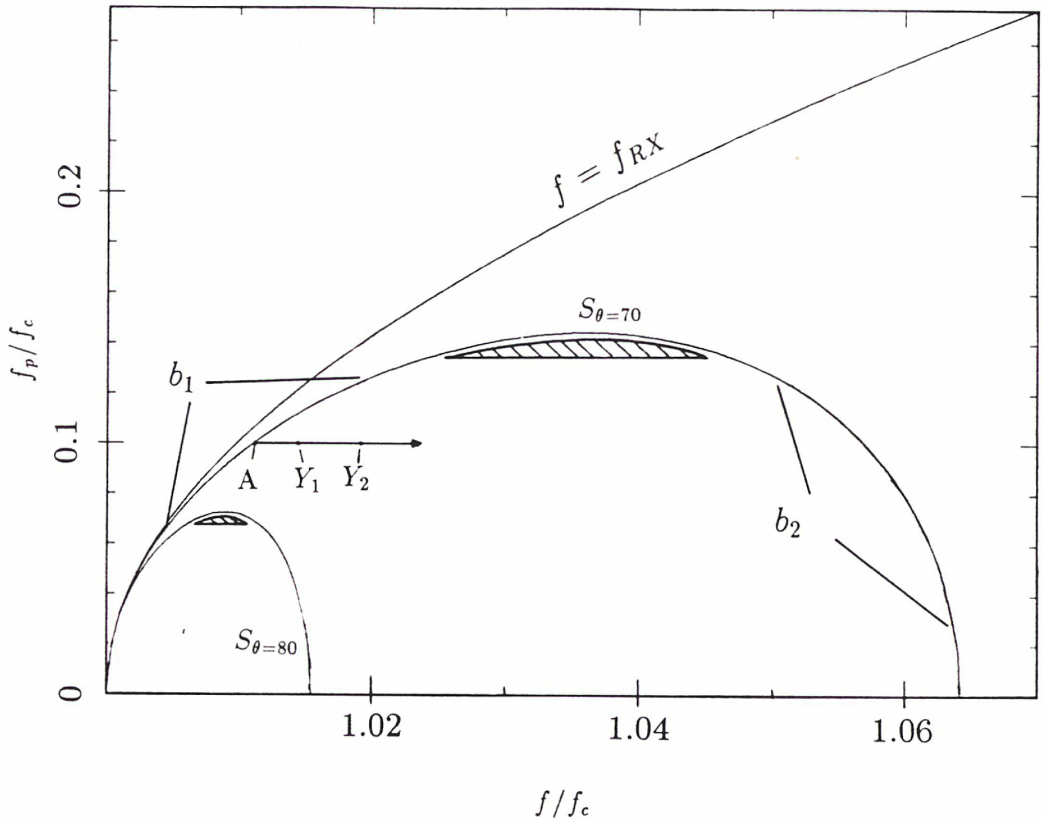

Figure D.6: Part of the f/f_c-f_p/f_c space extracted from Figure D.3. The curves represent the separatrices $S_{\theta=70}$ and $S_{\theta=80}$, respectively. An example of the ray path in this space serving for the calculation of T is visualized for f_p/f_c =0.1. At the point Y_1 which corresponds to l_1 in real space, the respective resonant ellipse enters the range of instability (corresponding to ellipse 1 in Figure D.5). Then the semimajor axis b increases while the wave travels from the separatrix into regions of decreasing B (increasing f/f_c) and at a given point Y_2, b exceeds the region of instability (see ellipse 2 in Figure D.5). For each value f_p/f_c, two regions for possible amplification exist near S_θ which are denoted b_1 (branch 1) and b_2 (branch 2). The wave particle interaction time T is largest for a given θ at plasma conditions within the shaded areas just below the vertices of S_θ (discussed later on in Figures D.8a, D.9a).

The calculation of T for a wave with given θ is performed as follows: For a value f_p/f_c (see example for $f_p/f_c = 0.1$ and $\theta = 70°$ in Figure D.6) the starting point is chosen at the respective separatrix $S_{\theta=70}$ which defines a value f/f_c (labeled A in Figure D.6). While f_p/f_c is kept constant, the wave travels along the arrow in Figure D.6 toward increasing f/f_c. When traveling away from the separatrix, the semimajor axis b increases and at the point Y_1 which corresponds to the point l_1 in real space, the ellipse is entering the unstable loss cone region (ellipse 1 in Figure D.5). Later on, it encounters the point Y_2 (corresponding to l_2 in real space) where the resonant contours leave the instability (ellipse 2 in Figure D.5). It is between these two points that the quantity T is calculated. For a given value f_p/f_c there exist two solutions of T near the branches b_1 and b_2 of the separatrix (Figure D.6). Branch b_1 corresponds to lower values of the refractive index n whereas branch b_2 is associated with higher n (Figure D.3).

D.3.3 Analysis

We have to make the link between the coordinates l_1 and l_2 in real space and Y_1 and Y_2 in the f/f_c=Y, f_p/f_c=X space. Let us set $f/f_c = Y = 1$ at the point r_o, thus r_o denotes the distance of the radio source ($f = f_c$) from the planet's origin. Then using approximations valid in a magnetic dipole field in the polar region $\vec{\nabla}B \| \vec{B}$, $\vec{\nabla}B \approx \partial B/\partial r$ (r: distance from the planet's origin), and $\partial B/\partial r = -3/rB$ we obtain

$$Y_{r-r_o} = \frac{f}{f_c}\|_{(r-ro)} = \frac{B(r_o)}{B(r_o) + \partial B(r_o)/\partial r \cdot (r - r_o)} = \frac{B(r_o)}{B(r_o) - 3/r_o B(r_o)(r - r_o)} \approx 1 + \frac{3}{r_o}(r - r_o)$$

and by differentiation

$dY = 3/r_o dr$

Inspecting Figure D.7 we see immediately

$$dl = dr/\cos\theta \ = dY \frac{r_o}{3\cos\theta} \tag{D.16}$$

and after replacing dl in Equation (D.15)

$$T = \frac{r_o}{3\cos\theta\ c} \int_{Y1}^{Y2} \frac{dY}{\beta_g} \tag{D.17}$$

where

$$\beta_g = v_g/c = \frac{1}{c}\left[\left(\frac{\partial\omega}{\partial k}\right)^2 + \frac{1}{k^2}\left(\frac{\partial\omega}{\partial\theta}\right)^2\right]^{1/2}$$

D.3.4 Results

Figures D.8 and D.9 show solutions of Equation (D.17) for $\theta = 70°$ and $80°$, respectively. The used electric field potential is 2 kV (Croley et al., 1978). In the case of Jupiter and Saturn, this potential difference between the radio sources and the ionosphere may certainly be higher, but the choice of ΔV is not of primary interest here. Figures D.8a and D.9a show the normalized interaction time T against f_p/f_c for the two branches b_1 and b_2 as defined in Figure D.6. We see that T is generally higher for branch b_1 which corresponds to lower refractive indices n and consequently to lower group velocities v_g. Moreover, a dramatic increase of T is observed when f_p/f_c is reaching its highest values. This can be easily understood in Figures D.8b and D.9b which show the interaction length L (between l_1 and l_2). We see a maximum of L reaching $10^{-2} r_o$ when f_p/f_c is near its maximum ($\theta = 70°$) and somewhat less for $\theta = 80°$. Assuming r_o to be about 2 - 3 planetary radii, we obtain $L \approx 100$ km for the earth and $L \approx 1000$ km for the giant planets Jupiter and Saturn ($\theta = 80°$). For $\theta = 70°$, the values L become ≈ 200 km and ≈ 2000 km, respectively. We note that for branch b_1 when considering low values of f_p/f_c (< 0.01) the interaction length L drops lower than $10^{-7} r_o$ which corresponds only to a few meters

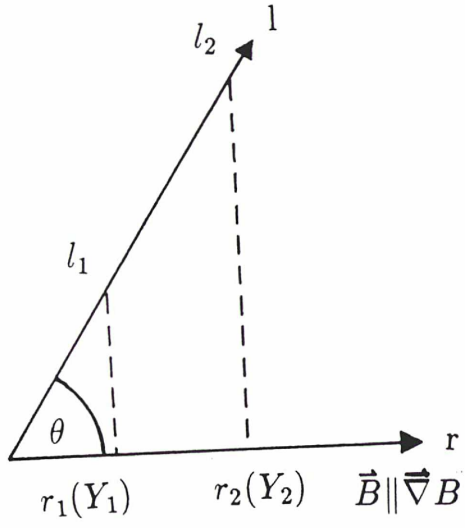

Figure D.7: Geometry used for the derivation of the interaction time T. l deviates from r by the angle θ, B is assumed to be a function of r, and $gradB\|B$.

in the case of the earth which might be not realistic. The previous findings can be discussed very critically when considering Figures D.8c and D.9c. There we have drawn the refractive indices given at l_1 (full line) and l_2 (dashed line). Inspecting branch b_1, we notice that even in the small interaction length given for small f_p/f_c the index of refraction changes substantially (from ≈ 0 to 0.1). Thus, the assumption that θ remains constant in this region is rather questionable, in particular when $gradB\|grad$ n. Moreover, after the short period of possible amplification, the amplitude of the wave is probably damped when the resonant contours encounter favourably regions with $\partial F/\partial v_\perp < 0$ above the loss cone feature. These facts are in particular relevant for branch b_1 and they are all working in the sense to quench the calculated amplification. Now it is also clear that a significant change of the refractive index within a few meters does no longer allow to use the tools of geometrical optics, even as local approximation. Therefore the results given for branch b_1, particulary at the smallest f_p/f_c must be taken with caution.

Looking at plasma conditions f_p/f_c where the peak interaction time T is reached (connection of branch b_1 and b_2), that means $f_p/f_c \approx 0.067$ for $\theta = 80°$ and $f_p/f_c \approx 0.137$ for $\theta = 70°$, the refractive index also changes significantly between l_1 and l_2, namely from about 0.65 to 0.85 (Figures D.8c and D.9c). Thus, important refraction is expected, too. It is, however, difficult to overcome this approximation of no refraction, because the refraction highly depends on the direction of $grad$ n, which is in general not necessarily parallel to $gradB$.

For the reasons given above, the interaction time T and consequently the overall growth may be significantly overestimated, in particular for branch b_1. Contrary, for branch b_2, the calculated T (shorter than for branch b_1) is reasonable within the context of our approximation because, firstly, the index of refraction is near unity which means that the effect of subsequent refraction is indeed negligible, and secondly, because the interaction length $\approx 10^{-3} r_o$ is comparable to the dimensions of an auroral arc.

Our results of the calculation of the interaction time T indicate that T exhibits a maximum where branches b_1 and b_2 are connected, or in other words, when f_p/f_c reaches a maximum at

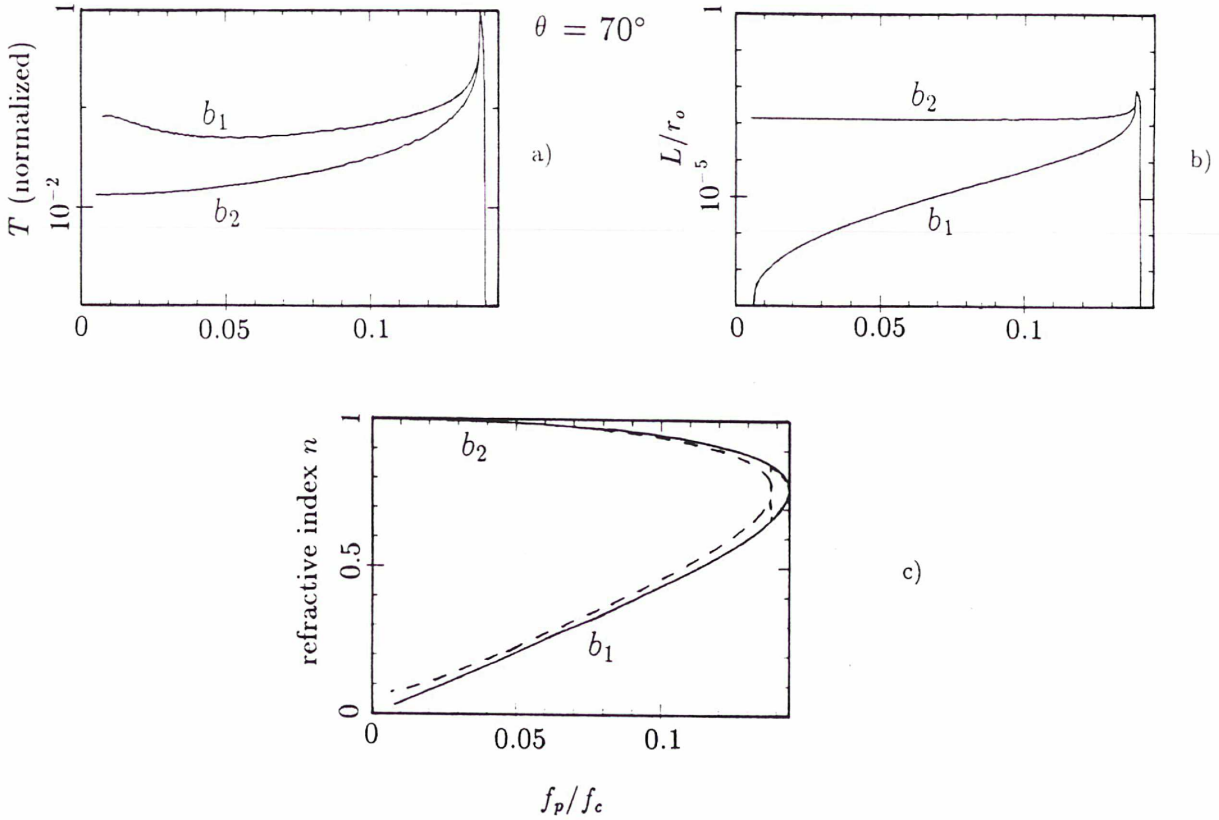

Figure D.8: Normalized interaction time T (a), interaction length L (b), and refractive index at l_1 (full line) and at l_2 (dashed line) for $\theta = 70°$ (c) at all possible values f_p/f_c along the separatrix $S_{\theta=70}$. The peak values for T and L are found for f_p/f_c just below the vertex of $S_{\theta=70}$ (compare Figure D.6).

the vertex of S_θ (shaded areas in Figure D.6). T might be overestimated also for these regions because of the approximations we have used: the assumption of no refraction along ray path, and no wave absorption after the phase of amplification are not very appropriate there. On the contrary, when considering low values $f_p/f_c < 0.01$, it is unlikely that the sources are located near $n \to 0$ (branch b_1), since the interaction lengths are probably to small. Moreover, it seems difficult for these waves to reach free space ($n = 1$) without suffering significant damping after the phase of amplification.

In Figures D.8a and D.9a we note that there is a link between the wave emergence angle θ and the value f_p/f_c where the interaction time T reaches a maximum. In a previous study, Le Queau et al. (1985) found the relation

$$\sin \theta_{crit} = \frac{1}{1 + 4(f_p/f_c)^2} \tag{D.18}$$

relating approximately f_p/f_c at the vertex of $S_{\theta crit}$ to θ_{crit}. The meaning of Equation (D.18) is that for a given f_p/f_c there exists an angle θ_{crit} above which amplification is impossible because f_p/f_c lies outside the resonant region enclosed by the separatrix for $S_{\theta>\theta crit}$. It can be seen in Figures D.8a and D.9a that the values f_p/f_c most favourable for amplification (maximum of T)

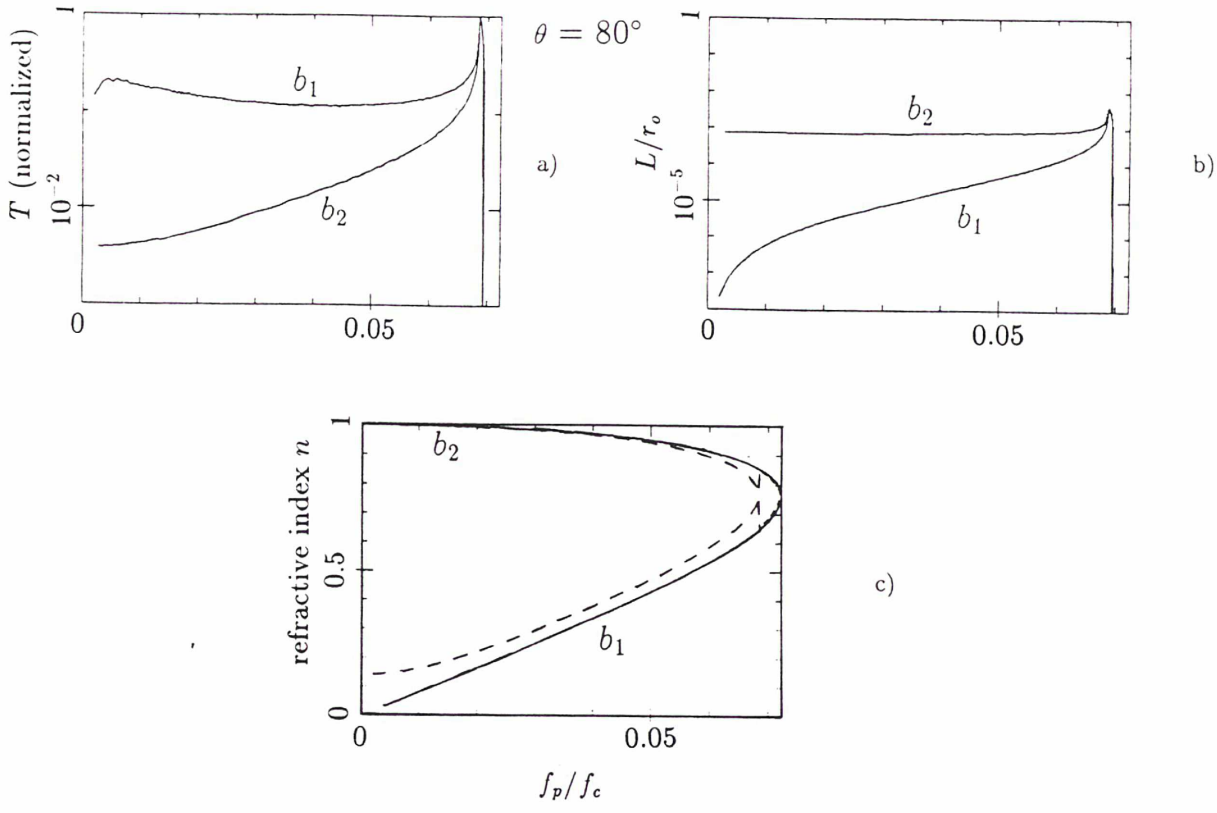

Figure D.9: Same as Figures D.8a-D.8c, but for $\theta = 80°$.

are located just below the vertex of S_θ (see Figure D.6) and can be simply related to θ of the amplified wave by Equation (D.18) with θ less but nearly equal θ_{crit}. The quantities f_p/f_c and f/f_c specifying typical points in the shaded areas (Figure D.6) may be expressed in terms of $\theta \approx \theta_{crit}$ and one obtains by inversion of Equation (D.18)

$$f_p/f_c = \sqrt{\frac{1 - \sin\,\theta}{4 \sin\,\theta}} \tag{D.19}$$

Inspecting Figure D.4, we see that the value f/f_c for the vertex of the separatrix S_θ can be approximated by

$$\frac{f}{f_c} = \frac{f/f_{cMax} - 1}{2} + 1 \tag{D.20}$$

where f/f_{cMax} is the maximum value f/f_c for which resonant ellipses for a given θ are possible. Combining Equations (D.9) and (D.10) and setting $n = 1$ we get

$$f/f_{cMax} = \frac{1}{\sin\,\theta} \tag{D.21}$$

and with Equation (D.20) we finally obtain

$$f/f_c \approx \frac{1+\sin\,\theta}{2\sin\,\theta} \tag{D.22}$$

The elimination of $\sin(\theta)$ from Equations (D.19) and (D.22) finally leads to

$$f/f_c = 1 + 2(f_p/f_c)^2 \tag{D.23}$$

which means that f/f_c and f_p/f_c are not independent from each other. In order to produce maximum amplification for a wave with θ obtained by Equations (D.19) and (D.22), Equation (D.23) must be fulfilled.

In section D.2 we have already expressed f/f_c in terms of the parallel bulk velocity $\beta_{\|o}$ via Equation (D.11). Replacing f/f_c by $\beta_{\|o}$ in Equation (D.23) leads to

$$f_p/f_c = h(\beta_{\|o}) = \left(\frac{1}{2\sqrt{1-\beta_{\|o}^2}} - \frac{1}{2}\right)^{1/2} \tag{D.24}$$

or, when assuming $\beta_{\|o}^2 << 1$

$$f_p/f_c = \frac{1}{2}\beta_{\|o} \tag{D.25}$$

Since $\beta_{\|o}$ is in the order of 0.05-0.1 (in case of the earth) we conclude that in a low density plasma where $f_p/f_c < 0.01$ which is the case for the lower frequency auroral sources of Jovian and Saturnian radio emissions (where we expect a similar $\beta_{\|o}$ as at the earth) Equation (D.25) cannot be fulfilled, because f_p/f_c is much too low. Plasma conditions as required for the hatched areas in Figure D.6 are therefore not occurring for a low density magnetoplasma. Additionally, during our investigation of the interaction time and length for varying f_p/f_c in Figures D.8 and D.9, we also found that for very low f_p/f_c it is unlikely that branch b_1 of the separatrix which is associated with $n \rightarrow 0$ is adapted for a net gain. The only possibility for wave growth in a low density plasma is therefore given for the branch b_2 of the separatrix for which $n \rightarrow 1$. Besides this, when recalling Equation (D.10)

$$n \cdot \cos\,\theta \;= d = \beta_{\|o}$$

it is clear that only for $n \rightarrow 1$ Equation (D.10) can be satisfied for arbitrary $\beta_{\|o}$, whereas for $n \rightarrow 0$, $\beta_{\|o}$ is restricted to values near 0, independently of the choice of θ. This, in turn, means that $d = \beta_{\|o}$ as required for optimization of the growth cannot be fulfilled for $n \rightarrow 0$ (branch 1). Contrary, in the limit $n \rightarrow 1$ (branch 2), Equation (D.10) writes

$$\cos\,\theta \;= \beta_{\|o} \tag{D.26}$$

thus Equations (D.11) and (D.26) give f/f_c and θ in terms of the parallel bulk velocity $\beta_{\|o}$. If $\beta_{\|o}$ is caused by the holelike feature of precipitating electrons, θ is replaced by $\pi - \theta$.

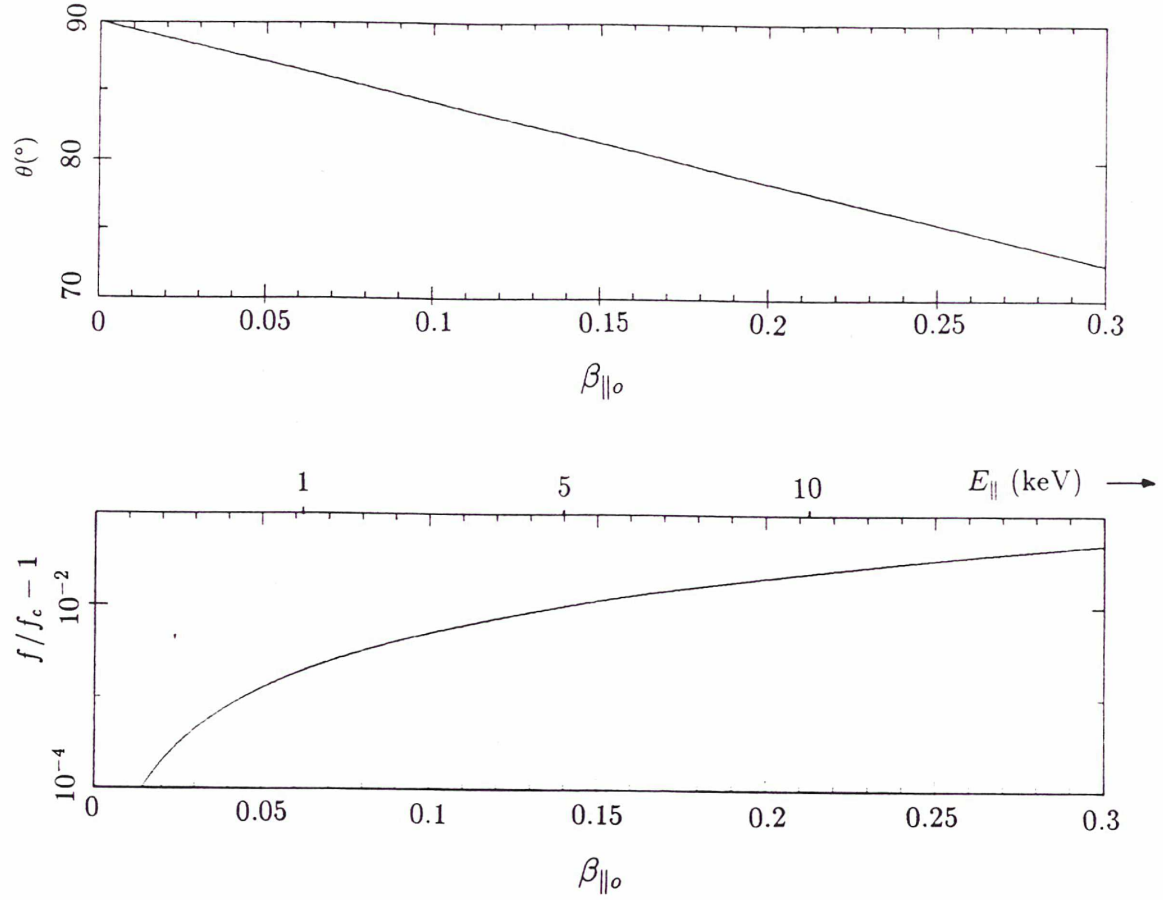

Figure D.10: Wave emergence angle θ and f/f_c against the parallel bulk velocity $\beta_{\|o}$. The scale for the electron energies E is also given assuming that $E_{\|} \approx E$.

We have plotted these two equations in Figure D.10. We also give the corresponding electron energies E in keV assuming $E_{\|} \approx E$. Interpreting Figure D.10 we can state the following for low density plasmas: for plausible values of E in the range from 1 to 10 keV, the emission propagates nearly perpendicular to the source magnetic field line ($\theta \approx 80°$) at a frequency slightly higher than the electron gyrofrequency ($f/f_c \approx 1.01$). Refraction of the wave during its propagation into free space is found to be negligible since the refractive index at the source is near unity. Consequently, $\theta \approx \theta_\infty$ where θ_∞ is the emergence angle measured far away from the source in free space. These results are consistent with the findings of Galopeau et al. (1989) who demonstrated a quasi perpendicular propagation of the SKR low frequencies generated in a low density magnetoplasma throughout their theoretical modeling of the Saturnian kilometric radio spectrum.

D.4 Discussion

During the present investigation we analyzed the CMI in plasmas which are largely dominated by the magnetic field ($f_p/f_c < 0.01$). This study is highly important, because of the applications

to the low-frequency auroral emissions of Jupiter and Saturn. With some useful and plausible simplifications, we derived the wave emergence angle θ and f/f_c at the source as a function of the parallel bulk velocity $\beta_{\|_o}$ (Equations D.11 and D.26) provided that the amplification of the wave is due to the loss cone or the holelike instability. Significant basic results obtained by Le Queau et al. (1985) were confirmed or elaborated in the present paper.

One of our most important findings is that the refractive index at the source is near unity because f/f_c has been shown to be about 1.01 for plausible electron energies (1-10 keV), thus, the source region is sufficiently separated from the R-X cutoff. The quenching of the interaction time due to the high group velocity v_g in this region is compensated by the long interaction length which is possibly as long as an auroral arc. On the other hand, when $n \rightarrow 0$ in a low density source region, the group velocity is very small which would enhance the gain, but the interaction length is only in the order of meters or even below which is probably not realistic.

Concerning the wave emergent angle θ at the source, which is found to be $\approx 80°$ for electron energies from 1 - 10 keV, the results agree favourably with the study of the theoretical radio spectrum of SKR performed by Galopeau et al. (1989). Therein, a nearly perpendicular emergence angle was obtained for the lower frequency sources of SKR which are imbedded in a low density plasma. In the case of Jupiter, the choice of a nearly perpendicular θ throughout the study of the hectometric radiation sources performed by Ladreiter and Leblanc (1990a,b) is strongly supported by the present results. The hectometric sources lie at high altitudes in the Jovian auroral zones which are also largely density depleted (Ladreiter and Leblanc, 1989, 1990a).

One of the main difficulties we encountered throughout our approximations is that in the case of a low density magnetoplasma, the hot electron component may gain over the cold component which is significantly changing the propagation of the radio waves. Pritchett and Strangeway (1985) dealt with this problem and performed particle simulations in high altitude auroral zones and took into account varying ratios of hot and cold electrons. Moreover, they include the effect of a parallel electric field making the analysis rather realistic. In their study, they found that the amplified radiation is highly concentrated in the perpendicular (with respect to the magnetic field) direction. Furthermore, the radiation tends to occur in regions where $kc/\omega_c \approx 0.96$ and $f/f_c \approx 0.99$, i.e. $n = kc/\omega \approx 1$. In fact by including the effect of hot electrons, the radiation occurs below the gyrofrequency. Propagation effects when leaving the auroral arc and entering the neighboring cold plasma may therefore cause a change of the behaviour of the radiation.

Appendix E

Ray tracing of electromagnetic waves in a magnetoplasma

E.1 Fundamentals

In the appendices B and C we used the ray tracing technique to localize the hectometric emission radio sources. In this appendix we will evaluate the mathematical tools which are used in the ray tracing program. Before the derivation of the ray differential equations which describe the characteristics of the ray paths throughout the wave propagation, it is necessary to develop some basic equations in the magnetoionic theory. This includes in particular the definition of the "refractive index surface" and the so-called "ray surface" in order to show the relationship between the ray (direction of energy flow and the wave normal direction. Then, the ray equations are determined and we demonstrate, how to proceed ray tracing in a magnetoplasma such as planetary magnetospheres.

E.1.1 Refractive index and refractive index surface in a medium

One characteristic quantity in a magnetoplasma (determined by the electron density N_e and the superimposed magnetic field with flux density B) is the refractive index n. For simplification, we neglect the contribution of ions. When collisions in the plasma are neglected, n is a real or an imaginary quantity but not complex. It is related to the phase velocity V of a wave by $n = c/V$ (c being the light velocity) and is given by the Appleton-Hartree formula

$$n^2 = 1 - \frac{X(1-X)}{1 - X - Y^2 \sin^2\vartheta/2 \pm \sqrt{Y^4 \sin^4\vartheta/4 + Y^2 \cos^2\vartheta (1-X)^2}} \tag{E.1}$$

the upper sign (+) refers to the ordinary (O) and the lower(−) to the extraordinary (X) mode. The quantities X and Y are given by

$$X = f_p^2/f^2 \quad f_p = \frac{1}{2\pi}\sqrt{\frac{e^2 N_e}{\epsilon_o m_e}} \tag{E.2}$$

$$Y = f_c/f \quad f_c = \frac{1}{2\pi}\frac{eB}{m_e}$$

f_p: electron plasma frequency, f_c: electron gyrofrequency, e: unit charge, N_e: electron number density, B: magnetic flux density, m_e: electron mass, ϵ_o: permittivity constant.

For a wave with frequency f, n is a function of N_e, B, and the direction ϑ of the wave normal with respect to B. The direction of the wave normal and the associated ray (direction of energy flow) are in general different, because the refractive index n depends on the direction of the wave normal with respect to $\vec{B}$.

For the definition of the refractive index surface, consider a coordinate system with the spherical coordinates r, θ, ϕ (Cartesian coordinates u, v, w) centered on a point in the plasma which is defined by N_e and $\vec{B}$. Let $\vec{B}$ be parallel to the w-axis. For a given frequency f, the refractive index depends only on ϑ. Consider a surface in which the radius to each point is equal to $n(\vartheta)$. According to Equation (E.1), there exist two such surfaces, one for the X-wave and one for the O-wave. Since n depends only on ϑ for a given point in the medium, each surface is a surface of revolution around the w-axis with the $u - v$-plane ($\vartheta = \pi/2$) as a plane of symmetry. The resulting surfaces are called "refractive index surfaces". In free space (N_e=B=0) both surfaces are simply unit spheres around the origin.

E.1.2 The directions of the wave normal and the ray

When there is no superimposed magnetic field, the refractive index n in a plasma does not depend on the direction of the wave propagation; the wave normal and the ray directions are therefore identical. The wave normal is defined to be perpendicular to the planes of constant phase, whereas the ray denotes the direction of energy flow. When the magnetic flux density is not zero, the directions of a ray and the associated wave normal are in general different, because the refractive index n depends on the direction of the wave normal. This is true in a homogeneous medium and a relation between the ray and the wave normal direction can be found. The results then can be used to trace the ray paths in an inhomogeneous, but slowly varying medium. To derive the ray direction for a given wave normal in a magnetoplasma we start from the expression of the wave electric field (e. g. Budden, 1961).

$$\iiint E(k,\vartheta,\varphi)\exp\, ik[ct - n(\vartheta)\{u\cos\varphi\sin\vartheta + v\sin\varphi\sin\vartheta + w\cos\vartheta\}]dkd\vartheta d\varphi \qquad \text{(E.3)}$$

Let us study the situation for specific values k_o, θ_o, and φ_o where E is supposed to exhibit a maximum. The direction of the wave normal is then given by ϑ_o and φ_o Now let us determine the direction of the ray with respect to the wave normal which is equal to the direction of energy flow. This direction is found by the condition that the exponent denoting the wave phase Φ in Equation (E.3) must be stationary with respect to variations of ϑ, φ and k. We obtain by differentiation:

$$\frac{\partial\Phi}{\partial\varphi} = n(\vartheta_o)[(v\cos\varphi_o - u\sin\varphi_o)\sin\vartheta_o] = 0 \qquad \text{(E.4)}$$

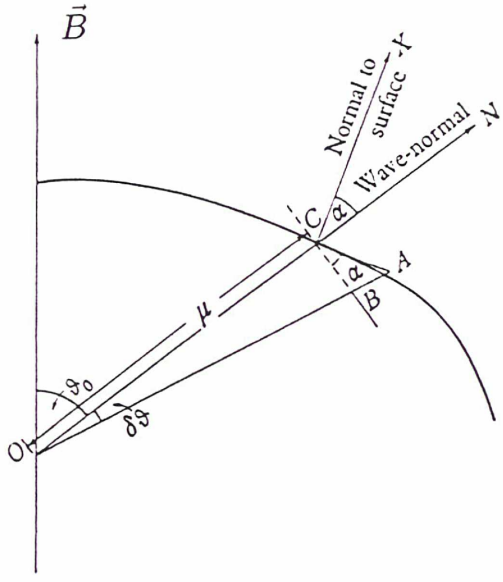

Figure E.1: Cross-section of refractive index surface by a plane containing the direction of the magnetic field. CX and CA are the normal and tangent, respectively, at the point C. The ray direction is therefore perpendicular to the refractive index surface.

$$\frac{\partial\Phi}{\partial\vartheta} = \frac{dn}{d\vartheta}|_{\vartheta=\vartheta_o}[(u\cos\varphi_o + v\sin\varphi_o)\sin\vartheta_o + w\cos\vartheta_o] + n[(u\cos\varphi_o + v\sin\varphi_o)\cos\vartheta_o - w\sin\vartheta_o] = 0 \tag{E.5}$$

From Equation (E.4), we see that φ=const i.e. the wave normal, the ray and the magnetic field are coplanar. Thus φ can be chosen to be 0. Let the ray direction make an angle α with the wave normal i.e. an angle $\theta_o - \alpha$ with respect to the w-axis and let r_o be the distance from the origin. We have $u = r_o\sin(\vartheta_o - \alpha)$, v=0, $w = r_o\cos(\vartheta_o - \alpha)$. By substituting u, v, w in Equation (E.5), we obtain the angle α which determines finally the ray direction. After some algebraic transformations we have

$$\tan\,\alpha\, = \frac{1}{n}\frac{\partial n}{\partial\vartheta}|_{\vartheta=\vartheta_o} \tag{E.6}$$

For the sake of illustration, see Figure E.1 (taken from Budden, 1961), which represents a cross section of the refractive index surface by the $x - w$-plane (φ=0). Clearly dn is related to the AB in the triangle ABC, and $nd\vartheta$ to CB. Since CA is normal to CX and CB is normal to CN, the ray direction is parallel to the normal to the refractive index surface.

Differentiation of Φ with respect to k leads to (φ=0)

$$\frac{\partial\Phi}{\partial k} = ct - n(u\sin\vartheta_o + w\cos\vartheta_o) + k\frac{\partial n}{\partial k}(u\cos\vartheta_o + w\sin\vartheta_o) = 0 \tag{E.7}$$

using the substitutions for u and w as above

$$ct = \left(n + k\frac{\partial n}{\partial k}\right) r_o \cos\alpha \tag{E.8}$$

replacing further k by $2\pi f/c$

$$ct = \frac{\partial(fn)}{\partial f} r_o \cos\alpha \tag{E.9}$$

t is the time taken for the wave packet on a ray to travel the distance r_o. Its velocity is called the group velocity U, and is given by

$$U = \frac{c \sec\alpha}{\partial(fn)/\partial f} \tag{E.10}$$

The quantity $\partial n/\partial f$, which is required in Equation (E.10) can be obtained by differentiation of Equation (E.1).

E.1.3 The ray velocity and the ray surface

Besides the group velocity U and the phase velocity $V = c/n$ (defining the velocity of a wave crest in the direction of the wave normal), we derive now another velocity, the so-called ray velocity. It is the velocity of a wave crest in the direction of the ray (inclined by α with respect to the wave normal). The point of intersection of the wave crest with the ray direction moves sideways as the wave advances. The ray velocity V_r is therefore

$$V_r = c/(n\cos\alpha) = V/\cos\alpha \tag{E.11}$$

the ratio U/V_r is given by

$$\frac{U}{V_r} = \frac{n}{n + f\partial n/\partial f} \tag{E.12}$$

Since $\partial n/\partial f$ is generally greater than 1, $V_r > U$. Similar to $n = c/V$ we can define a refractive index which belongs to the ray velocity V_r. We will call it the ray refractive index n_{ray}

$$n_{ray} = c/V_r \tag{E.13}$$

Now we are able to define a "ray surface" in a similar way as we did it for the refractive index surface. Again, we introduce spherical polar coordinates r, ϑ, φ and let the magnetic field be parallel to the w-axis. The direction of a given ray is then $\vartheta_r = \vartheta_o - \alpha$. Consider a surface in which the radius r to each point is equal to $V_r(\vartheta_r)$. There are two such surfaces for any medium, one for each of the two characteristic waves (O or X mode). These are the ray surfaces. Each is a surface of revolution about the w-axis, and has the plane $\vartheta = \pi/2$ as a plane of symmetry. The ray surface can be visualized as the wave front reached after unit time for a point source at the origin. Thus, the normal to the ray surface at any point is the wave normal.

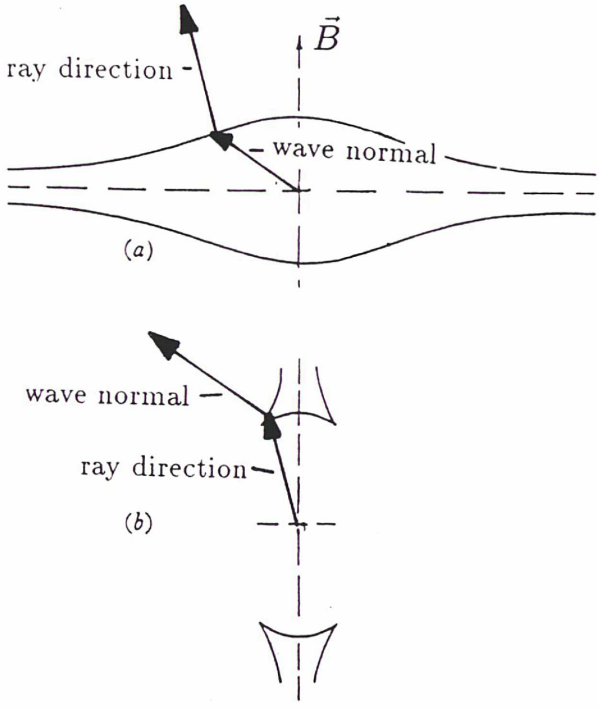

Figure E.2: Cross section in the magnetic meridian plane of (a) the refractive index surface, and (b) the ray surface, for whistler mode waves. Note the reciprocal properties of these surfaces.

We notice the important reciprocal properties of the wave normal and the ray. For a given point in the medium, the ray direction is the normal to the refractive index surface and the wave normal direction is the normal to the ray surface. This is emphasized in Figure E.2 (from Budden, 1961) where we show the refractive index surface and the ray surface for whistler mode waves which have frequencies below the gyrofrequency. We see that for any wave normal angle ϑ, the ray direction is confined within a small angular range around the magnetic field. This explains the "guiding" of whistlers along magnetic field lines.

E.2 The ray equations

E.2.1 Equations for the refractive index surface and the ray surface

With the results of the preceeding sections, we are able to determine qualitatively the ray path in a magnetoplasma. To describe the situation mathematically, we shall find equations which describe the refractive index surface and the ray surface. We recall that the instantaneous ray direction $d\vec{x}/dt$ is normal to the refractive index surface. This can be emphasized by

$$\frac{d\vec{x}}{dt} = const \cdot \vec{\nabla}_n G = const \cdot \left(\frac{\partial G}{\partial n_x} + \frac{\partial G}{\partial n_y} + \frac{\partial G}{\partial n_z} \right) \tag{E.14}$$

where $d\vec{x}/dt$ is the ray velocity V_r (t: time), n_x, n_y, n_z are the components of the refractive index n and G denotes the refractive index surface which we obtain as follows. We define a

three dimensional space to be called the "refractive index space" with the Cartesian coordinates n_x, n_y, n_z which are parallel to the axis x, y, z in ordinary space. Let the wave normal take all possible directions. Then the locus of the point n_x, n_y, n_z for all possible directions defines the refractive index surface. The refractive index is given by Appleton-Hartree formula (Equation E.1) and depends on the position x, y, z and the direction of the wave normal n_x, n_y, n_z. This is indicated by writing $n(x, y, z, n_x, n_y, n_z)$. The components of the refractive index occur only in the combination $n_x^2 + n_y^2 + n_z^2 = n^2$. The refractive index surface may then be written

$$G(x, y, z, n_x, n_y, n_z) = \frac{\sqrt{n_x^2 + n_y^2 + n_z^2}}{n(x, y, z, n_x, n_y, n_z)} = 1 \tag{E.15}$$

It can be shown that the constant of proportionality in Equation (E.14) is the light velocity c (Budden, 1961). Thus, Equation (E.14) becomes

$$\dot{x} = c\frac{\partial G}{\partial n_x} \quad \dot{y} = c\frac{\partial G}{\partial n_y} \quad \dot{z} = c\frac{\partial G}{\partial n_z} \tag{E.16}$$

where a dot represents d/dt.

In section E.1 we found that the wave normal direction is normal to the ray surface. This can be emphasized by writing

$$\vec{n} = const \cdot \vec{\nabla}_{\dot{r}} F = const \cdot \left(\frac{\partial F}{\partial \dot{x}} + \frac{\partial F}{\partial \dot{y}} + \frac{\partial F}{\partial \dot{z}}\right) \tag{E.17}$$

where F denotes the ray surface and we find it in a similar way as we found the refractive index surface. Consider a three dimensional space to be called the "ray space" in which the Cartesian coordinates are $\dot{x}$, $\dot{y}$, $\dot{z}$ and are parallel to x, y, z of the ordinary space. Draw a line from the origin of the ray space in the direction of the ray and with length equal to the ray velocity $V_r = \sqrt{\dot{x}^2 + \dot{y}^2 + \dot{z}^2}$. The end-points, which define the wave front after unit time, represent the ray surface. n_{ray} is the ray refractive index and is given by $n_{ray} = c/V_r$ (Equation E.13). It is a function of x, y, z and the ray direction which we indicate by $n_{ray}(x, y, z, \dot{x}, \dot{y}, \dot{z})$. The equation for the ray surface F can be written (by inversion of Equation E.13)

$$F(x, y, z, \dot{x}, \dot{y}, \dot{z}) = \sqrt{\dot{x}^2 + \dot{y}^2 + \dot{z}^2} \cdot n_{ray}(x, y, z, \dot{x}, \dot{y}, \dot{z})\frac{1}{c} = 1 \tag{E.18}$$

The constant of proportionality in Equation (E.17) is again the light velocity c and we obtain

$$n_x = c\frac{\partial F}{\partial \dot{x}} \quad n_y = c\frac{\partial F}{\partial \dot{y}} \quad n_z = c\frac{\partial F}{\partial \dot{z}} \tag{E.19}$$

Equations (E.16) and (E.19) mathematically describe that the ray direction is parallel to the normal to the refractive index surface G, and that the wave normal direction is parallel to the normal to the ray surface for a given point x, y, x in space. The refractive index surface G may be obtained by using the Appleton-Hartree formula (Equation E.1). The construction of F (Equation E.18) is more complicated. It is therefore convenient to express the ray surface F in terms of G.

E.2.2 Relations beween the refractive index surface and the ray surface and Fermat's principle of stationary time

Since F=1 (Equation E.18), the total derivative dF/dx=0 for each point x, y, z

$$\frac{dF}{dx} = \frac{\partial F}{\partial x} + \left(\frac{\partial F}{\partial \dot{x}}\frac{\partial \dot{x}}{\partial x} + \frac{\partial F}{\partial \dot{y}}\frac{\partial \dot{y}}{\partial x} + \frac{\partial F}{\partial \dot{z}}\frac{\partial \dot{z}}{\partial x}\right) = 0 \tag{E.20}$$

using Equations (E.19), one obtains

$$\frac{\partial F}{\partial x} = -\frac{1}{c}\left(n_x\frac{\partial \dot{x}}{\partial x} + n_y\frac{\partial \dot{y}}{\partial x} + n_z\frac{\partial \dot{z}}{\partial x}\right) \tag{E.21}$$

Similarly, setting dG/dx=0 and using Equations (E.16)

$$\frac{\partial G}{\partial x} = -\frac{1}{c}\left(\frac{\partial n_x}{\partial x}\dot{x} + \frac{\partial n_y}{\partial x}\dot{y} + \frac{\partial n_z}{\partial x}\dot{z}\right) \tag{E.22}$$

When also considering the derivatives $dG/dy = 0$ and $dG/dz = 0$ we finally obtain

$$\frac{dn_x}{dt} = \dot{n}_x = -c\frac{\partial G}{\partial x} \quad \dot{n}_y = -c\frac{\partial G}{\partial y} \quad \dot{n}_z = -c\frac{\partial G}{\partial z} \tag{E.23}$$

Equations (E.16) and (E.23) are called together the "ray equations". These are the relevant equations which determine the propagation of rays in a medium. Before discussing them in detail, we shall find some important relations between the refractive index surface G and the ray surface F.

We add Equations (E.21) and (E.22) and obtain

$$\frac{\partial G}{\partial x} + \frac{\partial F}{\partial x} = -\frac{1}{c}\frac{\partial}{\partial x}(\dot{x}n_x + \dot{y}n_y + \dot{z}n_z) = 0 \tag{E.24}$$

Equation (E.24) vanishes because $\dot{x}n_x + \dot{y}n_y + \dot{z}n_z = V_r \cdot n = c/(n\cos\alpha) \cdot n \cdot \cos\alpha = c = const.$ We obtain therefore

$$\frac{\partial F}{\partial x} = -\frac{\partial G}{\partial x} \quad \frac{\partial F}{\partial y} = -\frac{\partial G}{\partial y} \quad \frac{\partial F}{\partial z} = -\frac{\partial G}{\partial z} \tag{E.25}$$

the two latter equations are derived when setting $dF/dy = dG/dy = dF/dz = dG/dz = 0$. Now let us combine Equations (E.25), (E.23) and (E.16)

$$\frac{\partial F}{\partial x} = \frac{1}{c}\dot{n}_x = \frac{d}{dt}\frac{\partial F}{\partial \dot{x}} \tag{E.26}$$

$$\frac{\partial F}{\partial y} = \frac{d}{dt}\frac{\partial F}{\partial \dot{y}}$$

$$\frac{\partial F}{\partial z} = \frac{d}{dt}\frac{\partial F}{\partial \dot{z}}$$

These are the Lagrangian equations which are based on the formalism

$$\delta \int_a^b F dt = 0 \tag{E.27}$$

where a and b denote the end points on the ray path. When Equation (E.27) is evaluated for a number of ray paths between a and b, its value is an extremum for the actual ray path. Let us substitute dt by ds, using $(ds/dt)^2=\dot{x}^2 + \dot{y}^2 + \dot{z}^2$ and Equation (E.18). We obtain

$$\delta \int_a^b n_{ray} ds = 0 \tag{E.28}$$

which is Fermat's principle. It states that the time of travel of a wave crest along the ray path from a to b is stationary with respect to small variations of the path. Here, the time of travel is a minimum. In other words, the ray path from a to b is such that the time of travel of the wave front along this path becomes a minimum. Thus, by using the relations between G and F we have seen that the wave propagation accounts to Fermat's principle of stationary time. Equation (E.28) is given in Cartesian coordinates. However, Fermat's principle accounts for any chosen coordinate system. We may therefore introduce spherical polar coordinates which are more convenient to study ray paths in planetary magnetospheres. Therefore Equations (E.16) and (E.23) which are the ray equations can be written in spherical coordinates r, θ, ϕ

$$\dot{r} = c\frac{\partial G}{\partial n_r} \quad \dot{\theta} = c\frac{1}{r}\frac{\partial G}{\partial n_\theta} \quad \dot{\phi} = c\frac{1}{r\sin\theta}\frac{\partial G}{\partial n_\phi} \tag{E.29}$$

$$\frac{\dot{n}_r}{c} = \frac{1}{n}\frac{\partial n}{\partial r} + \frac{n_\theta}{r}\frac{\partial G}{\partial n_\theta} + \frac{n_\phi}{r}\frac{\partial G}{\partial n_\phi} \tag{E.30}$$

$$\frac{\dot{n}_\theta}{c} = \frac{1}{rn}\frac{\partial n}{\partial \theta} - \frac{n_\theta}{r}\frac{\partial G}{\partial n_r} + \frac{n_\phi \cot\theta}{r}\frac{\partial G}{\partial n_\phi}$$

$$\frac{\dot{n}_\phi}{c} = \frac{1}{rn\sin\theta}\frac{\partial n}{\partial \phi} - \frac{n_\phi}{r}\frac{\partial G}{\partial n_r} - \frac{n_\phi \cot\theta}{r}\frac{\partial G}{\partial n_\theta}$$

where

$$G = G(r,\theta,\phi,n_r,n_\theta,n_\phi) = \frac{\sqrt{n_r^2 + n_\theta^2 + n_\phi^2}}{n(r,\theta,\phi,n_r,n_\theta,n_\phi)} = 1 \tag{E.31}$$

n_r, n_θ, and n_ϕ refer to a polar coordinate system λ,φ which is centered on the point r, θ, ϕ. The components of n are

$$n_r = n\cos\varphi \quad n_\theta = n\sin\varphi\cos\lambda \quad n_\phi = n\sin\varphi\sin\lambda \tag{E.32}$$

Equations (E.29) and (E.30) are the ray equations in spherical polar coordinates. They are the basic equations for our purpose i.e. to show how to find the ray path for any given modeled magnetosphere where the magnetic flux density B and the electron number density N_e are known at each point in space. Equations (E.29) are used to determine the ray direction given by $\dot{r}, \dot{\theta}, \dot{\phi}$ for a given point $P_o(r_o, \theta_o, \phi_o)$ in space and a given wave normal direction $n_{ro}, n_{\theta o}, n_{\phi o}$. These two ingredients are initially required to calculate the refractive index surface G via Equation (E.31). By taking an incremental step Δt in time in the obtained ray direction, a new point in space $P_1(r_1 = r_o + \dot{r}\Delta t,\ \theta_1 = \theta_o + \dot{\theta}\Delta t,\ \phi_1 = \phi_o + \dot{\phi}\Delta t)$ is found. According to Snell's law, the wave normal direction has generally changed when the wave propagates from P_o to P_1. This is emphasized by Equations (E.30). A new wave normal direction $n_{r1} = n_{ro} + \dot{n}_r\Delta t$, $n_{\theta 1} = n_{\theta o} + \dot{n}_\theta\Delta t$, $n_{\phi 1} = n_{\phi o} + \dot{n}_\phi\Delta t$ occurs at the point P_1. At P_1, a new ray direction is calculated and the steps are repeated. Thus, the ray path through the medium is found. Before this procedure is amenable for calculation on a computer, the ray Equations (E.29) and (E.30) have to be expressed in terms of plasma density and magnetic field models which characterize the regarded medium (e.g. planetary magnetosphere, ionosphere etc.).

E.3 Application of the ray equations for ray tracing in planetary magnetospheres

By performing differentiations with respect to n_r, n_θ, and n_ϕ in Equations (E.29) we get

$$\frac{\dot{r}}{c} = \frac{1}{n^2}\left(n_r - n\frac{\partial n}{\partial n_r}\right) \tag{E.33}$$

$$\frac{\dot{\theta}}{c} = \frac{1}{rn^2}\left(n_\theta - n\frac{\partial n}{\partial n_\theta}\right)$$

$$\frac{\dot{\phi}}{c} = \frac{1}{r\sin\theta n^2}\left(n_\phi - n\frac{\partial n}{\partial n_\phi}\right)$$

Let us study now the derivatives $\partial n/\partial n_r$, $\partial n/\partial n_\theta$, $\partial n/\partial n_\phi$: They can be written

$$\frac{\partial n}{\partial n_r} = \frac{\partial n}{\partial \vartheta}\frac{\partial \vartheta}{\partial \varphi}\frac{\partial \varphi}{\partial n_r} \tag{E.34}$$

$$\frac{\partial n}{\partial n_\theta} = \frac{\partial n}{\partial \vartheta}\left(\frac{\partial \vartheta}{\partial \varphi}\frac{\partial \varphi}{\partial n_\theta} + \frac{\partial \vartheta}{\partial \lambda}\frac{\partial \lambda}{\partial n_\theta}\right)$$

$$\frac{\partial n}{\partial n_\phi} = \frac{\partial n}{\partial \vartheta}\left(\frac{\partial \vartheta}{\partial \varphi}\frac{\partial \varphi}{\partial n_\phi} + \frac{\partial \vartheta}{\partial \lambda}\frac{\partial \lambda}{\partial n_\phi}\right)$$

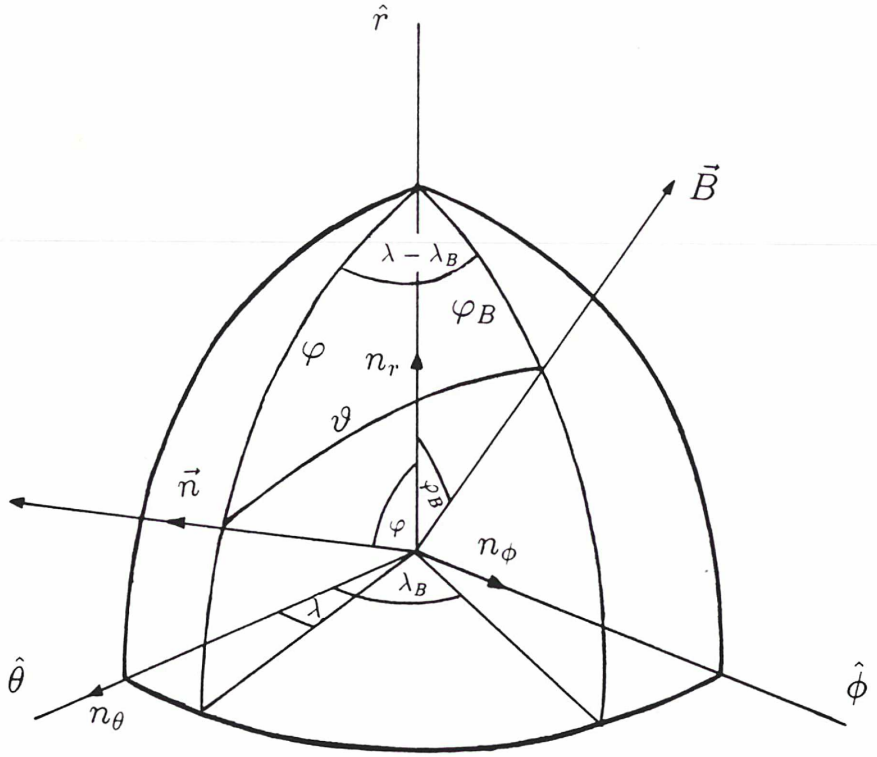

Figure E.3: Coordinate systems used for definition of the directions of the magnetic field $\vec{B}(\varphi_B, \lambda_B)$ and the refractive index $\vec{n}(\varphi, \lambda)$ which denotes the direction of the wave normal. The center of the coordinate systems is at a given point with spherical coordinates r, θ, ϕ, and n_r, n_θ, n_ϕ are parallel to $\hat{r}$, $\hat{\theta}$, and $\hat{\phi}$, respectively.

where φ and λ are the polar coordinates of n_r, n_θ n_ϕ (Equations E.32) and ϑ is the angle between the wave normal and the magnetic field.

The quantity $\partial n/\partial\vartheta$ can be easily calculated by differentiation of the refractive index (Equation E.1). To calculate $\partial\vartheta/\partial\varphi$ and $\partial\vartheta/\partial\lambda$ we have to determine $\vartheta(\varphi, \lambda)$. The situation is displayed in Figure E.3. The coordinate system is centered at a given point r, θ, ϕ in space. n_r, n_θ and n_ϕ coincide with the $\hat{r}$, $\hat{\theta}$ and $\hat{\phi}$ directions, respectively. The direction of n is determined by φ and λ using Equations (E.32).

Let the magnetic field direction have the polar angles φ_B and λ_B. They must be applied by a magnetic field model which provides $\vec{B}(r, \theta, \phi)$ at each point in the medium. Then, $\vartheta(\varphi, \lambda)$ can be derived (see Figure E.3).

$$\cos\vartheta = \cos\varphi\cos\varphi_B + \sin\varphi\sin\varphi_B\cos(\lambda_B - \lambda) \tag{E.35}$$

The quantities $\partial\vartheta/\partial\varphi$ and $\partial\vartheta/\partial\lambda$ are given by differentiation of Equation (E.35)

$$\frac{\partial\vartheta}{\partial\varphi} = \frac{1}{\sin\vartheta}[\sin\varphi\cos\varphi_B - \cos\varphi\sin\varphi_B\cos(\lambda_B - \lambda)] \tag{E.36}$$

$$\frac{\partial \vartheta}{\partial \lambda} = \frac{1}{\sin \vartheta}[\sin \varphi \sin \varphi_B \sin(\lambda - \lambda_B)]$$

Finally, the quantities $\partial\varphi/\partial n_r$, $\partial\varphi/\partial n_\theta$, $\partial\varphi/\partial n_\phi$, $\partial\lambda/\partial n_\theta$, and $\partial\lambda/\partial n_\phi$ are obtained by differentiation of Equations (E.32) using $n^2 = n_r^2 + n_\theta^2 + n_\phi^2$

$$\frac{\partial \varphi}{\partial n_r} = -\frac{1}{\sin \varphi} \frac{n^2 - n_r^2}{n^3} \tag{E.37}$$

$$\frac{\partial \varphi}{\partial n_\theta} = \frac{1}{\cos \varphi \cos \lambda} \frac{n^2 - n_\theta^2}{n^3}$$

$$\frac{\partial \varphi}{\partial n_\phi} = \frac{1}{\cos \varphi \sin \lambda} \frac{n^2 - n_\phi^2}{n^3}$$

$$\frac{\partial \lambda}{\partial n_\theta} = -\frac{1}{\sin \varphi \sin \lambda} \frac{n^2 - n_\theta^2}{n^3}$$

$$\frac{\partial \lambda}{\partial n_\phi} = \frac{1}{\sin \varphi \cos \lambda} \frac{n^2 - n_\phi^2}{n^3}$$

We use $\partial n/\partial \vartheta$ as derived from Equation (E.1), and further Equations (E.37), (E.34) and substitute them in the ray Equations (E.33). These equations determine the direction of the ray (defined by $\dot{r}, \dot{\theta}, \dot{\phi}$) at a given starting point and for a given wave normal direction when we provide a magnetic field model $\vec{B}(r, \theta, \phi)$ which intervenes in Equations (E.36).

We shall use the results from Equations (E.33) to calculate the variation in the wave normal direction during the wave propagation with the second set of ray Equations (E.30). Substitute Equations (E.29) in Equations (E.30)

$$\frac{\dot{n}_r}{c} = \frac{1}{n}\frac{\partial n}{\partial r} + \frac{n_\theta}{c}\dot{\theta} + \frac{n_\phi \sin \theta}{c}\dot{\phi} \tag{E.38}$$

$$\frac{\dot{n}_\theta}{c} = \frac{1}{r}\left(\frac{1}{n}\frac{\partial n}{\partial \theta} - \frac{n_\theta}{c}\dot{r} + \frac{n_\phi r \cos \theta}{c}\dot{\phi}\right)$$

$$\frac{\dot{n}_\phi}{c} = \frac{1}{r \sin \theta}\left(\frac{1}{n}\frac{\partial n}{\partial \phi} - \frac{n_\phi \sin \theta}{c}\dot{r} - \frac{n_\phi r \cos \theta}{c}\dot{\theta}\right)$$

These equations contain the derivatives $\partial n/\partial r$, $\partial n/\partial \theta$ (do not confuse with $\partial n/\partial \vartheta$), and $\partial n/\partial \phi$ which need further investigation. They can be written

$$\frac{\partial n}{\partial r} = \frac{\partial n}{\partial X}\frac{\partial X}{\partial N_e}\frac{\partial N_e}{\partial r} + \frac{\partial n}{\partial Y}\frac{\partial Y}{\partial B}\frac{\partial B}{\partial r} \tag{E.39}$$

$$\frac{\partial n}{\partial \theta} = \frac{\partial n}{\partial X}\frac{\partial X}{\partial N_e}\frac{\partial N_e}{\partial \theta} + \frac{\partial n}{\partial Y}\frac{\partial Y}{\partial B}\frac{\partial B}{\partial \theta}$$

$$\frac{\partial n}{\partial \phi} = \frac{\partial n}{\partial X}\frac{\partial X}{\partial N_e}\frac{\partial N_e}{\partial \phi} + \frac{\partial n}{\partial Y}\frac{\partial Y}{\partial B}\frac{\partial B}{\partial \phi}$$

where the derivatives $\partial n/\partial X$ and $\partial n/\partial Y$ can be obtained by differentiation of the Appleton-Hartree formula (Equation E.1). $\partial X/\partial N_e$ and $\partial Y/\partial B$ are derived via Equations (E.2). Finally, the derivatives $\partial N_e/\partial r$, $\partial N_e/\partial \theta$, $\partial N_e/\partial \phi$, and $\partial B/\partial r$, $\partial B/\partial \theta$, $\partial B/\partial \phi$ must be calculated from an analytical plasma density model $N_e(r, \theta, \phi)$ and magnetic field model $\vec{B}(r, \theta, \phi)$. We substitute Equations (E.39) in Equations (E.38) and calculate the variation of the wave normal direction $\dot{n}_r, \dot{n}_\theta, \dot{n}_\phi$ based on the given magnetic field and plasma models.

In this section we showed how to handle the ray equations (E.33) and (E.38) in order to calculate ray paths in a magnetoplasma which is determined by an electron density model $N_e(r, \theta, \phi)$ and a magnetic field model $\vec{B}(r, \theta, \phi)$. Since one needs also the derivatives of B and N_e with respect to r, θ, ϕ these models should be provided in analytical form. In all aspects of the ray tracing procedure, the wavelength should by small compared with any characteristic scales in the plasma. In other words the electron density and the magnetic flux density should not vary much within one wavelength.

References

Acuna, M. H., and N. F. Ness, The main magnetic field of Jupiter, *J. Geophys. Res., 81*, 2917, 1976.

Acuna., M. H., K. W. Behannon, and J. E. P. Connerney, Jupiter's magnetic field and magnetosphere, in *Physics of the Jovian Magnetosphere*, edited by A. J. Dessler, p. 1, Cambridge University Press, New York, 1983.

Alexander, J. K., M. D. Desch, M. L. Kaiser, and J. R. Thieman, Latitudinal beaming of Jupiter's low frequency radio emissions, *J. Geophys. Res., 84*, 5167, 1979.

Alexander, J. K., T. D. Carr, J. R. Thieman, J. J. Schauble, and A. C. Riddle, Synoptic observations of Jupiter's radio emissions: Average statistical properties observed by Voyager, *J. Geophys. Res., 86*, 8529, 1981.

Bagenal, F., and J. D. Sullivan, Direct plasma measurements in the Io torus and innner magnetosphere of Jupiter, *J. Geophys. Res., 86*, 8447, 1981.

Bagenal, F., R. L. McNutt, Jr., J. W. Belcher, H. S. Bridge, and J. D. Sullivan, Revised ion temperatures for Voyager plasma measurements in the Io plasma torus, *J. Geophys. Res., 90*, 1755, 1985.

Bagenal, F., and Y. Leblanc, Io's Alfvén wave pattern and the Jovian decametric arcs, *Astron. Astrophys., 197*, 311, 1988.

Barrow, C. H., Latitudinal beaming and local time effects in the decametre-wave radiation from Jupiter observed at the earth and from Voyager, *Astron. Astrophys., 101*, 142, 1981.

Barrow, C. H., A. Lecacheux, and Y. Leblanc, Arc structures in the Jovian decameter emission observed from the earth and from Voyager, *Astron. Astrophys., 106*, 94, 1982.

Barrow, C. H., and M. D. Desch, Solar wind control of Jupiter's hectometric radio emission, *Astron. Astrophys., 213*, 495, 1989.

Behannon, K. W., J. E. P. Connerney, and N. F. Ness, Saturn's magnetic tail: structure and dynamics, *Nature, 292*, 753, 1981.

Birmingham, T. J., J. K. Alexander, M. D. Desch, R. F. Hubbard, and B. M. Pedersen, Observations of electron gyroharmonic waves in the structure of the Io torus, *J. Geophys. Res., 86*, 8497, 1981.

Boischot, A., A. Lecacheux, M. L. Kaiser, M. D. Desch, J. K. Alexander, and J. W. Warwick, Radio Jupiter after Voyager: An overview of the Planetary Radio Astronomy observations, *J. Geophys. Res., 86*, 8213, 1981.

Boischot, A., Comparative study of the "Radio - Planets", in *Planetary Radio Emissions II*, edited by H.O. Rucker, S.J. Bauer, B.M. Pedersen, p. 15, Austrian Academy of Sciences Press Vienna, 1988.

Brown, L. W., Spectral behaviour of Jupiter near 1 MHz, *Astrophys. J., 194*, L159, 1974.

Budden, K. G., *Radio Waves in the Ionosphere*, Cambridge University Press, 1961.

Burke, B. F., and K. L. Franklin, Observations of a variable radio source associated with the planet Jupiter, *J. Geophys. Res., 60*, 213, 1955.

Carr, T. D., A. G. Smith, F. F. Donivan, and H. I. Register, The twelve-year periodicities of the decametric radiation of Jupiter, *Radio Sci., 5*, 495, 1970.

Carr, T. D., and M. D. Desch, Recent decametric and hectometric observations of Jupiter, in *Jupiter*, edited by T. Gehrels, p. 693, University of Arizona Press, Tucson, 1976.

Carr, T. D., M. D. Desch, and J. K. Alexander, Phenomenology of magnetospheric radio emissions, in *Physics of the Jovian Magnetosphere*, edited by A. J. Dessler, p. 226, Cambridge University Press, 1983.

Connerney, J. E. P., M. H. Acuna, and N. F. Ness, Modeling the Jovian current sheet and inner magnetosphere, *J. Geophys. Res., 86*, 8370, 1981.

Croley, D. R., P. F. Mizera, and J. F. Fennell, Signature of a parallel electric field in ion and electron distributions in velocity space, *J. Geophys. Res., 83*, 2701, 1978.

Daigne, G., and Y. Leblanc, Narrow band Jovian kilometric radiation; occurrence, polarization, and rotation period, J. Geophys. Res., 91, 7961, 1986.

Desch, M. D., and M. L. Kaiser, The occurrence rate, polarization character, and intensity of broadband Jovian kilometric radiation, *J. Geophys. Res., 85*,, 4248, 1980.

Desch, M. D., Evidence for solar wind control of Saturn radio emission, *J. Geophys. Res., 87*, 4549, 1982.

Desch, M. D., and H. O. Rucker, The relationship between Saturn kilometric radiation and the solar wind, *J. Geophys. Res., 88*, 8999, 1983.

Desch, M. D., and C. H. Barrow, Direct evidence for solar wind control of Jupiter's hectometer-wavelength radio emission, *J. Geophys. Res., 89*, 6819, 1984.

Divine, N., and H. B. Garrett, Charged particle distributions in Jupiter's magnetosphere, *J. Geophys. Res., 88*, 6889, 1983.

Dulk, G. A., Apparent changes in the rotation rate of Jupiter, *Icarus, 7*, 173, 1967.

Dusenbery, P. B., and L. R. Lyons, General concepts on the generation of auroral kilometric radiation, *J. Geophys. Res., 87*, 7467, 1982.

Gallagher, D. L., and N. D'Angelo, Correlations between solar wind parameters and auroral kilometric radiation intensity, *Geophys. Res. Lett.,8*, 1087, 1981.

Galopeau, P., P. Zarka, and D. Le Queau, Theoretical model of Saturn's kilometric radiation spectrum, *J. Geophys. Res., 94*, 8739, 1989.

Genova, F., Les emission radio aurorales des planetes, *Ann. Phys. Fr., 12*, 57, 1987.

Genova, F., P. Zarka, and C. H. Barrow, Voyager and Nancay observations of the Jovian radio-emission at different frequencies: Solar wind effect and source extent, *Astron. Astrophys., 182*, 159, 1987.

Goldstein, M. L., and J. R. Thieman, The formation of arcs in the dynamic spectra of Jovian decameter bursts, *J. Geophys. Res., 86*, 8569, 1981.

Goldstein, M. L., and C. K. Goertz, Theories of radio emissions and plasma waves, in *Physics of the Jovian Magnetosphere*, edited by A. J. Dessler, p. 317, Cambridge University Press, 1983.

Green, J. L., D. A. Gurnett, and S. D. Shawhan, The angular distribution of auroral kilometric radiation, *J. Geophys. Res., 82*, 1825, 1977.

Green, J. L., and D. A. Gurnett, Ray tracing of Jovian kilometric radiation, *Geophys. Res. Lett., 7*, 65, 1980.

Gulkis, S., and T. D. Carr, Radio rotation period of Jupiter, *Science, 154,*, 257, 1966.

Gulkis, S., and T. D. Carr, The main source of radio emission from the magnetosphere of Uranus, *J. Geophys. Res., 92*, 15159, 1987.

Gurnett, D. A., The earth as a radio source: Terrestrial kilometric radiation, *J. Geophys. Res., 79*, 4227, 1974.

Gurnett, D. A., and J. L. Green, On the polarization and origin of auroral kilometric radiation, *J. Geophys. Res., 83*, 689, 1978.

Haselgrove, J., Ray theory and a new method for ray tracing, in *Report of Conference on the Physics of the Ionosphere*, p. 355, London Physical Society, London, 1955.

Hashimoto, K., and M. L. Goldstein, A theory of the Io phase asymmetry of the Jovian decametric radiation, *J. Geophys. Res., 88*, 2010, 1983.

Hashimoto, K., A reconciliation of propagation modes of auroral kilometric radiation, *J. Geophys. Res., 89*, 7459, 1984.

Horanyi, M., T. E. Cravens, and H. J. Waite, The precipitation of energetic heavy ions into the upper atmosphere of Jupiter, *J. Geophys. Res., 93*, 7251, 1988.

Jones, D., and R. J. L. Grard, Propagation characteristics of electromagnetic waves in the magnetosphere, in *The Scientific Satellite Program During the International Magnetospheric Study*, edited by K. Knott and B. Battrick, p. 293, D. Reidel, Hingham Mass., 1976.

Jones, D., Latitudinal beaming of planetary radio emissions, *Nature, 288*, 225, 1980.

Jones, D., Radio wave emission from the Io torus, *Adv. Space Res., 1*, 333, 1981.

Jones, D., Io plasma torus and the source of Jovian kilometric radiation (bKOM), *Nature, 324*, 40, 1986.

Jones, D., and Y. Leblanc, Source of broadband kilometric radiation, *Ann. Geophys., Ser. A, 5*, 29, 1987.

Jones, D., and Y. Leblanc, Analysis of Jovian kilometric radiation simultaneously observed by Voyager 1 and Voyager 2, *Adv. Space Res., 8*, 453, 1989.

Kaiser, M. L., M. D. Desch, A. C. Riddle, A. Lecacheux, J. B. Pearce, J. K. Alexander, J. W. Warwick, and J. R. Thieman, Voyager spacecraft radio observations of Jupiter: Initial cruise results, *Geophys. Res. Lett., 6*, 507, 1979.

Kaiser, M. L., M. D. Desch, J. W. Warwick, and J. B. Pearce, Voyager detection of nonthermal radio emission from Saturn, *Science, 209*, 1238, 1980.

Kaiser, M. L., M. D. Desch, and A. Lecacheux, Saturnian kilometric radiation: Statistical properties and beam geometry, *Nature, 292*, 731, 1981.

Kaiser, M. L., and M. D. Desch, Saturnian kilometric radiation: Source locations, *J. Geophys. Res., 87*, 4555, 1982.

Kaiser, M. L., and M. D. Desch, Radio emissions from the planets earth, Jupiter and Saturn, *Rev. Geophys., 22,* 373, 1984.

Kurth, W. S., D. D. Barbosa, F. L. Scarf, D. A. Gurnett, and R. L. Poynter, Low frequency radio emissions from Jupiter: Jovian kilometric radiation, *Geophys. Res. Lett., 6,* 747, 1979.

Ladreiter, H. P., and Y. Leblanc, Jovian hectometric radiation - Beaming, polarization, source extension, and solar wind control, *Astron. Astrophys., 226*, 297, 1989. (=**Appendix A**)

Ladreiter, H. P., and Y. Leblanc, Source location of the Jovian hectometric radiation via ray-tracing technique, *J. Geophys. Res.*, 1990a, (in press). (=**Appendix B**)

Ladreiter, H. P., and Y. Leblanc, Modeling of the Jovian hectometric radiation: A three-dimensional study, *Ann. Geophys.*, 1990b, (in press). (=**Appendix C**)

Ladreiter, H. P., The cyclotron maser instability: Applications to low density magnetoplasmas, *Astrophys. J.*, 1990 (submitted). (=**Appendix D**)

Leblanc, Y., and G. Daigne, Broadband Jovian kilometric radiation: New results on polarization and beaming, *J. Geophys. Res., 90*, 12073, 1985a.

Leblanc, Y., and G. Daigne, The broadband Jovian kilometric radiation: Statistical properties and source model, in *Planetary Radio Emissions,* edited by H. O. Rucker and S. J. Bauer, p.112, Austrian Academy of Sciences Press, Vienna, 1985b.

Leblanc, Y., M. G. Aubier, A. Ortega-Molina, and A. Lecacheux, Overview of the Uranian radio emission: Polarization and constraints on source locations, *J. Geophys. Res., 92,* 15125, 1987.

Leblanc, Y., The kilometric Jovian radio sources at the Io torus, in *Planetary Radio Emissions II*, edited by H. O. Rucker, S. J. Bauer, and B. M. Pedersen, p. 149, Austrian Academy of Sciences Press, Vienna, 1988.

Lecacheux, A., B. M. Pedersen, A. C. Riddle, J. B. Pearce, A. Boischot, and J. W. Warwick, Some spectral characteristics of the hectometric Jovian emission, *J. Geophys. Res., 85*, 6877, 1980.

Lecacheux, A., Ray tracing in the Io plasma torus: Application to the PRA observations during Voyager 1's closest approach, *J. Geophys. Res., 86*, 8523, 1981.

Lecacheux, A., and F. Genova, Source location of Saturn kilometric radio emission, *J. Geophys. Res., 88*, 8993, 1983.

Lecacheux,A., and A. Ortega-Molina, Polarization and localization of the Uranian Radio Sources, *J. Geophys. Res., 92*, 15148, 1987.

Le Queau, D., R. Pellat, and A. Roux, Direct generation of the auroral kilometric radiation by the maser synchrotron instability: An analytical approach, *Phys. Fluids, 27*, 247, 1984a.

Le Queau, D., R. Pellat, and A. Roux, Direct generation of the auroral kilometric radiation by the Maser Synchrotron Instability: Physical mechanism and parametric study, *J. Geophys. Res., 89*, 2831, 1984b.

Le Queau, D., R. Pellat, and A. Roux, The maser synchrotron instability in an inhomogeneous medium: Application to the generation of the auroral kilometric radiation, *Ann. Geophys.,*

3, 273, 1985.

Le Queau, D., Planetary radio emissions from high magnetic latitudes: The "Cyclotron Maser" Theory, in *Planetary Radio Emissions II*, edited by H.O. Rucker, S.J. Bauer, and B.M. Pedersen, p. 381, Austrian Academy of Sciences Press, Vienna, 1988.

Louarn, P., A. Roux, H. de Feraudy, D. Le Queau, M. Andre, and L. Matson, Trapped electrons as a free energy source for the AKR, *J. Geophys. Res.*, 1990 (submitted).

Maeda,K., and T. D. Carr, Beam structure of Jupiter's decametric radiation, *Nature, 308*, 166, 1984.

Maeda, K., and T. D. Carr, Auroral origin of a component of Jupiter's decametric radiation, *J. Geophys. Res., 93*, 8491, 1988.

Menietti, J. D., J. L. Green, S. Gulkis, and N. F. Six, Jovian decametric arcs: An estimate of the required wave normal angles from three-dimensional ray tracing, *J. Geophys. Res., 89*, 9089, 1984.

Omidi, N., and D. A. Gurnett, Path-Integrated growth of auroral kilometric radiation, J. Geophys. Res., 89, 10801, 1984.

Omidi, N., C. S. Wu, and D. A. Gurnett, Generation of auroral kilometric and Z mode radiation by the cyclotron maser mechanism, *J. Geophys. Res, 89*, 883, 1984.

Ortega-Molina, A., and A. Lecacheux, Polarization response of the Voyager-PRA experiment at low frequencies, *Astron. Astrophys.*, 1990a (in press).

Ortega-Molina, A., and A. Lecacheux, Polarization of Jovian hectometric emission, *J. Geophys. Res.*, 1990b (in press).

Ortega-Molina, A., and G. Daigne, Polarization response of two crossed monopoles on a spacecraft, *Astron. Astrophys., 130*, 301, 1984.

Parker, E. N., Solar wind interaction with the geomagnetic field, *Rev. Geophys., 7*, 3, 1969.

Persson, H., Electric field parallel to the magnetic field in a low density plasma, *Phys. Fluids, 9*, 1090, 1966.

Poquerusse, M. and A. Lecacheux, First direct measurement of the beaming of Jupiter's decametric radiation, *Nature, 275*, 111, 1978.

Pritchett, P. L., and R. J. Strangeway, A simulation study of kilometric radiation generation along an auroral field line, *J. Geophys. Res., 90*, 9650, 1985.

Pritchett, P. L., and R. M. Winglee, Generation and propagation of kilometric radiation in the auroral plasma cavity, *J. Geophys. Res., 94*, 129, 1989.

Rabl,G. K. F., C. H. Barrow, and H. O. Rucker, Solar wind dependence of the Jovian hectometric radio emission: Comparison between Voyager 1 and 2 observations, *Astron. Astrophys.*, 1990 (in press).

Rucker, H. O., H. P. Ladreiter, Y. Leblanc, D. Jones, and W. S. Kurth, Jovian Plasma sheet density profile from low-frequency radio waves, *J. Geophys. Res, 94*, 3495, 1989.

Sandel, B. R., D. E. Shemansky, A. L. Broadfoot, J. B. Holberg, G. R. Smith, J. C. McConnell, D. F. Strobel, S. K. Atreya, T. M. Donahue, H. W. Moos, D. M. Hunten, R. B. Pomphrey,

and S. Linick, Extreme ultraviolet observations from the Voyager 2 encounter with Saturn, *Science, 215*, 548, 1982.

Spiegel, M. R., Statistics, Schaum's outline. McGraw Hill Book Co., 1976.

Staelin, D. H., Character of the Jovian decametric arcs, *J. Geophys.* Res., 86, 8581, 1981.

Stix, T. H. , *The Theory of Plasma Waves,* McGraw-Hill, New York, 1962.

Strangeway, R. J., Wave dispersion and ray propagation in a weakly relativistic electron plasma: Implications for the generation of auroral kilometric radiation, *J. Geophys. Res., 90,* 9675, 1985.

Warwick, J. W., Dynamic spectra of Jupiter's decametric emission, *Astrophys. J., 137,* 41, 1963.

Warwick, J. W., J. B. Pearce, R. G. Peltzer, and A. C. Riddle, Planetary radio astronomy experiment for Voyager missions, *Space Sci. Rev., 21*, 309, 1977.

Warwick, J. W., J. B. Pearce, A. C. Riddle, J. K. Alexander, M. D. Desch, M. L. Kaiser, J. R. Thieman, T. D. Carr, S. Gulkis, A. Boischot, C. C. Harvey, and B. M. Pedersen, Voyager 1 planetary radio astronomy observations near Jupiter, *Science, 204*, 955, 1979.

Wong, H. K., C. S. Wu, F. J. Ke, R. S. Schneider, and L. F. Ziebell, Electromagnetic cyclotron-loss-cone instability associated with weakly relativistic electrons, *J. Plasma Phys., 28,* 503, 1982.

Wu, C. S., and L. C. Lee, A theory of the terrestrial kilometric radiation, *Astrophys. J., 230,* 621, 1979.

Wu, C. S., H. K. Wong, D. J. Gorney, and L. C. Lee, Generation of auroral kilometric radiation, *J. Geophys. Res., 87,* 4476, 1982.

Wu, C. S., Kinetic cyclotron and synchrotron maser instabilities: Radio emission processes by direct amplification of radiation, *Space Sci. Rev., 41,* 215, 1985.

Zarka, P., and F. Genova, Low frequency Jovian emission and solar wind magnetic sector structure, *Nature, 306,* 767, 1983.

Zarka, P., D. Le Queau, and F. Genova, The maser synchrotron instability in an inhomogeneous medium: Determination of the spectral intensity of the auroral kilometric radiation, *J. Geophys. Res., 91,* 13542, 1986.